Mixture Preparation and Injection Strategy in Direct Injection Spark Ignition Engines



Joseph Camm

Exeter College

University of Oxford

A thesis submitted in partial fulfilment of the requirements for the degree of Doctor of Philosophy

Trinity 2016

Dedicated to my parents, Cheryl and John,
who taught me everything I know,
except the guitar

Acknowledgements

I would like to thank:

Professor Richard Stone; for his supervision and enthusiasm, for his expert technical guidance and problem resolving throughout the project, and for making possible my study in his research group at the University of Oxford.

Dave Richardson of Jaguar Land Rover; for his industrial supervision and insight, frequent meetings in Oxford and Coventry to discuss progress, the opportunity to present my findings to engineers at Jaguar Land Rover and receive feedback.

The University of Oxford Clarendon Fund, the EPSRC and Jaguar Land Rover for generous financial support.

Professor Martin Davy; for his interest in my work since joining the research group and many helpful discussions along the way, and for giving me a job afterwards.

Former and current fellow students Dr Mengchen Hu, Dr Felix Leach, Dr Nathan Hinton, Riyaz Ismail, Nick Papaioannou, Johannes Mutzke, Safwan Hanis bin Mohd Murad, Louis Nicholson, Blane Scott, Leo Fang and Priyav Shah of the Combustion and Engines research group, Dr Kun Liang and Dr Ian Berryman of the Cryogenics research group, Dr Christopher Willman of the Department of Physics, and academic visitor Dr Zhifu Zhou of Xi'an Jiao Tong University, China; for putting up with sharing an office with me for four years, and for providing intellectual stimulation as well as amusing diversion at necessary times.

Professor Ben Williams; for his great patience and help with laser diagnostics and optical engine operation as well as many theoretical aspects of optics.

Members of the Workshop, Maintenance, Electronics and IT teams at the Department of Engineering Science, for helping to design and build the spray chamber, and for working to keep my experiments and simulations running.

My wife, Katherine; for her unending support, for her superior grasp of the English language, and for mostly succeeding to keep me to a 9–5 work day.

My mother, Cheryl, and late father, John; for being the proudest parents in the world and for always encouraging me to new heights.

Abstract

Joseph Camm
Exeter College

Department of Engineering Science
Trinity 2016

The mixture preparation process in a Direct Injection Spark Ignition (DISI) engine has a strong influence on the processes that follow it, including combustion and the formation of pollutant emissions. The formation of particulate matter during DISI engine combustion is a complex phenomenon that has proven difficult to predict. Vehicle tailpipe emissions are subject to increasingly stringent particulate matter emissions worldwide; in Europe, particulate number emission limits came into force in 2014 and these will become an order of magnitude stricter in 2017. The choice of injection strategy can play an important role in reducing the source of these emissions during combustion, which are chiefly caused by rich mixture combustion. This in turn occurs due to mixture inhomogeneity and combustion around liquid films and liquid droplets.

This thesis outlines work undertaken to improve understanding of gasoline mixture preparation processes, simulation of droplet evaporation, flash boiling, spray evaporation and spray penetration, and experimental investigation of fuel sprays in an optical spray chamber and an optical engine. Assessments of the suitability of different sub-models for spray simulation were needed, in order to capture enough of the spray physics and fuel behaviour to aid correct prediction of spray evaporation, mixture homogeneity and fuel impingement by Computational Fluid Dynamics (CFD) packages. Phenomena have been explored on the individual droplet scale, including non-ideal behaviour of fuel mixtures, models for droplet heating/cooling during spray evaporation, the behaviour of superheated droplets under flash boiling conditions and multi-component fuel evaporation formulations. Detailed droplet evaporation routines have been created in MATLAB and single droplet studies performed under a range of conditions encountered in a DISI engine cylinder. From these results, recommendations have been made regarding the required complexity of droplet models for accurate predictions, at various fuel injection conditions.

It was found necessary to model the non-ideal vapour-liquid equilibrium of ethanol-containing model gasoline fuels, for ethanol content of 10% by volume and above, and to include models for a non-uniform droplet temperature model across most fuels and in-cylinder conditions studied. In addition, the effect of

finite liquid species mixing in the fuel droplet was deemed to be important to consider for non-ideal fuel mixtures.

Sub-models for droplet evaporation, incorporating non-ideal fuel behaviour, have been created for an OpenFOAM Lagrangian Particle Tracking spray CFD solver. Results from these runs confirm that trends observed at a single droplet level are typically apparent at the spray scale. It was then possible to predict the effects that different evaporation modelling approaches had on spray penetration, which is important when assessing the extent of fuel spray impingement. Including a model for the non-uniform temperature distribution inside the droplet (finite thermal conductivity) was found not to influence the overall spray behaviour as much as expected, due to the competing effects of droplet break-up, droplet collisions and gas phase cooling.

Numerical predictions have been compared with findings from spray imaging investigations in a purpose-built continuous flow, atmospheric pressure spray chamber, and with findings from optical engine experiments. In addition, adiabatic flash calculations have been performed to predict the degree of flash evaporation expected under flash boiling conditions, to help to interpret the results from flash boiling spray experiments.

Various images from fuel spray experiments that represent different engine conditions have been taken and analysed for axial penetration, fuel impingement, structure and evaporation rate. These have helped to understand how a certain spray might lead to conditions where increased particulate emissions are likely. The fuels used during these tests were model gasoline fuels, containing 15% methanol by volume. This type of mixture represented fuel commercially available in some markets and was chosen to investigate the effects of a highly non-ideal and volatile fuel under both superheated and sub-cooled spray conditions. It was found that, as the degree of superheat was increased, the spray collapse tended to intensify, leading eventually to increased liquid penetration, a greater degree of spray impingement and a stratification of fuel towards the cylinder centre.

Optical engine experiments have been performed using an early injection strategy for homogeneous operation, at 0.5 bar inlet plenum pressure, for various fuel temperatures and injection timings. Particulate number measurements were taken from the exhaust, and were found to be highest when the fuel was hottest and at typical early injection timings. Retarding or advancing the injection was found to reduce the particulate number count.

Contents

List of Abbreviations and Nomenclature **ix**

1 Introduction **1**

1.1 Gasoline Direct Injection Engines 1

1.2 Particulate Matter 3

1.2.1 Types of particulate emissions 3

1.2.2 Impacts on health 5

1.2.3 Gasoline particulate filters 6

1.2.4 Worldwide passenger car PM emissions legislation 6

1.3 Factors Affecting GDI Engine PM Emissions 9

1.3.1 The effects of the mixture preparation strategy 9

1.3.2 The effects of fuel composition 21

1.3.3 Other sources of particulate generation 25

1.3.4 Role of other engine parameters 26

1.4 Summary 27

2 Spray Simulation Theory and Techniques **29**

2.1 Droplet Evaporation Theory 29

2.1.1 Single component evaporation 29

2.1.2 Droplet temperature modelling 36

2.1.3 Multi-component droplet evaporation 42

2.1.4 Superheated droplets 55

2.1.5 Inter-droplet effects 57

2.1.6 Implementation in MATLAB 58

2.1.7 Model validation 61

2.2 Lagrangian Spray Simulation 68

2.3 Summary 69

3 Experimental Equipment and Techniques 71
3.1 Fuel Injector . . . 71
3.2 Spray Chamber . . . 72
3.2.1 Motivation for a spray chamber . . . 72
3.2.2 Spray chamber purge rate . . . 73
3.2.3 Spray chamber flow investigation . . . 75
3.2.4 Spray rig manufacturing design . . . 77
3.2.5 Ancillary equipment . . . 78
3.2.6 Completed spray chamber experiment . . . 87
3.3 Single Cylinder Optical Engine . . . 88
3.3.1 Particulate measurements . . . 92
3.4 Gasoline Model Fuels . . . 93
3.5 Image Analysis . . . 99
3.6 Summary . . . 102

4 Results and Recommendations from Single Droplet Studies 104
4.1 Droplet Sizes . . . 104
4.2 Droplet Number Density . . . 105
4.3 Simple Multi-Component Models for Gasoline . . . 108
4.3.1 Iso-octane/ethanol mixtures . . . 108
4.3.2 Multi-component mixtures with ethanol and methanol . . . 112
4.4 Droplet Temperature Modelling Results . . . 116
4.5 Liquid Diffusion-Controlled Multi-Component Models . . . 125
4.5.1 Binary liquid diffusion-controlled model . . . 125
4.5.2 Pseudo-binary multi-component liquid diffusion-controlled model . . . 133
4.6 Superheated Droplets . . . 138
4.7 Summary and Recommendations . . . 146

5 Single Hole Spray Simulations 150
5.1 OpenFOAM Spray Simulation and Sub-Models for GDI Sprays . . . 150
5.2 Multi-Component Evaporation Model and Non-Ideal Fuel Behaviour 159
5.2.1 Sensitivity studies . . . 159
5.2.2 CFD results . . . 162
5.3 Droplet Temperature Models . . . 173
5.4 Summary . . . 182

6 Spray Chamber Images and Analysis **186**
6.1 Backlit Images . . . 186
6.2 Mie Scattering Images . . . 192
6.2.1 Comparison to single droplet simulations . . . 203
6.3 Comparison With Engine Particulate Emissions . . . 208
6.3.1 Experiments performed . . . 208
6.3.2 Particulate matter measurement results . . . 210
6.3.3 Motoring fuel spray images . . . 214
6.4 Summary . . . 217

7 Original Work, Conclusions and Future Work **221**
7.1 Originalities . . . 221
7.2 Conclusions . . . 222
7.2.1 Non-ideal multi-component fuel models . . . 222
7.2.2 Spray droplet temperature and superheat models . . . 224
7.2.3 Spray droplet internal composition models . . . 225
7.2.4 Suitable model fuels for spray droplet evaporation . . . 226
7.2.5 Effect of fuel saturation pressure on spray structure . . . 226
7.2.6 Usage of single droplet models to predict spray trends . . . 228
7.2.7 Injection timing and spray superheat effects on M15 combustion and particulate emissions . . . 228
7.3 Possible Extension Work . . . 230
7.3.1 Droplet simulations . . . 230
7.3.2 CFD simulations . . . 231
7.3.3 Experimental work . . . 232
7.4 Publications Relating to this Thesis . . . 233

References **235**

List of Abbreviations and Nomenclature

Acronyms

ATDC . After Top Dead Centre

BDC . . Bottom Dead Centre

BTDC . Before Top Dead Centre

°CA . . . Degrees Crank Angle

CF . . . Conformity Factor

CFD . . Computational Fluid Dynamics

DAQ . . Data Acquisition System

DISI . . Direct Injection Spark Ignition

DMS . . Differential Mobility Spectrometer

DPF . . Diesel Particulate Filter

DVPE . Dry Vapour Pressure Equivalent

EGR . . Exhaust Gas Recirculation

ETCS . Engine Timing and Control System

EU . . . European Union

EVC . . Exhaust Valve Closure

EVO . . Exhaust Valve Opening

E*xx* . . . Gasoline containing $xx\%$ Ethanol by volume

e*xx* . . . Gasoline containing $xx\%$ Ethanol by mole

GDI . . Gasoline Direct Injection

HRM . . Homogeneous Relaxation Model

IVC . . . Inlet Valve Closure

IVO . . . Inlet Valve Opening

LPT . . Lagrangian Particle Tracking

M*xx* . . Gasoline containing $xx\%$ Methanol by volume

NO . . . Nitric Oxide

NO_2 . . Nitrogen Dioxide

NO_x . . mixture of Nitric Oxide and Nitrogen Dioxide

PAH . . Polycyclic Aromatic Hydrocarbons

PDE . . Partial Differential Equation

PEMS . Portable Emissions Measurement System

PFI . . . Port Fuel Injection

PM . . . Particulate Matter

RANS . Reynolds-Averaged Navier-Stokes

RDE . . Real Driving Emissions

RON . . Research Octane Number

RVP . . Reid Vapour Pressure

SGDI . . Spray-Guided Direct Injection

SMD . . Sauter Mean Diameter

SOI . . . Start Of Injection

TDC . . Top Dead Centre

TTL . . Transistor-Transistor Logic

TWC . . Three-Way Catalyst

T*xx* . . . Temperature at which $xx\%$ of liquid by volume has evaporated during distillation

UHC . . Unburnt Hydrocarbon

ULG . . Unleaded Gasoline

WGDI . Wall-Guided Direct Injection

WLTP . World-harmonized Light-duty Test Procedure

Nomenclature

A . . . . Droplet projected area, $\pi d^2/4$

A . . . . Plume section area

a_{mn} . . . UNIFAC model group interaction parameter

B . . . . Chamber bore

$[B]$ . . . Inverse diffusion coefficient matrix

B_T . . . . Spalding heat transfer number, $c_{p\mathrm{F}}(T_\infty - T_\mathrm{s})/L_\mathrm{eff}$

B_Y . . . Spalding mass transfer number, $(Y_\mathrm{Fs} - Y_{\mathrm{F}\infty})/(1 - Y_\mathrm{Fs})$

Bi . . . . Biot number, $k_T d/\lambda_\mathrm{L}$

C_D . . . Droplet drag coefficient, $D/\frac{1}{2}\rho U^2 A$

C_F . . . . Droplet friction coefficient

c . . . . . Specific heat capacity

c_p . . . . Specific heat capacity at constant pressure

D . . . . Diffusion coefficient

D . . . . Droplet drag force

$Đ$ . . . . Maxwell-Stefan diffusion coefficient

d . . . . . Droplet diameter

d_p . . . . Particulate diameter

f . . . . Fugacity

f . . . . Droplet frequency

G_E . . . . Excess Gibbs free energy due to non-ideal mixing

G_Ls . . . Droplet surface liquid temperature gradient

G_{12}, G_{21} . NRTL model binary mixture parameters

$\Delta g_{12}, \Delta g_{21}$ NRTL model fitting parameters

h . . . . Specific enthalpy

I . . . . . Image array

(J) . . . Vector of component mass fluxes

K . . . . d^2 law rate constant, $8\rho D \ln(1 + B_Y)/\rho_\mathrm{L}$

k . . . . . turbulent kinetic energy

k_T . . . . Heat transfer coefficient

k_Y . . . . Mass transfer coefficient

L . . . . Enthalpy of vaporization

L . . . . Chamber optical length

L_eff . . . Effective latent heat of vaporization, $L + \dot{Q}_\mathrm{L}/\dot{m}$

Le . . . . Lewis number, $\lambda/\rho c_p D$

l . . . . . UNIFAC model parameter

M . . . . Molar mass

m . . . . Droplet mass

$\dot{m}$ . . . . Evaporation rate

$\dot{m}_\mathrm{diff}$ . . . Diffusive component of evaporation rate

$\dot{m}_\mathrm{plume}$ . . Spray plume mass flow rate

N . . . . Number of components

N_r . . . . Number of radial grid-points

Nu . . . . Nusselt number, $k_T d/\lambda$

Nu' . . . Modified Nusselt number, $\mathrm{Nu} B_T/\ln(1 + B_T)$

Nu_0 . . . Nusselt number for hard sphere

n . . . . Number of moles present

n . . . . Rosin-Rammler exponent

Oh . . . . Ohnesorge number, $\mu_\mathrm{L}/\sqrt{\rho_\mathrm{L}\sigma d}$

Pe_T . . . Péclet number for heat transfer, $\mathrm{Re}\,\mathrm{Pr}$

Pr . . . . Prandtl number, $c_p\mu/\lambda$

p . . . . . Pressure

p_vap . . . Vapour pressure

Q . . . . Volume flow rate

Q_k . . . . Functional group normalized surface area

$\dot{Q}_\mathrm{L}$ . . . . Heat transferred into droplet

q . . . . . UNIFAC model normalized molecule surface area parameter

R . . . . Specific gas constant, R_0/M

R_k . . . . Functional group normalized volume

R_p . . . . Fuel saturation pressure ratio

R_0 . . . . Universal gas constant, 8315 J/kmol·K

RI . . . . Relevance index

Re . . . . Reynolds number, $\rho U d/\mu$

r . . . . . Radial co-ordinate

r . . . . . UNIFAC model normalized molecule volume parameter

r . . . . . Plume cone radius

S . . . . Droplet spacing

Sc . . . . Schmidt number, $\rho D/\mu$

Sh . . . . Sherwood number, $k_Y d/D$

Sh' . . . . Modified Sherwood number, $\mathrm{Sh} B_Y / \ln(1 + B_Y)$

Sh_0 . . . Sherwood number for hard sphere

T . . . . Temperature

t . . . . . Time

$t^\star$ . . . . Non-dimensional time

U . . . . Relative droplet velocity

U_{Lmax} . . Maximum liquid velocity inside droplet

u . . . . Radial velocity

V . . . . Volume

V . . . . Image array as column vector

V . . . . Weber number, $\rho_{\mathrm{A}} U^2 d/\sigma$

V . . . . Chamber volume

x . . . . Droplet position

Y . . . . Gas phase mass fraction

z . . . . . Co-ordination number, 10

z . . . . . Axial distance from nozzle

Greek:

α . . . . Thermal diffusivity

α . . . . NRTL model fitting parameter

Γ_k . . . . Diffusion thermodynamic correction factor

Γ_k . . . . UNIFAC model group residual activity coefficient

γ . . . . Activity coefficient

δ . . . . . Liquid thermal boundary layer thickness, $\sqrt{\pi \chi \alpha_{\mathrm{L}} t} \leqslant d/4.514$

δ . . . . . Vapour thermal or mass transfer boundary layer thickness

ε . . . . . Evaporative flux fraction

ε . . . . . Turbulent kinetic energy dissipation rate

η . . . . . Droplet interaction reduction factor

θ . . . . . UNIFAC model area fraction

θ . . . . . Injector plume half-angle

λ . . . . Thermal conductivity

λ . . . . Excess air ratio

μ . . . . Dynamic viscosity

$\mu^\star$ . . . . Chemical potential

ν_k . . . . Number of functional groups present

χ . . . . Enhancement to liquid thermal conductivity or liquid diffusion

ρ . . . . . Density

σ . . . . Surface tension

τ . . . . . Finite difference parameter, $\chi \alpha_{\mathrm{L}} \Delta t/(\Delta r)^2$ or $\chi_{\mathrm{mass}} D_{\mathrm{L}} \Delta t/(\Delta r)^2$

τ_{12}, τ_{21} . . NRTL model binary mixture parameters

Φ . . . . UNIFAC model volume fraction

ϕ . . . . Fugacity coefficient

Ψ_{mn} . . . UNIFAC model interaction parameter

Subscripts, superscripts and accents:

$\widetilde{a}$ . . . . . Mole fraction

amb . . . Ambient

A . . . . Air

b . . . . . Boiling point

c . . . . . Critical point

c . . . . . Critical

d . . . . . Droplet interior

cyl . . . . Cylinder

F . . . . Fuel vapour

inj . . . . Injection

iso . . . . Isolated droplet

j . . . . . Radial grid point number

k . . . . . Time step number

L . . . . Liquid

life . . . . Lifetime

n . . . . Droplet number

p . . . . . Particulates

ref . . . . Reference

RR . . . Rosin-Rammler

s . . . . . Droplet surface

SH . . . . Superheat

T . . . . Energy balance

vap . . . Vapour

WB . . . Wet-bulb

Y . . . . Mass balance

0 . . . . . Initial

∞ . . . . Far from the droplet

$\ominus$ . . . . Standard temperature and pressure

1 Introduction

The formation of particulate matter (PM) during gasoline direct injection (GDI) engine combustion is a complex phenomenon that is difficult to predict, yet its study is vital in order to comply with increasingly stringent worldwide standards in relation to vehicle tailpipe particulate matter emissions. These standards exist to mitigate the detrimental effect of airborne particulates on air quality and human health. Air/fuel mixture preparation can play an important role in reducing the source of these emissions, chiefly caused by rich mixture combustion, which in turn occurs due to mixture inhomogeneity and combustion around liquid films and liquid droplets.

This research aims to provide greater understanding of the fuel spray evaporation process and of spray shape formation, to provide insight into in-cylinder air/fuel mixture preparation. To improve understanding of how injection strategy, in-cylinder conditions and fuel composition affect the evaporation of droplets in fuel sprays in a GDI engine, a detailed single droplet model is used. Not only can this provide predictions of fuel spray evaporative performance at a given condition but it can also be used to assess different droplet and spray modelling strategies, in order to determine the level of detail required to model accurately the fuel spray evaporation process. Results from spray imaging provide comparison and validation for trends found in the droplet and spray modelling as well as additional insight into the behaviour of the spray, its propensity for impingement onto surfaces in a GDI engine, and hence the likelihood of creating a source for combustion-generated particulates.

1.1 Gasoline Direct Injection Engines

A Gasoline Direct Injection engine, also known as a Direct Injection Spark Ignition (DISI) engine, is a spark ignition engine in which fuel is delivered straight into the

engine cylinder, as shown in Figure 1.1. Typically these engines offer increased thermal efficiency and specific output, compared to traditional Port Fuel Injection (PFI) spark ignition engines. Consequently, GDI engines are often used in automotive systems as the sole prime mover (both in high and low power output applications) or as part of a hybrid system, *e.g.* [1, 2, 3, 4]. The injection of gasoline fuel directly into each cylinder causes evaporative cooling of the air charge, lowering the temperature throughout the cycle and in turn reducing heat transfer and allowing the use of a higher compression ratio. When an early injection strategy is used (*i.e.* injection occurs during the induction stroke) the engine operates in a homogeneous mode. During this, the lower charge temperature causes an increase in volumetric efficiency. The fuel delivery to each cylinder may be more accurately controlled using GDI techniques than when using PFI techniques, since some fuel may remain in fuel films or as fuel vapour and not be inducted into the engine when injected into the intake port. These factors each contribute to higher engine efficiencies at any speed or load. During part load operation, GDI allows the engine to operate in stratified mode, in which there is ignitable (rich) mixture near the spark plug, yet a lean overall mixture [5]. This also allows reduced throttling at part load, which in turn reduces engine pumping losses. This can result in further fuel consumption improvements. Due to the overall lean mixture, care must be taken when operating in this mode, as a traditional Three-Way Catalyst (TWC) will not operate efficiently to reduce nitrogen oxides (nitric oxide (NO) and nitrogen dioxide (NO_2), together known as NO_x). Therefore, it will be required to operate either with a very lean mixture, to dilute the combustion with large amounts of Exhaust Gas Recirculation (EGR) to reduce combustion temperatures, or to use a NO_x trap to remove the NO_x from the exhaust.

The time available for preparation of a homogeneous mixture is reduced in comparison to PFI engines, particularly with stratified operation. There is, therefore, a greater tendency towards localized rich mixture or liquid fuel combustion, which leads to higher PM and unburnt hydrocarbon (UHC) emissions from GDI engines [7].

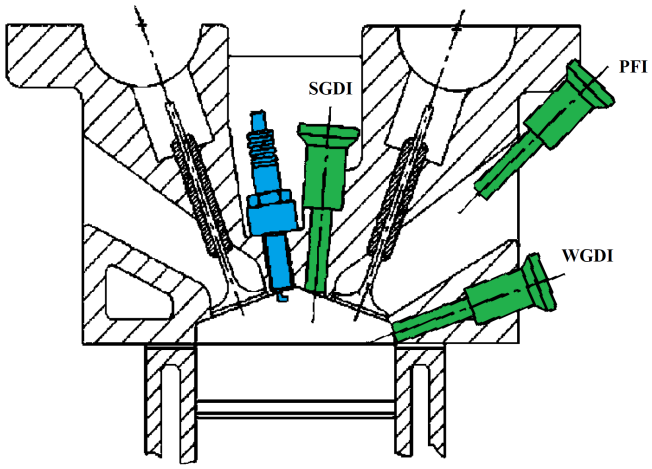


Figure 1.1: Schematics of potential injector locations for two types of GDI engine design, wall-guided (WGDI) and spray-guided (SGDI), and the non-GDI design also used in gasoline-powered engines, PFI, adapted from [6]

The first modern GDI combustion system for a car was designed and implemented by Mitsubishi, using a spherical bowl piston and a wall-guided GDI (WGDI) system [8]. These engines demonstrated increased efficiency; however, impingement of the fuel spray on the cylinder walls and piston crown caused pools of liquid fuel to form, resulting in high PM and UHC emissions when the liquid fuel burned. More recently, manufacturers of GDI engines have tended to utilize a spray-guided GDI (SGDI) system (for example [1]), using a high pressure fuel injector to introduce fuel and distribute it around the cylinder. This reduces the likelihood of high PM emissions caused by pool fires, as fuel is no longer directed at the walls or piston for part load operation and finer atomization of the fuel is achieved. In this thesis, the research is primarily concerned with SGDI technology which utilizes high pressure multi-hole fuel injection equipment (for example the technologies found in [9, 10, 11]).

1.2 Particulate Matter

1.2.1 Types of particulate emissions

Engine exhaust typically contains particulates ranging in size and composition. The largest size found in any abundance might be 1 µm [12] and the particulate size distribution is typically bimodal, as summarized in Figure 1.2. The smaller of the two modes, the nucleation mode, is made up of particulates with sizes under 50 nm

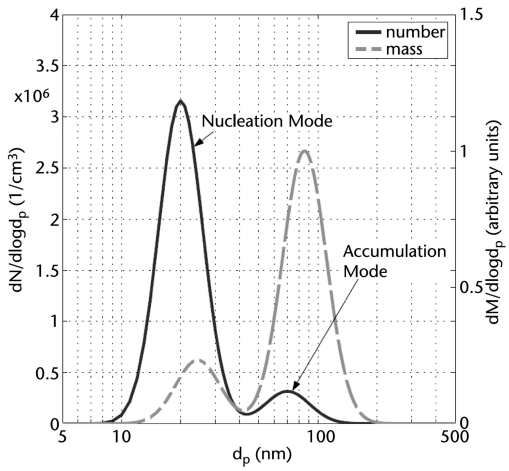


Figure 1.2: Typical engine exhaust particulate number count and particulate mass measurement as a function of particulate size, which shows a bimodal distribution, reproduced with permission from [7]. The smaller nucleation mode contains the majority of the number of particulates but the larger accumulation mode contains the larger share of the total particulate mass. The mass has been calculated by assuming spherical particles with a constant, arbitrary density

[12]. With regard to GDI engine emissions in particular, a size range of up to 20 nm was found [13]. Small primary particles (of roughly spherical shape and typically with high carbon content) tend to combine to form agglomerates, which make up the larger of the two modes, known as the accumulation mode. Particulates in this mode may have representative diameters between 50 nm to many hundreds of nm; however, the agglomerate shape may be far from spherical due to the random process of formation from the spherical primary particles.

The exhaust particulate composition is broadly sorted into five fractions. These fractions may be volatile (essentially in liquid phase) or non-volatile (essentially solid) [12]. The volatile fractions are sulphates, nitrates and organics (*e.g.* hydrocarbons), and the non-volatile fractions are classed as carbonaceous (mostly carbon) or ash (non-combustible material such as metallic elements). The term 'soot' is used to describe the particulates that begin to form in-cylinder during rich mixture combustion. At elevated temperatures and with a low concentration of immediate oxygen, other reactions (*e.g.* pyrolysis) can occur in preference to oxidation, causing the growth of polycyclic aromatic hydrocarbons (PAH) and their conversion to carbon-rich primary particles (see Section 1.3.2). These particulates are largely

carbonaceous, however, during the combustion process, the expansion stroke, the transit through the exhaust system and even the exit to the atmosphere, other fractions may adsorb onto the particulates' surfaces. The volatile fractions tend to condense from gas to form particulates in the exhaust system, or once in the atmosphere, and are part of the nucleation mode.

1.2.2 Impacts on health

Particulates below 10 µm can have serious effects on health when inhaled, due to their high deposition efficiency in the human respiratory system [12]. Particulates of size 1–10 µm would most likely be caught in the nasal passage before reaching the trachea, whereas smaller particulates would penetrate further, and deposit in the bronchi and deeper in the lungs. Ultra-fine particulates (defined as less than 100 nm) can cross the alveoli and enter the bloodstream [14]. This high deposition efficiency, summarized in Figure 1.3, has been shown to cause a range of problems including: allergic reactions, lung dysfunction, irritation, cancers [15]; inflammation of the eyes, nose and throat, susceptibility to lung infection and bronchitis, worsening of asthma [16]; breach of the pulmonary epithelium (lung walls) in the alveoli by very fine particulates, causing damage and possibly facilitating the passage of particulates into the bloodstream, increasing risk of cardio-pulmonary diseases [12]. Some of the particulate fractions consist of directly carcinogenic material (such as PAH) but it has been shown that even biologically inert particulates, when small enough, can induce toxic effects in the lungs [17].

There is concern that inhalation of the smallest particulates might pose the greatest health risk due to the ease with which they can pass into the bloodstream. This concern is reflected in the particulate number counts required in EU emissions legislation (see Section 1.2.4) since the smallest particulates tend to be produced in the greatest number [12, 20]. The EU particulate number test uses a measurement procedure that removes volatile particulates and has a count efficiency of 50% at 23 nm and 90% at 41 nm. In practice this means that only solid particulates, usually the particulate agglomerates that are found in the accumulation mode, are measured.

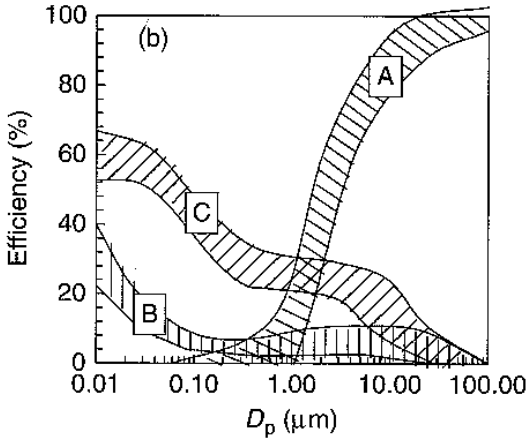


Figure 1.3: Likelihood of capture of various sizes of particles in different parts of the human respiratory system, taken from [12], citing Spengler and Wilson [18] and the International Commission on Radiological Protection [19]. Band A represents the nasal and pharynx (throat) areas, Band B represents the trachea and bronchus areas (primary passages into the lungs) and Band C represents pulmonary deposition (in the lungs). Permission to reproduce this figure has been granted by John Wiley and Sons

1.2.3 Gasoline particulate filters

In vehicles with a diesel engine, tailpipe particulate levels have been reduced by using Diesel Particulate Filters (DPFs). A similar device has been suggested for vehicles with GDI engines, known as a gasoline particulate filter. Once a DPF becomes full of PM, it undergoes regeneration by briefly operating the engine at higher load to give a high exhaust temperature, allowing the soot to be oxidized and the filter cleared. One hurdle to applying such a filter to a GDI engine system is that supplying the conditions for regeneration is more difficult, since with lean mixtures there is adequate oxygen for oxidation, but insufficient temperature, and at stoichiometric or rich conditions the exhaust is hot enough, but there is little oxygen. In addition, preventing many of the conditions for PM generation within the cylinder could be seen to be a more cost effective solution than providing another element in the exhaust aftertreatment system.

1.2.4 Worldwide passenger car PM emissions legislation

GDI engines are typically used only in passenger car (light duty) applications. PM emissions legislation varies worldwide and new standards are introduced from

Table 1.1: Summary of PM emissions limits worldwide for vehicles with GDI engines, showing dates of implementation and the drive cycle used [21, 22, 23, 24, 25, 26]. Note that, in the EU, there is both a particulate number limit and a particulate mass limit but compliance with the number limit is more difficult to achieve

Location (Reference)	Standard name	Legislative organization	Type of measurement	Drive cycle	Allowable amount	Date of implementation
EU [18]	Euro 6b	EU	Number	NEDC	6×10^{12}/km	September 2014
	Euro 6c	EU	Number	NEDC	6×10^{11}/km	September 2017
USA [19]	EPA Tier 2	US EPA	Mass	FTP-75	10 mg/mi (20 mg/mi for bins 7 and 8)	Phase in: 2004-2009
[20]	EPA Tier 3	US EPA	Mass	FTP-75	3 mg/mi	Phase in: 2017-2021
California, USA [21]	LEV III	CARB	Mass	FTP-75	10 mg/mi 3 mg/mi 1 mg/mi	2015 2017-2021 2025-2028
Japan [22]	New Post Long-Term Standards	Japan MOE	Mass	JC08	5 mg/km	2009
	-	Japan MOE	Mass	WLTP	5 mg/km	2018
China [23]	China 5	China MEP	Mass	NEDC	4.5 mg/km	Phase in: 2013-2018

time-to-time that reduce the allowed amount from a legislative test. Before a vehicle can be sold in a certain market it must meet these criteria in a test known as type-approval. The levels of PM emission are recorded over a drive cycle and then expressed as a mean amount per km or per mile driven; the drive cycles also differ around the world and are subject to change to enable them to more closely reflect vehicle use in practice. The current and expected future emissions requirements are summarized in Table 1.1.

In order to ensure that PM emissions from the legislative test correspond more closely to those occurring in real vehicle usage, some regions (EU - [27, 28], Japan – Table 1.1) are planning a switch to the WLTP test cycle, which has a higher average speed and periods of greater vehicle acceleration [29], but with the same emissions limit per km. The vehicle speed profiles for both the NEDC and WLTP cycle are shown in Figure 1.4. The WLTP procedure places tighter restrictions on vehicle set-up options, which may make it more difficult for vehicle manufacturers to meet the standard. Hence, there will be an expanded envelope of speed and load points that the engine will encounter during the drive cycle, which must be

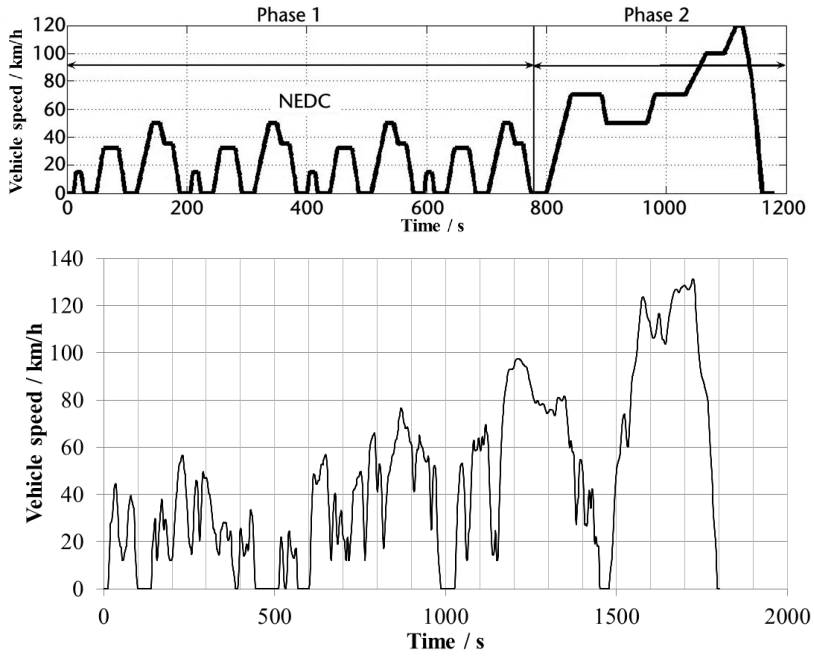


Figure 1.4: Both the NEDC and the WLTP drive cycle as a function of time. The NEDC cycle image was taken from [7] (used with permission) and the WLTP cycle was taken from [13], created from data presented in [30]

considered when an engine combustion and direct injection system is designed for meeting a PM emission target.

In addition to the WLTP, there are plans for a European Real Driving Emissions (RDE) program to be introduced for vehicle type-approval, which may include a vehicle-emitted particulate number count. This was originally planned for introduction in 2017, to coincide with the introduction of Euro 6c [31]. This would involve a Portable Emission Measurement System (PEMS) to be attached to the rear of a vehicle, which would then be driven around a real road system within a set of limits (*e.g.* road gradient, ambient temperature, vehicle acceleration). The particulate number count per km would be measured by the PEMS and a Conformity Factor (CF) would be found, equal to the RDE value divided by the drive cycle value. A threshold for CF would be set that, in order for type-approval to be granted, could not be exceeded. During an RDE test, the engine would encounter a greater range of speed and load combinations meaning that in-cylinder PM sources would need to be considered across the full range of engine speeds and loads.

1.3 Factors Affecting GDI Engine PM Emissions

1.3.1 The effects of the mixture preparation strategy

Fuel injection timing

For homogeneous operation under normal running conditions, fuel injection often takes place during the induction stroke. This is typically between 180 degrees crank angle (°CA) before combustion top dead centre (TDC) and 360 crank angle degrees before combustion top dead centre. This will usually coincide with the inlet valve opening period and injection will avoid the exhaust valve opening period. Very early injection will cause the fuel spray to impinge onto the piston crown, leading to the formation of a liquid film. If this is not evaporated or broken up by in-cylinder gas motion by the time of spark ignition, then a flame front that propagates near to the film will burn with a rich diffusion combustion flame. Under these conditions, PM is generated [9, 10, 11, 12, 32]. Potentially, the greater amount of fuel that impinges onto the piston, the greater the extent of the fuel film (in depth and area) and the more likely it is to persist until combustion begins; though there will be additional factors to consider, such as droplet splashing and plume to plume interaction. Therefore, it is often seen ([16, 33]) that, when start of injection (SOI) occurs in the early part of the induction stroke, PM emissions increase. In addition, injection timing will influence whether a particular plume impinges onto the cylinder liner or onto the piston. Liner fuel films may behave differently due to varying interactions with the in-cylinder air motion and differences in surface temperature.

As the start of injection is retarded towards bottom dead centre (BDC) or into the compression stroke, the time available for fuel droplet or fuel film vaporization will be reduced. This can cause increased PM emissions through the burning of a greater amount of the fuel in a rich diffusion combustion flame. During the compression stroke, both temperature and pressure will rise: an increased temperature will enhance droplet and film evaporation rate while an increased pressure will slow the evaporation rates. With very late injection timing, close to

spark ignition timing, the issue of spray impingement will again become problematic and with much less time for film evaporation.

For injection during the induction stroke, as engine speed is increased, the time required for vaporization of the fuel will not change greatly, since the temperature and pressure are roughly constant throughout the stroke. However, the vaporization will require a greater proportion of the engine cycle to complete. Thus, at higher speeds, injection may need to start earlier to ensure a gaseous, homogeneous charge at spark ignition timing that will result in low PM emissions. This could cause problems if injection was then required to start early enough to cause significant piston or liner spray impingement. In addition, the injection duration itself may take place over a greater number of °CA at higher engine speeds, which would mean that the final liquid emerging from the injector would have less time to vaporize and might encounter the piston returning towards the injector during the early compression stroke.

Downsized, highly-boosted GDI engines have been developed (*e.g.* [34]) to increase thermal efficiency further. Due to the increase in inducted air mass, a greater amount of fuel is injected to reach a given air/fuel ratio. This may require a longer injection duration than for naturally aspirated engines if the injector and injection pressure are maintained the same and the earlier mentioned injection timing issues could be exacerbated.

Injection pressure

The typical fuel injection pressure assumed for GDI in this thesis is 150 bar, which is the maximum fuel pressure used in the AJV8 engine [1] and accompanying optical access engine (see Chapter 3). The peak injection pressures used in practice and in research can reach up to 400 bar [9, 10]. As injection pressure is increased, it is found that atomization improves and droplets are smaller: Elkotb [35] found that spray droplet diameter $d_0 \sim \Delta p^{-0.54}$. The precise mechanisms behind liquid spray atomization are subject to discussion [36], however, with a greater pressure differential across the injector nozzles the fuel jet does have a larger initial velocity.

It is thought that with the combination of greater jet momentum and higher shearing forces between air and jet smaller fuel ligaments and droplets will form. In addition, these first primary droplets may undergo secondary break-up when travelling at a higher velocity relative to the entrained air in the spray ([36, 37]) and the secondary break-up process may have most influence over the distribution of droplet sizes formed far from the injector tip. Smaller fuel droplets, of any shape, will evaporate more quickly and will experience a greater deceleration due to aerodynamic drag. A higher injection pressure will also allow the same quantity of fuel to be delivered in a shorter duration, meaning that the end of injection will be earlier in the cycle with potential consequences for spray impingement.

Thus, there are several competing effects that influence the mixture preparation and, potentially, PM formation. A larger fuel jet velocity (and droplet initial velocity), related to the injection pressure through $v_{jet} = C_v\sqrt{2\Delta p/\rho_{\mathrm{L}}}$, will tend to increase spray penetration, whereas the greater droplet deceleration will tend to limit spray penetration and align the droplets with the in-cylinder flow more quickly. In addition, the smaller initial droplet size will promote a faster vaporization and so a greater relative velocity reduction rate. In practice, these factors often balance and the penetration distance does not increase or decrease greatly with the injection pressure [11]. However, this will vary under different conditions and, most importantly, the spray that is formed from a higher injection pressure is thought to vaporize faster due to the reduced droplet size, which will aid mixture preparation and the avoidance of rich mixture combustion.

If the engine fuel pump is driven by the engine, at part load the fuel injection pressure generated may be reduced, which could lead to increased droplet sizes in-cylinder. This would affect the mixture homogeneity at spark ignition unless measures were taken to correct for this.

Fuel injector design

In the context of multi-hole GDI injectors, the design choices available are typically the number of injector holes; their arrangement and targeting pattern; the diameter of the holes and their geometry (tapering or stepping).

The targeting of the holes will affect whether fuel spray impingement occurs. Typically there is a compromise between avoiding the cylinder liner and preventing too much of the fuel from being directed axially downwards, straight at the piston crown. For stratified operation, there may be targeting conditions relating to providing a rich mixture right at the spark plug (for example the AJV8 [1]). Increasing the number of injector holes reduces plume spacing, which alters flash boiling collapse conditions, but may disperse the fuel around the combustion chamber more evenly under sub-cooled conditions.

The reported effects of reducing the hole size varies in the literature. However, most correlations based on experimental studies predict that a reduced nozzle diameter will result in a reduced mean diameter or Sauter mean diameter (SMD) (*e.g.* [35] and the many correlations in [36], pp. 202–203). The SMD is defined as the diameter of the droplet that has the same liquid volume to liquid surface area ratio as the entire spray. Primary atomization is thought to be improved by a smaller jet size and higher velocity of fuel issuing from the nozzle. The jet cross-sectional area may be smaller than the nozzle area, due to cavitation in the injector internal channels or other phenomena [38], the presence of which will also be determined by the injector's internal design. However, once primary ligaments and droplets have been formed, the size of the nozzle is thought to have little direct effect; rather the velocity of the liquid principally determines secondary break-up, as previously described.

The hole geometry and manufacturing technique will influence the in-nozzle flow, and hence the initial fuel jet. Typically, nozzle holes are stepped with the initial diameter around 200 µm, then increasing to a counterbore hole or pre-hole around 350–500 µm ([39, 40, 41]) before opening into the cylinder. The counterbore hole aims to provide some protection of the inner nozzle hole from injector coking deposits that form in service due to combustion; the presence of carbonaceous deposits around the nozzle outlet may interfere with the fuel jet, altering its behaviour from that intended, which may adversely affect PM emissions. Even when a clean injector is used, fuel leaving the smaller diameter initial hole may touch the sides of the counterbore hole. The interaction with the counterbore hole and the first interaction

with the in-cylinder air will depend on: the internal cavitation and asymmetry of the flow exiting the first hole; the jet velocity and induced jet turbulence which controls the jet cone angle; and whether the fuel is superheated. The shape and targeting of the jet will be influenced by its interaction with the counterbore hole.

In addition, fuel jet interaction with the internal walls of the counterbore hole, or fuel spreading around the external corner onto the injector tip, can result in the generation of fuel films [9]. The induced air motion inside and close to the counterbore hole will be important here in understanding how fuel ligaments in the spray are directed onto the injector tip. Fuel films on the injector tip are usually only a problem with coked injectors, see Section 1.3.3.

The manufacturing technique influences the internal surface roughness and also the tolerance of the injector internal features, such as corner rounding and tapering of the holes. These will affect flow turbulence and cavitation. The two methods currently available are Electrical Discharge (or Spark Erosion) and Laser Drilling. By using the laser drilling technique, non-circular hole shapes are possible, which may result in further optimization of spray shape for PM emissions reduction [42]. In a comparison between two nominally similar injectors [39], one laser drilled, one spark eroded, the laser drilled injector produced a slightly wider plume with subsequent reduced plume penetration. In addition, the laser drilled injector resulted in a reduced measured droplet size (SMD) during the injection period but showed a similar or increased droplet size overall. This could indicate improved primary atomization but also the formation of large droplets at the end of injection, during the needle closing phase. These factors will influence the mixture preparation and, possibly, subsequent PM formation.

Flash boiling

In a firing GDI engine, the fuel inside the injector will heat up due to its location in the hot cylinder head and proximity to the heat from the combustion chamber. If the temperature of the fuel that is injected exceeds the saturation temperature of that fuel at the in-cylinder pressure at the start of injection, then the fuel is said to

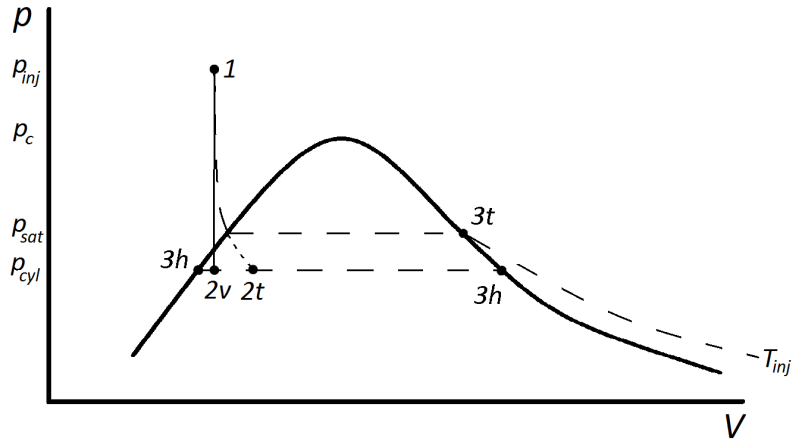


Figure 1.5: Flash boiling process p-V diagram. The fluid that forms the spray has a composition somewhere between state (2) and state (3), depending on the rate of return to equilibrium

be superheated. Before injection begins, the hot fuel is prevented from evaporating by the high injection pressure. The rapid depressurization into the cylinder brings the fuel into the two-phase vapour-liquid region, as shown in Figure 1.5.

Once the superheated fuel is exposed to the lower pressure, it will initially remain as liquid, although its equilibrium state should be as a vapour-liquid mixture. With reference to Figure 1.5, before the injector opens (1), the fuel is in compressed liquid form, at temperature T_{inj} and typically at a pressure p_{inj} higher than the fuel critical pressure p_{c}. The fuel pressure is rapidly reduced to that of the cylinder p_{cyl}, which, in the flash boiling case, is below the saturation pressure of the fuel p_{sat}, evaluated at the fuel temperature T_{inj}. There are two end points shown: (2v) represents constant volume (isochoric) depressurization, with a lowering of fuel temperature, and (2t) represents constant temperature (isothermal) depressurization at temperature T_{inj}. The fuel can exist at state (2v) or (2t) as a metastable superheated (non-equilibrium) liquid before any vaporization begins. The line from the saturated liquid line to (2t) is the superheated liquid isotherm for temperature T_{inj}, which passes through metastable states at T_{inj}. The fuel then proceeds towards equilibrium as the liquid state moves back towards the saturated liquid line and fuel vapour is created on the saturated vapour line. There are two specific cases for this process. The first is an isothermal one, requiring heat input from the surroundings, which gives a

final temperature of T_{inj} at point (3t); for pure components this will result in 100% of the fuel converting into vapour. The second is an adiabatic (isenthalpic) process, which results in a reduction in fuel temperature to T_{sat}, evaluated at p_{cyl}, and a mix of vapour and liquid at equilibrium, even for pure component fuels, at points (3h). This transformation to the equilibrium state cannot happen instantaneously. It is controlled by the nucleation of the vapour phase within the liquid, potentially at preferential sites, and the growth of vapour bubbles or pockets until equilibrium is attained throughout the mixture. This process competes with other short-timescale events during high pressure fuel injection: cavitation due to local pressure reduction; turbulent flow through the injector sac volume and nozzle and into the cylinder; and atomization and secondary break-up. It is therefore difficult to ascertain whether equilibrium is attained.

Once fuel vapour is formed it occupies a much greater volume than the liquid fuel, even at very low mass fractions, due to the much lower density of fuel vapour. When a single-phase, non-flashing jet leaves an injector orifice, the jet cross-sectional area will increase as it travels away from the nozzle, due to air entrainment. When a two-phase fuel jet leaves the nozzle, it will tend to expand with a larger plume angle, due to the presence of low density vapour inside the jet [43], and may also initially have a larger axial velocity than a single-phase jet, for the same reason. In addition, coalescence of vapour bubbles and regions inside the jet will promote atomization by separating regions of liquid from each other, creating ligaments and increasing the liquid surface area available for interaction with the surrounding air.

Thus the flash boiling process can significantly influence mixture preparation in the engine cylinder, particularly with multi-hole injectors. The enhancement to atomization typically leads to a reduced droplet diameter [41, 43, 44, 45], which is beneficial for an enhanced spray evaporation rate and, potentially, a reduced spray penetration, as smaller droplets experience a greater deceleration due to drag. However, it should be noted that, in the flash boiling case, the droplets will initially be surrounded by a larger vapour concentration, they will decelerate more quickly relative to the air/fuel vapour due to their smaller size and, for multi-component

fuels, may have lost some of their more volatile components. These three effects will tend to reduce droplet evaporation rate.

With regard to individual plumes, the increased jet angle observed during flash boiling will cause plume penetration to decrease, due to continuity considerations. This may help to avoid the formation of fuel films by reducing the likelihood of spray impingement. However, in a multi-hole injector implementation, as plume angles increase, adjacent plumes may interact, scattering droplets in many directions as they collide. The whole spray would begin to take the shape of a continuous conical curtain of droplets with a hollow centre. Even under sub-cooled conditions, each fast moving plume will generate air vortices as they transfer shear at their boundary, both outside and inside the spray cone, as is illustrated in Figure 1.6.

Under flash boiling conditions, there will be a low pressure zone inside the spray cone, formed by the higher air entrainment flow that is initiated by the increased plume angle. Some droplets will be sent inwards due to collisions at the plume interaction points. A stronger external vortex flow will be initiated, circulating the droplets and pushing them inwards at the vortex peak, persisting even after the end of injection. It is often reported that flash boiling injection causes enhanced atomization [44], resulting in an overall reduced droplet size, that will make the droplets more susceptible to changing direction upon interaction with pressure differentials and flow structures.

The consequences of the fuel spray collapse that can be observed under highly superheated flash boiling conditions (Figure 1.6, right image) are varied and depend on the injector hole pattern and the level of superheat for the particular fuel that is being injected. At low levels of spray superheat, the collapsing spray will tend to have a reduced axial penetration compared with a sub-cooled spray [43, 44], even though the spray collapse turns the plumes towards the axial direction. The reduced penetration is considered to be due to the smaller droplet size that results from better atomization and also the faster evaporation caused by higher droplet temperatures, under flash boiling conditions. As previously discussed, when the separate plumes interact, some droplets are turned from the jet direction. Droplets

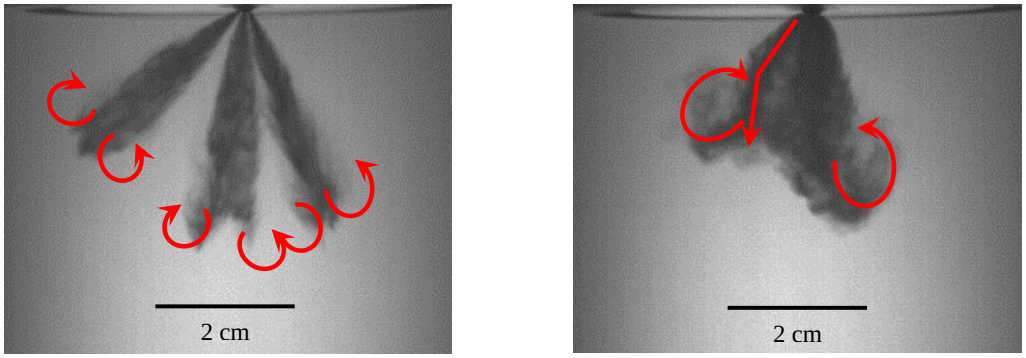


Figure 1.6: A sub-cooled spray (*left*) and a superheated flash boiling spray (*right*). The vortices that develop on the sub-cooled spray plumes broaden the leading edge of the spray by displacing some droplets laterally. In the flash boiling spray, the tip vortices can influence the motion of the main plume when they recirculate; this is observed in the left-most plume, whose course is visibly altered by the interaction with the vortex

in a less dense plume could experience reduced droplet shielding, which leaves more droplets subject to higher deceleration due to drag. Upon collapse, the overall spray angle will decrease. These phenomena are likely to reduce the chance of either piston crown or liner wetting, which can help to reduce PM emission sources in the combustion chamber.

At higher levels of superheat, the degree of collapse increases, with more of the spray drawn into the centre, and with the spray ultimately taking on the shape of a single axial jet [44, 45]. Two reasons for this could be: the expected greater generation of vapour inside the nozzle and in the fuel jets themselves, creating an expansion effect which increases the plume velocity; and an earlier and greater alignment of the plumes towards the axial direction due a more intense low pressure region generated between the plumes, which concentrates momentum in the axial direction and creates a denser jet where droplets are shielded more effectively, experiencing less aerodynamic drag. In Zeng *et al.* [43], the axial penetration was characterized with fuel superheat ratio $p_{\mathrm{amb}}/p_{\mathrm{vap}}$ where p_{vap} is the fuel vapour pressure evaluated at the fuel injector temperature. This study found that, as the fuel superheat was increased and the ratio $p_{\mathrm{amb}}/p_{\mathrm{vap}}$ dropped further below one, the axial penetration decreased until the ratio reached 0.3, at which point the axial penetration began to increase again on further ratio reduction, as shown in Figure 1.7.

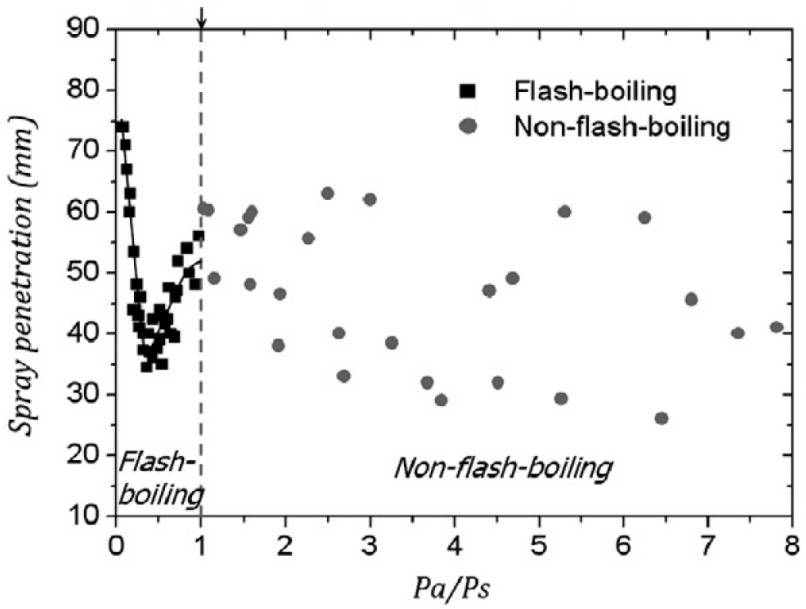


Figure 1.7: Spray penetration for flashing and non-flashing GDI sprays, as measured by Zeng *et al.* [43] for an eight-hole equally spaced injector. Permission to reproduce this figure has been granted by Elsevier

Zeng *et al.* marked the critical point as the spray moving from the 'transition stage' to the 'flare flashing' regime. This agrees with work presented in Chapter 6 of this thesis and in the related work shown in [46], which also uses a six hole high pressure GDI injector. Our work found that penetration decreased when the superheat pressure ratio was reduced from 0.5 to 0.2, and the penetration increased again on reducing the ratio to 0.14. The exact value of the critical superheat ratio is expected to be dependent on the injector internal details as well as the hole pattern.

Furthermore, Zeng *et al.* found that the SMD droplet size reduced progressively as the fuel superheat ratio was reduced below unity, but that below 0.3 the size remained stable [44]. One conclusion is that, at very high fuel superheat, there would be an increased likelihood of piston crown impingement, but with no additional benefit from reduced droplet size, which implies the possibility of an increase in PM emission generation at the fuel film.

Many studies have been performed to analyse the effect of fuel superheat on the resulting spray. Oza and Sinnamon [47] considered a bubble growth model inside a single hole injector and an outwardly opening pintle injector, both at an injection pressure of around 100 bar and various low chamber pressures. For

their experimental conditions, they concluded that bubble nucleation must be homogeneous. This means that bubbles form in the bulk liquid and not at any particular preferential sites, perhaps due to the longer residence time inside the injector. By tracking bubble size for different chamber pressures, they could predict when bubbles might reach a critical size and volume fraction in the nozzle, so that they might coalesce to form sprays with improved atomization.

Senda and co-workers [48, 49, 50, 51]) have taken the approach that nucleation must be heterogeneous and, in particular, that bubble nucleation under superheated conditions occurs principally on existing dissolved air bubbles in the fuel. They used data on the number density of air bubbles in liquid as a function of their size, typically 1–10 µm. Their studies assumed a critical initial radius above which the bubble would be of sufficient size to grow once depressurization occurred. Bubbles smaller than their critical size could collapse in on themselves. It is not certain whether their approach has taken into account the fact that air dissolved in the fuel at room temperature is released from solution when the fuel is heated, assuming that the fuel is placed in a sealed fuel system. Their method is used to predict growth of bubbles inside the injector channels [48] or inside droplets, in order to predict micro-explosions [50]. A volume void fraction of between 0.45 ([49]) and 0.55 [50] is used to determine when bubbles touch and coalesce to atomize the liquid.

Schmidt and co-workers [52, 40], Bilicki and Kestin [53], and Bianchi and co-workers [54, 55] use a Homogeneous Relaxation Model (HRM) to explicitly model the transfer from the metastable superheated liquid state towards the equilibrium vapour and liquid mixture. This can be implemented into CFD simulations of in-nozzle flow and the spray near field, to allow incorporation of the simultaneous effects of turbulence, pressure variation (and hence cavitation), and spray break-up. In addition, the transient nature of in-nozzle flow during injection can be captured by using moving meshes. The HRM predicts the generation of vapour that would be expected in the nozzle inner hole, counterbore hole and early jet region (spray near field). Typical results ([52, 40]) show a vapour volume fraction of around 0.5–0.75 inside the counterbore and early jet region. Following the assumptions of

Senda and co-workers, this would result in coalescence of bubbles and subsequent explosive atomization of the jet, as they estimated a vapour volume fraction of between 0.45 and 0.55 would cause this, for spherical bubbles.

Induction pressure

The gas ambient pressure into which the fuel is injected (or 'backpressure') has several effects on the fuel spray and subsequent mixture preparation. As discussed, this pressure will determine the spray's flash boiling characteristic and also the residual superheat level of droplets once formed. Once the spray is in the cylinder, the ambient pressure will also determine the evaporation rate of droplets and liquid films, with a high pressure acting to suppress the evaporation by increasing the liquid boiling temperature. The diffusional flow rate of vapour away from the liquid phase, which can be an evaporation rate controlling factor, will be independent of pressure, at the low cylinder pressures experienced during most GDI injection processes [56]. With a higher air pressure and hence higher air density, it is typically observed that plume penetration is reduced [41].

During throttled homogeneous operation, the early injection that occurs in the induction stroke will experience a low gas pressure, typically 0.5 bar. At this pressure, evaporation and superheat levels are improved, meaning faster spray vaporization than if the gas pressure was atmospheric. However, there will be an increased spray penetration, as previously discussed, meaning that a compromise will be needed in order to avoid excess fuel film generation. Under boosted conditions the air pressures could exceed atmospheric, further reducing penetration, and if the air temperature is increased from the naturally aspirated case then the spray evaporation rate would not be greatly reduced.

If injection occurs very early, while the intake valve is still at a low lift, then the cylinder pressure will be further reduced below that of the inlet manifold, due to the restriction created by the inlet valve. This will further enhance the spray evaporation during this low valve lift period and increase the degree of any flash

boiling atomization. The local curtain flow around the valve will have a higher velocity, which could be more disruptive to the spray.

Conversely, with later injection during the compression stroke (*e.g.* for stratified operation or the catalyst heating phase), both the pressure and temperature will rise and act to greatly reduce liquid penetration. This will aid in preventing piston wetting as the piston moves towards TDC, which is of high importance, since fuel films which are created this close to the start of combustion will be much less likely to fully evaporate before the flame front reaches them.

1.3.2 The effects of fuel composition

The composition and quality of gasoline fuels varies between the different markets in which modern vehicles with GDI engines are sold. This variation can influence strategies for reducing particulate emissions. Even within individual countries, there may exist different fuel grades for different seasons [57] and, in terms of oxygenate content, ranges of available blends (*e.g.* in Brazil, E20–E100; in China, M15–M85).

Hydrocarbon fuel composition

For pure hydrocarbon fuels, the two main fuel properties that influence the initial formation of in-cylinder PM are fuel volatility and fuel aromatic content [58, 59, 60, 61], for both GDI and PFI vehicles.

The fuel volatility will affect how quickly the fuel evaporates when sprayed into the engine, which determines the presence of wall and piston fuel films and liquid droplets in the combustion chamber, as well as general mixture homogeneity. Since gasoline is a mixture of many hundreds of hydrocarbons, it boils over a wide range of temperatures, with 'light' components evaporating first and 'heavy' components evaporating last, at the highest temperature. Therefore, its volatility can be measured in a number of ways. The vapour pressure at a low temperature (38°C for the RVP or DVPE tests) can indicate the volatility of the light end of the mixture, whereas the T50 or T90 from a fuel distillation curve (the temperature at which 50% or 90% by volume of the liquid has evaporated) will give an indication of the volatility of the medium or heavier volatility components. In Leach, 2014,

[13], the DVPE was used to help characterize the effect of fuel properties on PM emissions, as DVPE data is readily available for commercial fuels. This approach offers insight into how well a fuel might evaporate during the induction stroke of a GDI engine at low load, as the temperature used to evaluate DVPE is representative of the temperatures during this process. In addition to the RVP at 100°F (38°C) and T50, Sobotowski and co-workers ([61, 62]) used the index of Aikawa and Jetter [60], where fuel vapour pressure is evaluated at 443 K. This may be more representative of the T90 conditions, or even conditions at the fuel's final boiling point (or higher). This could also provide useful information about mixture preparation, since, to avoid combustion around liquid fuel around droplets or wall films, all of the fuel must evaporate during mixture preparation and the volatility of the heaviest components might be the critical factor in determining this. Part of this thesis aims to investigate how fuel droplets evaporate in the cylinder, accounting explicitly not only for the complete range of gasoline volatility, but also for the other physical processes that occur during mixture preparation. For example, a volatile fuel will have a greater droplet size reduction rate, which will mean that, other things being equal, these droplets will penetrate shorter distances into the cylinder and will be less likely to impinge onto the liner or piston.

Aromatic species contain at least one benzene ring. It is thought that these molecules, more than any others, contribute to soot formation [13, 63]. Polycyclic Aromatic Hydrocarbons (PAH) are aromatics formed of multiple benzene rings, which, at high temperatures and rich conditions during combustion, can be created as smaller aromatic rings react to join together. This leads to the removal of hydrogen atoms and hence, an increase in the molecule carbon content. These molecules act as layers of nearly pure carbon, which can stack together in a manner similar to graphite. This leads to the formation of primary soot particles, of typical size around 10–20 nm for GDI combustion. Aromatic content in gasoline is up to 35% by volume in Europe [57] and the EU reference fuel for emissions testing also specifies a minimum content of 29% by volume [64]. The US reference fuel requires a range between 20.5%–25.5% [23]. Some of the aromatic content is already polycyclic

in nature (*e.g.* naphthalene with formula $C_{10}H_8$). Controlled experiments have found that the quantity of aromatics in fuel that is combusted in an engine relates strongly to the particulate mass and particulate number counts measured [13, 62]. In a study of a diesel combustion flame, Aizawa *et al.* [65] found that the addition of 6.5% naphthalene increased the amount of carbonaceous particulate formations within the very rich part of the flame. Sobotowski *et al.*, 2015, [62] found that the addition of larger aromatic species in particular (10 carbon atoms or more), which had a higher boiling point, had the greatest impact on particulate emissions. The addition of smaller, more volatile aromatic species, such as toluene, had a lower impact. It is not certain whether this is a volatility effect or a result of the size of the molecule: the larger aromatic molecules will likely have more than one benzene ring and a greater carbon-hydrogen ratio. Therefore, attention must be paid to the composition of the aromatic fraction in the gasoline, as well as the overall amount.

Oxygenate content

Blending of alcohol fuels (typically methanol, ethanol and various butanol isomers) with gasoline occurs worldwide, in order to aid local energy security and reduce carbon emissions. This has several competing effects on the generation of particulates. Therefore, the exhaust PM emissions may increase or decrease, depending on engine operating condition.

The oxygenate group provides a source of oxygen atoms to react with the fuel-bound carbon and hydrogen atoms, which is available right at the fuel molecule and therefore, under rich conditions, does not need to be brought in by a transport process. It is thought that this aids in reducing carbonaceous particulate generation from rich mixture combustion by allowing a greater amount of the large hydrocarbon molecules, thought to be soot precursors, to oxidize before causing soot formation [66]. In general, this trend is borne out in a large amount of research from diesel engine experiments with oxygenated diesel fuels [67, 68].

In addition, methanol and ethanol mix in a highly non-ideal fashion with hydrocarbons [56], which means that the addition of a small amount by volume

to gasoline can increase the fuel vapour pressure by a significant amount. Two possibilities then arise. If the alcohol is splash-blended with gasoline (*i.e.* simply added to an existing gasoline without the underlying gasoline properties being changed) then a fuel with a higher vapour pressure will result. This will improve initial fuel vaporization rates in the engine cylinder, reducing the likelihood of mixture inhomogeneity or fuel films persisting until combustion starts, and increase the degree of flash boiling that occurs if the fuel in the injector is superheated. However, it also might be that less volatile hydrocarbon components are included in the fuel mixture such that the resulting ethanol/gasoline mixture has similar volatility (RVP) to the pure hydrocarbon gasoline. This may have more complex consequences on the fuel spray evaporation lifetime as will be discussed in the course of this thesis.

Alcohols will increase the mixture enthalpy of vaporization due to their high enthalpy of vaporization in pure form, see Table 1.2. This will reduce the droplet temperature in the evaporating spray [69] and tends to offset some of the gain in evaporation time gotten through the higher volatility. In addition, the increased charge cooling that will results can lower the gas temperature around the spray or formed fuel films, further increasing evaporation times. In Chen *et al.* [6], two splash-blended E10 derivatives proved to have longer spray evaporation times than their base gasoline mixtures, under homogeneous operation. A slower evaporation rate will increase the likelihood of mixture inhomogeneity, slightly increase spray penetration and reduce the rate of fuel film evaporation. This was confirmed by Chen *et al.* [6] who observed that, under stoichiometric operation in a V8 engine, the E10 derivatives also yielded more visible in-cylinder soot during combustion and an increased particulate number count and particulate mass filter measurement than the base gasolines, except at late injection timings (after 150°CA before TDC). Similar conclusions are drawn in [61, 62]. When the E10 blend did give a higher PM exhaust measurement in [6], the fraction of it that was soot (carbonaceous material) was higher. Under rich conditions ($\lambda = 0.9$) the presence of ethanol greatly reduced the PM emissions in their tests. In addition, as the combustion

Table 1.2: Enthalpy of vaporization of a typical ULG and three alcohols used in gasoline fuels. Values from [6] and [71]

ULG	n-butanol	ethanol	methanol
357 kJ/kg	689 kJ/kg	912 kJ/kg	1042 kJ/kg

Table 1.3: Enthalpy of combustion of liquid fuels (lower calorific value). Values from [7] and [71]

ULG	n-butanol	ethanol	methanol
43.9 MJ/kg	33.2 MJ/kg	26.9 MJ/kg	20.0 MJ/kg

mode moves to stratified operation with a later injection and a locally relatively rich mixture, where combustion-formed soot levels will be higher, it is typically found that the addition of ethanol becomes beneficial for PM emission reduction [70], as the effect of mixture preparation becomes less important than the soot generation phase during combustion.

Alcohol fuels, particularly methanol and ethanol, have a lower volumetric energy density than hydrocarbons, since the presence of the O atom adds mass to the substance but does not contribute to calorific value. Concerning mixture preparation, this means that a longer injection duration may have to be used to achieve the same mixture energy content, particularly for blends such as E85. Therefore, attention must be paid to the end of injection to ensure there is still adequate time for evaporation and charge mixing, and to avoid spray impingement, particularly at higher speeds.

1.3.3 Other sources of particulate generation

One notable source for the generation of particulates during GDI combustion originates from the carbonaceous deposits that form on injector tips in service, known as injector coking. As fuel molecules come into contact with the deposits, either through injector tip wetting or as vapour adsorbs onto the deposits as pressure rises during the compression stroke, some of the fuel can be stored in the deposits.

The temperature rise due to combustion and pressure reduction due to expansion will cause some of the fuel to leave the deposits, which can cause locally rich combustion near the injector tip towards the end of or after the main combustion. This is often known as a tip diffusion flame and can be a significant source of in-service PM emissions once the engine is fully warmed up [9].

Another source of PM generation is from oil that has leaked into the combustion chamber, which then participates in the combustion reaction. The oil will also contain metallic compounds, which contribute to ash generation. Since the volatility of engine oil will be much lower than gasoline then, if present, it will cause similar problems to when gasoline does not vaporize before combustion. The sources of oil ingress could be past turbocharger seals, past intake valve stem seals, past the piston rings and via the crankcase ventilation system [9].

For the optical engine experiments undertaken in this work, the engine was oil-free and the same, aged injector was used for each test, which means that any contribution from diffusion flames would be constant during each measurement.

1.3.4 Role of other engine parameters

Engine air/fuel ratio will have a great impact on soot generation, since the global air/fuel ratio will influence the local stoichiometry during combustion and, as previously discussed, rich mixture combustion will cause increased generation of carbonaceous particulates and a lack of oxygen later in combustion will inhibit soot oxidation. GDI engines will typically run at stoichiometric conditions to enable the use of a TWC, or lean in stratified mode, but overall rich mixture will be used at high speed and load, and will occur during transient operation.

A higher engine load will increase the induction stroke cylinder pressure, the effects of which have been discussed in Section 1.3.1. At higher loads, the amount of fuel injected increases, which increases the quantity of molecules that are able to form soot precursor molecules and the amount of soot generated, under similar in-cylinder conditions, will increase. However, the amount of soot oxidized will also vary, due to the different temperature and pressure history in the cylinder.

Therefore, there is not a linear relationship between the amount of fuel injected and the amount of particulates released into the exhaust. Higher engine loads will also increase the temperature of the combustion products, which may increase post-flame oxidation of particulate matter and affect the behaviour of particulates through the exhaust system and into the atmosphere [12].

Spark ignition timing will influence both particulate generation and soot oxidation by altering the phasing and duration of combustion. Advancing the ignition (earlier in the compression stroke) can result in combustion occurring over a longer period, with corresponding reduced peak temperatures and pressure, which could cause a lower rate of particulate generation [13]. Retarded ignition (towards or after TDC) will delay combustion, increasing temperatures later in the expansion stroke, which could increase soot oxidation and encourage or inhibit changes in all classes of particulates in the expansion stroke and on into the exhaust system [13].

Inlet air temperatures, levels of EGR and the levels of exhaust gas residuals left in the cylinder after the exhaust process will influence temperatures during mixture preparation, throughout the combustion process and also throughout the expansion stroke and into the exhaust system. Thus, the spray and wall film evaporation rate, soot formation and oxidation processes, and particulate conversion in the exhaust systems are each affected by these parameters.

1.4 Summary

This Chapter has outlined some of the challenges facing future DISI engines, in terms of tighter standards for tailpipe particulate matter emissions and more onerous test cycles that take a vehicle through a wider range of potential engine operating points. These standards aim to limit the impact of IC engine-generated particulate matter on air quality and health, due to evidence of their detrimental effect on the human respiratory and circulatory systems. Factors of engine design and operation that influence the formation and emission of particulates have been discussed and it has been noted that many of these are related to the GDI fuel spray and subsequent air/fuel mixture preparation. These have a strong effect on

the presence of areas of rich mixture combustion after spark ignition, and hence the formation of particulate matter.

The rest of this thesis is dedicated to investigating the engine fuel injection process, and how this influences mixture preparation and the subsequent generation of particulates during combustion. A large part of the research has been focussed on better understanding the modelling of GDI fuel sprays, in particular the liquid droplet vaporization process is examined in Chapters 2 and 4, due to the important role this has in determining the in-cylinder conditions just prior to combustion. This will aid in the development of more accurate tools to analyse and predict GDI engine mixture preparation. Single hole spray simulations have been performed in OpenFOAM CFD code, in Chapter 5, using some of the detailed single droplet models introduced in this thesis, for sub-cooled fuel sprays only. Non-ideal multi-component model fuels have been chosen in Chapter 3 to reflect real gasoline mixtures, which will tend to have an increased alcohol content in the future. These fuels have been utilized for the droplet and spray evaporation simulations and during experimental work investigating the structure and behaviour of fuel sprays. A bespoke spray chamber was designed, presented in Chapter 3, which acts as a companion to an existing optical engine. Experiments were performed with a view to understanding how fuel composition and injected fuel temperature might influence factors such as spray impingement, fuel evaporation and mixture homogeneity, with results presented in Chapter 6. Particular attention has been paid to flash boiling sprays, due to their interesting behaviour with respect to improved mixture preparation. Finally, also presented in Chapter 6, experience from spray modelling and spray experiments has been used to explain and understand particulate measurements taken from single cylinder engine experiments, using a methanol-containing model gasoline fuel with a high susceptibility to flash boiling.

2 Spray Simulation Theory and Techniques

2.1 Droplet Evaporation Theory

2.1.1 Single component evaporation

The lifetime of a single, stationary, spherical droplet composed of only one liquid species in a stagnant gas is calculable from well-established theory, from which the following section draws (*e.g.* [36, 72, 73, 74, 75]). This classical theory assumes that the droplet remains at a uniform temperature (the wet-bulb temperature) throughout its lifetime. This is the temperature at which the heat transferred to the droplet from the surroundings is exactly equal to the heat required to evaporate the liquid at the surface at the current evaporation rate. Additionally, it is assumed that the droplet surface moves inwards slowly; pressure is uniform; surface tension is ignored; no air dissolves into the droplet; there is no radiation heating of the droplet; there is no combustion; mass diffusion is described by Fick's law and heat conduction by Fourier's law [74].

For droplets evaporating in the cylinder of a GDI engine, the initial temperature of the liquid fuel will likely be quite hot (up to 120°C) and the steady state wet-bulb temperature will be lower than the cylinder air temperature, meaning that the wet-bulb temperature is likely to be lower than the initial fuel temperature for early injection. Therefore, most droplets formed during early homogeneous GDI operation will first cool towards the wet-bulb temperature. Figure 2.1 shows the cooling process by depicting the temperature in the droplet and in surrounding air at various times after injection.

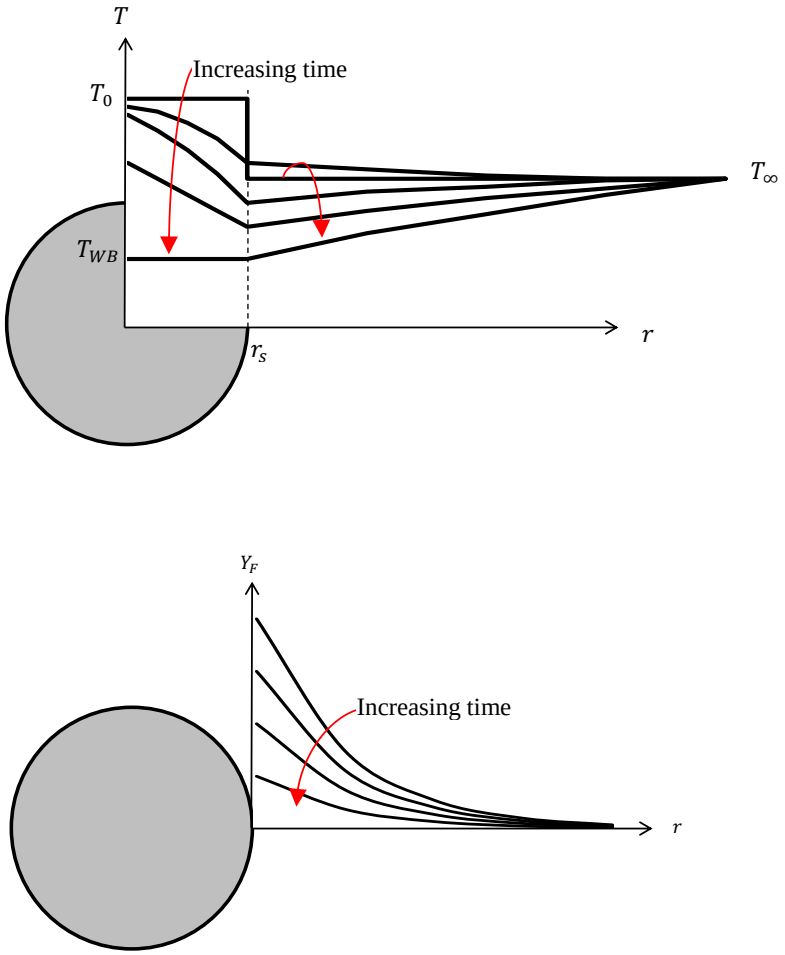


Figure 2.1: Temperature distribution inside and outside the droplet and fuel vapour distribution outside the droplet, varying with time from the droplet's first introduction into the ambient gas. The droplet temperature converges from the initial temperature T_0 towards the wet-bulb temperature T_{WB} but may not reach this before evaporation completes

By using the above assumptions, it is possible to solve the equations for conservation of the fuel species and conservation of energy in the gas phase around the droplet, considering the gas phase to be quasi-steady. Only two species in the gas phase are considered: air and fuel, with mass fractions Y_{A} and Y_{F} respectively, such that $Y_{\mathrm{A}} = 1 - Y_{\mathrm{F}}$. The equations are [74, 75]:

$$\frac{\mathrm{d}}{\mathrm{d}r}\left(\rho u r^2 Y_{\mathrm{F}} - \rho D r^2 \frac{\mathrm{d}Y_{\mathrm{F}}}{\mathrm{d}r}\right) = 0, \tag{2.1}$$

$$\frac{\mathrm{d}}{\mathrm{d}r}\left(\rho u r^2 h - \lambda r^2 \frac{\mathrm{d}T}{\mathrm{d}r}\right) = 0, \tag{2.2}$$

where r is the radial coordinate from the droplet centre; ρ is the air/fuel vapour mixture density; u is the air/fuel vapour radial convective velocity relative to the surface; D is the binary diffusion coefficient of the fuel vapour through air; h is the fuel vapour enthalpy; λ is the mixture thermal conductivity and T is the gas phase temperature. The first term in Equation 2.1 represents Stefan flow (discussed in [76]): the outward motion of the fuel species relative to the regressing droplet surface. The second term in Equation 2.1 represents outward molecular diffusion, with mass diffusivity D. In Equation 2.2, the first term represents outward advection of enthalpy relative to the regressing surface and the second term represents outward heat conduction, via thermal conductivity λ. Upon double integration of each of these, two equivalent expressions for evaporation rate $\dot{m}$ are obtained:

$$\dot{m}_{\mathrm{st}} = 2\pi d\rho D \ln(1 + B_Y) = 2\pi d \frac{\lambda}{c_{p\mathrm{F}}} \ln(1 + B_T), \tag{2.3}$$

where d is the current droplet diameter and $c_{p\mathrm{F}}$ is the specific heat capacity of the fuel species only. The Spalding mass and heat transfer numbers are B_Y and B_T respectively and are given by

$$B_Y = \frac{Y_{\mathrm{Fs}} - Y_{\mathrm{F}\infty}}{1 - Y_{\mathrm{Fs}}} \quad \text{and} \quad B_T = \frac{c_{p\mathrm{F}}(T_\infty - T_{\mathrm{s}})}{L_{\mathrm{eff}}}, \tag{2.4}$$

where subscript s refers to the droplet surface, subscript ∞ refers to conditions far from the droplet and L_{eff} is an effective enthalpy of vaporization for the fuel species given by

$$L_{\mathrm{eff}} = L + \dot{Q}_{\mathrm{L}}/\dot{m}, \tag{2.5}$$

in which the heat transferred from the droplet surface towards the droplet interior is $\dot{Q}_{\mathrm{L}}$. Under steady state conditions, the temperature is uniform and therefore no heat conducts inwards from the droplet surface, thus $\dot{Q}_{\mathrm{L}} = 0$ and $L_{\mathrm{eff}} = L$.

When the pressure is low, no ambient gas will dissolve in the droplet and Dalton's law of partial pressures is applicable. If the temperature is below the liquid boiling point, then the surface will reach equilibrium and the equilibrium fuel vapour mole fraction $\widetilde{Y}_{\mathrm{Fs}}$ can be calculated using the saturation vapour pressure p_{vap} and ambient pressure p. The fuel vapour mass fraction at the surface can be found by converting this to a mass fraction using the fuel and air molar masses M_{F} and M_{A}:

$$\widetilde{Y}_{\mathrm{Fs}} = \frac{p_{\mathrm{vap}}}{p}, \tag{2.6}$$

$$Y_{\mathrm{Fs}} = \frac{M_{\mathrm{F}}\widetilde{Y}_{\mathrm{Fs}}}{M_{\mathrm{F}}\widetilde{Y}_{\mathrm{Fs}} + M_{\mathrm{A}}(1 - M_{\mathrm{F}}\widetilde{Y}_{\mathrm{Fs}})}. \tag{2.7}$$

The fuel vapour pressure will be a function of droplet surface temperature. In this work all fuel vapour pressures have been calculated using guidance in [77].

At steady state, Equation 2.3 for evaporation rate produces the d^2 law of droplet evaporation, whereby

$$\frac{\mathrm{d}d^2}{\mathrm{d}t} = -K = -\frac{8\rho D \ln(1 + B_Y)}{\rho_{\mathrm{L}}} \tag{2.8}$$

for a given liquid fuel density ρ_{L}. Thus, the droplet lifetime is d_0^2/K.

Droplets initially have a very high velocity, due to the high injection pressures used, which leads to a convective enhancement of the heat and mass transfer between the droplet surface and the surrounding gas phase. For mass and heat diffusion from a sphere of constant size, the Sherwood number ($\mathrm{Sh} = k_Y d/D$) and Nusselt ($\mathrm{Nu} = k_T d/\lambda$) number both equal 2, in the absence of convection [78]. Here, k_Y and k_T are mass and heat transfer coefficients. However, when there is also evaporation $\mathrm{Sh} \neq 2$ and $\mathrm{Nu} \neq 2$, due to the presence of Stefan convection. Taking the Sherwood number as an example, the enhanced diffusive mass flux due to forced convection is

$$\dot{m}_{\mathrm{diff}} = k_Y A_{\mathrm{s}} \rho (Y_{\mathrm{Fs}} - Y_{\mathrm{F}\infty}), \tag{2.9}$$

where $\rho(Y_{\mathrm{Fs}} - Y_{\mathrm{F}\infty})$ is the driving mass concentration difference and A_{s} is the droplet surface area. The diffusive part of the fuel mass flow rate from the surface can be retrieved as

$$\dot{m}_{\text{diff}} = (1 - Y_{\text{Fs}})\dot{m}. \tag{2.10}$$

By combining the definition of the Sherwood number with Equations 2.3, 2.9 and 2.10, an appropriate altered Sherwood number for droplet evaporation is given by $\text{Sh}' = \text{Sh}B_Y/\ln(1 + B_Y)$, such that

$$\dot{m} = \pi d\rho D\text{Sh}' \ln(1 + B_Y) \tag{2.11}$$

$$= \pi d\rho D\text{Sh}\ B_Y. \tag{2.12}$$

A similar argument may be made with the Nusselt number and the evaporation rate solution containing B_T:

$$\dot{m} = \pi d\frac{\lambda}{c_{p\text{F}}}\text{Nu}' \ln(1 + B_T) \tag{2.13}$$

$$= \pi d\frac{\lambda}{c_{p\text{F}}}\text{Nu}\ B_T. \tag{2.14}$$

Enhanced Sherwood and Nusselt numbers for mass and heat transfer from solid spheres in convective flow will take the form $\text{Sh}_0 = f(\text{Re},\ \text{Sc})$ and $\text{Nu}_0 = f(\text{Re},\ \text{Pr})$, where the droplet Reynolds number is $\text{Re} = \rho U d/\mu$; the Schmidt number is $\text{Sc} = \mu/\rho D$; the Prandtl number is $\text{Pr} = c_p\mu/\lambda$; U is the relative velocity between droplet and air and μ is the dynamic viscosity of air/fuel mixture. The Ranz-Marshall correlation [75] is often used, where

$$\text{Sh}_0 = 2 + 0.6\text{Re}^{1/2}\,\text{Sc}^{1/3} \quad \text{and} \quad \text{Nu}_0 = 2 + 0.6\text{Re}^{1/2}\,\text{Pr}^{1/3}, \tag{2.15}$$

and the factor of 0.6 may be replaced by 0.552 to obtain the earlier Frossling correlation [75]. Abramzon and Sirignano [79] presented correction factors for the thickening effect of the Stefan flow on the mass and thermal boundary layers, to account for the convective enhancement around an evaporating droplet, for a large range of B_Y and B_T. This is known as the blowing effect and it can have a great effect on evaporation rate at very high evaporation rates [80] (when the

Stefan flow is largest). To use the Abramzon and Sirignano correction from [79], Equation 2.11 must be used, where

$$\mathrm{Sh}' = 2 + \frac{(\mathrm{Sh}_0 - 2)B_Y}{(1+B_Y)^{0.7}\ln(1+B_Y)}. \tag{2.16}$$

and a similar expression can be found for Nu', using B_T instead of B_Y. The correction factor was numerically generated, for $B_Y, B_T \leqslant 20$ and $1 \leqslant \mathrm{Sc}, \mathrm{Pr} \leqslant 3$.

Any appropriate expression for Sh_0 may be used, provided that it does not already implicitly account for the blowing effect. In this work, the Ranz-Marshall correlation (Equation 2.15) and the Clift *et al.* correlation [81] have been used. The Clift correlation is, for $\mathrm{Re} \leqslant 400$:

$$\mathrm{Sh}_0 = 1 + (1 + \mathrm{Re}\,\mathrm{Sc})^{1/3}\ \max\left[1, \mathrm{Re}^{0.077}\right]. \tag{2.17}$$

At low evaporation rates, where the blowing effect is minimal ($B_Y < 1$, according to [80]), Equation 2.12 may be used with $\mathrm{Sh} = \mathrm{Sh}_0$. Alternatively, at Reynolds numbers between 20 and 2000, the correlation from Haywood *et al.* [82] may be used in Equation 2.12, given as

$$\mathrm{Sh} = \frac{2 + 0.87\mathrm{Re}^{1/2}\,\mathrm{Sc}^{1/3}}{(1+B_Y)^{0.7}} \quad \text{and} \quad \mathrm{Nu} = \frac{2 + 0.57\mathrm{Re}^{1/2}\,\mathrm{Pr}^{1/3}}{(1+B_T)^{0.7}}, \tag{2.18}$$

as this was derived from a numerical analysis of an evaporating droplet and implicitly includes complex effects such as the blowing effect.

Droplet motion

The drag force D, and hence the drag coefficient C_D, on a small sphere at very low Reynolds number was calculated by Stokes (see [36]) as

$$C_D \equiv \frac{D}{0.5\rho_\mathrm{A}U^2A} = \frac{24}{\mathrm{Re}} \tag{2.19}$$

where $A = \pi d^2/4$. Experimental data can be better approximated for $\mathrm{Re} < 1000$ ([36, 74]) if the drag coefficient is taken as

$$C_D = \frac{24}{\mathrm{Re}} + \frac{4}{\mathrm{Re}^{1/3}}, \tag{2.20}$$

which is used throughout this work. It is assumed that the aerodynamic forces on the droplet do not significantly distort its shape from spherical.

The relative velocity that an isolated droplet experiences may be higher than that experienced by droplets within a dense spray, since there will be shielding inside the spray and air will be entrained into the spray. This will affect both the droplet's penetration distance from the injector and the convective enhancement to heat and mass transfer it receives during evaporation..

Physical properties

The gas phase (air and fuel vapour mixture) physical properties are assumed constant with radius r, varying from $d/2$ to ∞, in order to integrate Equations 2.1 and 2.2 simply. In reality, the properties $\rho, D, \lambda, c_{p\mathrm{F}}, \mu$ will all depend on local composition and temperature. Therefore, a reference value of composition and temperature is chosen at which to evaluate these 'constant' physical properties. Typically used is the 1/3–reference rule ([74, 75]):

$$T_{\mathrm{ref}} = \frac{2}{3}T_{\mathrm{s}} + \frac{1}{3}T_{\infty} \quad \text{and} \quad Y_{\mathrm{Fref}} = \frac{2}{3}Y_{\mathrm{Fs}} + \frac{1}{3}Y_{\mathrm{F}\infty}. \tag{2.21}$$

The density ρ used in the definition of the Reynolds number is usually taken as the air density alone, given as $\rho = pM_{\mathrm{A}}/R_0T_{\infty}$ by the ideal gas law, with R_0 the universal gas constant. The viscosity μ is evaluated at the reference conditions.

In the definition of B_T, it is important to note that it is correct to use $c_{p\mathrm{F}}\Delta T$ rather than Δh_{F} as $c_{p\mathrm{F}}$ is taken outside the integral when the reference conditions are introduced.

In the single droplet simulations presented in this work, the methods used for physical property calculation are summarized in Table 2.1.

Table 2.1: Summary of physical property models used in implementation of the single droplet evaporation simulations [56]

Physical property	Method of estimation
Air/fuel vapour mixture density	Soave-Redlich-Kwong equation of state
Fuel vapour binary diffusion coefficient in air	Method of Fuller *et al.*
Air/fuel vapour mixture thermal conductivity	Roy and Thodos method for fuels, fitted polynomials for oxygen and nitrogen; Mason and Saxena mixing rules
Fuel vapour specific heat capacity	Lee-Kesler method of corresponding states
Air/fuel vapour mixture dynamic viscosity	Lucas corresponding states method with Lucas mixing rules
Latent heat of evaporation	Pitzer acentric factor conrrelation
Liquid specific heat capacity	Rowlinson-Bondi method; for ethanol, Missenard group contribution method
Liquid kinematic viscosity	Orrick and Erbar group method
Liquid density	Modified Rackett correlation
Liquid thermal conductivity	Method of Latini *et al.*

2.1.2 Droplet temperature modelling

Several approaches are possible for modelling the droplet temperature in an evaporating spray. Since the evaporation rate is strongly dependent on the surface temperature, through Equations 2.3, 2.4 and 2.6, it is of primary importance to calculate the surface temperature accurately. The droplet may be assumed to instantaneously cool or warm to its wet-bulb temperature (the steady state temperature). However, this is applicable only to single component fuels and, since the evaporation rate will differ in the transient temperature change period, this approach will introduce inaccuracies to droplet lifetime estimates. This approach will not be used in this thesis. The simplest model that will be investigated first is the model where the droplet temperature is assumed uniform but can vary with time.

Uniform droplet temperature model

The approximation of uniform droplet temperature, also known as a lumped temperature model, is attractive in its simplicity. This is the simplest temperature model for a single droplet simulation and is sometimes known as the infinite conductivity model. It is the typical choice for implementation into commercial CFD codes, such as StarCD [83]. The approximation seems well-justified if the droplet Biot number is examined. The Biot number is defined as $\mathrm{Bi} = k_T d/\lambda_\mathrm{L}$, which can be rearranged to give $\mathrm{Bi} = \mathrm{Nu}\,\lambda/\lambda_\mathrm{L}$. A typical value for a hot, fast-moving, volatile droplet might be

$$\mathrm{Bi} = \frac{\mathrm{Nu}\lambda}{\lambda_\mathrm{L}} \sim \frac{10 \cdot 0.03}{0.1} = 3, \tag{2.22}$$

and for a stationary, cold droplet a typical value might be

$$\mathrm{Bi} = \frac{\mathrm{Nu}\lambda}{\lambda_\mathrm{L}} \sim \frac{2 \cdot 0.01}{0.1} = 0.2. \tag{2.23}$$

Typically, if $\mathrm{Bi} << 1$ then internal heat transfer is very fast compared to heat transfer between the surroundings and the surface, and the internal temperature is assumed to be uniform. Therefore, it is expected that a uniform droplet temperature model would become more accurate at lower temperatures and relative velocities.

By rearranging the two expressions for $\dot{m}$ in Equations 2.11 and 2.13, an expression for B_T in terms of B_Y is found:

$$B_T = \left(1 + B_Y\right)^{\mathrm{Sh}'/(\mathrm{Le}\,\mathrm{Nu}')}, \tag{2.24}$$

where $\mathrm{Le} = \lambda/\rho D c_{p\mathrm{F}}$ is the Lewis number. Then, the heat transferred to the droplet is calculated from Equations 2.4 and 2.5 as

$$\dot{Q}_\mathrm{L} = \dot{m}\left(\frac{c_{p\mathrm{F}}(T_\infty - T_\mathrm{s})}{B_T} - L\right), \tag{2.25}$$

which may be positive or negative, depicting droplet heating or droplet cooling respectively. Since the droplet evaporation rate is required for this expression, it

must be calculated first from Equation 2.11. Finally, for the uniform temperature model, the rate of change of droplet temperature is given by

$$\frac{\mathrm{d}T_\mathrm{L}}{\mathrm{d}t} = \frac{6\dot{Q}_\mathrm{L}}{\pi\rho_\mathrm{L}c_\mathrm{L}d^3}. \tag{2.26}$$

Droplet heat equation model

It is possible to solve for the droplet internal temperature field as a function of time throughout its lifetime. If the temperature field is spherically symmetric, with the liquid phase stationary relative to the droplet, $T_\mathrm{L}(r,t)$ can be found by solving the heat equation for the liquid:

$$\frac{\partial T_\mathrm{L}}{\partial t} = \frac{1}{\rho_\mathrm{L}c_\mathrm{L}}\frac{1}{r^2}\frac{\partial}{\partial r}\left(\lambda_\mathrm{L}r^2\frac{\partial T_\mathrm{L}}{\partial r}\right), \tag{2.27}$$

which is known as a conduction-limited model. This model and the uniform temperature (infinite conductivity) model together form the limiting cases for droplet temperature evolution. Equation 2.27 can be simplified to

$$\frac{\partial T_\mathrm{L}}{\partial t} = \alpha_\mathrm{L}\left(\frac{2}{r}\frac{\partial T_\mathrm{L}}{\partial r} + \frac{\partial^2 T_\mathrm{L}}{\partial r^2}\right), \tag{2.28}$$

in the case where variations of liquid thermal conductivity λ_L are ignored. The liquid thermal diffusivity is $\alpha_\mathrm{L} = \lambda_\mathrm{L}/\rho_\mathrm{L}c_\mathrm{L}$. Two boundary conditions are required:

$$\left.\frac{\partial T_\mathrm{L}}{\partial r}\right|_0 = 0, \tag{2.29}$$

$$\left.\frac{\partial T_\mathrm{L}}{\partial r}\right|_s = G_\mathrm{Ls} = \frac{\dot{Q}_\mathrm{L}}{\pi\lambda_\mathrm{L}d^2}. \tag{2.30}$$

The first describes symmetry at the droplet centre and the second relates the incoming heat $\dot{Q}_\mathrm{L}$ to the surface liquid temperature gradient $G_\mathrm{Ls} = \left.\frac{\partial T_\mathrm{L}}{\partial r}\right|_\mathrm{s}$.

In practice, when the droplets have a high relative velocity, there will be a shearing action on their surface, which will cause rapid internal circulation. This will alter the heat transfer within the droplet by providing a convective enhancement and will change the temperature field from spherically symmetric to axisymmetric

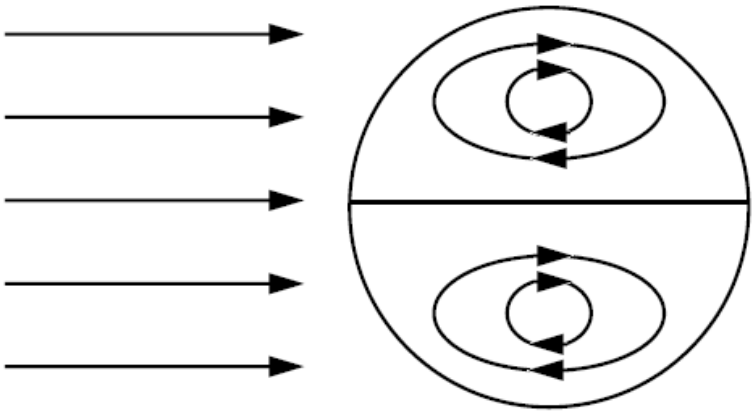


Figure 2.2: Predicted shape of the spherical vortex that occurs inside droplets moving rapidly through an ambient gas, adapted from [75]

(see Figure 2.2). Thus, the real droplet temperature evolution rate will lie somewhere between the two limiting case models. Approaches have been developed to account for this. In [84], a theoretical treatment of Hill's spherical vortex [85] was performed as an approximation of the circulation in the droplet. In [82], transport equations for mass, fuel species, momentum and energy were solved for regions inside and outside a spherical droplet, leading to a general vortex solution.

A simpler approach, introduced by Abramzon and Sirignano [79], has been used here. In their formulation, the heat equation is solved as for the spherically symmetric (conduction-limited) case but with an enhancement factor χ applied to the thermal conductivity. The enhancement factor depends on the level of circulation, which is described by the internal liquid Péclet number for heat transfer:

$$\mathrm{Pe}_T = \mathrm{Re}_\mathrm{L}\,\mathrm{Pr}_\mathrm{L} = \frac{\rho_\mathrm{L} U_\mathrm{Lmax} dc_\mathrm{L}}{\lambda_\mathrm{L}}. \tag{2.31}$$

The maximum liquid velocity U_Lmax is found from a shear force balance at the surface, with the assumption that the gas phase only applies shear force over the front half of the droplet's surface. The maximum velocity is found to be

$$U_\mathrm{Lmax} = \frac{\mu C_F \mathrm{Re}\, U}{6\pi\mu_\mathrm{L}} \tag{2.32}$$

where C_F is the friction coefficient for the evaporating droplet [75]. Abramzon and Sirignano recommended taking the friction coefficient determined experimentally for a rigid sphere and reducing this by a factor relating to the mass transfer number B_Y. For experimental values of $B_Y < 0.78$ and $10 < \mathrm{Re} < 100$, Renksizbulut and Yuen (referenced in [79]) found that

$$C_F = \frac{12.69}{\mathrm{Re}^{2/3}\,(1 + B_Y)}, \tag{2.33}$$

although it is expected that at higher values of B_Y this will not be accurate. Once a Péclet number is obtained, it can be used to calculate χ from the formula below, fitted by Abramzon and Sirignano [79] to the data of Johns and Beckmann [86]:

$$\chi = 1.86 + 0.86 \tanh\Big(2.245 \log_{10}(\mathrm{Pe}_T/30)\Big). \tag{2.34}$$

The value of χ is a maximum at very high Péclet numbers, corresponding with high droplet relative motion and rapid internal motion, taking the value 2.72. In this case, the estimated Biot numbers must be reduced by a factor of 2.72, which would make the uniform temperature model an even better approximation than when a stationary liquid phase was assumed.

The boundary conditions employed at the droplet surface must now change from Equation 2.30 to

$$\left.\frac{\partial T_\mathrm{L}}{\partial r}\right|_s = G_\mathrm{Ls} = \frac{\dot{Q}_\mathrm{L}}{\pi \chi \lambda_\mathrm{L} d^2}. \tag{2.35}$$

The model which uses the heat equation with an enhanced thermal conductivity is usually known as an effective conductivity model. It should be noted that the liquid temperature history calculated from this model is intended to be accurate only at the droplet surface. The surface temperature is a controlling factor in the estimation of the evaporation rate. The calculated internal temperature field will have one stationary point at the droplet centre but not at the vortex centre, as would be expected from the nature of the in-droplet flow. Discrepancies in internal temperature could lead to discrepancies in liquid physical property measurements that are evaluated at the liquid temperature.

Two-point droplet temperature model

To evaluate the droplet temperature throughout the radius, using Equation 2.28, requires a numerical scheme (*e.g.* finite differences) and the tracking of temperature at a number of grid points, which introduces additional variables to a CFD model. An alternative approach was developed by Ra and Reitz [87, 88], where the surface temperature T_s is tracked, along with the 'droplet interior' temperature T_d. The heat transferred between surface and interior was modelled as occurring across a surface thermal boundary layer of thickness

$$\delta = \sqrt{\pi \chi \alpha_\mathrm{L} t} \leqslant \frac{d}{4.514}, \tag{2.36}$$

where t is the current droplet lifetime. The liquid thermal diffusivity was enhanced by the factor χ, as introduced in the previous section in Equation 2.34, and the boundary layer thickness was limited to a preset fraction of the droplet size, following observations of heat transfer through solids. Thus, the heat transferred from the surface to the interior is

$$\dot{Q}_\mathrm{L} = \chi \lambda_\mathrm{L} \pi d^2 \frac{T_\mathrm{s} - T_\mathrm{d}}{\delta}, \tag{2.37}$$

and the rate of change of the droplet interior temperature is given by Equation 2.26. The surface temperature is found from an energy balance at the surface, where the heat transferred from the surroundings to the surface equals the heat required to evaporate the liquid at the current evaporation rate plus the heat transferred from the surface to the liquid interior. This is given in [87] as

$$\pi d^2 k_T (T_\infty - T_\mathrm{s}) = \dot{m} L + \dot{Q}_\mathrm{L} \tag{2.38}$$

where k_T is the heat transfer coefficient between the surroundings and the droplet, which is calculated from the Nusselt number as $k_T = \mathrm{Nu}\lambda/d = \mathrm{Nu}'\lambda \ln(1+B_T)/dB_T$. Any model for Nusselt number can be used, following the approach in either Equation 2.16 or Equation 2.18. Note that the heat transfer due to interdiffusion

(differential diffusion of different fuel vapour species) that was dealt with in [87, 88] is ignored here.

To calculate T_s, Equation 2.38 may be rearranged to give

$$T_\mathrm{s} = \frac{aT_\infty + bT_\mathrm{d} - \delta B_T \dot{m} L}{a+b}, \tag{2.39}$$

where

$$a = \pi d \lambda \mathrm{Nu}' \, \delta \ln(1+B_T) = \pi d \lambda \mathrm{Nu} \, \delta B_T = \dot{m} c_{p\mathrm{F}} \delta, \tag{2.40}$$

and

$$b = \pi d^2 \chi \lambda_\mathrm{L} B_T. \tag{2.41}$$

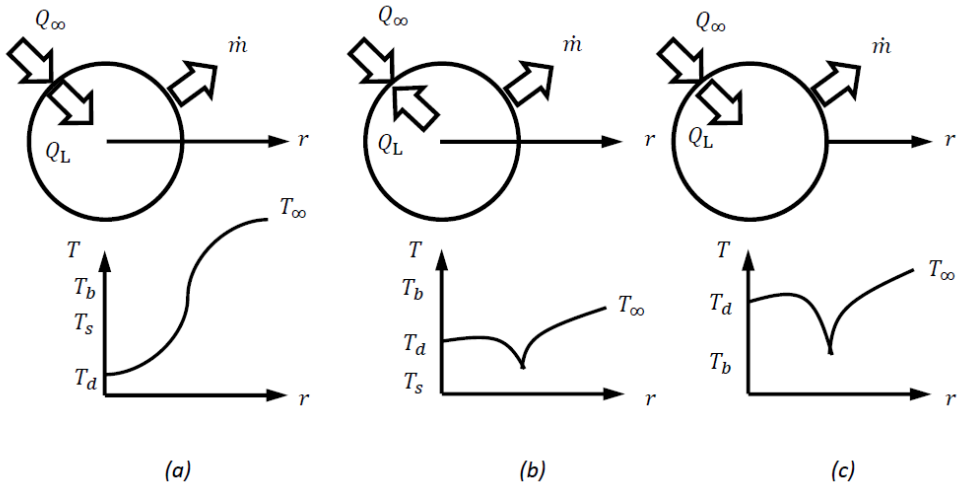


Figure 2.3: Schematic of radial energy fluxes at the droplet surface, adapted from [87], for *(a)* normal evaporation with droplet heating, *(b)* normal evaporation with droplet cooling, *(c)* flash boiling evaporation

2.1.3 Multi-component droplet evaporation

When there is more than one species present in the fuel, modifications must be made to the droplet evaporation model. Real fuels and even simplified model fuels almost always have at least two components, so multi-component droplet evaporation modelling is required.

As different fuel species leave the droplet from the surface, the composition of the liquid begins to change. The evaporating fuel has a composition determined by the mass flux fraction ε_i, given by [75]:

$$\varepsilon_i = \frac{Y_{\mathrm{Fs}i}}{\sum_i Y_{\mathrm{Fs}i}}. \tag{2.42}$$

The evaporation rate of each species is given by

$$\dot{m}_i = \varepsilon_i \dot{m} = \pi d \rho D_i \mathrm{Sh}'_i \ln(1 + B_{Yi}) \tag{2.43}$$

$$= \pi d \rho D_i \mathrm{Sh}_i B_{Yi}, \tag{2.44}$$

where each vapour species has a different binary diffusion coefficient through air (D_i); each species has its own Sherwood number ($\mathrm{Sh}_i = f(\mathrm{Re}, \mathrm{Sc}_i)$) based on an overall average Reynolds number but individual Schmidt numbers; and the species Spalding mass transfer number is given by $B_{Yi} = (Y_{\mathrm{Fs}i} - Y_{\mathrm{F}\infty i})/(\varepsilon_i - Y_{\mathrm{Fs}i})$. The overall evaporation rate may be expressed by Equations 2.11 and 2.12, if an appropriate average overall diffusion coefficient D is used. If Equation 2.12 is used (*e.g.* with Equation 2.18 or if the blowing effect is ignored), then

$$D = \frac{\sum_i D_i \mathrm{Sh}_i B_{Yi}}{\mathrm{Sh} B_Y} \tag{2.45}$$

where the overall mass transfer number is $B_Y = (\sum_i Y_{\mathrm{Fs}i} - \sum_i Y_{\mathrm{F}\infty i})/(1 - \sum_i Y_{\mathrm{Fs}i})$.

The gas and liquid phase physical properties must be adjusted in a suitable way to deal with the mixture of species. In this work, the methods adopted are listed in Table 2.2.

Multi-component vapour-liquid equilibrium

The vapour-liquid equilibrium state at the droplet surface must be modelled accurately, as it is required to estimate the total surface fuel vapour concentration $Y_{\mathrm{Fs}} = \sum_i Y_{\mathrm{Fs}i}$, on which the evaporation rate depends. The liquid mixture may be ideal or non-ideal, depending on how the molecules of the liquid species interact. The gas phase (multi-component fuel vapour and air) may also be non-ideal, depending

Table 2.2: Summary of physical property mixing rules used in implementation of the multi-component droplet evaporation simulations, from [56] unless otherwise stated

Physical property	**Rule for multi-component estimation**
Binary diffusion coefficient in air	$D = \sum_i \widetilde{Y}_{\mathrm{F}i} D_i / \sum_i \widetilde{Y}_{\mathrm{F}i}$ or use Equation 2.45
Fuel vapour specific heat capacity	$c_{p\mathrm{F}} = \sum_i \varepsilon_i c_{p\mathrm{F}i}$
Latent heat of evaporation	$L = \sum_i \varepsilon_i L_i$
Liquid specific heat capacity	$c_{p\mathrm{L}} = \sum_i X_i c_{p\mathrm{L}i}$
Liquid kinematic viscosity	Combined as a dynamic viscosity: $\mu_{\mathrm{L}} = \rho_{\mathrm{L}} \sum_i X_i \nu_{\mathrm{L}i}$
Liquid thermal conductivity	Power law method [77]: $\lambda_{\mathrm{L}} = \left(\sum_i X_i \lambda_{\mathrm{L}i}^{-2} \right)^{-0.5}$

on the species present and the ambient pressure. At equilibrium, the molar liquid concentration $\widetilde{X}_i$ of species i is related to the molar vapour concentration $\widetilde{Y}_i$ of species i, through the equality of the fugacities of each phase [56]:

$$f_i^{\mathrm{L}} = f_i^{\mathrm{V}}, \tag{2.46}$$

$$\gamma_i \phi_i^{\mathrm{sat}} \exp\left(\int_{p_{\mathrm{vap}\,i}}^{p} \frac{\mathrm{d}p}{\rho_{\mathrm{L}i} R_i T} \right) \widetilde{X}_i p_{\mathrm{vap}\,i} = \phi_i \widetilde{Y}_i p, \tag{2.47}$$

where γ_i is the liquid activity coefficient evaluated at the interface temperature and system pressure, ϕ_i is the vapour fugacity coefficient at the interface temperature and system pressure, ϕ_i^{sat} is the vapour fugacity coefficient at the interface temperature and at the saturation pressure, and R_i is the specific gas constant. The exponential term is know as the Poynting factor and evaluates the contribution to the liquid phase fugacity from the system pressure acting on the liquid species i being in fact larger than the vapour pressure from just species i. At moderate temperatures and pressures, the liquid may be assumed to be incompressible ($\rho_{\mathrm{L}i}$ is constant). In particular, at the relatively low pressures and temperatures encountered by fuel droplets in a GDI engine cylinder (particularly in homogeneous operation), a simplified form of Equation 2.47 is considered:

$$\gamma_i \widetilde{X}_i p_{\mathrm{vap}\,i} = \widetilde{Y}_i p, \tag{2.48}$$

where all the coefficients apart from the activity coefficient are roughly equal to unity; this approach reflects findings from [89].

When liquids are combined in a mixture, at constant temperature and pressure, the Gibbs free energy of the mixture is different to that of the sum of the individual components. One part of this change is the decrease in Gibbs free energy resulting from the increase in the system entropy due to mixing. If there is a change in the system enthalpy upon mixing, due to mutual attractive or repulsive intermolecular forces between the different molecule types, then there will be an additional change to the Gibbs free energy of the mixture. This excess change in Gibbs free energy is related to the activity coefficient via the relationship [56]

$$G_{\mathrm{E}} = \sum_i n_i R_0 T \ln \gamma_i. \tag{2.49}$$

For similar types of molecules, such as mixtures of saturated hydrocarbons (paraffins), there is close to zero excess Gibbs free energy on mixing and the activity coefficient for each species is very close to unity. Such a liquid mixture is known as ideal and Equation 2.48 becomes Raoult's law:

$$\widetilde{X}_i p_{\mathrm{vap}\,i} = \widetilde{Y}_i p. \tag{2.50}$$

When there is only one liquid component, $\widetilde{X}_i = 1$ and Equation 2.6 is obtained.

When there are different functional groups present in the molecules of a mixture, *e.g.* aromatic hydrocarbons with saturated hydrocarbons or oxygenated hydrocarbons with saturated hydrocarbons, net intermolecular forces arise. This causes activity coefficients to differ from unity and the mixture is known as non-ideal. The activity coefficients will be highly composition dependent since the change in enthalpy upon mixing will depend on the quantity of molecules involved in a non-ideal intermolecular interaction. For pure hydrocarbon gasoline mixtures, Raoult's law is a reasonable approximation but it was deemed necessary to account for non-unity

activity coefficients due to the interaction of aromatic species with paraffinic species in [13]. When alcohol is present in the fuel, the degree of non-ideality is greatly increased due to the polarity of the –OH functional group. The high polarity can cause a highly repulsive intermolecular force and an increased excess Gibbs energy. Therefore, activity coefficients are much larger than one, which means that Equation 2.48 must be used.

Various models for γ_i exist and are summarized in Chapter 8 of [56]. In this work, two models are employed: NRTL (Non Random Two Liquid) and UNIFAC (Universal Functional Activity Coefficient).

The NRTL model may be fitted to experimental binary vapour-liquid equilibrium data, which means that it can be highly accurate. The binary activity coefficients are found by:

$$\ln \gamma_1 = \widetilde{X}_2^2 \left[\tau_{21} \left(\frac{G_{21}}{\widetilde{X}_1 + \widetilde{X}_2 G_{21}} \right) + \frac{\tau_{12} G_{12}}{\left(\widetilde{X}_2 + \widetilde{X}_1 G_{12} \right)^2} \right], \tag{2.51}$$

where $\tau_{12} = \frac{\Delta g_{12}}{R_0 T}$, $\tau_{21} = \frac{\Delta g_{21}}{R_0 T}$, $G_{12} = \exp(-\alpha \tau_{12})$ and $G_{21} = \exp(-\alpha \tau_{21})$. The three parameters Δg_{12}, Δg_{21} and α are fitted to experimental data. Temperature dependence comes through the τ variables and the appropriate temperature for droplet evaporation is the droplet surface temperature. The activity coefficient γ_2 may be obtained by swapping the subscripts. It is possible to find activity coefficients for mixtures of three or more species by using experimental data for mixtures of each pair of species. However, this becomes arduous as the number of species present begins to rise and is not attempted here.

For mixtures where there exists no vapour-liquid equilibrium data or where there are many components, the activity coefficients may be estimated using the UNIFAC method [90]. This method requires only pure component data for each species, which is readily available, and can provide a reasonable estimate even for mixtures containing azeotropes [56]. The interaction between the different functional groups present in a mixture is estimated, based on experimental findings, to help estimate the activity coefficients. The UNIFAC model breaks the calculation for the activity

coefficient into two parts. The first part is known as the combinatorial part, which describes the molecular interactions due to differences in molecule shape and size. The second part of the model is the residual part, which describes functional group interactions. In UNIFAC, this requires data on the functional groups present in each molecule, which replaces the need for the experimental binary vapour-liquid equilibrium data. The equations modelled in this thesis are those presented in [77] and shown below for species i. The counter variable k moves through all the functional groups present in the mixture and $\nu_k^{(i)}$ is the number of occurrences of that group in molecule i, which could be zero.

$$\ln \gamma_i = \ln \gamma_i^{\text{Comb}} + \ln \gamma_i^{\text{Res}}, \tag{2.52}$$

$$\ln \gamma_i^{\text{Comb}} = \ln \frac{\Phi_i}{\widetilde{X}_i} + \frac{z}{2} q_i \ln \frac{\theta_i}{\Phi_i} + l_i - \frac{\Phi_i}{\widetilde{X}_i} \sum_j \widetilde{X}_j l_j, \tag{2.53}$$

$$\ln \gamma_i^{\text{Res}} = \sum_k \nu_k^{(i)} \left(\ln \Gamma_k - \ln \Gamma_k^{(i)} \right), \tag{2.54}$$

where

$$l_i = \frac{z}{2}(r_i - q_i) - (r_i - 1), \tag{2.55}$$

$$\theta_i = \frac{q_i \widetilde{X}_i}{\sum_j q_j \widetilde{X}_j} \quad \text{and} \quad \Phi_i = \frac{r_i \widetilde{X}_i}{\sum_j r_j \widetilde{X}_j}, \tag{2.56}$$

$$r_i = \sum_k \nu_k^{(i)} R_k \quad \text{and} \quad q_i = \sum_k \nu_k^{(i)} Q_k, \tag{2.57}$$

$$\ln \Gamma_k = Q_k \left[1 - \ln \left(\sum_m \theta_m \Psi_{mk} \right) - \sum_m \frac{\theta_m \Psi_{km}}{\sum_n \theta_n \Psi_{nm}} \right], \tag{2.58}$$

$$\theta_m = \frac{Q_m \widetilde{X}_m}{\sum_n Q_n \widetilde{X}_n}, \tag{2.59}$$

$$\Psi_{mn} = \exp \left(-\frac{a_{mn}}{T} \right). \tag{2.60}$$

In Equations 2.55 to 2.57, R_k and Q_k are, respectively, the functional group volume and surface area, normalized by the volume and surface area of a –CH_2– group in a very long saturated hydrocarbon chain. Thus, r_i and q_i are normalized molecule volume and surface area parameters respectively, and Φ_i and θ_i are molecule volume and surface area fraction parameters respectively. The parameter z is the

co-ordination number, which describes how many other molecules surround each molecule in 3-D space, and is usually taken as equal to 10 [56, 77].

A group surface area fraction parameter θ_m is calculated in Equation 2.59 for each group m, by calculating the surface area that this group occupies in the mixture compared to the surface area that all groups in the mixture occupy. Here, $\widetilde{X}_m$ is calculated as $\sum_i \widetilde{X}_i \nu_m^{(i)} / \sum_i \left(\widetilde{X}_i \sum_m \nu_m^{(i)} \right)$. In Equation 2.54, Γ_k is the residual activity coefficient for group k in the mixture (and is the same for all molecules i) and $\Gamma_k^{(i)}$ is the residual activity coefficient for group k in a pure liquid of species i (which occurs due to interactions between different groups on adjacent molecules of the same species). Equation 2.58 is used to calculate $\Gamma_k^{(i)}$ as well Γ_k, taking $\widetilde{X}_m^{(i)} = \nu_m^{(i)} / \sum_m \nu_m^{(i)}$ in the case of $\Gamma_k^{(i)}$.

There is a distinction between the main group type and the secondary group designation in the UNIFAC model. A main group type is a classification, such as 'paraffins' or 'aromatics', whereas the secondary groups will differentiate between the individual instances of the main group type, such as the difference between the paraffinic groups –CH_3 and –CH_2–. Since each secondary group has a different size, these require different data for R_k and Q_k, sourced from [77]. However, it is assumed that groups in adjacent molecules belonging to the same main group type do not induce non-ideal interactions. Therefore, the group interaction parameter a_{mn} is zero when the two secondary groups m and n are in the same main group type. Thus, data for a_{mn} for pairs of groups belonging to the different main group types is sourced from [77].

Non-equilibrium models have been formulated that account for evaporation rate kinetics and have been shown to give more reliable results under conditions with very fast vaporization [91]. However, at more moderate temperatures, similar to those of interest in this work, both equilibrium and non-equilibrium models were shown to give similar results.

Droplet internal mixing models

It is typically assumed that the multi-component mixture composition evolves by a well-mixed process. In this assumption, more volatile components that evaporate preferentially from the droplet surface (a higher value of ε_i) are instantaneously replenished from the bulk so that they may continue to evaporate. This model is also known as batch distillation or infinite liquid diffusivity. It is analogous to the uniform droplet temperature model as the compositions of all species are uniform throughout the droplet. Component i loses a mass equal to $\varepsilon_i \dot{m}\,\Delta t$ during each time interval Δt and the internal composition evolves as

$$X_i(t+\Delta t) = \frac{X_i(t)m(t) - \varepsilon_i(t)\dot{m}(t)\Delta t}{m(t+\Delta t)}. \tag{2.61}$$

It is thought that when the evaporation time is much longer than the typical time to diffuse mass from the droplet interior to the surface, the well-mixed model will give a good approximation of the surface composition and hence the droplet evaporation rate.

The opposite limiting case occurs when no liquid mixing occurs inside the droplet and $X_i(t) = X_i(0)$. This is known as the unmixed model. Alternatively, it is known as the rapid regression limit, reflecting the case when evaporation is so fast that the surface regression rate is faster than the liquid species' diffusive velocity. Two possibilities exist for the surface vapour concentration: either $\varepsilon_i = X_i$, which is known as the onion-skin model and leads directly to the simplified Raoult's law with $\gamma_i = 1$, or Equations 2.42 and 2.48 may be used in the case of non-ideal mixtures. If the evaporation rate is so fast as to preclude liquid mixing then it is possible that surface equilibrium is also unlikely to be reached and the onion-skin model may become more appropriate.

The internal droplet vortex described in Figure 2.2 enhances mass transfer in the droplet. The liquid diffusion coefficient for species i moving through species j in a moving spray droplet is usually enhanced by the factor of $\chi_{\text{mass}} = 2.72$, which is calculated in a similar fashion to χ. This will increase the ability of the species to mix inside the droplet. However, if a mass transfer analogue of the Biot number is

defined as $\mathrm{Bi}_{\mathrm{mass}} = k_Y d/D_{\mathrm{L,\,eff}} = \mathrm{Sh}\, D/\chi D_{\mathrm{L}}$, it is found that this is typically much larger than one, even if the droplet is considered stationary and evaporation slow:

$$\mathrm{Bi}_{\mathrm{mass}} = \frac{\mathrm{Sh}\, D}{\chi D_{\mathrm{L}}} \sim \frac{2 \cdot 1 \times 10^{-5}}{2.72 \cdot 1 \times 10^{-8}} \sim 700. \tag{2.62}$$

Therefore, it is appropriate to consider finite liquid mixing rates to occur at all droplet conditions and it is expected that, as the evaporation rate increases, the discrepancy between the actual surface composition and the well-mixed surface composition will increase. Therefore, the lifetime estimate given by the well-mixed model will become less accurate.

Although concentration gradient-driven liquid diffusion is slow at the internal droplet conditions, this is the only mass transfer mechanism considered here. Typical thermal diffusion coefficients (the constant of proportionality between temperature gradient and contribution to mass transfer from thermal diffusion) are around three orders of magnitude below concentration diffusion coefficients [92] and the differential thermal diffusion will be much smaller than mass concentration diffusion and vortex mixing.

Diffusion-controlled model - binary mixtures

For a binary fuel mixture, only one species equation needs to be considered, since the other species is given by mass balance. The spherically symmetric diffusion equation is used to approximate the process, assuming negligible bulk liquid velocity relative to the droplet centre, and the liquid density and the binary diffusion coefficient are taken as constant:

$$\frac{\partial X_1}{\partial t} = \chi_{\mathrm{mass}} D_{\mathrm{L12}} \left(\frac{2}{r} \frac{\partial X_1}{\partial r} + \frac{\partial^2 X_1}{\partial r^2} \right) \tag{2.63}$$

where the liquid diffusion coefficient for species 1 through species 2 (D_{L12}) has also been enhanced by a factor χ_{mass}. This is calculated from Equation 2.34 using $\mathrm{Pe}_Y = \mathrm{Re}_{\mathrm{L}}\, \mathrm{Sc}_{\mathrm{L}} = U_{\mathrm{Lmax}} d/D_{\mathrm{L12}}$ instead of Pe_T. As with the effective conductivity model, the internal composition will be in error, with the primary aim to achieve a reliable surface composition. The boundary conditions are [75]:

$$\left.\frac{\partial X_1}{\partial r}\right|_{r=0} = 0, \tag{2.64}$$

$$\left.\frac{\partial X_1}{\partial r}\right|_{\mathrm{s}} = \dot{m}\frac{X_{\mathrm{s1}} - \varepsilon_1}{\pi\rho_{\mathrm{L}}\chi_{\mathrm{mass}}D_{\mathrm{L12}}d^2}. \tag{2.65}$$

The liquid diffusion coefficient is calculated in stages. First, an infinite dilution diffusion coefficient D_{ij}^0 is calculated for a trace amount of species i diffusing through species j. In this thesis, the Tyn and Calus method has been used [77, 93], which may be given by

$$D_{ij}^0 = 1.10 \times 10^{-9}\,\frac{V_{cj}^{0.279}}{V_{ci}^{0.454}}\frac{T_{\mathrm{L}}}{\mu_{\mathrm{L}j}}\left(\frac{\sigma_j}{\sigma_i}\right)^{0.15}, \tag{2.66}$$

where D_{ij}^0 is given in $\mathrm{m^2/s}$, V_{c} is the critical molar volume in $\mathrm{cm^3/mol}$, μ_{L} is the liquid dynamic viscosity in $\mathrm{N\,s/m^2}$ and σ is the surface tension at the boiling temperature. Note that $D_{ij}^0 \neq D_{ji}^0$ and $(\sigma_j/\sigma_i)^{0.15} \approx 1$. When species j is ethanol or methanol, there is an under-prediction of D_{ij}^0; therefore, a multiplicative factor is applied to $V_{\mathrm{c}j}$, equal to $0.08\mu_{\mathrm{L}j}$, where $\mu_{\mathrm{L}j}$ is the pure component viscosity in $\mathrm{Ns/m^2}$ [56].

The infinite dilution diffusion coefficient should be corrected for composition effects and non-ideal mixture effects; these may have a significant effect on the magnitude of the coefficient. The effect of composition is included by using the empirical Vignes relationship [77, 93] and a thermodynamic correction factor Γ [77, 93] accounts for non-ideal effects:

$$D_{ij} = D_{ji} = \Gamma Đ_{ij} = \Gamma(D_{ij}^0)^{1-X_i}(D_{ji}^0)^{X_i}, \tag{2.67}$$

where $Đ_{ij}$ is the Maxwell-Stefan diffusion coefficient.

The thermodynamic correction factor accounts for the fact that diffusion occurs in practice due to a gradient in chemical potential, rather than concentration, as implied in Equation 2.63. The chemical potential of a liquid species i is the derivative of the mixture total Gibbs free energy with respect to the number of moles n_i of that species and, for an ideal mixture, it is given by

$$\mu_i^\star = \mu_i^\ominus + R_0 T \ln \widetilde{X}_i. \tag{2.68}$$

where $\mu_i^\ominus$ is a reference value at standard conditions (*e.g.* 1 bar and 298 K). A small change in chemical potential becomes $\mathrm{d}\mu_i^\star = R_0 T \,\mathrm{d}\ln \widetilde{X}_i = (R_0 T/\widetilde{X}_i)\,\mathrm{d}\widetilde{X}_i$ at constant temperature, which gives rise to the link between diffusion and a concentration gradient.

When there is a non-ideal mixture and an excess Gibbs free energy is created, as specified in Equation 2.49, each species' chemical potential is increased by an amount $R_0 T \ln \gamma_i$. Therefore, a small change in chemical potential becomes $\mathrm{d}\mu_i^\star = R_0 T \left(\mathrm{d}\ln \widetilde{X}_i + \mathrm{d}\ln \gamma_i\right)$. This enables the definition of the correction factor Γ to account for the non-ideal liquid mixture behaviour:

$$\Gamma = 1 + \left.\frac{\partial \ln \gamma_i}{\partial \ln \widetilde{X}_i}\right|_{p,\,T} = 1 + \left.\frac{\widetilde{X}_i}{\gamma_i}\frac{\partial \gamma_i}{\partial \widetilde{X}_i}\right|_{p,\,T}. \tag{2.69}$$

The derivatives with respect to mole fraction are evaluated at constant pressure and liquid temperature, and the total mole fraction must always sum to one. For ideal mixtures, $\ln \gamma_i = 0$ and $\Gamma = 1$. For mutually repulsive non-ideal mixtures, such as alcohols and hydrocarbons, Γ can be much smaller than one, which greatly reduces the diffusion coefficient. In extreme cases, $\Gamma < 0$, which indicates liquid phase instability leading to phase separation.

Diffusion-controlled model - multi-component mixtures

When there are $N \geqslant 3$ components present in the fuel droplet, it becomes necessary to consider $N-1$ liquid diffusion equations, such that the N^{th}species mass fraction distribution is given by a mass balance. The system of equations may be written for a droplet as

$$\rho_\mathrm{L} \frac{\partial(\mathbf{X})}{\partial t} = -\nabla \cdot (\mathbf{J}) = \rho_\mathrm{L}[\mathbf{D}_\mathrm{L}](\nabla^2 \mathbf{X}), \tag{2.70}$$

where $(\mathbf{X})$ is the vector of component compositions, $(\mathbf{J})$ is the vector of component mass fluxes, $[\mathbf{D}_\mathrm{L}]$ is the liquid diffusion coefficient matrix and $(\boldsymbol{\nabla^2 \mathbf{X}})$ is the vector of the Laplacians of the component compositions. These partial differential equations

(PDEs) are coupled due to the presence of non-zero off-diagonal terms: $D_{\mathrm{L}ij}$ for $i \neq j$. The matrix $[\mathbf{D}_{\mathrm{L}}]$ can be computed using techniques from [93] (Chapter 2):

$$[\mathbf{D}_{\mathrm{L}}] = [\mathbf{B}]^{-1}[\mathbf{\Gamma}], \tag{2.71}$$

where the diagonal and off-diagonal elements of $[\mathbf{B}]$ are given by

$$B_{ii} = \frac{\widetilde{X}_i}{Đ_{iN}} + \sum_{\substack{k=1 \\ k\neq i}}^{N} \frac{\widetilde{X}_k}{Đ_{ik}}, \tag{2.72}$$

$$B_{ij} = -\widetilde{X}_i \left(\frac{1}{Đ_{ij}} - \frac{1}{Đ_{iN}} \right), \tag{2.73}$$

and the elements of the thermodynamic correction matrix $[\mathbf{\Gamma}]$ are given by

$$\Gamma_{ij} = \delta_{ij} + \frac{\widetilde{X}_i}{\gamma_i} \frac{\partial \gamma_i}{\partial \widetilde{X}_j}\bigg|_{p,\,T}. \tag{2.74}$$

The form of the $[\mathbf{B}]$ matrix arises from the fact that the diffusional flux of the N^{th}component is not independent. The value of δ_{ij} is 1 if $i = j$ and 0 otherwise. The derivatives are evaluated at constant pressure and temperature, and with total mole fractions summing to one (with $\widetilde{X}_N$ adjusted accordingly). The composition dependence for multi-component mixtures is approximated through an average Vignes relationship [93]:

$$Đ_{ij} = (D^0_{ij})^{(1-X_i+X_j)/2} \, (D^0_{ji})^{(1-X_j+X_i)/2}. \tag{2.75}$$

Since alcohol species mix non-ideally with hydrocarbons, these will have larger activity coefficients and, hence, smaller, possibly negative, values for $D_{\mathrm{L}ii}$ (the self-diffusion coefficient), due to the reduced non-ideal thermodynamic correction factor Γ_{ii}. Thus, in a multicomponent mixture representative of gasoline with alcohol content, the rate of mixing of alcohol species will be much lower than that of the hydrocarbon species. Therefore, to investigate whether the surface composition predicted by a diffusion-controlled model is significantly different from the well-mixed case, a pseudo-binary model has been created. This models the

diffusion of the alcohol component throughout the droplet and treats the remaining components as well-mixed within the remaining mass fraction.

Therefore, for gasoline fuels containing three or more components, the solving of the coupled PDEs will not be attempted and, instead, a pseudo-binary formulation has been developed, requiring only the diffusion equation to be solved. Equation 2.63 has been used to find $X_1(r,t)$, with species 1 set to be the alcohol component. The radial distribution of the remaining hydrocarbon fractions is given by $X_{2-N}(r,t) = 1 - X_1(r,t)$ and each individual hydrocarbon fraction is weighted by the surface mass fraction for that species:

$$X_j(r,t) = (1 - X_1(r,t)) \frac{X_{\mathrm{s}j}}{\sum_{m=2}^{N} X_{\mathrm{s}m}}, \quad \text{for } j \geqslant 2, \tag{2.76}$$

The diffusive mass flux (units of kg/m^2·s) of the alcohol species (species 1) is given by $J_1 = -\rho_{\mathrm{L}} \sum_{j=1}^{N-1} D_{\mathrm{L}1j} \nabla X_j$. In the spherically symmetric case, and with reference to the assumed mass fraction profiles in Equation 2.76, the gradient of the hydrocarbon species becomes

$$\nabla X_j = \frac{\partial X_j}{\partial r} = -\frac{\partial X_1}{\partial r} \frac{X_{\mathrm{s}j}}{\sum_{m=2}^{N} X_{\mathrm{s}m}} \quad \text{for } j \geqslant 2. \tag{2.77}$$

Therefore, the liquid diffusion coefficient D_{L} has been set to

$$D_{\mathrm{L}} = D_{\mathrm{L}11} - \sum_{j=2}^{N-1} D_{\mathrm{L}1j} \frac{X_{\mathrm{s}j}}{\sum_{m=2}^{N} X_{\mathrm{s}m}}. \tag{2.78}$$

The surface composition of the hydrocarbon components ($j \geqslant 2$) is calculated by substituting Equation 2.76 into the integral for the total mass of each component remaining within the droplet:

$$m_j = 4\pi \int_0^{d/2} \rho_{\mathrm{L}}(r) X_j(r) r^2 \, \mathrm{d}r. \tag{2.79}$$

The remaining mass of each component m_j must therefore be tracked throughout the droplet lifetime.

2.1.4 Superheated droplets

As was discussed in Section 1.3.1, fuel sprays are often superheated with respect to the ambient pressure conditions and the droplets created can contain superheated liquid. If the droplet surface is assumed to be in equilibrium, then the surface temperature will be equal to the boiling temperature T_b, for the current droplet surface composition. Two things become apparent. Firstly, if the droplet is to retain any level of superheat, a non-uniform droplet temperature model must be used to allow for droplet internal temperatures to be above the boiling temperature. Secondly, Equation 2.13 or 2.14 must be used since at the boiling temperature, $Y_\mathrm{Fs} \to 1$ and $B_Y \to \infty$. Therefore, the evaporation rate becomes limited by heat transfer and remains finite, as is observed in experiments with flash boiling sprays.

The first attempt to include enhancements to spray droplet evaporation rate due to superheat were detailed in [49], developed for a hollow cone spray in a PFI system. They recommended an additional superheat evaporation rate $\dot{m}_\mathrm{sh}$ be added to the evaporation rate $\dot{m}$ to account for flash evaporation:

$$\dot{m}_\mathrm{sh} = \frac{\alpha_\mathrm{sh}(T_\mathrm{d} - T_\mathrm{b})\pi d^2}{L}, \tag{2.80}$$

where α_sh is a superheat boiling heat transfer coefficient with units $\mathrm{W/m^2{\cdot}K}$, specified as

$$\alpha_\mathrm{sh} = \begin{cases} 760\Delta T^{0.26} & 0 \leqslant \Delta T \leqslant 5 \\ 27\Delta T^{2.33} & 5 \leqslant \Delta T \leqslant 25 \\ 13800\Delta T^{0.39} & \Delta T \geqslant 25 \end{cases} \tag{2.81}$$

where $\Delta T = T_\mathrm{d} - T_\mathrm{b}$ is measured in kelvin. No indication is given in [49] of how the droplet temperature evolves with time. Therefore, it may be that a uniform temperature model is used and the fact that the droplet surface is superheated (*i.e.* not at equilibrium) is ignored.

In [87, 88], the two-point droplet temperature model is used to account for superheated droplets, using the same superheat boiling heat transfer coefficient

as [49]. Thus, the heat transferred from the surface to the interior (*i.e.* in the negative r-direction) becomes

$$\dot{Q}_{\mathrm{L}} = -\pi d^2 \left(\frac{\chi \lambda_{\mathrm{L}}}{\delta} + \alpha_{\mathrm{sh}} \right) (T_{\mathrm{d}} - T_{\mathrm{b}}). \tag{2.82}$$

The evaporation rate is then calculated from Equation 2.13 or 2.14, with the knowledge that B_T is a function of $\dot{m}$ so an iterative approach is needed. This approach has been extended here, so that it can be used with the droplet heat equation model, where $\dot{Q}_{\mathrm{L}}$ becomes

$$\dot{Q}_{\mathrm{L}} = -\pi d^2 \Big(\alpha_{\mathrm{sh}} (T(r=0) - T_{\mathrm{b}}) - \chi \lambda_{\mathrm{L}} G_{\mathrm{Ls}} \Big), \tag{2.83}$$

allowing G_{Ls} to be extracted and used as a boundary condition for Equation 2.28.

In the implementation of [87], the evaporation rate calculated when the surface temperature is equal to the boiling temperature is compared to the evaporation rate calculated when the surface temperature is just below the boiling temperature. If the slightly sub-cooled evaporation rate exceeds the boiling one, the surface temperature T_{s} is set equal to the boiling temperature. This was based on the expected breakdown in the applicability of Equation 2.11 as $T_{\mathrm{s}} \to T_{\mathrm{b}}$ and $Y_{\mathrm{Fs}} \to 1$.

However, another approach is postulated here. At surface temperatures just below boiling, the evaporation rate is calculated separately from both the mass balance and the energy balance (Equations 2.11 and 2.13) and compared. If the evaporation rate from the energy balance is largest, then the droplet evaporation rate would be mass transfer limited at that temperature and the additional energy would be retained by keeping the surface at its boiling temperature. If the evaporation rate from the mass balance is larger, then the droplet evaporation rate must be heat transfer limited at that temperature and additional energy would be taken from the droplet surface, thereby giving a lower surface temperature than boiling. When the droplet surface is slightly sub-cooled, a surface temperature is calculated iteratively by assuming that the two expressions for $\dot{m}$ are equal (Equations 2.11 and 2.13). Since Equation 2.13 should always give sensible evaporation rates for any surface temperature, this approach is deemed valid. In addition, this approach allows the

surface to reduce below its boiling temperature as the whole droplet begins to chill (if in a cool enough ambient condition) without arbitrarily holding it at its boiling temperature. This is important for multi-component evaporation as the boiling temperature will rise as the droplet evaporates, with volatile components leaving first. The effects of varying these assumptions is discussed in Chapter 4.

2.1.5 Inter-droplet effects

Sirignano and co-workers [94, 95] have modelled groups of droplets without a forced convective velocity and presented correlations based on the average spacing and the size of the group. They found that droplets in the centre of large groups have greatly reduced evaporation rates, even at relatively high spacings. However, as shown in Section 4.2, in a typical convective environment, the influence zone for heat and mass transfer (also known as the heat and mass transfer film thickness) is typically much smaller than the droplet spacing. In addition, in the engine flow environment, there will always exist convective enhancement of heat and mass transfer, even at zero droplet slip velocity, due to the turbulent nature of the air motion. Therefore, inter-droplet effects of the sort described in [94, 95] will be ignored in this thesis.

However, as a droplet moves relative to the air it will deposit vapour in and add or remove heat from the air inside the heat and mass transfer film, which subsequent droplets will have to travel through. Therefore, correlations have been developed for modified evaporation rates of droplets in droplet streams, for example [96, 97]. These works observed experimentally a range of spacings from $3d$ to $7d$, for initial droplet diameters of $d_0 \approx 0.1$ mm and velocities of around 10 m/s. They found that the spacing had a moderate impact on the convective enhancements and hence on evaporation rate. The reduction factor for Nusselt and Sherwood numbers was presented in the form

$$\eta = \frac{(\text{Sh or Nu})}{(\text{Sh or Nu})_{\text{iso}}} = \frac{1 - A}{(Bt^\star + 1)^C} + A, \tag{2.84}$$

where $t^\star$ is a dimensionless time given by

$$t^\star = \frac{f\delta}{u} = \frac{\pi d^2 U \rho \delta}{\dot{m} S}. \tag{2.85}$$

Here, δ is the film thickness for heat or mass transfer in the gas phase (see Equation 4.8), $f = U/S$ is the droplet stream frequency, u is the Stefan convective velocity used in Equations 2.1 and 2.2, S is the droplet spacing, and A, B and C are fitted constants. The evaporation rate $\dot{m}$ for the isolated droplet must be used to calculate $t^\star$, then η can be used to calculate the non-isolated droplet evaporation rate. Two sets of the constants B and C are suggested in [96]. The effect of one-dimensional droplet shielding is implicitly accounted for in this correlation, as the isolated Sherwood and Nusselt numbers will use the isolated droplet relative velocity, rather than that experienced by a droplet in a group.

2.1.6 Implementation in MATLAB

Each of the single droplet models described in this thesis have been implemented in Matlab, in order to calculate the droplet history from creation to full evaporation. Each of the relevant parameters are recorded throughout the lifetime: droplet diameter d, mass m, composition X_i, temperature T_L, velocity U. A time step Δt is chosen and the droplet mass, diameter, velocity and position are updated using a simple forward difference scheme. At step k, corresponding to time $t = k\,\Delta t$:

$$m^{k+1} = m^k - \dot{m}^k\,\Delta t, \tag{2.86}$$

$$d^{k+1} = \left(\frac{6m^{k+1}}{\pi\rho_\mathrm{L}}\right)^{1/3}, \tag{2.87}$$

$$U^{k+1} = U^k + \frac{3C_D\rho|U^k|U^k}{4\rho_\mathrm{L}d^k}\,\Delta t, \tag{2.88}$$

$$x^{k+1} = x^k + U^k\,\Delta t. \tag{2.89}$$

For the uniform droplet temperature model, the temperature can be updated in a similar fashion as $T^{k+1} = T^k + \dot{T}\,\Delta t$. For the droplet heat equation model, the droplet radius is discretized into N_r grid points with spacing $\Delta r = d/\Big(2(N_r - 1)\Big)$, where the j^{th}grid point corresponds to a radius of $r = (j-1)\Delta r$. The temperature derivatives are approximated using forward differences, for points $j = 2$ to $j = N_r - 1$, as

$$\frac{\partial T_{\mathrm{L}}}{\partial t} \approx \frac{T_j^{k+1} - T_j^k}{\Delta t}, \quad \frac{\partial T_{\mathrm{L}}}{\partial r} \approx \frac{T_{j+1}^k - T_j^k}{\Delta r} \quad \text{and} \quad \frac{\partial^2 T_{\mathrm{L}}}{\partial r^2} \approx \frac{T_{j+1}^k - 2T_j^k + T_{j-1}^k}{(\Delta r)^2}. \tag{2.90}$$

This allows Equation 2.28 to be implemented as

$$T_j^{k+1} = \tau T_{j-1}^k + \left(1 - 2\tau \frac{j}{j-1}\right) T_j^k + \tau \frac{j+1}{j-1} T_{j+1}^k, \tag{2.91}$$

where $\tau = \chi \alpha_{\mathrm{L}} \Delta t / (\Delta r)^2$. At the droplet centre, $j = 1$, a central difference approximation of the symmetry boundary condition, Equation 2.29, gives $T(-\Delta r) = T(\Delta r)$, resulting in

$$T_1^{k+1} = (1 - 2\tau) T_1^k + 2\tau T_2^k. \tag{2.92}$$

At the droplet surface, $j = N_r$, the surface temperature gradient G_{Ls} is prescribed and is inserted directly into the discretized heat equation, giving

$$T_{N_r}^{k+1} = (1 - \tau) T_{N_r}^k + \tau T_{N_r - 1}^k + \tau G_{\mathrm{Ls}} \Delta r \, \frac{N_r + 1}{N_r - 1}. \tag{2.93}$$

Equations 2.91 to 2.93 can be set into matrix form as

$$(T)^{k+1} = [A]_T (T)^k + (B)_T, \tag{2.94}$$

to allow a rapid update of the temperature throughout the droplet. As the droplet evaporates and as the liquid temperature and, hence, the liquid density changes, the droplet size will change. To account for this, the grid points regress inwards as the size reduces, to maintain N_r points between surface and centre, and values are interpolated to give corrected values of $(T)^{k+1}$ to be passed into the calculations at the next time step (this method is used in [97]). The alternative is a formulation with a non-dimensionalized radius, as described in [75], which was also undertaken and provided very similar droplet surface temperature results.

In the superheated droplet models, there is a need to update the temperature throughout the droplet with the boundary condition of a preset surface temperature

T_s (*e.g.* with the surface at the boiling temperature). In this case, only $N_r - 1$ difference equations are needed, with the temperature at $j = N_r - 1$ evolving as

$$T^{k+1}_{N_r-1} = \left(1 - 2\tau\frac{N_r - 1}{N_r - 2}\right) T^k_{N_r-1} + \tau T^k_{N_r-2} + \tau T_\mathrm{s}\frac{N_r}{N_r - 2}. \tag{2.95}$$

Then, the surface liquid temperature gradient may be found as $G_\mathrm{Ls} = (T_\mathrm{s} - T^{k+1}_{N_r-1})/\Delta r$.

The evaporation rate is calculated from Equation 2.13, using the iterative formula

$$\dot{m} = B\left(L - \frac{B_T L_\mathrm{eff}}{\exp\left(\frac{\dot{m}}{A}\right) - 1}\right)^{-1}, \tag{2.96}$$

where $A = \pi d\lambda \mathrm{Nu}'/c_{p\mathrm{F}}$ and $B = (\alpha_\mathrm{sh}(T(r = 0) - T_\mathrm{b}) - \chi\lambda_\mathrm{L}G_\mathrm{Ls})\pi d^2$. This can be used when the droplet is superheated or sub-cooled (in which case, $\alpha_\mathrm{sh} = 0$). This form of the expression, with the exponential function, will not yield complex solutions in an iterative search for the correct value of $\dot{m}$. One equation is used for the total evaporation rate from a multi-component droplet, instead of one equation for each species. This is advantageous in reducing the calculation complexity when that droplet is superheated.

For the diffusion-controlled droplet internal composition calculation, an approach similar to Equations 2.91 to 2.93 was used. The number of grid points for the diffusion equation was not necessarily the same and τ was set to equal $\chi_\mathrm{mass}D_\mathrm{L}\Delta t/(\Delta r)^2$. Typically, more grid points were used in the composition equation solutions, due to the slower nature of the liquid diffusion process, in order to resolve the surface gradients and more accurately capture the effect of the regressing surface.

Diffusion coefficient matrices required for the pseudo-binary diffusion-controlled model can either be generated beforehand, for a number of specific alcohol mass fractions, or during the droplet simulation. If the matrices are generated first, then a supposed composition will be used for the two or more hydrocarbons, *e.g.* the initial composition. Then, given the actual alcohol mass fraction in the droplet at a given time and position, interpolation can be used to find a suitable diffusion

coefficient matrix. The hydrocarbon composition will also vary throughout the droplet life, so this may introduce errors. It was found that the diffusion matrix can be generated at every time step to get a more exact estimate of the alcohol diffusion coefficient in the presence of the actual composition of hydrocarbon species present at that time. This technique was used in generating all of the multi-component diffusion-controlled droplet simulation results in this thesis, which resulted in an increased simulation time.

2.1.7 Model validation

Some of the models described are based on existing formulations that have been well-validated, for example, the various approaches to convective enhancement and the droplet temperature models [75]. Therefore, these may be used with confidence and can be validated against existing model results. The non-ideal multi-component models employed here are able to predict fuel vapour pressures and fuel distillation curves accurately (see Section 3.4). Therefore, their applicability to non-ideal multi-component droplet models is assured if the surface concentration is accurate.

Validation has typically been carried out on drops larger than those seen in a gasoline spray (*e.g.* 0.9 mm–1.5 mm [98], 1.5 mm–1.7 mm [99], 120 µm [97], 100 µm–130 µm [96])albeit with dimensionless groups relevant to the smaller droplets in the corresponding application. In terms of internal heat and mass transfer, a larger droplet may allow a larger convective enhancement due to internal droplet motion as mixing may occur over a larger range of scales. The typical spherical Hill's vortex shape, or other observed internal liquid motions, is assumed for droplets in the spray, whereas more complex motion with different heat and mass transfer enhancements may be possible, for larger droplets.

Two sets of experimental data are used to validate the models. Firstly, single component fuel droplets tests presented in [100] are compared with model results. These are shown in Figure 2.4, for the fuels iso-octane, toluene and n-decane. During the tests, the size histories of droplets suspended from a needle where measured. The needle had a special anti-wicking coating applied, which allowed the droplet

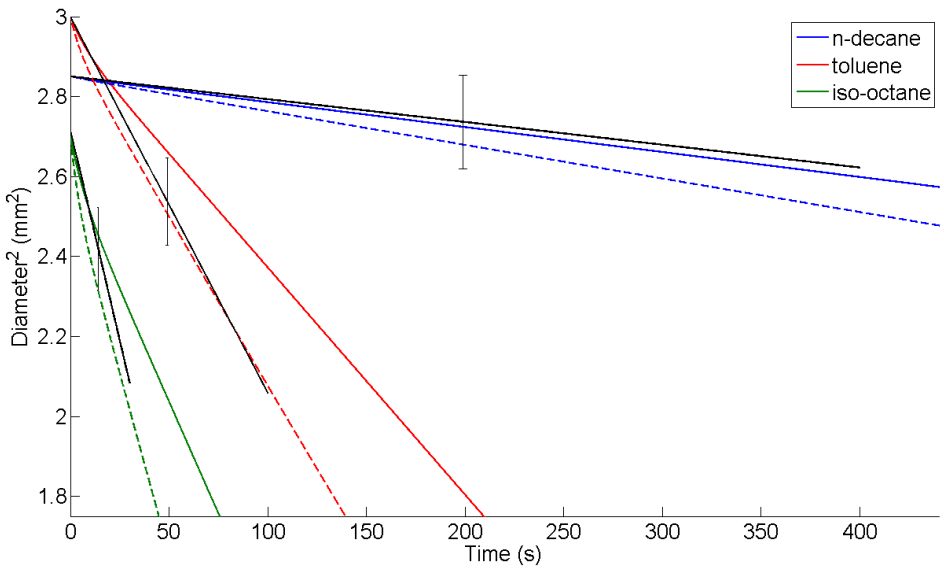


Figure 2.4: Single component droplet evaporation model validation, comparing the spherically symmetric (Stefan convection only) case (solid lines) and the case with natural convection convective enhancement (dashed lines) to the experimental results of [100] (black lines), for the fuels n-decane, toluene and iso-octane. Error bars represent the maximum error in diameter squared resulting from the assumption that the suspended droplet was spherical

to freely suspend from the needle with a shape close to spherical. Two models are used: one with no convective enhancement and one with a natural convection enhancement, which uses the correlations derived in [98].

The comparison between the experimental data and the model results is quite good. An error bar has been put on for the experimental results, which shows the error in diameter squared. This has been estimated based on volume error estimates undertaken in [100] that account for the fact that the suspended droplet takes a non-spherical shape in the experiment. The lighter component fuels seem to follow well the size history predicted by the natural convection model and the heavier n-decane fuel follows best the stationary model.

Secondly, data collected by Daïf *et al.* [98] was compared with results from single component and two component simulations. They performed natural and forced convection experiments and simulated both these situations with good agreement. They utilized the Haywood *et al.* correlation (Equation 2.18) in conjunction with Equation 2.12, which was also used here for comparison. The in-droplet liquid

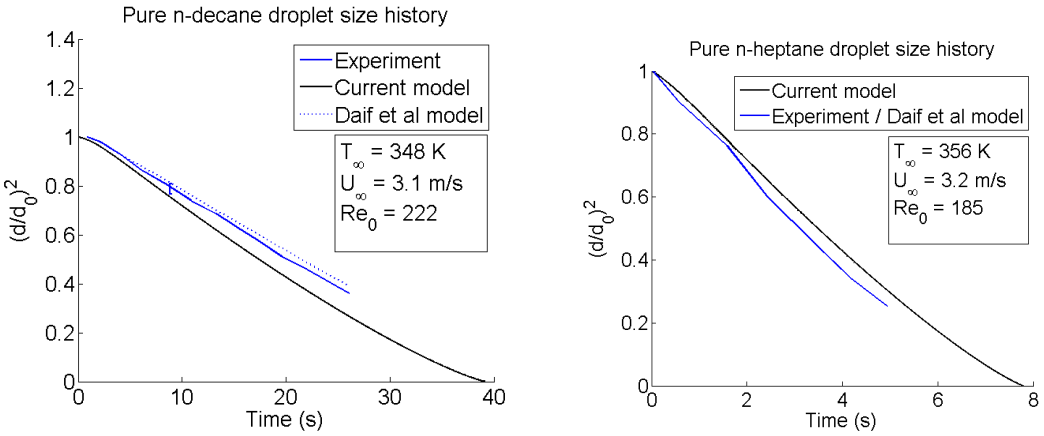


Figure 2.5: Comparison of droplet size history calculated from the models investigated in this thesis with experimental single droplet results and associated modelling in [98], for pure n-decane and n-heptane droplets in a convective environment

diffusion equation was solved, with convective enhancement, for the binary cases. Thus, they used an effective diffusivity model. The experimental set-up used by Daïf *et al.* consisted of droplets of size range 0.9 mm–1.5 mm suspended from a glass capilliary, which were exposed to a constant flow of air at velocities around 3 m/s. The surrounding air was heated up to a maximum of 390 K. The initial Reynolds numbers for the droplet experiments were between 152 and 232. Their experimental results and model predictions and the results from the current models are shown in Figures 2.5 to 2.9. Experimental error bars, based on imaging resolution and the accuracy of the thermographic system used in [98], are presented where available from the original work.

The n-decane results from the current model over-predict the vaporization rate, which is caused by a faster rate of increase in surface temperature compared to both the modelling and experimental results in Daïf *et al.*, as seen in Figure 2.6. The over-prediction at 5 sec is of the order 3 K, which is within the accuracy of the temperature measurement quoted in [98]. However, this may also be due to a greater than expected inaccuracy in an estimated physical property for the n-decane fuel. For example, when the model for enthalpy of vaporization was changed from that recommended, in general, by [56] to data from [71], the discrepancy was reduced.

Overall, the models described in this thesis performed well in comparison to

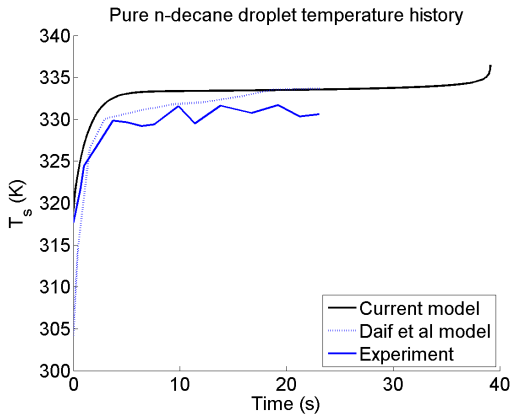


Figure 2.6: Comparison of droplet surface temperature from the models investigated in this thesis with experimental single droplet results and associated modelling in [98], for the pure n-decane droplet modelled in Figure 2.5. Note the over-prediction in surface temperature by both models

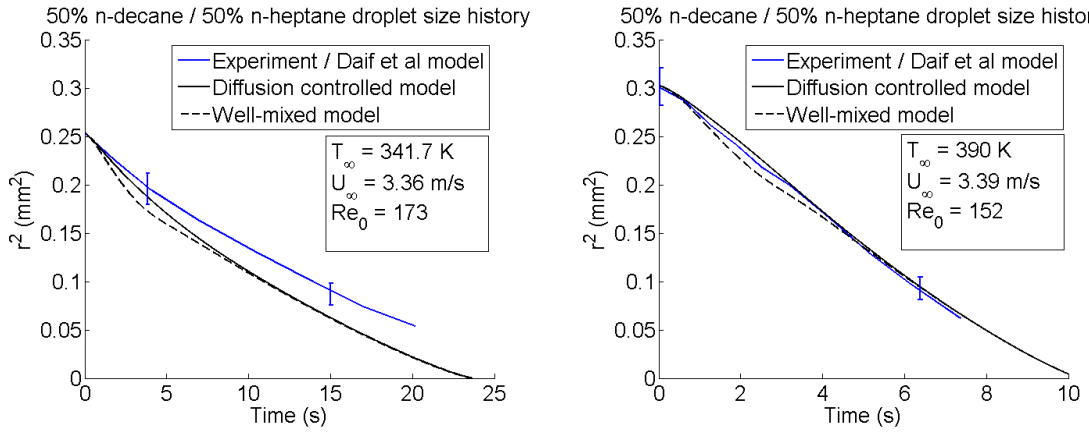


Figure 2.7: Comparison of droplet size history calculated from the multi-component models investigated in this thesis with experimental single droplet results and associated modelling in [98], for an equal mixture of n-heptane and n-decane by volume, at two different initial temperatures. A good match is seen at the higher temperature but there is a slight deviation at the lower temperature

the models in [98] with some of the error in droplet size history possibly due to inaccuracies in physical property selection.

Confidence in the simplified liquid diffusion-controlled model for three or more components, introduced in Section 2.1.3 (known as the pseudo-binary model), has been built by comparing results for surface composition history and droplet size history between the pseudo-binary model and the well-mixed model in cases where mixing is thought to be fast.

A ternary blend of n-pentane, iso-octane and toluene, with equal parts by volume

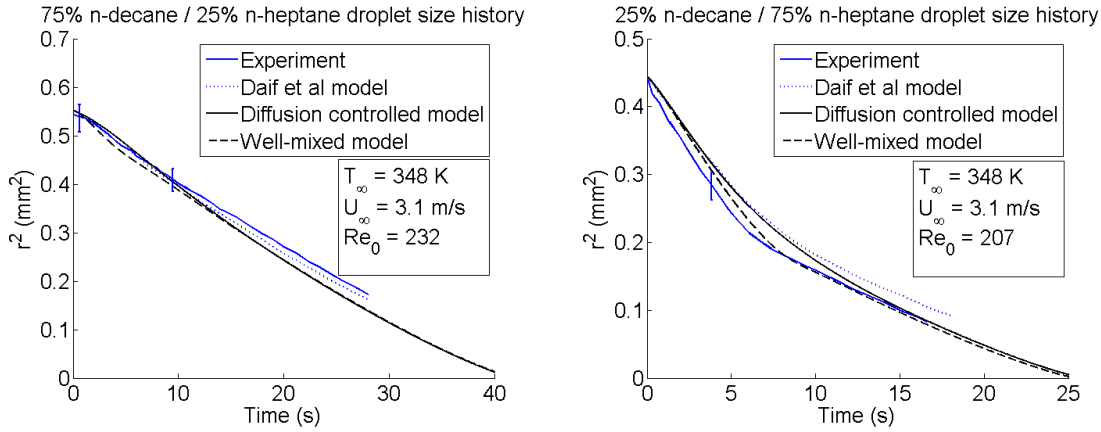


Figure 2.8: Comparison of droplet size history calculated from the multi-component models investigated in this thesis with experimental single droplet results and associated modelling in [98], for two different n-decane/n-heptane mixtures. The two models investigated give similar results, reflecting the fast mixing of the two hydrocarbon species

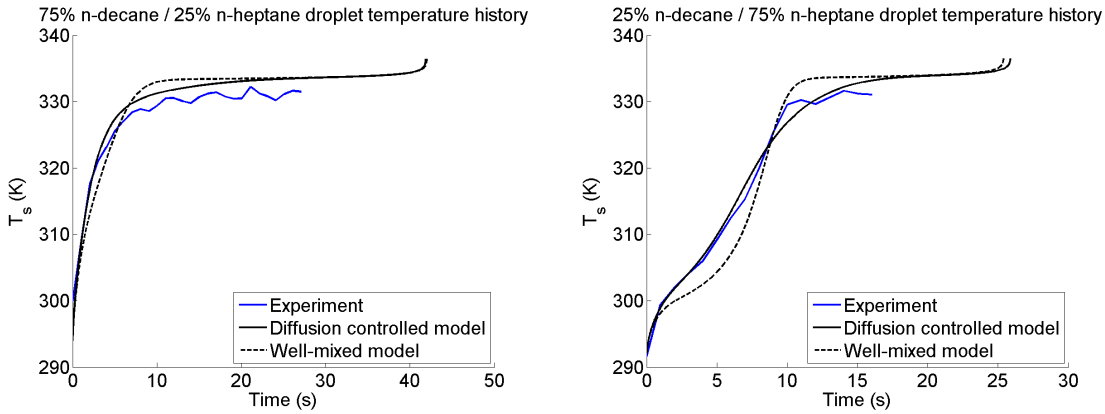


Figure 2.9: Comparison of droplet surface temperature for the cases investigated in Figure 2.8. The diffusion-controlled model tracks the surface temperature more closely during the transient phase, showing that this model has a more accurate surface composition, upon which the surface temperature will depend

initial composition, was investigated. This mixture behaves similarly to an ideal liquid mixture, with activity coefficients of the order unity, and diffusion coefficients of the order of 10^{-9} m^2/s or more. Each component was taken in turn as component 1 while the other two were set as well-mixed (using Equation 2.76). The results of these simulations are compared with the well-mixed result in Figure 2.10. The diffusion coefficient matrix was calculated at each time step to get a new diffusion coefficient for component 1. The initial liquid temperature was set to 330 K, the ambient temperature to 373 K, the ambient pressure to 1 bar, the initial droplet size to 1.5 mm, and a constant convective velocity of 3 m/s was applied. This

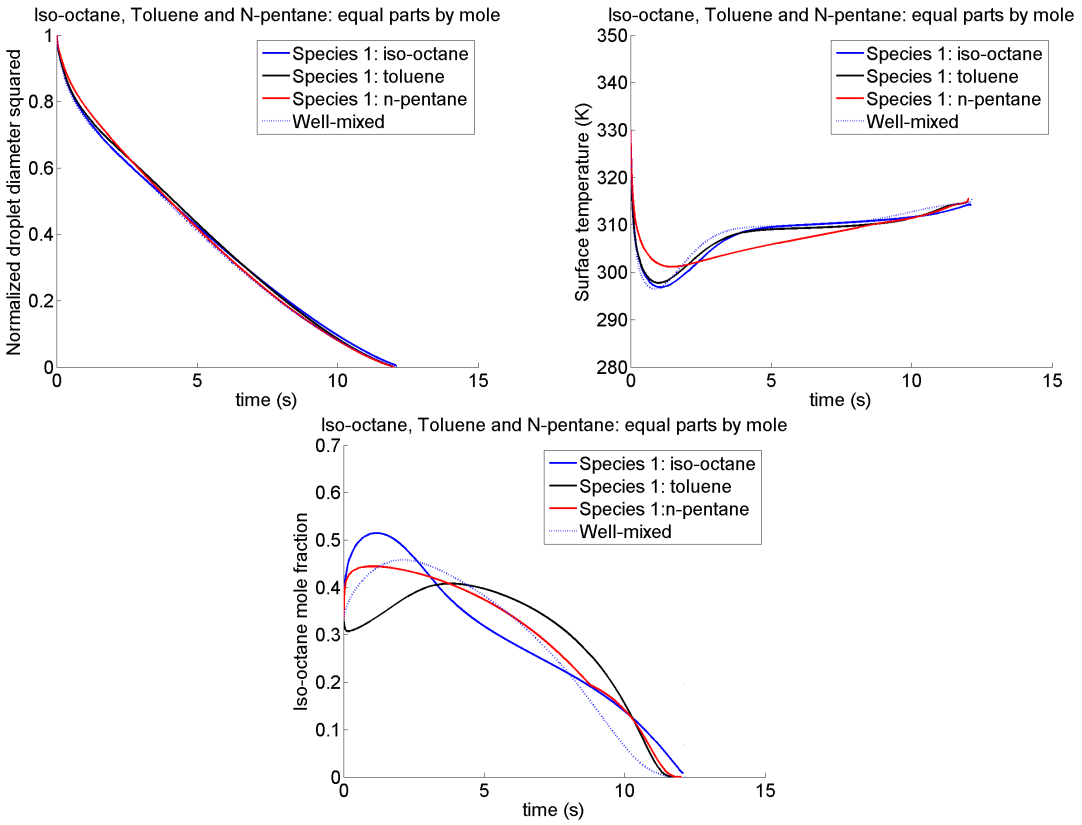


Figure 2.10: Droplet histories for the ternary mixture of n-pentane, iso-octane and toluene: (*a*) the droplet diameter squared history, (*b*) the droplet surface temperature history, (*c*) the surface mole fraction history for the iso-octane component

corresponds to an initial droplet Reynolds number of 386, an initial Nusselt number of 9.5, an initial Sherwood number of 8.8, an initial Lewis number of 0.64, an initial B_T of 43.8 and an initial B_Y of 12.9. The initial molar composition was equal parts of each component. The Clift *et al.* convective correlations (Equation 2.17) were used.

The well-mixed model and the three pseudo-binary diffusion-controlled models predict very similar droplet lifetimes (∼12.1 sec). The general shape of the plots of surface temperature and surface iso-octane mole fraction are in good agreement. This shows that this particular blend at these initial conditions may be well approximated by the well-mixed model and that the pseudo-binary method provides a reasonable estimate of the real multi-component situation.

The n-pentane constituent was then replaced by ethanol, which will have a much lower diffusion coefficient due to its non-ideal interaction with the other hydrocarbons. The same simulations were then performed, with equal parts by

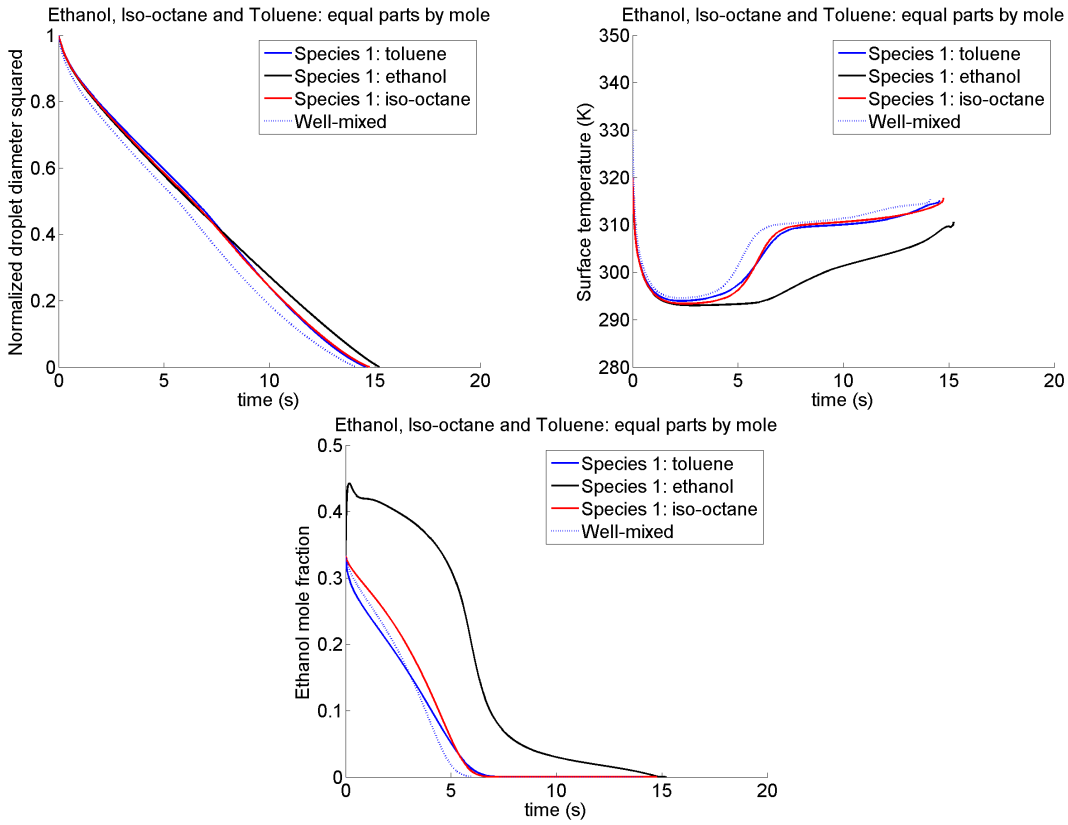


Figure 2.11: Droplet histories for the ternary mixture of ethanol, toluene and iso-octane: (a) the droplet diameter squared history, (b) the droplet surface temperature history, (c) the surface mole fraction history for the ethanol component

mole of ethanol, toluene and iso-octane as the initial composition.

Since there is a component present that will experience a very slow liquid diffusion rate, there are noticeable differences between the three different liquid diffusion-controlled simulations, as seen in Figure 2.11. If the ethanol distribution is explicitly calculated, it rapidly accumulates at the surface (since it is not the most volatile component at this composition), before reducing again once some of the other components have begun to evaporate. In the other two cases, the non-ideality has a smaller influence as ethanol is lumped in the well-mixed fraction. Therefore, as expected, these cases predict similar droplet lifetimes. The well-mixed model predicts a slightly shorter lifetime than the two pseudo-binary diffusion-controlled models, which is due to the loss of the ethanol from the surface around 1 sec earlier in the lifetime (Figure 2.11(c)). Due to the high enthalpy of vaporization of ethanol, once it is no longer at the surface, the surface temperature rises (as

seen in Figure 2.11(b)) and the vaporization rate increases. The link between droplet surface temperature and evaporation rate is strong due to the dependence on the surface temperature of B_Y, and because B_Y appears in the evaporation rate expression, Equation 2.11. Apart from this offset, the form of the well-mixed results match these two diffusion-controlled model results well.

2.2 Lagrangian Spray Simulation

One application for the single droplet evaporation model is as sub-model in CFD simulations of the two-phase flow in a spray. An efficient and common approach is to use Lagrangian Particle Tracking (LPT) to model the dispersed liquid phase (known as the Lagrangian phase). This kind of modelling approach was described by Dukowicz [101]. Particles of liquid are referred to a moving, or Lagrangian, frame of reference and each particle is tracked until it is fully converted to the vapour phase. Usually, each particle contains many droplets, each with the same size, temperature, velocity etc, that coexist at the position occupied by the particle. This is more computationally efficient than tracking each individual droplet and is shown to still give useful results. The gas phase, containing the ambient gas and the fuel vapour species, is then modelled in an Eulerian (fixed reference frame) sense using, for example, a Finite Volume approach. Any single-phase simulation type can be employed: a time averaged approach, *e.g.* Reynolds-averaged Navier-Stokes or Favre-averaged Navier-Stokes, or a more complex model of turbulent flow, *e.g.* Large Eddy Simulations [102]. This requires the solution of transport equations for mass, momentum, energy and the mass fraction of each gas and fuel vapour species, plus any turbulence parameters particular to the turbulence model employed, *e.g.* turbulent kinetic energy or turbulent dissipation [102]. Due to the Lagrangian phase, source terms will be present in the gas phase transport equations, to account for the mass added to the gas phase by evaporation and the exchange of energy and momentum that the droplets will have with the gas phase. The source terms for mass, mass fraction and energy transport equations will come from the evaporation sub-model, whereas the momentum source terms comes from the droplet drag force

sub-model. Various other sub-models are required for modelling droplet collisions, droplet wall interaction, droplet secondary break-up, and other particle body forces.

Another consideration is that, in Equation 2.4, the properties of the surrounding gas, with subscript ∞, will actually utilize the gas phase value of temperature or mass fraction in the cell in which the particle currently resides. This is seen as appropriate for fast moving droplets, following the discussion in Section 4.2, and is used even for slow moving droplets (relative to the gas).

The droplets contained within the particles themselves evolve as in Equations 2.86 to 2.89, with vector descriptions of position and velocity. A suitable model for the droplet temperature and droplet composition is selected, from the models discussed in this chapter.

Various liquid phase initial conditions are typically required for a LPT simulation of an injected spray, including the spray cone angle, flow rate and droplet size distribution. These can be determined from experiment or a previous simulation of the injector internal flow or atomization of the liquid jet. The groupings of identical droplets into Lagrangian particles is done in a way to conserve liquid continuity and the statistics of any desired droplet size distribution.

2.3 Summary

In this chapter, fundamental equations have been set out for the motion, evaporation, heating and composition of a vaporizing droplet in an environment typical of a fuel spray. Different models for heat and mass transfer convective enhancement, droplet heating, internal droplet mixing, vapour-liquid equilibrium, superheated droplet evaporation and inter-droplet interactions have been put forward and discussed. These have been selected based on the currently available literature on the topic of droplet evaporation, in order to ascertain which models may be most appropriate for accurately predicting GDI spray evaporation and to identify the level of complexity required for an accurate solution. Some of the more complex models that have been described and implemented have been validated in this chapter, against existing experimental data and an existing modelling study. The droplet heat equation

solution and droplet internal liquid diffusion solutions showed good agreement with the data of [98]. The novel pseudo-binary multi-component approach was validated against well-mixed models and was found to agree well for pure hydrocarbon mixtures (as expected) and to provide the expected discrepancy when an alcohol component was added, making the mixture non-ideal.

3 Experimental Equipment and Techniques

3.1 Fuel Injector

The fuel injector type used throughout this thesis is a prototype multi-hole high pressure solenoid-actuated GDI injector, manufactured by Bosch for Jaguar. This injector was used in both the purpose-built spray chamber (see Section 3.2) and the optical engine (see Section 3.3). It has six holes, with nozzle diameter nominally 200 µm opening to a 500 µm pre-hole, and a design maximum fuel pressure of 150 bar. The nominal spray pattern is shown in Figure 3.1, adapted from [103]. The rationale behind this pattern is described in Section 3.3, with reference to the combustion system for which it was designed, as the Optical Engine used in this thesis employed the same injector type.

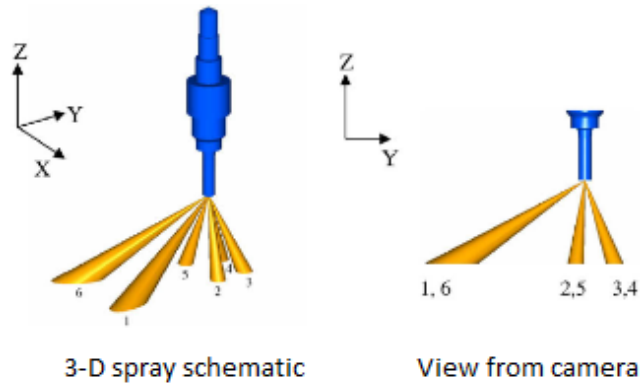


Figure 3.1: Multi-hole fuel injector plume orientations (adapted from Serras-Pereira *et al.* [103] where the same injector was used)

3.2 Spray Chamber

3.2.1 Motivation for a spray chamber

To provide experimental validation of the trends and quantitative results gathered from the detailed droplet evaporation modelling, fuel spray experiments have been performed. The information that can be gathered from a spray, for comparison with spray modelling, includes spray tip penetration, plume angles, droplet size distribution, droplet velocity distribution, and vapour penetration, composition and temperature. Fuel sprays may be imaged directly to ascertain macroscopic properties of the spray and understand its structure. Otherwise, optical diagnostic techniques may be used to estimate details of individual droplets (*e.g.* Phase Doppler Velocimetry) or of properties of the surrounding air and fuel vapour mixture (*e.g.* Laser-Induced Fluorescence).

Initially, spray images were taken using the Jaguar direct injection optical engine (see Section 3.3) with a full optical cylinder liner installed for optical access to the spray. The pillars supporting the engine cylinder head and the cylinder head itself obstructed both the illumination and the imaging of the spray and the existing engine instrumentation would make it difficult to mount additional diagnostic equipment to investigate the sprays in the engine cylinder. Therefore, the design and construction of a separate experimental rig was undertaken, with emphasis on full optical access to the spray and flexibility of operation. Spray chamber experiments would enable the effects of fuel volatility and fuel temperature on vaporization rate, flash boiling characterization, homogeneity characterization and penetration to be isolated from the in-cylinder air motion.

It was decided to spray the fuel into room temperature air at atmospheric pressure. However, the injector block would be heated so that fuel can be injected with an initial degree of superheat for imaging of flash boiling sprays. The injector would be operated continuously at engine-like frequencies so as to reliably image steady state operation of the injector. This would require continuous purging of the fuel vapour from the previous spray before the next injection. The flow rate

of fresh air through the spray rig would need to be low enough not to disrupt the spray pattern. For simplicity, the fuel injector would be vertically mounted with images to be taken from the side only. An existing fused quartz optical liner from the optical engine would be used to provide 360° optical access; it has an inner diameter of 89 mm and outer diameter of 117 mm.

3.2.2 Spray chamber purge rate

Between injections, the spray chamber must be purged to remove spray droplets and evaporated fuel vapour as these would influence the evaporation rate of the sprays and could show up in imaging tests for subsequent injections, distorting results. SolidWorks 3-D CAD software was used to construct a model of the spray chamber that could be used to perform CFD analysis of the flow through the chamber and to generate technical drawings for manufacture. Top and bottom pieces were designed around the dimensions of the existing optical liner. Since there was to be a centrally mounted injector block, air would be drawn in through an annular gap. It was estimated as follows that the volume flow rate required would be 5 L/s, for operation at 5 Hz.

As designed, the visible axial length of the chamber is $L = 118$ mm and the bore is $B = 89$ mm. This gives a volume of

$$V = \frac{\pi B^2 L}{4} = 7.3 \times 10^{-4} \mathrm{m}^3. \tag{3.1}$$

Since the chamber will be supplied with air at atmospheric pressure and approximately room temperature, the air density will 1.225 kg/m^3. Thus the mass of air in the visible part of the chamber is $m = \rho V = 0.9$ g. It has been conservatively estimated that 0.3 g of fuel could be added, which would be roughly equivalent to an equivalence ratio of between 3 and 5, depending on the fuel. Thus, 1.2 g of air and fuel would need to be purged after each injection. With 5 injections per second, around 6 g/s or 5 L/s would be needed.

There exists guidance for spray chamber purging in the SAE International standard for GDI Fuel Injector Spray Measurement and Characterization [104].

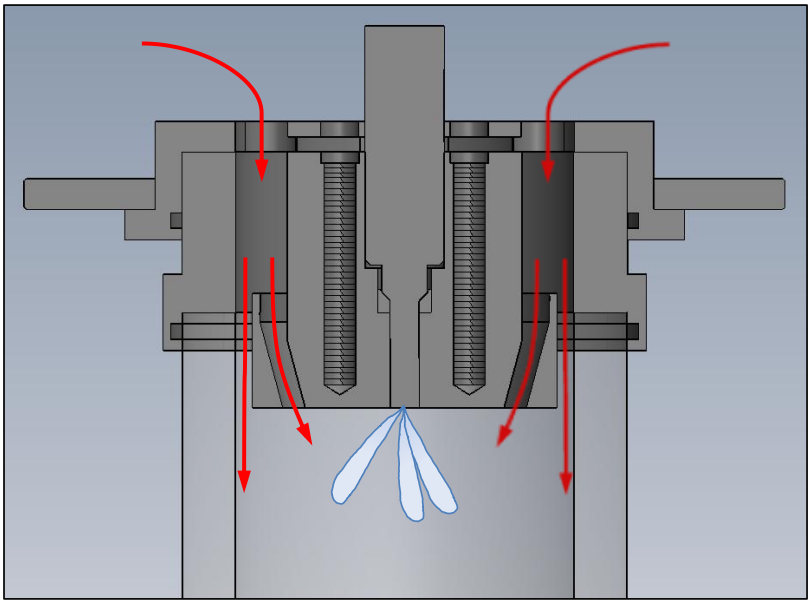


Figure 3.2: Section through the top of the spray chamber, showing the injector in its holding block and the annular air passage through which ambient air is drawn. The air paths are shown in red, clearing fuel vapour and droplets from near the chamber walls (due to impingement) and from around the injector tip

This standard recommends using a mean purge velocity range of 1.3–2.6 m/s for a GDI injector test.

The mean purge velocity of the chamber with a 5 L/s flow rate would be 0.80 m/s, which is well below the maximum; hence, the spray structure should not be disturbed. The standard recommends running the injector at 20 Hz, hence the inclusion of a minimum recommended mean purge velocity of 1.3 m/s to ensure fuel vapour and droplets are removed from a chamber's test region before the next injection, 50 ms later. Since the spray chamber was run at the slower injection frequency of 5 Hz for all tests in this thesis, the lower mean purge velocity was deemed acceptable. The Oxford spray chamber was designed to have continuous purging for simplicity and has a dual air inlet around the fuel injector (see Figure 3.2). Therefore, the lower mean flow velocity will not disturb the spray with eddies in the air flow. An injector frequency of 5 Hz corresponds to an engine running speed of 600 rpm.

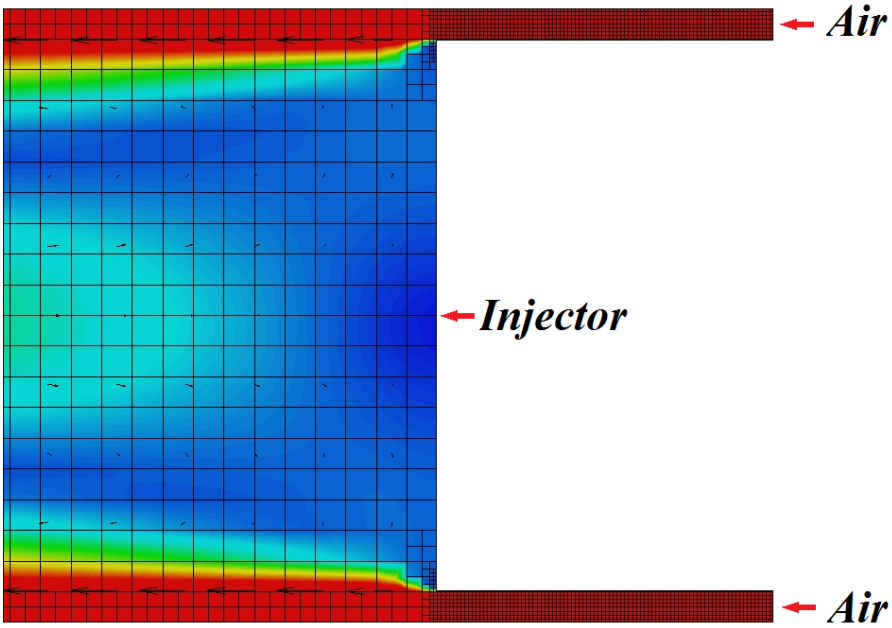


Figure 3.3: Velocity magnitude field plot for first iteration of the spray chamber inlet design, showing typical mesh resolution and velocity vectors at distributed locations. Most of the air flow stays close to the cylinder liner, which would give good purging of any fuel near to the wall. Note that, the velocity vectors near to the cylinder axis are directed back towards the injector, due to the large, low velocity recirculation zones. This means that fuel droplets and vapour would not readily be purged from the chamber

3.2.3 Spray chamber flow investigation

The purging flow was investigated using the SolidWorks Flow Simulation tool, which generated fluid meshes direct from the 3-D solid model, allowing a swift iterative design process. The tool can model both laminar and turbulent steady state flow, using the Favre-averaged Navier-Stokes equations and the k-ε turbulence model, switching between them as necessary [105]. The model was set up with a mass flow rate boundary condition of 6 g/s of air at 20°C at the inlet (top) and a pressure boundary condition of 1.013 bar at the outlet (bottom), and uniform constant temperature. Initial tests suggested that a simple annular flow past a cylindrical injector block that suddenly expanded into the main chamber would not be ideal, due to flow recirculation, which would cause fuel droplets and vapour to remain in the chamber until the next injection (see Figure 3.3). Therefore, a second piece was designed that would divert some of the flow towards the centre of the chamber to

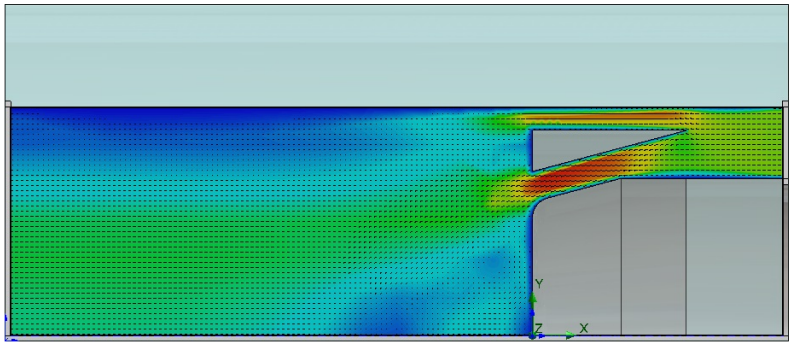


Figure 3.4: One half of the rig with the split air inlet design, showing near uniform axial air flow over two-thirds of the radius and slower velocities at the cylinder liner wall and near the injector

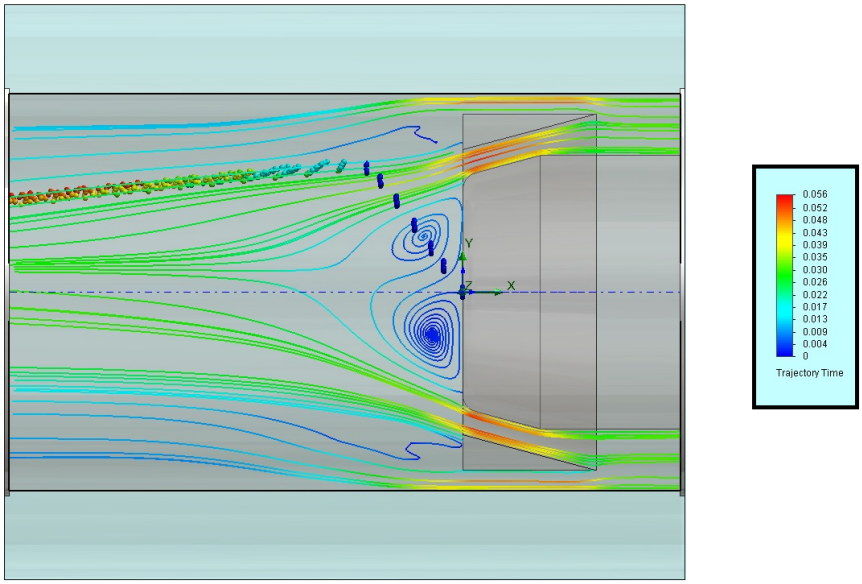


Figure 3.5: Final design, as manufactured. The streamlines show a smooth flow into the main chamber region with only a small region of low velocity circulation, near the injector. It is expected that, this close to the injector, the flow during injection will be dominated by the induced air motion from the spray. Particle trajectories are show which follow the nominal direction of plumes 1 and 6 (see Figure 3.1

avoid a stagnant zone near the injector, as shown in Figure 3.4. Parameters were varied, including passage widths, lengths and angles, to achieve a design that gave a small recirculation zone and a low, uniform maximum velocity in the main chamber. The final design resulted in the shape given in Figure 3.2 and the streamlines, velocity field and particle study for this design are shown in Figure 3.5.

To check for spray droplet residency time, particles of size 10–20 µm and density

750 kg/m^3 were injected at 100 m/s in the direction of the plumes of the injector (see Figure 3.1. In SolidWorks Flow Simulation, a similar droplet drag law to Equation 2.20 is used. The slowest plumes were those numbered 1 and 6, with reference to Figure 3.1, whose trajectory is seen in Figure 3.5, which left the visible region after 56 ms with a 6 g/s inlet flow rate. Spray droplets that reach the walls will encounter the streamlines with velocity of approximately 1 m/s, which is still adequate to remove the droplets and vapour within 200 ms.

3.2.4 Spray rig manufacturing design

The 3-D model was refined to allow for manufacture and instrumentation. The injector block contains a central hole designed to fit the profile of the multi-hole injector and four holes around this for heating elements. There was also a 3 mm hole for a thermocouple or platinum resistance thermometer to measure the block temperature. A lid piece was designed containing four arc-slot holes that form the annular air inlet. The injector block is bolted underneath the lid and each of the holes in the top of this block is repeated in the lid. This allows the injector and heating element wires to pass through from the injector block up through the lid to be connected as required. Good thermal contact between the heated block and the injector body was ensured by the presence of a profiled copper washer between the two.

To make as much use of the length of the existing 153 mm optical liner, an annular spacer was design that sits between the lid and the optical liner. This positions the injector tip close to the top of the liner to give a large optical access region below the injector. This piece can be changed in the future to adapt to any future liner, for example one with plane windows or for a pressurized chamber. The liner is supported by the bottom piece, which is open at the bottom to allow the air and fuel vapour to leave through a flow control valve and on into the extraction system. The lid piece and bottom piece have a 200 mm flange with holes for four aluminium columns on a 150 mm square base. These keep the spray rig together

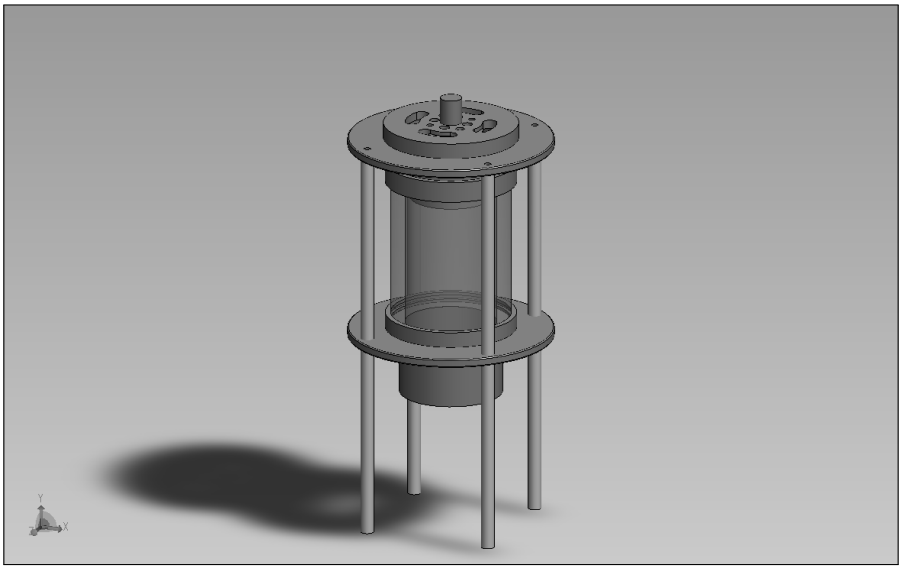


Figure 3.6: 3-D model of spray chamber complete with quartz barrel and supporting pillars

and allow it to be mounted on a standard optical table, which has 25 mm spaced tapped holes. The final design for manufacture is shown in Figure 3.6.

3.2.5 Ancillary equipment

In addition to the spray rig and injector itself, various items are needed to run the experiment. There has to be a method of storing and pressurizing fuel up to 350 bar; a system to control and measure the flow of air through the chamber; illumination and a camera to image the spray; and a data acquisition and control system for the triggering of the cameras, lighting, injector and other instruments and logging of temperatures, pressures and flow rates.

Fuel pump

The standard fuel injection pressure used in this work is 150 bar. However, it was decided that future research would need higher fuel injection pressures as this was the current trend in GDI engines [9, 10, 11]; therefore, 350 bar was chosen as the design pressure.

Various methods for pumping liquids to this pressure are available. Some pumps are driven, by engine or electric motor, for example in-line and rotary pumps for diesel engines or GDI engines. However, for the experimental rig, it would be best

to have a statically operating pump. In the laboratory, compressed air is available at around 6 bar, so it was decided to use this to pressurize the fuel. In the event, compressed nitrogen from a gas bottle was used. A piston arrangement would be required to separate the air side and the fuel chamber; this would also provide the magnification of the air pressure up to 350 bar through the ratio of areas of each side of the piston. The fuel pump was manufactured by the Department of Engineering Science main workshop.

A diagram of the fuel pump is shown in Figure 3.7, showing the air side of the piston with diameter 149.5 mm and the fuel side with diameter of ¾" which is 19.05 mm. This gives a nominal pressure ratio of 61.6, allowing a maximum fuel pressure of nearly 370 bar when the fuel pump is supplied with compressed air at 6 bar. The regulator shown in Figure 3.7 controls the inlet air pressure and the fuel pressure supplied to the injector.

For filling or emptying the fuel chamber, extra features are required on the fuel pump. To fill the chamber, a glass fuel syringe is attached to the cross fitting on the fuel side and low pressure air (0.3 bar gauge) is directed onto the reverse side of the large end of the piston. The piston will then slowly travel downwards drawing in fuel from the syringe. To empty the current fuel out, this low pressure air is directed onto the main side of the large end of the piston and the drain valve opened, allowing the fuel to be pushed out slowly by the piston. Therefore, a low pressure regulator was fitted and valves positioned to allow this air to be applied to either side of the air piston as required. A high pressure transducer was fitted into the fuel delivery side of the pump, with range 0–400 bar to measure the fuel pressure.

Air flow control valve

To measure and set the volume flow rate of air through the chamber, a simple system was designed, again with few moving parts. The flow rate measurement would be done with a viscous flowmeter, whereby the flow passes through an element with small flow channels, leading to a pressure drop. By measuring the pressure change across the element with a differential pressure transducer, the flow rate can be

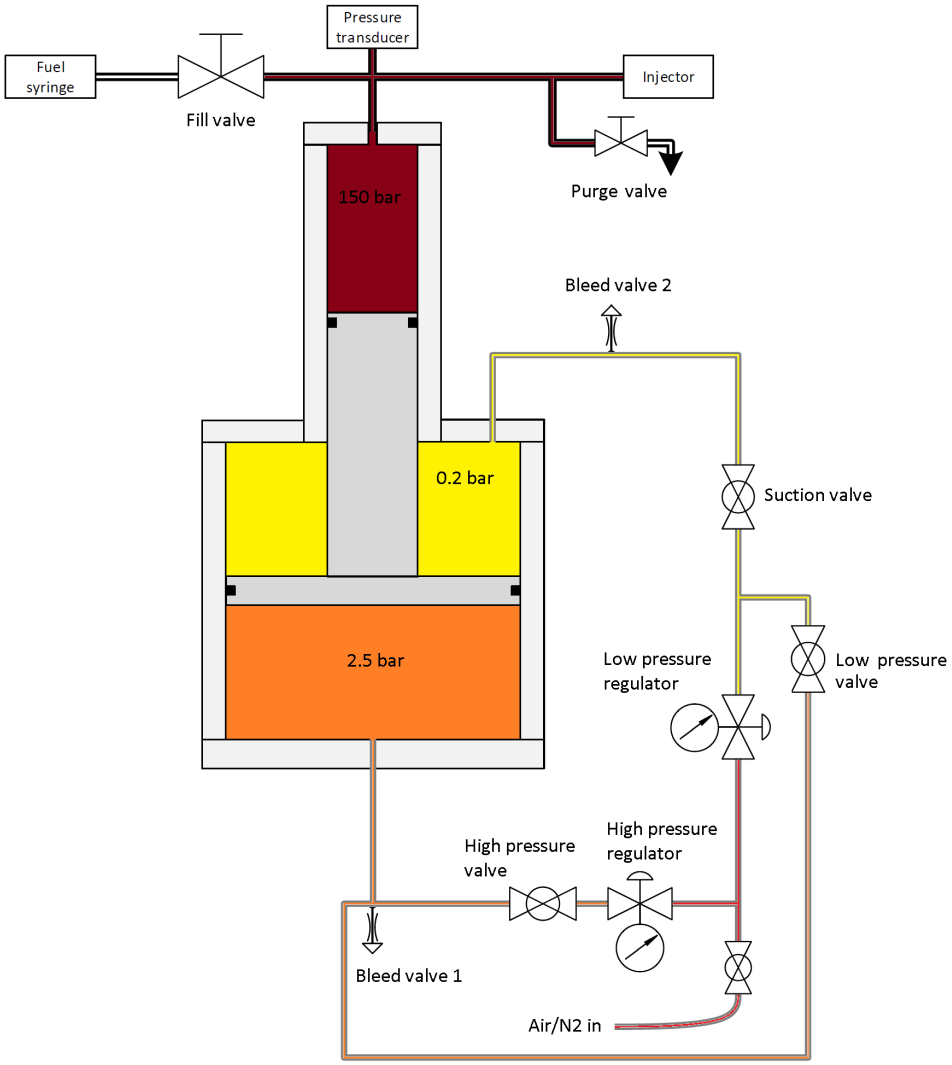


Figure 3.7: Schematic diagram of the fuel pump and pipework for the compressed air and fuel delivery. The bleed valve on the pressure side must be open during fuel pressurization or purging, to allow the piston to move upwards, and the bleed valve on the high pressure side must be open during fuel filling, to allow the piston to move downwards. The diagram shows possible gauge pressures in the system that may be achieved during fuel filling or fuel pressurization. Not to scale

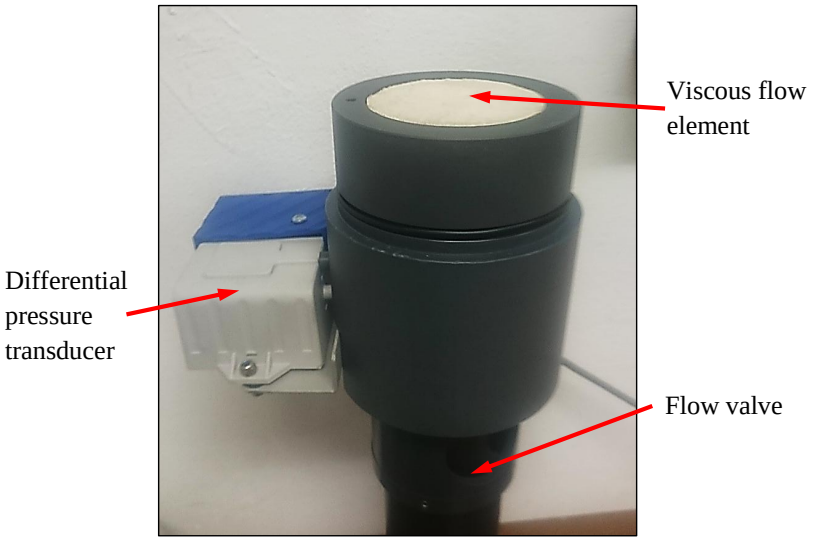


Figure 3.8: Photo of the viscous flowmeter and the flow valve. The honeycomb insert at the top creates the pressure drop that is measured by the differential pressure transducer, which is attached to the left. This is connected to two tappings, the top one of which can be seen on the top surface of the housing, which is open to the inside of the spray chamber. The housing has an O-ring for a tight fit into the spray chamber bottom piece and the adjustable collar valve is visible at the base of the housing, partially open

inferred after a calibration has been performed. A bespoke plastic piece was made to hold the element, which connects to the bottom of the metal spray chamber. Bolted to this is a differential pressure transducer (the 5266 Very Low Range Differential Pressure Transmitter from Gems Sensors), which connects to two pressure tappings open to each side of the flow element. This requires a 24 V DC supply. Since the pressure drop across the element is small, the full range of differential pressure that can be measured by the transducer is ± 1 kPa, with a quoted accuracy of ± 10 Pa.

The air flow rate is controlled via a rotating collar, which controls the opening of an air port below the viscous flowmeter. After flowing through the viscous flowmeter and valve, the air travels down a length of pipe into the laboratory exhaust extraction and dilution system. Therefore, as the port is opened, more air is drawn from the room through the port, causing the flow rate through the spray chamber to reduce. Details of the viscous flowmeter and flow valve are shown in Figure 3.8.

Illumination and imaging

For spray imaging, two simple techniques are used. The spray can be imaged with illumination from the side (the axis of the camera and light system being at right angles), whereby light scattered off the droplets and liquid jets illuminates the spray against a dark background. This is known as Mie scattering. Alternatively, the spray can be illuminated from the rear through a diffusing screen (with spray between the camera and light system), whereby the spray will appear dark on a light background. This is known as a backlit image or shadowgraph image. Both of these systems have been realized with an array of LEDs for the lighting system. A square array of 100 LEDs of size 20 $\times$ 20 mm was chosen (Bridgelux BXRA-56C9000), which has a pulsed peak output of 9750 lumens and an lighting angle of 120°, within which, the light intensity is 50% of the maximum. Light from the LED array could be focussed towards the spray to allow more light to be incident onto the spray.

The LED array and its circuit board must be kept below 70°C to retain its peak light output and below 110°C as a maximum temperature. For cooling, a heat sink assembly with heat pipes and a fin heat exchanger was used. The fins are cooled by a PC fan. The LED array has a case temperature test point, which can be used to verify its temperature.

The LED array is rated at 30 V, to receive a typical current of 2.8 A. In fact, the LEDs are used in a pulsed operation with a 50 V power supply that delivers a rated current of up to 5 A. The LED array is switched on and off by supplying the base of a power transistor (TIP 142) with a TTL pulse (around 5 V), allowing current to flow through the LED array. This results in a measured peak current of 20 A for a short duration. The set-up is summarized in Figure 3.9. A typical illumination pulse width used to image the sprays in the spray chamber is 20 ms with a period of 200 ms. This is long enough to capture the whole evolution of a spray with 3 ms injection duration and short enough to prevent the LED array from overheating. This also prevents the power supply current protection from tripping.

High speed images are captured on a Photron Fastcam 1024 PCI camera, using a $f = 50$ mm focal length lens. The shutter speed and the aperture width were

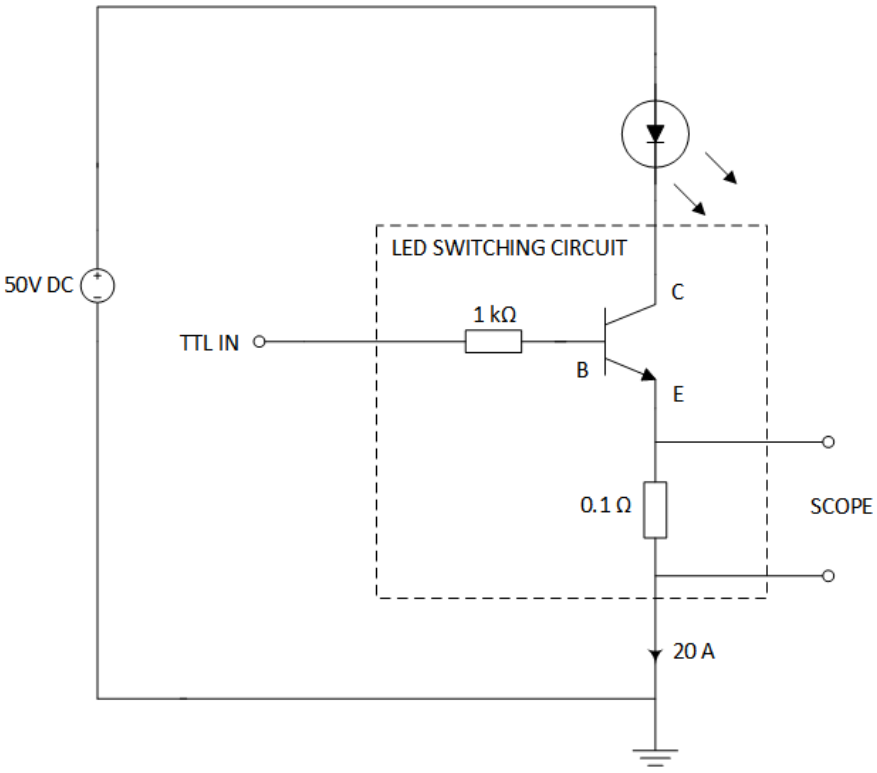


Figure 3.9: Circuit diagram of the LED power circuit, used on the spray rig experiment. Around 20 A flows into the transistor collector and through the LED array, due to the high gain of the power transistor. A 0.1 Ω resistor is provided to allow a voltage measurement across the resistor to be used to estimate the current flowing. The transistor is actually a Darlington pair

adjusted to achieve the best compromise between capturing a frozen image of the spray and getting a good depth of field. For both the Mie scattering and backlit images, this is also balanced with achieving a good contrast between the background and the spray. For Mie scattering, an exposure duration of 3.30 µs with aperture size of $f/1.2$ was ultimately used. For the backlit images, the camera's minimum exposure duration of 1.52 µs could be used, with an aperture of $f/2.8$. The frame rate was limited by the camera data transfer rate and is dependent therefore on the pixel size selected for the image. Typically, images of size 384 × 480 were taken at 4500 frames per second.

Data acquisition and control

The requirements of the data acquisition (DAQ) and control system are summarized in Table 3.1.

Table 3.1: Requirements of the DAQ system for the Spray Chamber experiment

System	**Input or Output Signal**	**Requirements**
Temperature measurement	Input	Continuous reading of four thermocouples (air inlet, air outlet, injector block, spare) and conversion to temperature units
Fuel pressure measurement	Input	Continuous reading of one pressure transducer
Air flow measurement	Input	Continuous reading of one differential pressure transducer and conversion to volume flow rate
Heater control	Output	Continuous control of fuel injector heaters using pulse width modulation (*i.e.* heaters fully on or fully off). Variable temperature set point
LED control	Output	Generate TTL pulses to turn on the LED array and LED control circuit. Variable pulse width, frequency and number of illuminations
High speed camera triggering	Output	Generate TTL pulses to trigger the high speed camera. Variable number of sets of images. Number and frequency of images within a set is controlled by the camera software on a separate PC
Injector operation	Output	Generate TTL pulses to turn on the injector. These are sent to a Bosch injector driver module, which converts the square wave pulses into the signals required to activate the injector needle. Variable injection duration, frequency and number of injections

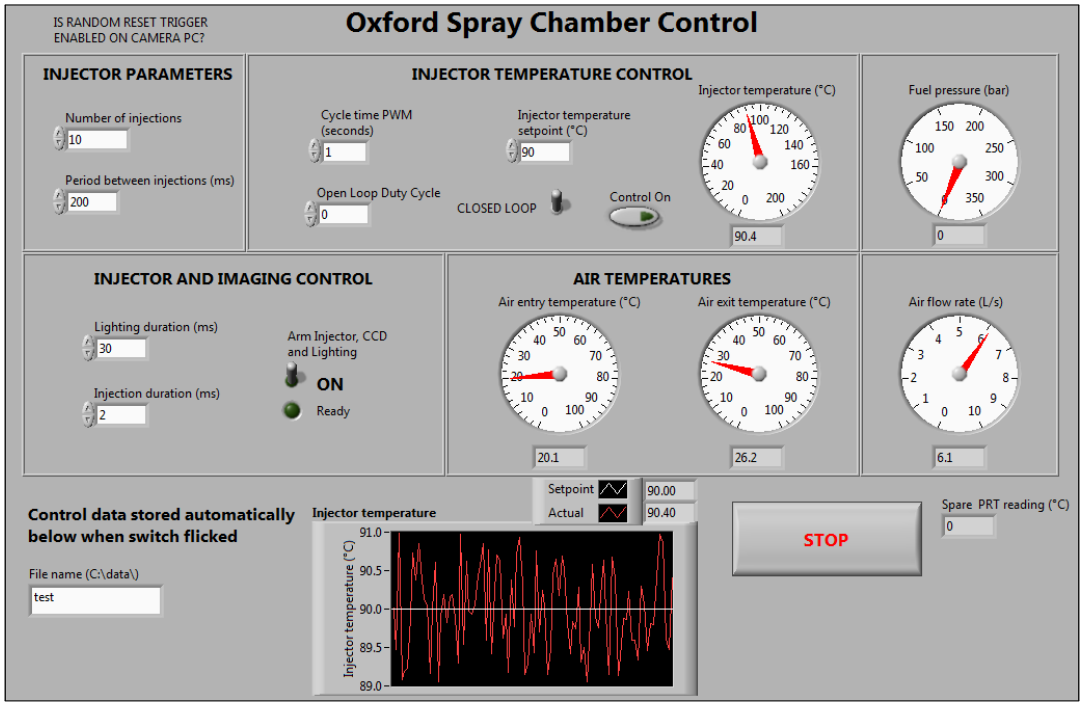


Figure 3.10: Operating panel for controlling the spray chamber experiment and recording data

A National Instruments USB-6211 DAQ module was chosen for this task, since it is compact and has enough input and output channels with sufficient sample rates [106]. In addition, it could be connected to a laptop or PC when needed. The module was programmed using National Instruments LabVIEW software. The final LabVIEW user interface is shown in Figure 3.10.

The channels available on the USB-6211 DAQ module are: 16 analogue inputs (or 8 differential analogue inputs) that are inputted using a 16-bit analogue-to-digital converter; 2 analogue outputs; 4 digital inputs; 4 digital outputs; and 2 counter channels. Each counter channel can be configured to provide either pulse train generation (output) or to count events on the connected line (input). The DAQ module outputs were connected to devices capable of creating a large current, such as the injector driver or lighting control circuits. Therefore, in case of a fault, all of the outputs utilized were protected using optical isolator circuits, ensuring there was no physical wire connection between the module and the hardware to which it was sending signals.

The six analogue measurements were collected as differential inputs, where the common ground from the output of each sensor or amplifiers was supplied to the negative pin of each differential pair. The fuel pressure transducer gives an output in the range 0–5 V DC directly, with 5 V corresponding nominally to 400 bar. The differential pressure transducer for air flow measurement outputs 0–10 V DC directly, with 5 V corresponding to zero differential pressure. The signals from the four resistance thermometers were first amplified by a 4–20 mA amplifying circuit, to provide an output voltage in the range 2–10 V across a 500 Ω resistor. This was then inputted to the DAQ module, where 2 V corresponds to 0°C and 10 V to 100°C (or 200°C in the case of the injector block thermometer).

A timing diagram for the digital TTL pulses for the LED, camera and injector control signals is shown in Figure 3.11. For the DAQ module available, it was found that, to be able to alter the period and pulse width of generated digital pulse trains without stopping the program, it was necessary to program them as infinite pulse trains. Since continuous operation of the LabVIEW program was preferable, the injection trigger signal was set to be an infinite pulse train on a counter channel, with user-controlled variable period and pulse width. Then, the output trigger signal for the camera and LED array was combined into one output using an analogue output channel, which was set to a 5 V reconfigurable, finite pulse train. The duration of each pulse would only affect the time that the LED array was energized, since the camera software is triggered by the rising edge and the frequency and number of images to be taken is set previously, from within the camera software. Once a finite pulse train for the desired number of injections is created on the analogue output channel, this is combined with the counter channel infinite pulse train in a logical AND gate, to give a finite pulse train of the correct pulse width that can be sent to the injector driver.

The four heating elements are controlled using a pulse width modulation technique, where the control variable is the heater duty cycle, ranging from 0% (always off) to 100% (always on). The period was set to one second. A feedback controller was implemented using the temperature measured in the injector

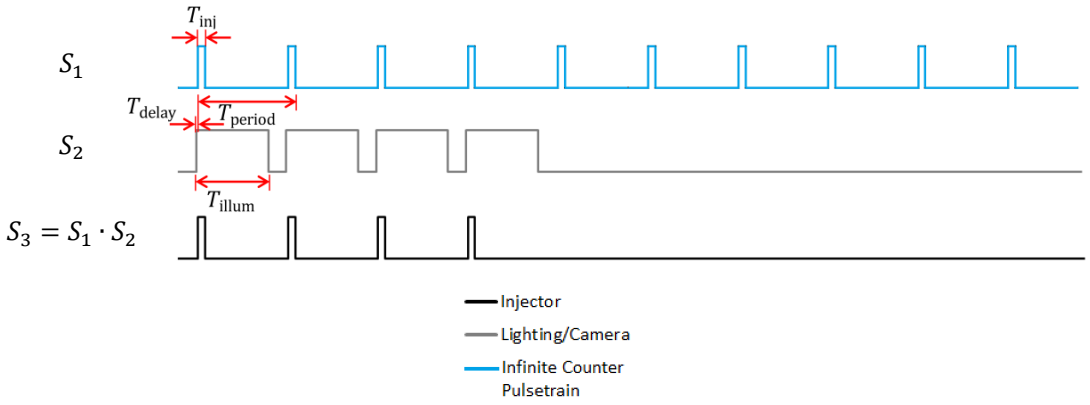


Figure 3.11: Pulse trains for the lighting system and camera S_2, and the fuel injector S_3. The S_3 signal is formed by the logical AND of the infinite counter pulse S_1 and the illumination/camera finite pulse S_2

heater block as the process variable, to be compared with a desired injector temperature setpoint.

Proportional-Integral closed-loop control was used where the proportional and integral gains were selected using the Ziegler-Nichols open-loop Process Reaction Curve method [107]. First, the heaters were operated at a steady open-loop operating point, giving a steady injector temperature reading. Then, a step change was applied to the control variable, *e.g.* a step change in duty cycle of 10%. Finally, the resulting variation in process variable (injector temperature) was recorded. The process variable response is analysed to estimate values of gain (change in temperature divided by change in duty cycle), delay and time constant. These values are used to find recommended proportional and integral gains using the rules of this method.

A digital output channel was used on the DAQ module, which was set to turn off and on in accordance with the demanded duty cycle outputted from the controller. This TTL signal then switched the 24 V, 5 A heater supply via a solid-state relay.

3.2.6 Completed spray chamber experiment

The completed experimental layout is shown in Figure 3.12.

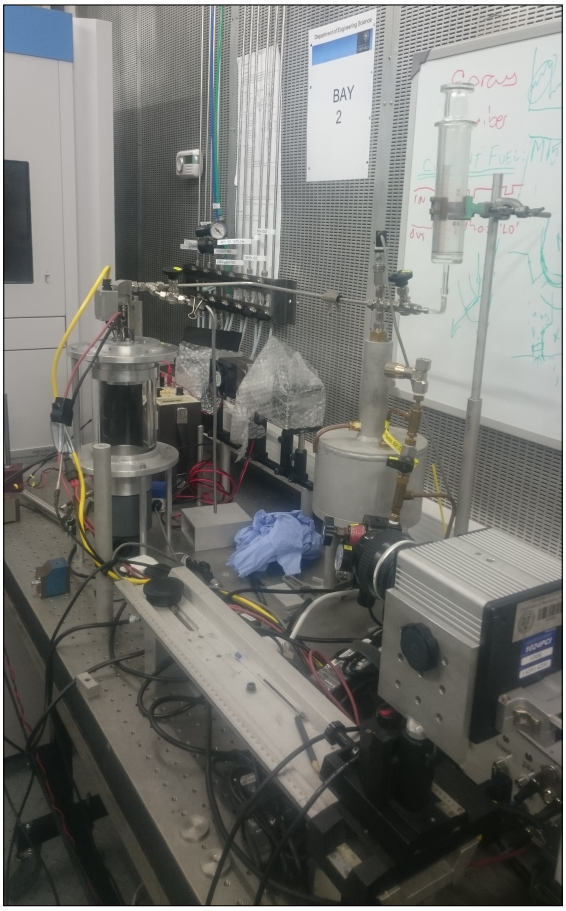


Figure 3.12: Spray chamber, fuel pump and high speed camera with adjusting rail, on the optical bench

3.3 Single Cylinder Optical Engine

Experiments have been performed using an optical access research engine, including fuel spray imaging under motored conditions and combustion imaging under firing conditions. In addition, particulate emissions from the combustion can be measured for comparison with the spray behaviour and other mixture preparation indicators. The optical engine that was used is a single cylinder engine provided by Jaguar Land Rover, with a combustion system based on the Jaguar 5 litre AJV8 GDI engine, described in detail in [1]. Both engines have a four valve pent-roof combustion chamber, with a centrally mounted SGDI injector and spark plug, as shown in Figure 3.13.

The orientation of the six plumes is, of course, the same as in Figure 3.1. In

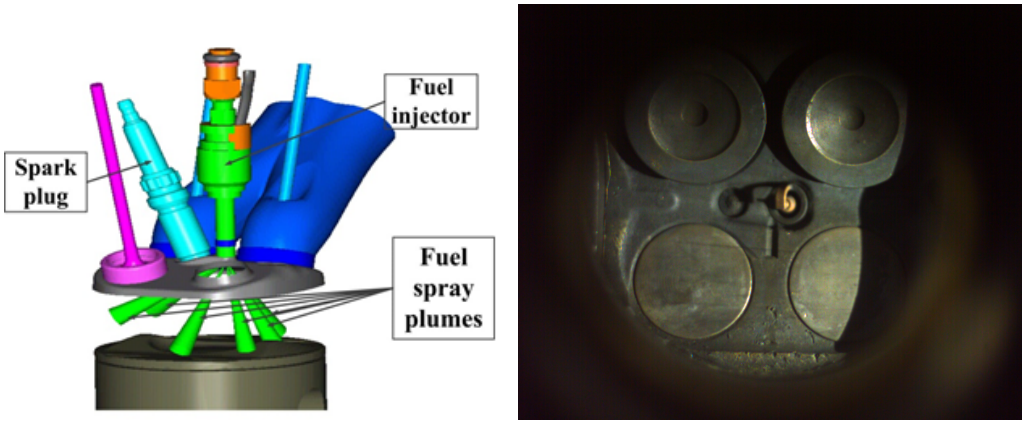


Figure 3.13: *Left*: Combustion system from the Jaguar AJV8 engine, adapted from [13], originally from [1], showing a centrally mounted fuel injector and six spray plumes (green), an inclined spark plug (cyan), intake ports and valves on the far side (blue) and one exhaust valve (magenta). The orientation of injector and spark plug is parallel to the crankshaft axis. *Right*: View of the optical engine valves, injector and spark plug from below. The optical engine at Oxford uses the same injector and very similar combustion chamber layout as the AJV8 engine; however, typically the piston is flat topped

Figure 3.13, two plumes are travelling towards the left side of the combustion chamber to provide a rich mixture close to the spark plug, which sits between them, during stratified operation.

A Bowditch piston design is used, with a fixed 45° mirror between the top and bottom piston that can be used to collect images of the combustion chamber through a window in the top piston, as seen in Figure 3.14. For fuel sprays, this provides images in the so-called 'Base' view, looking upwards towards the injector. There is also optical access to the combustion chamber via the options of a full length optical liner, a short optical annulus and through a flat pent-roof window.

The other advantages of using a single cylinder optical engine include: there are no cylinder-to-cylinder variations during experiments; less fuel is used; the experiment is more compact; and a lower power dynamometer and control system may be used [108]. However, the optical engine will not be thermodynamically identical to the multi-cylinder engine it is based on, since the different materials and dimensions can cause a difference in surface temperature and heat transfer. Useful images and trends can still be found using an optical engine and any hypotheses conjectured may be tested using the multi-cylinder engine. The speed will be

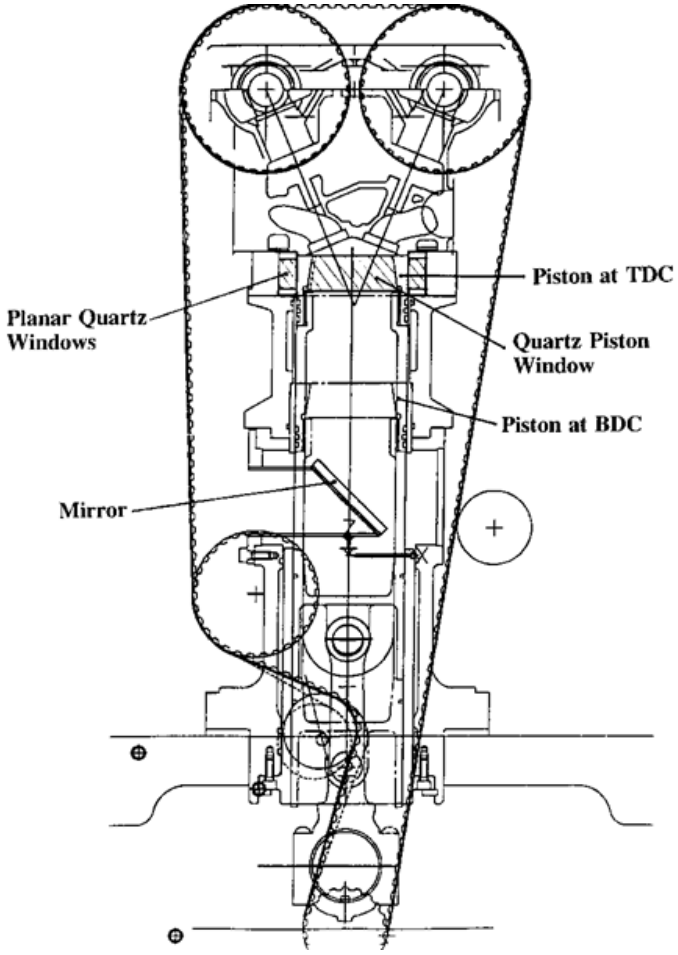


Figure 3.14: Schematic of a single cylinder optical engine with Bowditch piston layout. By positioning a camera to view the 45° mirror from the left, the combustion chamber may be imaged from below. This diagram shows cylinder wall cut-outs, whereas the optical engine used in this research has the option of optical access through a full fused silica annulus or flat windows in a metal annulus. There is also a pent-roof window in the cylinder head

limited to around 2000 rpm due to the long, heavy piston and optical access may deteriorate over time as deposits collect on the windows.

The Jaguar Land Rover optical engine has the capability to inject fuel into the air intake plenum (simulating PFI), to allow comparison between the PFI and GDI injection strategies. Other engine parameters are summarized in Table 3.2. Of note is the late IVC timing of 117°CA BTDC, which gives a low effective compression ratio, and also means that the GDI spray droplets experience a relatively low in-cylinder pressure and temperature until just 82°CA before spark ignition.

Self-lubricating piston rings, manufactured from a high temperature plastic

Table 3.2: Optical engine specifications

Bore × Stroke	89 × 90.3 mm
Displacement	562 cm^3
Valves per Cylinder	2 intake, 2 exhaust
Compression Ratio	11.1
Fuel Pressure	150 bar
Valve Timing (°CA ATDC)	IVO 33°, IVC 243°, EVO 475°, EVC 5°

(Torlon), are utilized, which removes the need for oil lubrication in the engine meaning there will be no oil contamination in the combustion chamber.

Imaging with the optical engine is performed using the same Photron high speed camera as is used with the spray chamber. Images have been taken mainly through the full optical liner, for imaging sprays under motored conditions, and through the optical annulus and piston window, for imaging combustion. For fuel spray illumination, two techniques have been used. First, light from an overdriven, water-cooled array of six LEDs was directed through the pent-roof window onto the spray, as described in [13]. Secondly, light was directed horizontally onto the 45° mirror to illuminate the sprays from below, using the same LED array as used for the spray chamber. This produces a very low level of unwanted light reflections, compared with illuminating the spray from the side. In either case, the LEDs were pulsed and operated using the circuit described in Figure 3.9.

The optical engine is instrumented with thermocouples, pressure transducers, an exhaust lambda sensor and an air flow rate meter. Torque and speed is measured using a four quadrant controller connected to the DC dynamometer on which the engine is mounted. The operation and timing of the injection, ignition and trigger signals for the camera and lighting systems are controlled using a Engine Timing Control System (ETCS), which is fully described in [109]. Cycle-averaged data such as exhaust temperature are collected by a low speed data acquisition system, whereas crank angle resolved data such as in-cylinder pressure are collected by a high speed data acquisition system. The ETCS and both DAQs are controlled by a PC using LabVIEW.

3.3.1 Particulate measurements

The exhaust gas from the firing engine tests was sampled and analysed by a fast response differential mobility spectrometer: the Cambustion DMS500 Mark II. The gas was conveyed via a heated sampling line, which tends to inhibit the condensation of further volatile nucleation mode particulates and the further growth of particulates.

The operation of the DMS500 is documented in [110]. The particulates are charged upon entering the instrument classifier section. The diluted exhaust gas travels through an annular passage, with a co-flow of air, between two electrodes. The outer electrode is composed of 22 separate grounded rings and the core is at high voltage. The particulates are slowed due to aerodynamic drag and drift radially towards one of the 22 rings, due to the electric field. The current developed on each ring allows the particulates that landed there to be counted (per unit time) and post-processing performed by the DMS500 software allows a size spectrum and total particulate number density per volume of exhaust to be found. The particulates may be far from spherical in shape, so the calculated diameters are based on the charge to drag ratio of the particulates, that is, the diameter will be that of a sphere with the same charge to drag ratio. Corrections are made for the fact that some particulates will acquire greater charge than others, which is a function of the particulate size.

To reliably compare exhaust particulate spectra and total number counts between different tests, the exhaust temperature was held constant. The temperatures that the exhaust gas experiences can greatly affect the formation or conversion of different types of particulates, so it is important for this to be consistent. The exhaust temperature was measured just outside the engine cylinder head and particulate measurements were taken at an exhaust temperature of 300°C.

During a legislative particulate measurement test in the EU, the instrument used has specified count efficiencies at certain sizes: greater than 90% at 41 nm and 50% at 23 nm [111]. However, the DMS500 has very high count efficiencies down to 5 nm. Therefore, to replicate the type of results that would be achieved in a legislative test, the particulate spectra are digitally filtered using a mathematical

function. This has been shown to produce results that are comparable to those that would be obtained from a legislative test using a compliant Condensation Particle Counter system [58]. This reduces the number count at the smaller sizes, principally affecting nucleation mode particulates. The function chosen is a Wiebe function, as described in [16], and given as

$$f = \begin{cases} 1 - \exp\left[-3.54\left(\frac{d_\mathrm{p}-14}{40}\right)^{1.09}\right] & \text{if } d_\mathrm{p} \geqslant 14, \\ 0 & \text{if } d_\mathrm{p} \leqslant 14, \end{cases} \tag{3.2}$$

where d_p is the measured particulate diameter in units of nm.

As noted in [13], the components used in the particular engine build can have a large effect on the amount of particulates measured in the exhaust. Optical components made of fused silica have different thermal properties to the metal components (lower thermal conductivity and lower thermal diffusivity), meaning heat transfer and surface temperatures can be different. These will have an effect on the rate of evaporation of spray droplets and of surface films, subsequently altering the conditions for particulate generation. Particulates results are, therefore, quoted with which piston, liner and annulus were used during the test. Typically, a full metal piston was used with a full height metal liner or a metal liner with an optical annulus. The quartz pent-roof window was always present.

3.4 Gasoline Model Fuels

The simplest model fuel for gasoline, for spark ignition engines, is often iso-octane. It is widely available and there is a great amount of data about its properties, since it is a reference fuel for octane number tests [7]. However, it cannot match the wide boiling range of a multi-component gasoline and, since it has a much lower vapour pressure, cannot reproduce the superheated, flash boiling behaviour of a hot gasoline fuel spray.

In the EU and the USA, gasoline typically contains a small amount of ethanol by volume, produced from biomass, and there is scope for these volume fractions to increase [112, 113]. Gasoline fuels which contain low-volume fractions of methanol

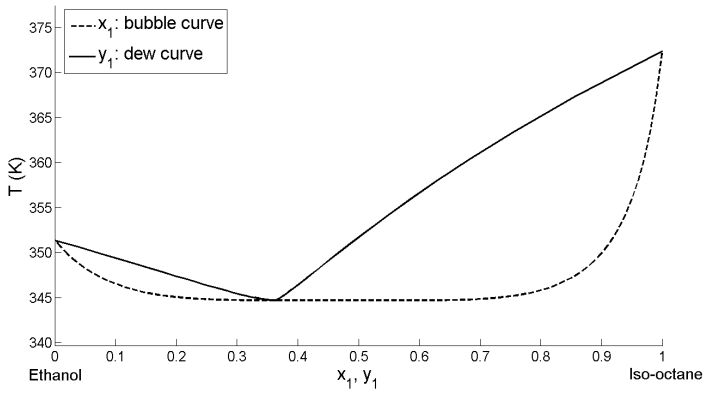


Figure 3.15: Equilibrium phase diagram for iso-octane/ethanol at 1 atm. The equilibrium temperatures at each composition are calculated using the method described in [77]. The NRTL method, in conjunction with Equation 2.48, is used to predict the total fuel vapour pressure. Component 1 is iso-octane. Note the plateau in the bubble curve for a very wide range of compositions; this persists at all fuel vapour pressures currently of interest

are also available (typically in China [114]), produced from fossil fuels, biomass [115] or air-captured CO_2 [116]. Blends with higher proportions of alcohol, such as E85, are also available. As discussed in Section 2.1.3, the resulting mixture is non-ideal, which means that the ethanol fraction must be modelled in order to predict correctly the evaporative properties of the fuel. Therefore, the most basic fuel examined in this study is a mixture of iso-octane and ethanol, which has been examined in detail by [89]. Since reliable experimental binary vapour-liquid equilibrium data exists for this mixture at atmospheric pressure [117], the NRTL method can be employed (Equation 2.51) to model the vapour-liquid equilibrium for this fuel. An atmospheric pressure equilibrium phase diagram ($T-xy$ diagram) is plotted in Figure 3.15, which shows the azeotrope composition at ∼36% iso-octane by mole (e64). Compositions which contain more iso-octane than this will lose ethanol from the the droplet first, whereas compositions containing more ethanol than this will lose iso-octane from the droplet first. It is the total fuel vapour pressure, at the droplet surface, which will determine the location of the azeotrope. If the pressure surrounding the droplet is atmospheric and if the surface temperature is below boiling, the fuel vapour pressure will be less than atmospheric. As the pressure reduces, the azeotropic composition moves towards that of pure iso-octane, to ∼45% iso-octane by mole at 0.2 bar.

Table 3.3: D10 fuel compositions, % by volume [13]

Component	Base	E20	M15	E50	M35	E85	M56
n-pentane	5.00	4.00	4.25	2.50	3.25	0.75	2.20
iso-octane	41.68	33.34	35.43	20.84	27.09	6.25	18.34
n-octane	13.89	11.11	11.81	6.95	9.03	2.08	6.11
toluene	29.93	23.94	25.44	14.97	19.45	4.49	13.17
2,2,3,3-tetramethylhexane	1.48	1.18	1.26	0.74	0.96	0.22	0.65
n-decane	4.69	3.75	3.99	2.35	3.05	0.70	2.06
1,3,5-trimethylbenzene	3.33	2.66	2.83	1.67	2.16	0.50	1.47
ethanol	0	20.00	0	50.00	0	85.00	0
methanol	0	0	15.00	0	35.00	0	56.00
Calculated vapour pressure (kPa)	14.9	26.0	44.1	25.3	43.5	20.6	43.5

Three multi-component (three or more) model gasoline fuels have been used in this study. Their vapour-liquid equilibrium is modelled using the UNIFAC method for simplicity. The vapour pressure of the fuels has been calculated at the temperature of 37.8°C, which is the standard temperature for a DVPE/RVP test. The fuel vapour pressure is calculated using Equation 2.48 and summing across all components; however, no consideration is made of the vapour-to-liquid volume ratio that is used in the standard test apparatus. Equation 2.48 is used to determine the vapour pressure at the surface of a droplet in an evaporating spray so is an appropriate measure to compare the volatility of fuels here. A low volatility blend, known as D10, has been taken from [13], which contains 10% heavy components (n-decane, 2,2,3,3-tetramethylhexane and 1,3,5-trimethylbenzene), 85% medium volatility components (iso-octane, n-octane and toluene) and 5% light components (n-pentane) by volume. This base hydrocarbon fuel has been used to create oxygenate fuels: E20, E50, E85, M15, M35 and M56. The M56 fuel gives a similar air/fuel ratio to E85 [118]. The composition of all of these D10 blends is shown in Table 3.3.

A model fuel used to represent an indolene gasoline blend was used in [119] and has been used here, with between 0% and 20% ethanol by volume. The full

Table 3.4: Model indolene fuel compositions, % by volume

Component	E0	E5	E10	E15	E20
Ethanol	0	5.00	10.00	15.00	20.00
n-Butane	6.09	5.78	5.48	5.18	4.87
iso-pentane	16.13	15.32	14.51	13.71	12.90
Cyclohexane	18.27	17.35	16.44	15.53	14.61
iso-octane	16.22	15.41	14.60	13.79	12.97
Toluene	15.81	15.02	14.23	13.44	12.65
Ethylbenzene	12.68	12.04	11.41	10.77	10.14
n-Decane	12.46	11.84	11.21	10.59	9.97
Naphthalene	2.35	2.23	2.12	2.00	1.88
Calculated vapour pressure (kPa)	61.7	68.9	69.0	68.3	67.5

compositions for this fuel are shown in Table 3.4.

Methanol/gasoline blends with 15% methanol by volume (M15) were created for study, in both single droplet simulations and in engine motoring and firing experiments. Four M15 blends were created and their composition is shown in Table 3.5. The fuels A, A^+ and A^- all have a relatively low final boiling point, due to their lack of heavy components. The initial point (and hence vapour pressure) of these fuels varies, with Fuel A^- having the highest initial boiling point and lowest vapour pressure while Fuel A^+ has the lowest initial boiling point and highest vapour pressure. The final fuel was Fuel B, which was designed to have similar vapour pressure and initial boiling point to Fuel A but with a much higher final boiling point due to the addition of heavier components. Fuel B is also the only M15 model fuel used here to contain aromatic components (toluene). Some of the fuels contain 3% iso-butanol by volume, which helps to prevent phase separation. Iso-butanol has both an alcohol functional group and a significant carbon chain content and is therefore able to form intermolecular bonds with both methanol and hydrocarbons. The calculated distillation curves for the fuels are shown in Figure 3.16 and an experimental comparison for Fuel A and Fuel B is shown in Figure 3.17. The experimental work was carried out to the ASTM D86-12

Table 3.5: Volumetric composition of model M15 fuels with 15% methanol by volume. N-undecane is a saturated straight carbon chain molecule with formula $C_{11}H_{24}$

Component	Fuel A$^-$	Fuel A	Fuel A$^+$	Fuel B
methanol	15	15	15	15
n-pentane	0	40	80	45
iso-octane	82	42	5	0
iso-butanol	3	3	0	0
Toluene	0	0	0	28
n-decane	0	0	0	7
n-undecane	0	0	0	5
Calculated vapour pressure (kPa)	42.8	89.9	127.3	91.2
Calculated RON	101	86	71	72

standard [120] and the data were provided by Shanghai Jiao Tong University, as temperature versus weight fraction evaporated [121].

Methanol/gasoline blends have been studied here due to their interesting volatility properties and high quantity of oxygen that methanol adds to the fuel. The very high vapour pressure that the methanol content adds to the fuel, both because of the high volatility of methanol itself and the highly non-ideal behaviour when mixed with hydrocarbons boosts the vapour pressure. This may have a range of positive or negative effects on the fuel spray, as discussed in Section 1.3.1. The additional oxygen content of the fuel may be beneficial to reduce the rate of formation of soot precursor molecules.

Since the M15 fuels described in Table 3.5 were to be combusted in the optical access engine (Section 3.3), they additionally required a suitable octane number to avoid combustion knock in the engine. Due to the retarded IVC timing (Table 3.2), the engine has a relatively low effective compression ratio, which means combustion experiments could be successfully run with a Research Octane Number (RON) of at least 70. The values for the fuels were calculated from a weighted sum of blending octane numbers from [13] or, if these were unavailable, the raw RON.

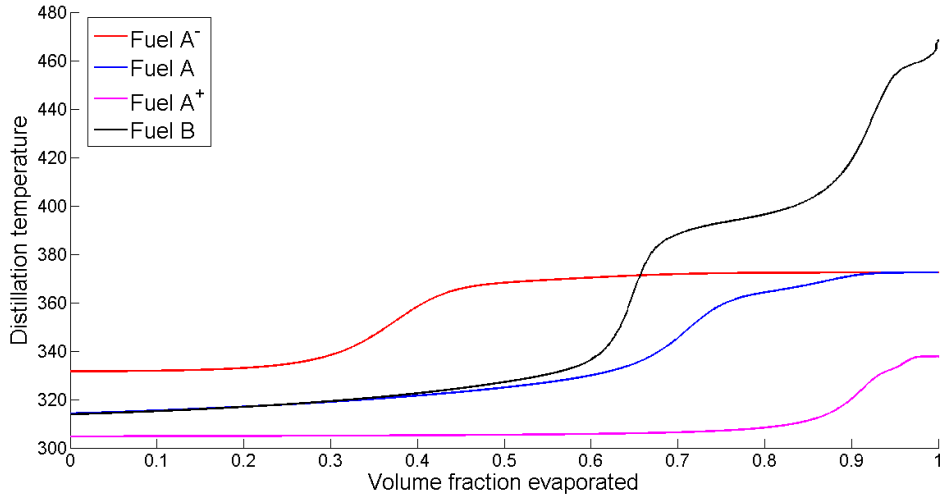


Figure 3.16: Calculated distillation curves for the M15 fuels in Table 3.5. These have been generated iteratively from the initial fuel composition, by calculating the temperature required to give a fuel vapour pressure of 1 atm then using the fuel vapour composition to assess the change in remaining liquid composition for a fixed reduction in amount of liquid. This allows a temperature to be estimated for the new liquid composition and so on. This method is similar to that from [13]

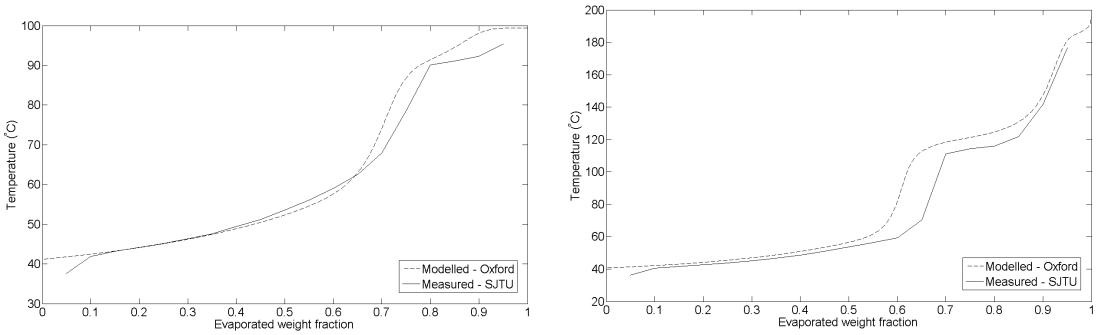


Figure 3.17: Comparison of modelled distillation curves and experimentally obtained distillation curves, by weight fraction evaporated. *Left*: Fuel A, *Right*: Fuel B. There is a good agreement for most of the evaporation period. As expected, there is a discrepancy early on, due to the modelling requirement that the fuel vapour pressure equals atmospheric. Particularly with Fuel B, there is a lag in the temperature rise around 0.6–0.7 weight fraction evaporated, which is approximately when the last methanol vaporizes

3.5 Image Analysis

Spray images taken by the Photron camera were post-processed to facilitate analysis of the spray behaviour, particularly overall spray evaporation rate and spray penetration. These have a great effect on the presence of liquid fuel at the time of spark ignition and, hence, on the possibility of particulate matter formation during combustion.

In both the engine and the chamber fuel spray imaging experiments, images are taken before the spray appears in the field of view. A suitable steady image is selected as a background image, often the second one, as the lighting is still to reach maximum output during the exposure period of the first image. This background is subtracted pixel-wise from all subsequent images of the spray to remove scattered light and other objects from the image. For engine motoring images where the piston is moving in the field of view, a background sequence, at various °CA, may be taken without any fuel spray. The background features may change slightly during the injection as light is reflected off the droplets and around the cylinder. In addition, if spray moves near areas of relatively high background light intensity, these areas will have proportionally more background light removed from them, leading to a lower signal-to-noise ratio, which may distort the view of the spray. However, this technique works well at isolating the spray and more easily allows the remaining analysis techniques.

For a given image, the relative amount of spray liquid remaining in the field of view can be estimated by summing the pixel values of the background subtracted image; this quantity is from now on known as the spray integral. From Mie scattering theory, the light scattered from droplets is roughly proportional to the droplet surface area [122]. Therefore, the spray integral gives an idea of the total surface area of the spray. Some of the spray will be shielded from the incident light or from the camera and there will be multiple reflection. Therefore, there is not direct proportionality across the whole spray. A locally bright area could be due to

a dense region of small droplets or fewer large droplets at the same spacing. Both of these correspond to spray regions with a smaller spacing to diameter ratio (S/d).

Before summing the pixel values, the edge of the spray is identified using a suitable pixel value threshold. This value will depend on the lighting system and the amount of background light that remains. Typical values used in this thesis are between 5% and 8% of the maximum (255 for 8-bit images). The choice will be subjective so sensitivity tests can be undertaken. The thresholding technique allows a mask to be created, which only includes pixels above the threshold value. Isolated regions within the mask below a certain size threshold are discounted as these will be due to small patches of particularly bright background, not the spray. Thus, thresholding also removes stray background light and ensures only pixels belonging to the spray are counted. Finally, a plot of spray integral against frame number or time can be generated for the comparison of different fuels or injection strategies.

To account for shot-to-shot variations in the light output of the light source and to any reduction in incident light intensity during each spray event, a light weighting technique was conceived for the spray chamber images. This would ensure that a more quantitative set of spray integral values would be extracted from a set of spray images. An area of background was selected that was away from any part of the cylinder where spray would reach and that did not tend to saturate in the raw spray images. If the light incident on the spray changed during the injection, the light levels in this region would also change. Therefore, the spray integral value can be weighted by the sum of the pixel values in the pre-selected region. An example region is shown in Figure 3.18.

To improve visualization, the mask created during image thresholding can be used to generate a false colour image, with any colour map, which allows much easier comparison of two spray images than with greyscale images.

Spray tip penetration can be found from the thresholded images. Of most importance in this work is the axial penetration of the fuel spray, that is, down the axis of the cylinder towards the piston. This is used to understand whether the fuel spray is likely to impinge onto the piston, which is linked to the creation of conditions

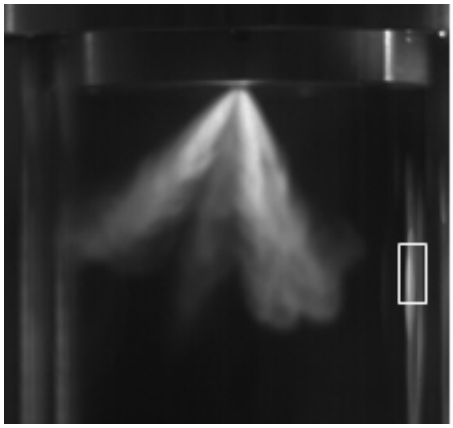


Figure 3.18: Typical illuminated spray image taken in the spray chamber showing the location of the region that was monitored to estimate the light actually incident on the spray during any given frame, and used to weight the subsequently calculated spray integrals. The light is incident from the right hand side in the image

where particulate matter may be generated. Once again, the value found will be subjective, due to the choice of threshold, and sensitivity studies may be performed. The axial penetration in pixels may be easily found by searching the thresholded image for the bottom-most non-zero pixel value. The row index can be subtracted from the row index for the location of the injector. This is converted to a length by a scale factor. The scale factor was determined in both the spray chamber and the engine by imaging a printed grid of known size, set vertically along the cylinder centreline, as in Figure 3.19. The axial penetration calculated in this way does not account for perspective errors, which are thought to be small with this set-up.

If the image frame rate is known, the axial spray tip velocity can be calculated, provided one plume is clearly the most penetrating. The top-most non-zero pixel can be thought of as corresponding to the trailing edge of the spray and can be used to help quantify how dispersed axially the remaining liquid is in the cylinder.

Due to the injection pattern, see Figure 3.1, there is also a possibility of liner impingement from plumes 1 and 6. This tended to happen only if the fuel is not superheated. Determining whether liner impingement occurs may easily be done by observing the images and locating the point of liner impingement can be done by finding the top-most and bottom-most non-zero pixels within a give range of horizontal positions corresponding to the likely areas of impingement by these two

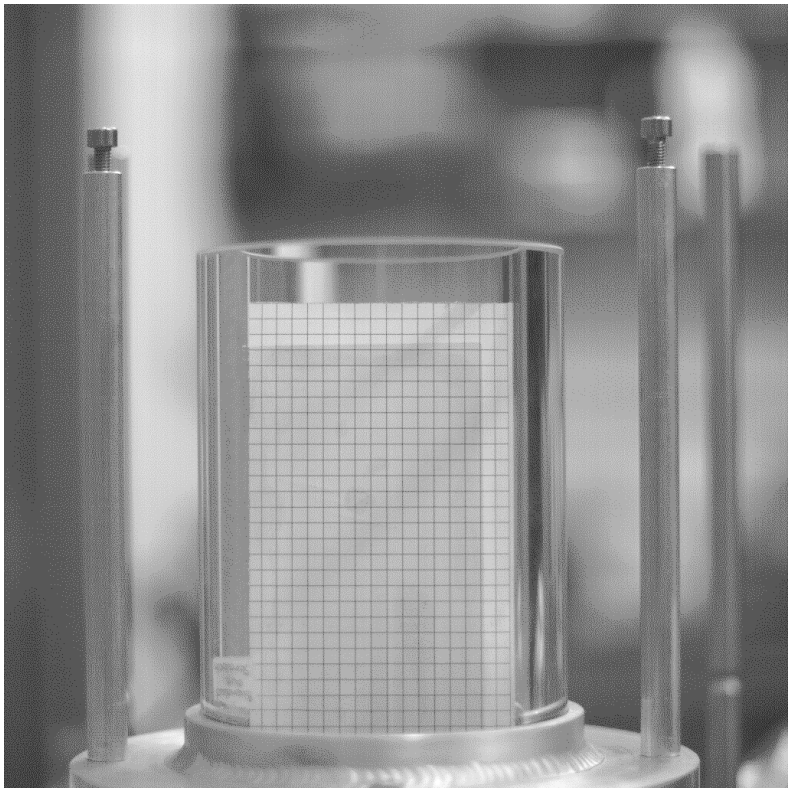


Figure 3.19: Image used to provide scale factor between pixels and real length to be used with the spray chamber images. It is also possible to use the intersection points to map the distortion caused by the cylindrical barrel and the viewing angle; however, this was found to be unnecessary

plumes. This is only possible if the injector orientation is such that the areas of liner impingement do not coincide with light from other plumes.

3.6 Summary

In this chapter, the experimental hardware used in this study has been described. Images of gasoline fuel sprays may be taken either in the purposely-built spray chamber, or under motored conditions in the Jaguar Land Rover optical engine. Regarding the engine, there is the option to run fired tests to investigate how the observed mixture preparation affects combustion and emissions, with the focus of this study ultimately on particulate emissions. Fuel spray experiments may be performed in both chamber and engine and compared. In the chamber, there is superior optical access and tighter control over the ambient air motion and fuel

temperature, whereas the engine tests allow observation of mixture preparation with in-cylinder flow in a real engine and subsequent pollutant formation.

Model fuels representing gasoline have been discussed and the fuels that will be used throughout the thesis have been introduced. These each contain a small number of components (under ten) to facilitate numerical modelling of the simulated fuels and ease of blending of the experimental fuels. This also allows tight control over their properties.

Image analysis techniques have been outlined for calculating measures of spray evaporation and spray penetration, which can be used to compare different fuel sprays, whether the images are captured in the spray chamber or optical engine.

4 Results and Recommendations from Single Droplet Studies

4.1 Droplet Sizes

To give representative lifetimes for droplet and spray evaporation under different conditions, a suitable maximum expected droplet size must be chosen. After fuel jet atomization, there may be secondary droplet break-up, including bag break-up and stripping of fluid from the edges of the droplet, if the Weber number exceeds a critical value. The Weber number is the ratio of the aerodynamic forces on a liquid surface to the surface tension forces within the liquid and is given by

$$\mathrm{We} = \frac{\rho_{\mathrm{A}} U^2 d}{\sigma}, \tag{4.1}$$

where ρ_{A} is the ambient air density, U is the relative velocity, d is the droplet diameter and σ is the fuel surface tension. The aerodynamic forces exceed the surface tension forces for a spherical droplet when $\mathrm{We} > 8/C_D$. Various practical critical We have been reported for actual droplet break-up, including 7–17 [36] and 12–60 [74], depending on Re, the temperature and pressure conditions and the liquid. The effect of liquid viscosity can also be included by calculating the Ohnesorge number, which is given by

$$\mathrm{Oh} = \frac{\mu_{\mathrm{L}}}{\sqrt{\rho_{\mathrm{L}} \sigma d}}. \tag{4.2}$$

One empirically-based criterion proposed in [36] suggested the critical Weber number would increase when liquid viscosity is taken into account, and would be equal to the critical Weber number for inviscid conditions plus a factor equal to 14 Oh, .

For an iso-octane droplet at 20°C travelling at 100 m/s, with diameter 30 µm, through still air at 20°C, the Reynolds number is 214 (based on air density but reference mixture viscosity). From Equation 2.20, this gives a drag coefficient of 0.78 and the critical Weber number is estimated as $\mathrm{We}_{\mathrm{crit}} = 8/C_D = 10.2$ or 10.6 if the Ohnesorge viscosity contribution is included. The actual Weber number for this droplet is 19.0, indicating some kind of secondary break-up is likely, on a relatively short time scale. For the same conditions, a 15 µm droplet has $\mathrm{We}_{\mathrm{crit}} = 8$ and the actual Weber number is 9.5, and at 10 µm the $\mathrm{We}_{\mathrm{crit}} = 6.7$ and the actual Weber number is 6.3. This indicates that the secondary break-up of iso-octane droplets much bigger than 10–15 µm is likely to occur in a spray at 20°C ambient and liquid temperatures. In a real spray there will be entrained air, which will act to reduce the relative droplet velocity compared to the absolute velocity and increase the critical droplet size.

These estimations agree with measured droplet sizes and velocities from previous experiments for iso-octane sprays [41], but it should be remembered that the droplet size at SOI or EOI may be larger due to transient effects and a slower egress velocity (which may cause worse atomization).

As ambient temperature increases, the Reynolds number and the critical Weber number will reduce but so will the actual Weber number. As the liquid temperature increases, the Reynolds number will increase (due to lower air/fuel vapour mixture viscosity) and the critical Weber number will increase. The actual Weber number will, however, also increase due to the reduced surface tension. Therefore, the expected droplet sizes are valid for a range of temperature conditions.

Throughout this thesis, initial droplet diameters have been taken as 10 µm or 15 µm to reflect these estimated maximum possible droplet sizes.

4.2 Droplet Number Density

Using single droplet simulations to infer behaviour of an entire spray assumes that there is limited interference between droplets as sources (or sinks) for heat and as sources for fuel vapour, and also limited aerodynamic interference between droplets.

Although the single droplet evaporation model can be used as a sub-model in a spray CFD simulation, it was also intended to use the model to explore how different fuels evaporated, at different in-cylinder conditions, without resorting to a time-consuming CFD simulation. In order to explore when this approach may be applicable, the expected spray density from a typical GDI spray can be estimated.

A basic model for droplet number density can be defined by considering the continuity of the liquid fuel phase in the spray. For an experimentally observed cone half-angle θ for an injector, the cone radius at a distance z from the injector tip is

$$r(z) = \frac{d_{\mathrm{n}}}{2} + z \tan\theta, \tag{4.3}$$

and the plume section area is

$$A(z) = \pi r^2(z) \sim \pi z^2 \tan^2\theta. \tag{4.4}$$

By continuity, and with negligible evaporation, the partial liquid density of fuel in a plume at a distance z is

$$\rho_{\mathrm{plume}}(z) = \frac{\dot{m}_{\mathrm{plume}}}{A(z) U_{\mathrm{plume}}(z)}. \tag{4.5}$$

Here, $\dot{m}_{\mathrm{plume}}$ is the injector mass flow rate (assumed roughly constant) divided by the number of holes and $U_{\mathrm{plume}}(z)$ is liquid velocity in the absolute frame. If the spray is approximated as monodisperse at a given distance from the injector tip, with a representative droplet diameter $d(z)$, then the spray liquid density is also given by

$$\rho_{\mathrm{plume}}(z) = \frac{\rho_{\mathrm{L}} \pi d^3(z)}{6} \rho_n(z), \tag{4.6}$$

where $\rho_n(z)$ is the droplet number density in units of number per m^3. From Equations 4.5 and 4.6, with the average droplet spacing equal to $S = \rho_n^{-1/3}$, the spacing can be written as

$$S(z) = d(z) \left(\frac{U(z) \pi^2 z^2 \tan^2\theta}{6 Q_{\mathrm{plume}}} \right)^{1/3}, \tag{4.7}$$

where Q_{plume} is the volume flow rate per plume. From typical spray image analysis (Chapter 6), the spray half-angle is taken as $\theta = 10°$ and the absolute spray velocity has been assumed to be equal to the spray tip velocity, measured as around 50 m/s. The total steady state injector volume flow rate for the injector used in this study (Chapter 3), at the operating pressure of 150 bar, reported in [123], was 0.02 L/s, which is shared between six holes. This gives a $S(z)/d(z)$ ratio of 6 for $z = 20$ mm, 12 for $z = 50$ mm and 19 for $z = 100$ mm.

These spacing estimates may be compared to gas phase heat and mass transfer film thicknesses, which are defined in *e.g.* [79]:

$$\delta_Y = \frac{d}{\text{Sh}' - 2} \quad \text{and} \quad \delta_T = \frac{d}{\text{Nu}' - 2}. \tag{4.8}$$

In order for heat and mass transfer boundary layers to interact in a direction transverse to the direction of droplet travel, the spacing must be smaller than twice the thickness of the films. For $S(z)/d(z) \sim 6$, this requires $\text{Sh}' < 2.33$, which would correspond to a relatively slow moving droplet (perhaps 1 m/s). Thus, it is concluded that, when the droplets are in motion relative to the air, the boundary layers of adjacent droplets are not likely to overlap once they are away from the nozzle. However, after the end of injection, the resulting cloud of slower droplets (or those following the gas phase streamlines) may experience boundary layer overlap, since their Sherwood number will reduce to a value close to 2. In the case of moving spray droplets, it is expected that corrections of the form of Equation 2.84 may still be required, since droplets will move through air that has been altered in temperature and composition by the droplets ahead of it and through air that has undergone turbulent mixing due to air entrainment caused by the spray. In the LPT spray simulations, the gas phase temperature and composition is uniform across the computational cell, meaning local effects of a droplet altering the gas phase temperature and composition for the following droplets will be missed.

The droplet densities predicted here for a distance 20 mm from the nozzle ($S(z)/d(z) \sim 6$) are around 4600/mm^3 if $d = 10$ µm and around 1000/mm^3 if $d = 15$ µm. These broadly agree with quoted values from [124] (2400/mm^3 at

8 mm from a gasoline pressure swirl nozzle) and with the calculated value of 4000–10000/mm^3 in the CFD simulations in this work (Chapter 5), at 15 mm from the nozzle for 293 K simulations at a gas pressure of 1 bar.

4.3 Simple Multi-Component Models for Gasoline

4.3.1 Iso-octane/ethanol mixtures

Droplet simulations of the binary fuel, iso-octane plus ethanol, have been run, with both the well-mixed and the unmixed (fixed composition) model applied for determining the droplet liquid composition. This fuel, as described in Section 3.4, was deemed to be the simplest gasoline model fuel, due to the prevalence of increasing quantities of ethanol in gasoline. The heat equation model was used to calculate droplet temperature for these tests.

In Figure 4.1, droplet diameter histories for the bi-component droplets are presented, for a stationary droplet of initial diameter 15 µm; for combinations of ambient pressure (0.5 bar or 1 bar) and initial droplet temperature and ambient temperature (293 K and 333 K). The initial composition was specified by mole, signified by a lower case e. The fuel e10 is similar to 4% ethanol by volume, e25 is similar to 11% ethanol by volume, e40 is similar to 19% ethanol by volume, e75 is similar to 50% ethanol by volume and e95 is similar to 85% ethanol by volume. Pure iso-octane is also modelled, labelled as e0. The results for the e10 simulations were not strongly dependent on whether the fuel was modelled to be ideal or non-ideal. However, there was increasing divergence between the ideal and non-ideal predicted droplet lifetimes as ethanol content was increased, and subsequently all fuels were modelled as non-ideal. This is in agreement with the expected errors, which arise from assuming ideal behaviour for iso-octane/ethanol mixtures, as predicted by [89].

For the slowest evaporating droplets in Figure 4.1(a-b), at temperatures of 293 K and pressure at 1 bar, pure iso-octane is the slowest fuel to fully evaporate. The well-mixed model e10 fuel result was very similar. This suggests that blends with a small amount of ethanol may be adequately modelled as pure hydrocarbons when

evaporation is very slow, which is the case when the well-mixed assumption is most valid. At this condition, the unmixed model lifetime predictions were shorter than the well-mixed ones, by 7% for e10, 5% for e25 and 3% for e40. The e75 and e95 fuels are on the ethanol side of the azeotrope and so will become pure ethanol towards the end of the droplet lifetime. Pure ethanol will have a lower steady state temperature than pure iso-octane, due to the higher enthalpy of vaporization, and is seen to evaporate more slowly in Figure 4.1*(b)*. The intermediate mixtures of iso-octane and ethanol evaporate most quickly, due to the boosted vapour pressure caused by the non-ideal liquid interaction. This is demonstrated by the fact that the unmixed e75 and e95 fuel simulations evaporate more quickly than the well-mixed ones.

Compared to the 293 K simulations at 1 bar (Figure 4.1(a-b)), reducing the pressure (Figure 4.1(c-d)) and increasing the temperatures (Figure 4.1(e-f)) shortens the lifetime. Increasing both the air and fuel temperatures by 40 K had a more significant effect than reducing the pressure by a factor of two. This causes the well-mixed model to show an increased evaporation rate compared to the unmixed model. In addition, the pure iso-octane droplet is the fastest to evaporate under these conditions. The different fuels and models do not predict particularly differing droplet lifetimes for e0, e10, e25 and e40 at 0.5 bar and 293 K, but there is a greater spread at the combination of conditions that gives the fastest evaporation, which is 1 bar and 333 K. The unmixed model is slower by 10% for the e10 and e25 fuels and by 6% for the e40 fuel at 1 bar, 333 K. Therefore, under conditions when there is a faster evaporation rate, attention must be given to the multi-component liquid composition model, even at low concentrations of ethanol.

The droplet surface temperature histories are shown in Figure 4.2, for each of the cases simulated. It is noted that there is a ∼10 K difference between the well-mixed steady state temperatures and the unmixed steady state temperatures for the e10, e25 and e40 blends (Figure 4.2*(a, c, e)*) but that there is a smaller discrepancy for the e75 and e95 blends (Figure 4.2*(b, d, f)*). Since the high ethanol content blends show the greatest discrepancy in lifetime between the two model types, it is important also to note the composition history, *i.e.* when one component

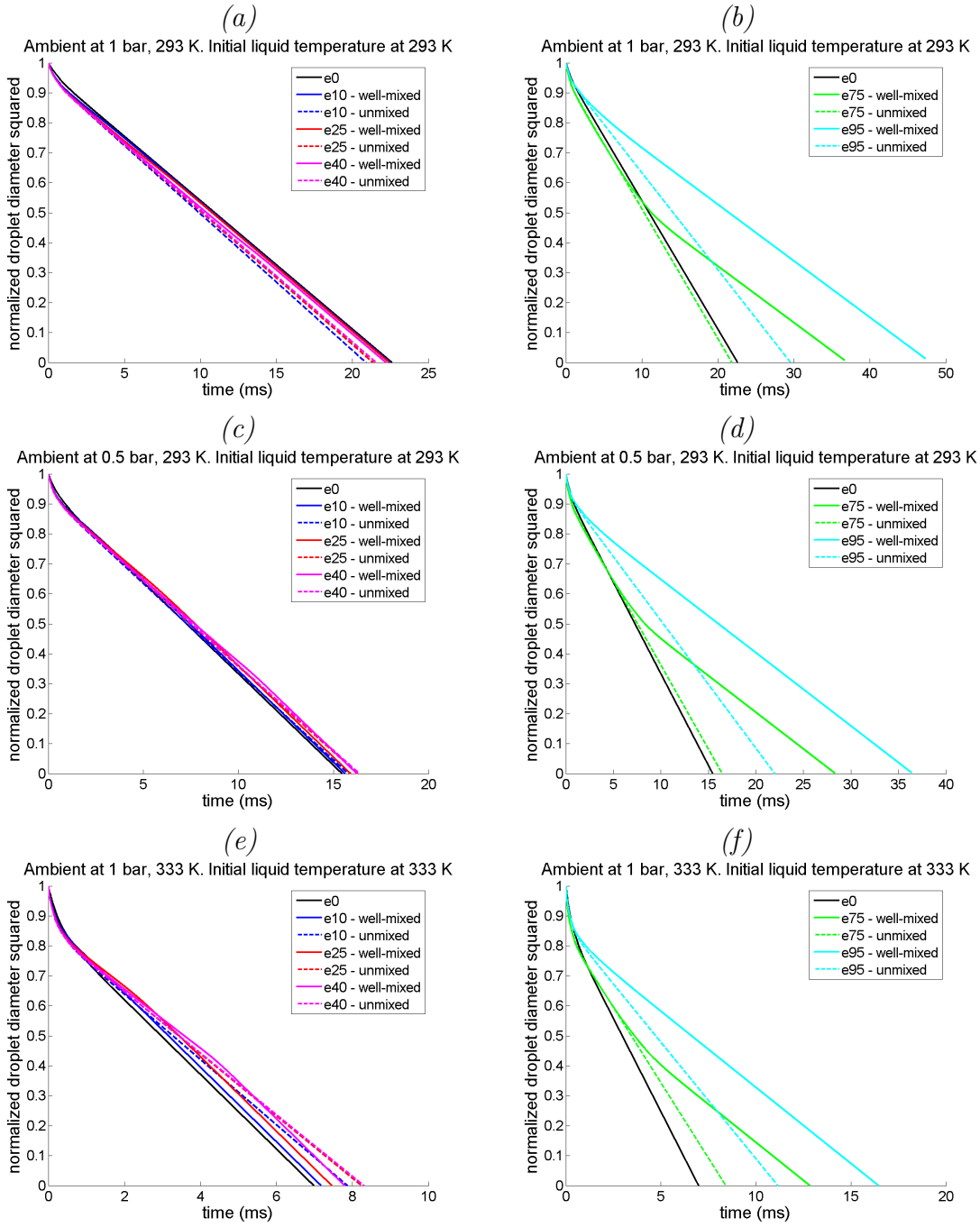


Figure 4.1: Droplet diameter histories, for three different initial conditions and a range of initial compositions of the binary iso-octane/ethanol fuel. Note the different time scales on each plot

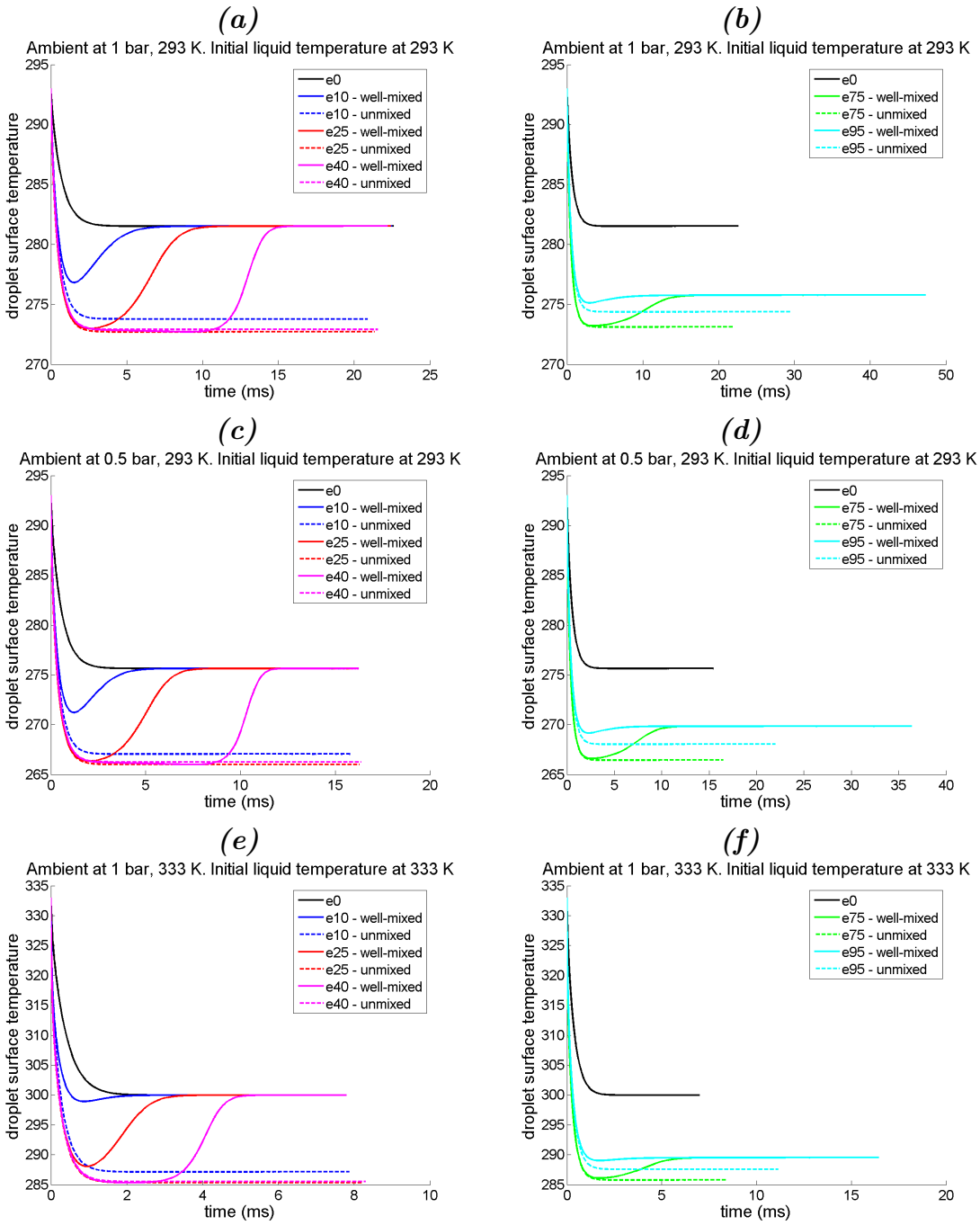


Figure 4.2: Droplet surface temperature histories, for the simulations of three different initial conditions and a range of initial compositions of the binary iso-octane/ethanol fuel

has fully evaporated. Here, the iso-octane/ethanol mixture is more volatile than pure ethanol, even at a reduced surface temperature.

4.3.2 Multi-component mixtures with ethanol and methanol

The multi-component D10 fuel (see Table 3.3) was simulated using the well-mixed model and the unmixed (fixed composition) model. Each of the D10 oxygenate derivatives was also simulated. The aim of this was to observe how the diameter, temperature and composition history evolved throughout the droplet lifetime, and how this depended on the model used for the multi-component formulation. Non-ideal vapour-liquid equilibrium was used throughout, utilizing the UNIFAC method. The initial diameter was 15 µm, the droplets were modelled as stationary (since droplet motion does not affect the difference in behaviour between the well-mixed and the unmixed evaporation) and the heat equation model was used for droplet temperature calculation, with $N_r = 8$. The initial liquid temperature was set to 293 K, the ambient temperature to 333 K and the ambient pressure to 0.5 bar. These conditions were intended to represent early injection at part load under homogeneous operation, with a cold fuel injector and cylinder head. All of the fuels are initially sub-cooled at this condition and remained so during their lifetime. The droplet diameter histories calculated using the well-mixed model, for all D10 fuel blends, are shown in Figure 4.3. A search was performed and it was discovered that, for these fuels, with the droplet at rest, the droplet diameter to power 3/2 decreased roughly linearly. This is in contrast to the d^2–law for single component fuels at constant temperature, where the droplet diameter squared decreases linearly (see Equation 2.8).

The addition of 20% ethanol by volume slightly reduces the predicted lifetime (0.8%), at these conditions, and the addition of the 15% methanol by volume slightly increases the lifetime (3.0%). The addition of further quantities of ethanol or methanol extends the lifetime predicted by the well-mixed model. This was confirmed for blends with alcohol compositions intermediate to those in Figure 4.3. There will be reduced surface temperatures that occur when the alcohol species are present, which can be attributed to their high enthalpy of vaporization and the non-ideal interaction with the hydrocarbons. This will reduce the value of B_Y and

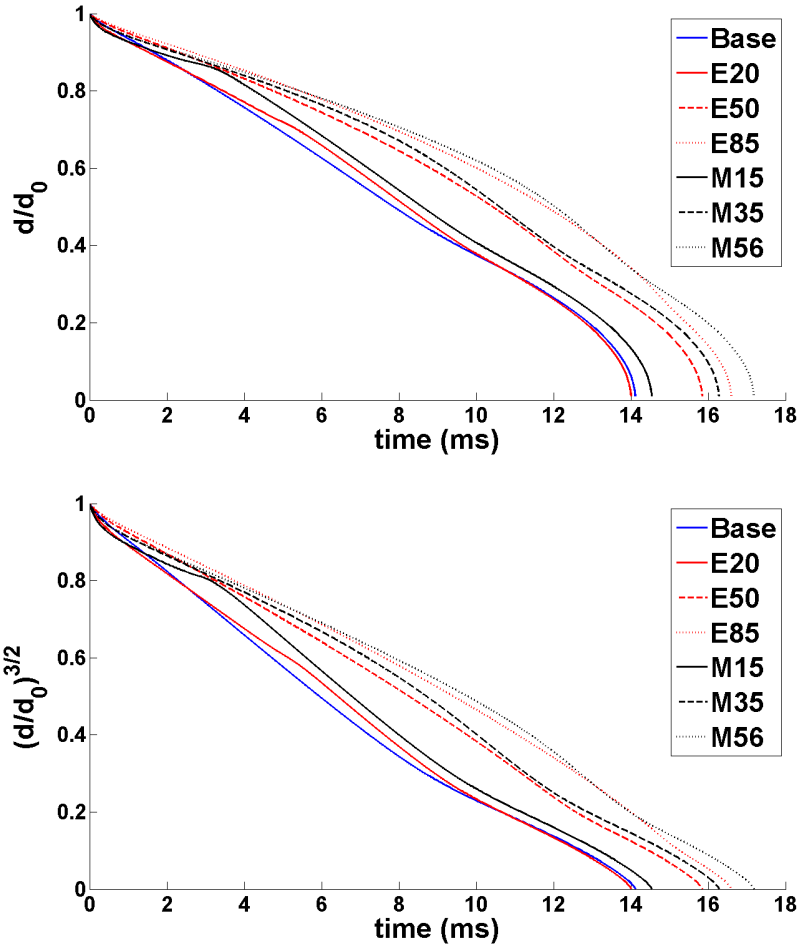


Figure 4.3: Well-mixed model droplet diameter histories for the D10 multi-component blends at 293 K initial liquid temperature, 333 K ambient temperature and 0.5 bar ambient pressure. *Top:* Normalized droplet diameter against time. *Bottom:* Normalized droplet diameter to the power 3/2, which gives a close to linear relationship for the D10 fuels

that of the vapour diffusion coefficient D, whereas the air/fuel vapour density ρ will increase. The reduction of B_Y is seen to dominate here, as whilst the alcohol species is present and temperature remains low, the more volatile hydrocarbon components (starting with n-pentane) are allowed to evaporate, greatly reducing the remaining liquid's volatility. Equation 2.11 shows that the evaporation rate will decrease.

The temperature histories for both the well-mixed and the unmixed models, for the base D10 fuel and the E20 and M15 derivatives, are shown in Figure 4.4.

The droplet surface temperature for the well-mixed models reduces initially, before increasing as the volatile components evaporate preferentially. The loss of surface volatility allows a greater proportion of the heat that is incident on the

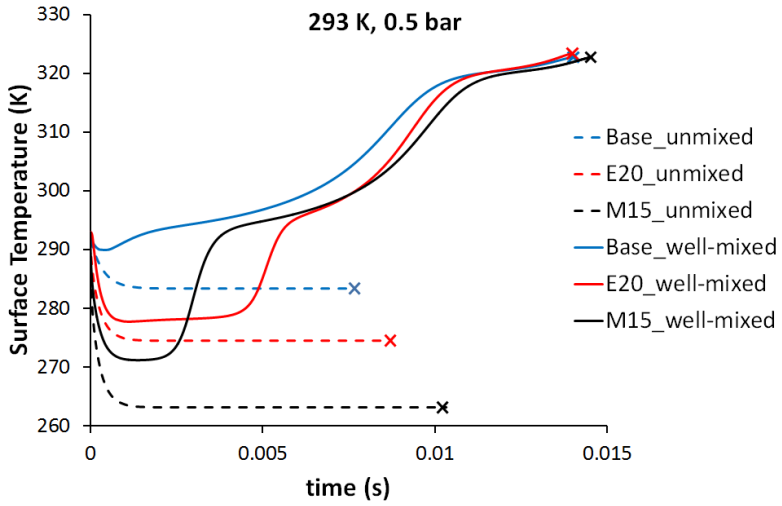


Figure 4.4: Droplet surface temperature predictions for the base D10 fuel and E20 and M15 derivatives, with both well-mixed and unmixed models. The ambient gas is at 293 K and 0.5 bar. The unmixed models predict a very low steady state temperature, reflecting the constant high volatility throughout the droplet lifetime and continued high enthalpy of vaporization in the oxygenated fuel cases. The '×' represents the end of the droplet lifetime

droplet surface (from the surroundings or from the droplet interior) to increase the liquid temperature rather than to evaporate the liquid. The addition of oxygenates boosts the vapour pressure and hence the values of B_Y, while the oxygenate remains in the droplet. However, the high oxygenate enthalpy of vaporization (see Table 1.2) reduces surface temperature early in the lifetime, which competes with the increased volatility. The initial fuel mixture enthalpy of vaporization (as weighted by mass flux fraction in Table 2.2) and initial mixture vapour pressure will demonstrate the expected interaction of these effects. At the condition shown in Figure 4.4, these competing effects are well-balanced in the well-mixed model, since the three fuel types have similar droplet lifetimes.

For the droplets studied here, the well-mixed model seems to cause a slower overall evaporation than the unmixed model, despite the higher temperatures observed during the latter parts of the lifetimes. This can be attributed to the lower volatility of the remaining liquid as lighter components evaporate. Therefore, the surface fuel vapour mass fraction (and hence B_Y) will decrease, even as the temperature increases. The unmixed model, on the other hand, predicts very low

steady state temperatures, due to the requirement for surface equilibrium, but will still predict a high value of B_Y, due to the presence of the volatile components. A useful investigation could be made into whether the surface would actually reach equilibrium at those reduced temperatures or whether the steady state temperature would be higher. The non-equilibrium Langmuir-Knudsen model by [91] might be used to model this.

These findings for the multi-component model gasoline are in contrast to some of the binary iso-octane/ethanol model for gasoline, where the unmixed model predicts a similar droplet lifetime to the well-mixed (sometimes longer, sometimes shorter, see Figure 4.1). This is due to heavy components only present in the multi-component fuel and hence the wider volatility range, which greatly slows the well-mixed evaporation rate at the end of the droplet lifetime compared to the unmixed model.

There will be some differences in droplet composition history between the fuels, in terms of the different interaction that the alcohol components have with the hydrocarbon components. This will cause the promotion or hindrance of the evaporation of different species, while the OH group is present; so as to change the composition (and hence evaporation rate) later in lifetime. This is shown by the vapour flux fraction ε_i, which is plotted in Figure 4.5, for the same three fuels as displayed in Figure 4.4.

Despite the higher vapour pressures observed for the oxygenated fuels in Table 3.3, the actual droplet lifetimes for all the fuels under the conditions studied increased over the base fuel, apart from the E20 fuel. This has been attributed to the higher enthalpies of vaporization as discussed. This has implication for fuel composition selection for the evaporation of real gasoline sprays under engine conditions. If, as may be the case in practice, the underlying hydrocarbon composition of the oxygenated blends is altered so that the fuel vapour pressure is similar to the base fuel, the droplet lifetime may increase further, due to the shift towards less volatile hydrocarbon components. Since spray evaporation is dependent on mixture enthalpy of vaporization, this ought to be considered in the design of oxygenated gasoline fuels and in their comparison in the context of GDI sprays.

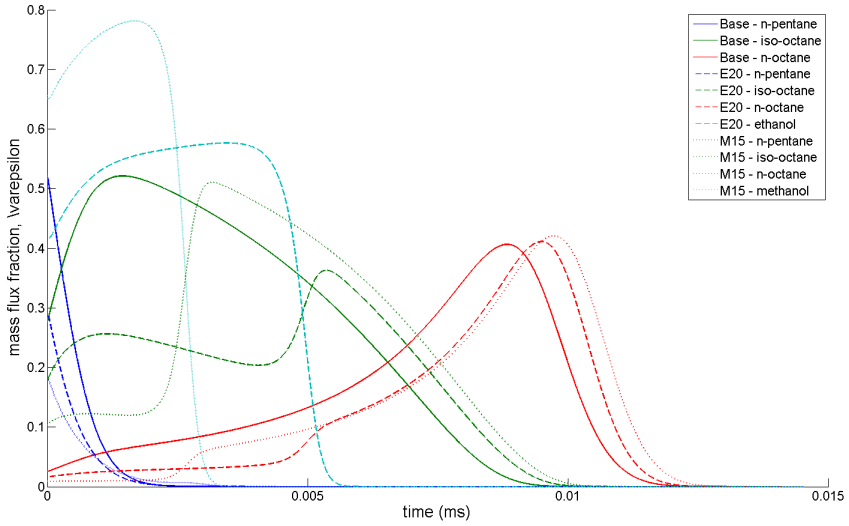


Figure 4.5: Mass flux fraction ε_i of the evaporating components, up to n-octane, for the base D10 fuel and E20 and M15 deriviatives. The alcohols suppress the evaporation of some of the other light components, when present early in the lifetime. This applies to methanol in particular, due to its greater non-ideality and volatility. This effectively delays the evaporation of the n-pentane, iso-octane, n-octane *etc.*, even as the droplet surface temperature recovers once the methanol is depleted

4.4 Droplet Temperature Modelling Results

The droplet heat equation model was tested to assess the grid dependency of the temperature distribution history and subsequent droplet lifetime predictions. A test case was chosen, which was the e40 fuel droplet at 1 bar, 333 K initial liquid temperature and 333 K ambient temperature, which contained two temperature transients within its lifetime (see Figure 4.2*(e)*). This simulation was re-run using $N_r = 4$, 8, 16, 32, 64 and 128. The predicted steady temperatures during two parts of the droplet lifetime, with reference to Figure 4.2*(e)*, were predicted to the same value by all the runs. The error in predicted surface temperature, between the runs with $N_r = 4$ and $N_r = 128$, was briefly 4.5 K in the first few time steps, after this the maximum error was 1.45 K. This resulted, in a lifetime error of just 0.057 ms, which is 0.7%. In contrast the observed differences between the model with $N_r = 64$ and the model with $N_r = 128$ was 0.33 K early in the lifetime and was below 0.03 K after 40 µs. The lifetime difference between the model with $N_r = 64$ and model with

$N_r = 128$ was less than 0.02%, showing good convergence to an accurate solution.

With an understanding of the baseline error due to discretization in the droplet heat equation model, single droplet simulations were performed with a range of initial conditions and with two types of multi-component fuel: the binary mix of iso-octane and ethanol, and the range of model indolene and ethanol blends (see Table 3.4). For the binary mixtures, all of the initial compositions chosen were on the ethanol side of the azeotrope, meaning ethanol would leave the droplet before the iso-octane under the well-mixed assumption. These tests aimed to compare three droplet heating models that were described in Section 2.1.2: the uniform droplet temperature model, the droplet heat equation model with vortex enhancement and the two-point droplet temperature model with vortex enhancement. The conditions are intended to reflect the range of environments in which a gasoline droplet will evaporate for DISI engine operation, from cold start to hot fuel conditions and from part load, early injection (homogeneous operation) to injection during the compression stroke. These initial conditions were also characterized in terms of their initial Reynolds, Prandtl and Schmidt numbers and the initial values of B_Y and B_T.

Table 4.1: Iso-octane/ethanol mixtures - droplet temperature model simulations: average initial conditions and maximum lifetime percentage differences (expressed as $\Delta t_{\text{life}} = (t_{\text{life, othermodel}} - t_{\text{life, heateqn}})/t_{\text{life, heateqn}}$). The different initial dimensionless groups differed very little between the four fuels tested: E5, E10, E15 and E20 by volume

									Uniform temperature				Two-point temperature	
			Average initial conditions						Well-mixed		Unmixed		Well-mixed	
p (bar)	T_{L0} (K)	T_∞ (K)	Le	Re	Pr	Sc	B_Y	B_T	Fuel	Δt_{life}	Fuel	Δt_{life}	Fuel	Δt_{life}
0.5	293	293	0.975	48.2	0.814	1.11	0.653	0.755	E5	-4.5	E10	-4.7	E20	-0.1
		373	0.939	35.2	0.822	1.12	0.653	0.793	E10	-3.9	E15	-3.4	E10	0.9
		453	0.904	27.1	0.832	1.13	0.653	0.830	E10	-1.7	E10	-3.4	E10	1.3
1	293	293	0.973	88.0	0.809	1.31	0.293	0.358	E5	-3.3	E20	-3.4	E10	0.1
		373	0.936	64.4	0.813	1.32	0.293	0.372	E15	-2.1	E15	-1.4	E10	0.9
		453	1.01	49.7	0.797	1.33	0.293	0.341	E5	6.3	E5	-1.5	E20	1.3
3	293	453	0.991	140	0.761	1.51	0.0912	0.114	E5	8.3	E15	2.7	E5	2.2
		573	1.05	102	0.764	1.51	0.0912	0.107	E5	10.0	E5	3.7	E15	0.7
	363	453	0.587	189	0.875	0.673	3.95	12.6	E20	-8.1	E15	-8.2	E5	0.3
		573	0.595	137	0.871	0.684	3.95	12.4	E5	2.4	E20	-6.6	E15	-1.8
6	293	453	0.893	275	0.749	1.56	0.0450	0.0630	E5	8.4	E10	3.9	E5	0.7
		573	0.955	200	0.754	1.57	0.0450	0.0585	E5	13.2	E5	5.5	E15	0.7
	363	453	0.649	314	0.922	0.943	1.09	2.30	E20	-5.5	E10	-5.5	E15	0.8
		573	0.692	229	0.892	0.951	1.09	2.09	E5	6.4	E15	-4.5	E10	1.4
	393	453	0.499	385	0.921	0.599	7.47	45.2	E20	-13.1	E20	-11.2	E20	-1.8
		573	0.538	280	0.878	0.611	7.47	36.7	E5	-4.9	E10	-9.3	E20	-1.4

Tables 4.1 and 4.2 summarize the initial conditions, and the difference in lifetime between the different models. As the droplet heat equation model and two-point temperature model behaved quite similarly, the unmixed model was not re-run for the two-point temperature model. The pressures, gas temperatures and initial liquid temperatures were largely similar for both fuels, except that the tests with initial liquid temperatures of 363 K and 393 K were reduced by 10 K for the indolene mixtures, to prevent the liquids from being superheated. All the models were run sub-cooled. The initial droplet velocity was set to a representative value of 80 m/s, the number of grid points for the droplet heat equation model was $N_r = 5$ and the initial droplet diameter was 15 µm. Both the heat equation model and the two-point model used the effective conductivity method with the vortex enhancement χ (Equation 2.34) applied to liquid thermal conductivity.

Table 4.2: Model indolene/ethanol mixtures - droplet temperature model simulations: average initial conditions and maximum lifetime percentage differences (expressed as $\Delta t_{\text{life}} = (t_{\text{life, othermodel}} - t_{\text{life, heateqn}})/t_{\text{life, heateqn}}$). The different initial dimensionless groups differed very little between the five fuels tested: E0, E5, E10, E15 and E20 by volume, except for B_Y and B_T at 6 bar pressure and 383 K initial fuel temperature

									Uniform temperature				Two-point temperature	
			Average initial conditions						Well-mixed		Unmixed		Well-mixed	
p (bar)	T_{L0} (K)	T_∞ (K)	Le	Re	Pr	Sc	B_Y	B_T	Fuel	Δt_{life}	Fuel	Δt_{life}	Fuel	Δt_{life}
0.5	293	293	0.701	67.5	0.792	0.669	5.45	12.3	E20	-0.7	E5	-8.5	E20	0.0
		373	0.712	48.8	0.785	0.681	5.45	12.0	E15	-2.0	E20	-6.4	E0	0.4
		453	0.703	37.3	0.793	0.692	5.45	12.5	E0	1.6	E0	-5.4	E15	0.7
1	293	293	0.862	107	0.83	0.976	1.24	1.70			E0	-7.0		
		373	0.876	78.2	0.820	0.987	1.24	1.67	E10	-0.9	E5	-4.6	E0	0.5
		453	0.865	60.1	0.823	0.996	1.24	1.70	E0	2.7	E10	-4.7	E0	0.8
3	293	453	1.04	151	0.789	1.38	0.302	0.348	E0	5.2	E0	1.4	E0	1.0
		573	1.01	109	0.798	1.38	0.302	0.360	E0	10.1	E15	3.2	E15	1.1
	353	453	0.623	211	0.810	0.632	1.04	3.95	E0	-7.1			E5	-0.7
		573	0.632	153	0.809	0.643	1.04	3.88	E5	-4.7			E0	-0.4
6	293	453	0.968	286	0.778	1.51	0.142	0.183	E0	6.0	E0	4.1	E15	1.0
		573	1.03	208	0.775	1.52	0.142	0.171	E0	12.0	E0	5.0	E0	1.2
	353	453	0.731	338	0.869	0.925	1.53	2.85	E20	-4.5			E10	0.3
		573	0.736	246	0.865	0.935	1.53	2.82	E10	-2.1			E0	1.1
	383	453	0.575	412	0.835	0.602	21.5	172	E0	-10.1			E0	-0.5
		573	0.596	299	0.819	0.615	21.5	149	E20	-6.7			E0	-1.2

The two-point model, where the surface temperature and interior temperature are tracked, predicted a droplet lifetime in close agreement with the heat equation model, where the droplet temperature is tracked throughout the radius. The maximum lifetime discrepancy for the binary fuel was 2.2% at conditions of 3 bar and 453 K with initial liquid temperature at 293 K for the E5 fuel, where the two-point model predicted a shorter lifetime. The average absolute difference was 0.5% for the 0.5 bar and 1 bar cases collectively, which is comparable to the 0.7% error obtained from using a small number of grid points in the heat equation solution. The average absolute difference was 1.6% for the 3 bar and 6 bar cases collectively. This might be expected as the change in droplet temperature over the droplet lifetime was much larger during the higher pressure, higher temperature cases, leading to a greater chance for discrepancy in the predicted droplet temperatures and, hence, in the evaporation rate. The iso-octane/ethanol droplet with the maximum lifetime discrepancy was simulated again with the heat equation model, using a much finer discretization ($N_r = 64$). This provided a slightly faster initial rate of increase in the surface temperature but the two-point model still predicted the fastest temperature rise rate and shortest droplet lifetime.

For the multi-component indolene/ethanol blends, the agreement between the two-point model and the heat equation model is even better, with an average difference of 0.4% for the low pressure cases (0.5 bar and 1 bar) and an average difference of 0.7% for the high pressure cases (3 bar and 6 bar). The greatest difference was 1.2%, for the E0 fuel at the initial condition of 6 bar and 573 K with initial liquid temperature of 293 K (a similar set of conditions to the case for the binary fuel that gave the greatest difference in predicted lifetime). The temperature histories of this case are shown in Figure 4.6.

As can be seen from Figure 4.6, the major part of the droplet temperature discrepancy between the models is in the early heat-up phase. The two-point predicts a steeper rise in surface temperature than the heat equation model. The disagreement in predicted lifetime in the multi-component cases tend to be lower in magnitude since the rapid heat-up period occupies a smaller portion of the total

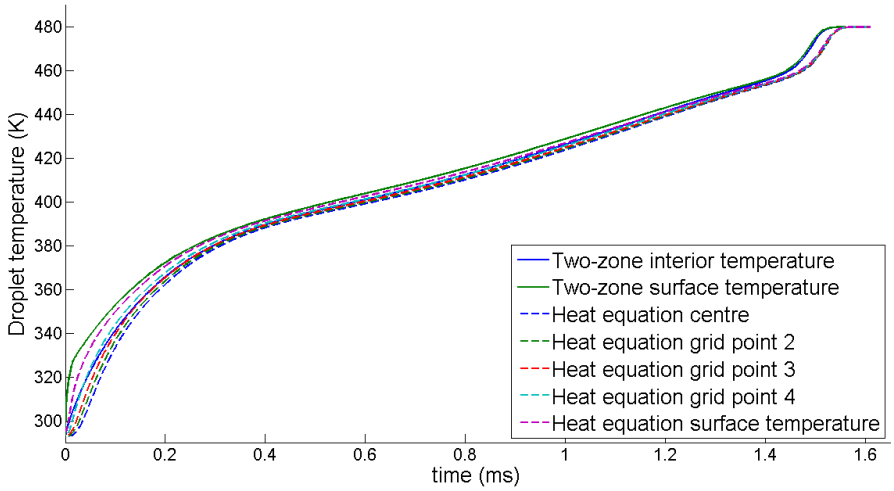


Figure 4.6: Droplet temperature history for both the heat equation model and the two-point model for droplet temperature. The case shown was for an ambient pressure of 6 bar, an initial liquid temperature of 293 K, an ambient temperature of 573 K, with the model indolene E0 fuel. The two-point interior temperature is between the heat equation grid point 3 and 4 temperatures, from 0.1 ms to 1 ms

droplet lifetime. However, in general it can be seen that the two-point model and heat equation model are equally applicable for accurate droplet lifetime predictions across a range of environmental conditions.

The droplet lifetime predictions of the heat equation model and the uniform temperature model, presented in Tables 4.1 and 4.2, do not agree quite as well. For the binary iso-octane/ethanol mixtures, the maximum lifetime discrepancy is 13.2%, for the well-mixed model applied to the droplet with initial conditions of 6 bar pressure, 293 K initial liquid temperature and 573 K ambient temperature, with the E5 version of the fuel. There was a similar swing in predicted lifetime in the opposite direction for other conditions, so the accuracy of the uniform temperature model (assuming the heat equation model to be accurate) is $\pm 13\%$.

For the indolene/ethanol mixtures, the predicted lifetime discrepancies were very low for the well-mixed model at the low pressure and temperature conditions (average difference of 0.9%, at 0.5 bar and 1 bar) but higher under the unmixed model at the same conditions (average difference of 5.1%). This is due to the much shorter lifetime predicted by the unmixed model, for these fuels, meaning the discrepancies

caused by the heat-up or cool down period take up a greater proportion of the droplet lifetime. At the higher pressures and temperature conditions (3 bar and 6 bar), the maximum discrepancy for the well-mixed model was 12.0% (at 6 bar, 573 K ambient and 293 K initial liquid temperature, for fuel E0) and for the unmixed model, it was 10.1% (at 6 bar, 453 K ambient and 383 K initial liquid temperature, for fuel E0). Both of these conditions showed initial periods of rapid temperature change.

Across all of the cases run, there was no strong effect of the amount of ethanol in the fuel on the agreement of the models. At higher gas temperatures and pressures (453 K and 573 K, 3 bar and 6 bar), which tended to cause a sharper change in droplet temperature early in the droplet lifetime, increasing the ethanol content in the binary mixture tended to make the uniform temperature model shorter in comparison to the heat equation model, as shown in Figure 4.7. Increasing amounts of ethanol brings the initial composition further into the temperature plateau region for this mixture (assuming equilibrium, see Figure 3.15). This means that the composition is more likely to tend to a low droplet temperature first (as a mixture of ethanol and iso-octane) and then heat up again to a hotter temperature that a droplet of pure iso-octane will experience. The unmixed model will not experience these temperature variations as composition will not change.

The greatest trend is to be found by considering the volatility of the fuel at its initial temperature. Regardless of the initial fuel temperature or model used, most fuel mixtures will settle to a similar droplet temperature history, after an initial heating or cooling period. Therefore, it is the rate of change of temperature early in the droplet lifetime that will determine whether differences in how the droplet temperature is modelled will affect lifetime predictions. The initial B_Y (function of pressure, initial composition and initial liquid temperature only) was plotted against lifetime discrepancy and is shown in Figure 4.8.

Figure 4.8 shows that, for droplets that are relatively cool compared to the atmosphere they are in (that is, below the wet-bulb temperature for the current surface composition and having a low B_Y value), the uniform temperature model over-predicts lifetime, meaning that it has under-predicted surface temperature.

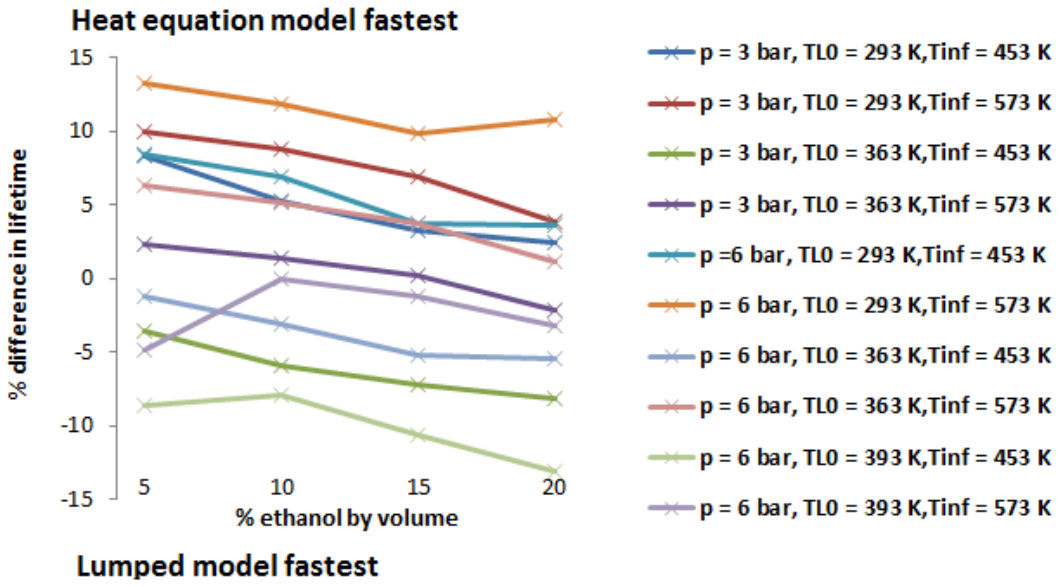


Figure 4.7: Effect of ethanol content in the iso-octane/ethanol mixture, for the high temperature and pressure cases and the well-mixed model. Increasing amounts of ethanol tend to shift the comparison towards a shorter droplet lifetime predicted by the lumped model. However, the results are still evenly distributed about 0% predicted lifetime difference, for the whole set of data

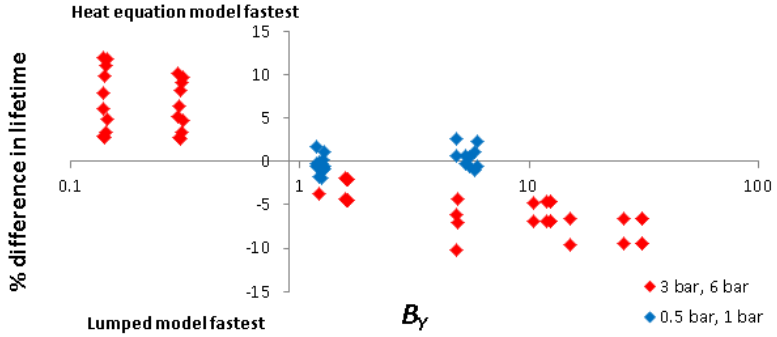


Figure 4.8: Graph of relative lifetime for the indolene/ethanol fuels, comparing the predicted lifetime from the uniform temperature model and the heat equation model. The abscissa is the initial value of B_Y for the individual cases that were modelled. This reflects the initially volatility of the liquid and will indicate the rapidity of initial temperature change that the droplet will undergo, which will be modelled differently by the different temperature models

As the droplet temperature changes, with the uniform temperature model, some of the energy exchange causes the droplet interior to heat up or cool down faster than it might actually do (due to the uniform temperature requirement). Thus, the surface temperature changes less quickly than if a non-uniform temperature is allowed. If the droplet is heating up, as a multi-component droplet will as light components are removed, the uniform temperature will, therefore, under-predict surface temperature, evaporation rate and so over-predict lifetime.

Conversely, high values of B_Y mean the droplet is relatively hot compared to its atmosphere and that it will cool down by consuming its own heat energy for vaporization at the surface, before possibly warming up again as the volatility of the surface components reduces. In this scenario, the uniform temperature model will again predict a slower droplet temperature change, as shown in Figure 4.9, which here will mean an over-predicted surface temperature and lower droplet lifetime. Hence, B_Y can be used to decide whether spray droplets are likely to undergo rapid temperature change and thus require a more detailed temperature model (heat equation model or two-point model). Otherwise, if there are rapid changes in droplet temperature in a spray simulation, an alternative model to the uniform temperature model may be considered for a more accurate solution.

4.5 Liquid Diffusion-Controlled Multi-Component Models

4.5.1 Binary liquid diffusion-controlled model

The solution of the liquid diffusion equation requires the use of a finite number of grid points. The sensitivity to the grid size was tested by running the droplet evaporation of the two ternary fuel blends examined in Section 2.1.7 with a range of number of grid points N_r from 10 to 250. The error in droplet lifetime between using $N_r = 10$ and using $N_r = 250$ was 0.25% for the pure hydrocarbon ternary blend (n-pentane, iso-octane and toluene) and 0.4% for the ethanol-containing blend with ethanol as component 1. Therefore, the diffusion equation was solved using

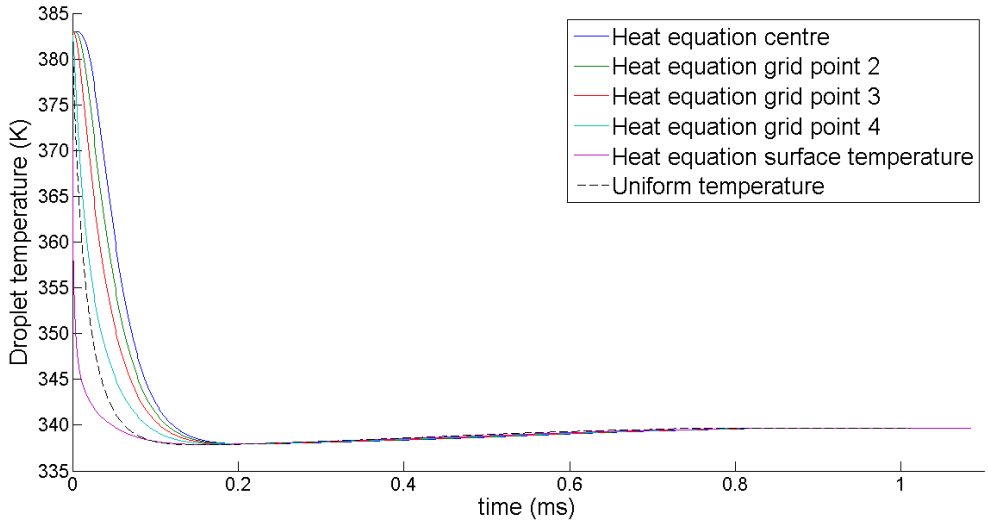


Figure 4.9: Droplet temperature histories for the heat equation model and the uniform temperature model. The predicted temperature from the uniform temperature model lags behind the surface temperature from the heat equation model early in the droplet lifetime, which causes the evaporation rate to be over-predicted. There are also discrepancies in internal temperature predictions, which could affect liquid property estimation

$N_r = 50$ throughout, giving better than 0.4% lifetime precision (*i.e.* better than the 10 grid point model) and acceptable simulation run times.

Determining whether the composition in a droplet can be adequately modelled as well-mixed at conditions relevant to various combustion technologies has been a subject of great interest and is discussed at length in [75]. Accounting for this phenomenon would add considerable complexity to the droplet evaporation model used in CFD calculations. The additional factor considered here is the reduced liquid diffusivity encountered when there is an alcohol species present in the gasoline mixture, due to non-ideal liquid behaviour. In this section, the effects of finite liquid diffusivity are investigated for the binary mixture iso-octane and ethanol.

The liquid diffusion coefficient for mixtures of iso-octane and ethanol is shown in Figure 4.10 for a liquid temperature of 293 K. The Vignes relationship was used (Equation 2.67) and curves are shown for both the case when the thermodynamic correction factor Γ is set to unity (ideal liquid) and when it is calculated by Equation 2.69. The NRTL method was used to calculate the activity coefficients

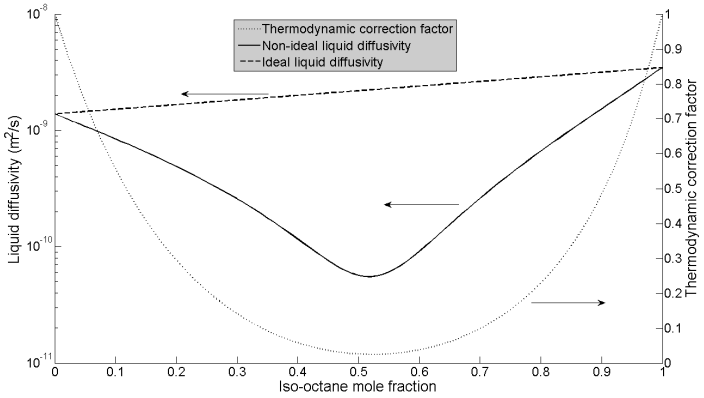


Figure 4.10: The calculated ideal ($\Gamma = 1$) and non-ideal (Γ variable) liquid diffusivities for the iso-octane/ethanol system and the thermodynamic correction factor Γ, at 20°C. Over one order of magnitude separates the two diffusion coefficient estimates at equal parts iso-octane and ethanol. At higher liquid temperatures, Γ and the non-ideal liquid diffusivity will increase

and Γ, using exact solutions to Equation 2.69 from [93].

Due to the low level of mixing that is predicted to occur at intermediate compositions, the behaviour of some mixtures is expected to be similar to an unmixed model. As shown in Section 4.3, the differences between well-mixed and unmixed behaviour can introduce error into droplet lifetime estimations. To investigate under which conditions the well-mixed assumptions produced significantly different results to the diffusion-controlled assumption, droplet simulations were run using the binary fuel at a range of compositions. Since the diffusion-controlled model should give a more accurate droplet surface composition, this would inform when the well-mixed model would be in error, for a non-ideal fuel mixture.

The effects of including the finite liquid diffusion coefficient are shown in Figure 4.11, where the droplet diameter history from the well-mixed model (infinite liquid diffusion coefficient) is compared with results from the diffusion-controlled model, for two sets of initial conditions. The iso-octane/ethanol mixture has been treated as ideal and non-ideal, in terms of liquid diffusion, for comparison; the vapour-liquid equilibrium was non-ideal in both cases. The initial composition was 40% ethanol by mole (e40). The two initial conditions were 40°C initial liquid temperature with ambient conditions at 20°C and 0.5 bar, and 100°C

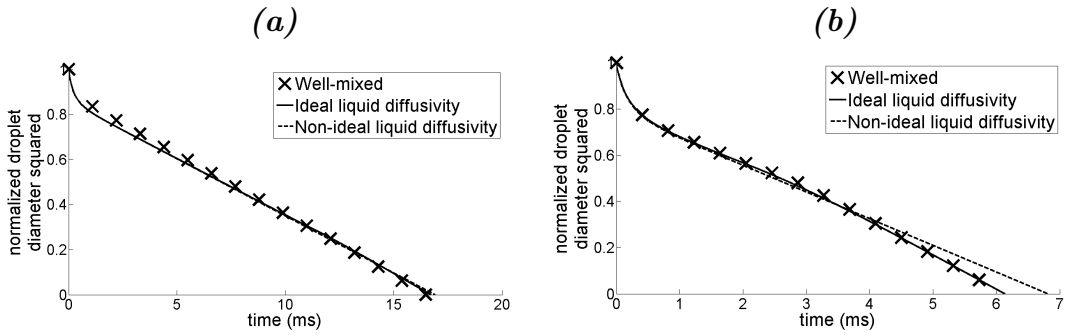


Figure 4.11: Stationary droplet diameter squared histories with fuel e40. *(a)*: 40°C initial liquid temperature, ambient conditions of 20°C and 0.5 bar, *(b)*: 100°C initial liquid temperature, ambient conditions of 100°C and 3 bar. The cooler droplet in *(a)* has very similar results for all three models (within 2.5%), whereas the hotter droplet has a lifetime over 10% longer with the non-ideal liquid diffusion-controlled model

initial liquid temperature with ambient conditions at 100°C and 3 bar. The heat equation model was used to calculate the droplet temperature and the droplets were modelled as stationary.

From Figure 4.11, it can be seen that the liquid diffusion-controlled model, with the ideal liquid assumption and the thermodynamic correction factor set to unity, gives a very similar droplet lifetime result to the well-mixed model at both conditions. Despite the expected error in surface composition present in the well-mixed model, this will not greatly alter the surface temperature and, hence, the evaporation rate. This is due to the plateau in evaporating liquid temperature with composition for this non-ideal blend, as shown in Figure 3.15. When the non-ideality is taken into account, the lifetime is over-predicted in each case, by the greatest amount at the hotter condition, when evaporation is fastest. With this model, ethanol remains in the droplet in significant quantities until the droplet evaporates, due to the slow diffusion. With this fuel mixture, as discussed in Section 4.3, the increased enthalpy of vaporization causes a lower surface temperature, which outweighs any gain in volatility due to the presence of the ethanol at the droplet surface. The initial conditions will determine the magnitude of this effect and whether it increases or reduces the droplet lifetime.

Figure 4.12 shows the in-droplet composition distribution for the three models at the high temperature and pressure case (referring to Figure 4.11*(b)*), as a function

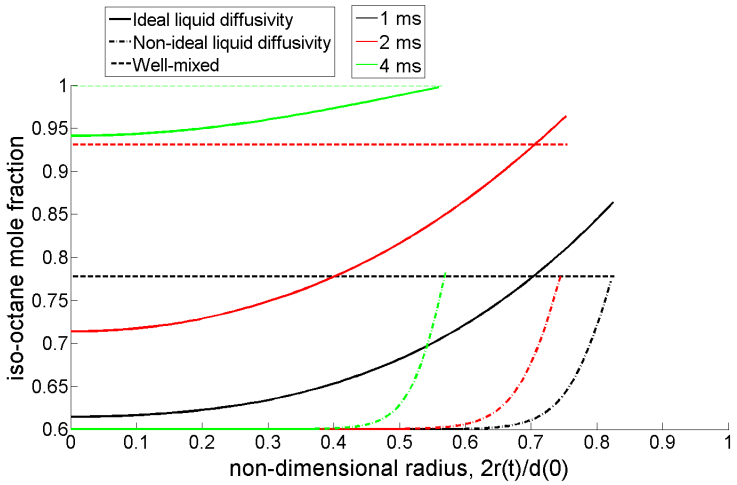


Figure 4.12: Droplet internal iso-octane composition as a function of non-dimensionalized radius, $r(t)/(d(0)/2)$, for the e40 droplet at 100°C initial liquid temperature, ambient conditions of 100°C and 3 bar. Three times throughout the lifetime are shown (1 ms, 2 ms and 4 ms) and there are results from the well-mixed model and the liquid diffusion-controlled model, with both ideal liquid diffusivity ($\Gamma = 1$) and non-ideal liquid diffusivity (Γ variable)

of non-dimensionalized droplet radius. Three different instances throughout the droplet lifetime are presented, to show the evolution of the composition for each model. Compared to the non-ideal liquid diffusion-controlled model, the surface composition of the other models are expected to be in error, as they ignore in-droplet mixing or the non-ideal behaviour of the liquid mixture. The internal composition modelled by the liquid diffusion-controlled model does not necessarily represent the actual internal composition if vortex enhancement is used (the 'effective diffusivity method'), meaning that the compositions at low values of non-dimensionalized radii are more likely to represent conditions at the vortex centre.

Therefore, a range of initial conditions and binary fuel compositions were tested to further investigate the internal liquid mixing. These corresponded to homogeneous mode gasoline direct injection under low and moderate load conditions. The ambient pressures tested were 0.5 bar and 1 bar, the ambient temperatures 293 K, 373 K and 453 K, and the initial liquid temperatures 293 K, 333 K and 373 K. Some of the initial liquid temperatures caused the droplet to be initially superheated. This was dealt with using the alternative method introduced in Section 4.6. The initial droplet diameter was 15 µm and the initial velocity was 80 m/s. The parameter

χ_{mass}, which enhances the liquid diffusion coefficient in Equation 2.63, is used and remains larger than unity for around half of the droplet lifetime, even at quite low relative velocities, due to the large liquid Péclet number. Therefore, the level of mixing observed here will be applicable to droplets in sprays, where relative velocity stays higher for longer, due to the entrained air. The initial compositions tested were 5%, 10%, 15%, 20%, 30% and 40% ethanol by volume. The higher ethanol content compositions were on the iso-octane side of the azeotrope, meaning that, under well-mixed assumptions, iso-octane would leave the droplet preferentially and pure ethanol would remain, towards the end of the droplet lifetime.

The droplet lifetime predictions, from both the well-mixed model and the binary liquid diffusion-controlled model, are presented for all the simulated iso-octane and ethanol droplets in Figure 4.13. For the 0.5 bar simulations (Figure 4.13*(a)-(c)*) and most of the 1 bar simulations (Figure 4.13*(d)-(f)*), at initial compositions between 5% and 20% ethanol by volume, the diffusion-controlled model predicts a longer droplet evaporation time. This can be attributed to the reduced droplet surface temperature that will persist in the diffusion-controlled case, due to the continuing presence of ethanol in the droplet, as previously discussed. However, at the higher pressure of 1 bar and coldest temperatures (T_∞ = 293 K and T_{L0} = 293 K or 333 K), which was the slowest evaporating case, the well-mixed model gave a slightly faster droplet life. Therefore, the relative compromise between steady state temperature and droplet volatility appears to be different here.

The droplet lifetime for the 30% and 40% ethanol by volume cases was predicted by the simulations to increase under the well-mixed model, which was expected from theory, due to the lower surface temperature and lower evaporation rate that occurs with pure ethanol evaporation compared to pure iso-octane evaporation. However, the variation of the lifetimes predicted under the liquid diffusion-controlled assumption is relatively independent of initial composition, due to the plateau in evaporation surface temperature, as discussed in Section 4.3.

The case simulated with conditions of 0.5 bar and 373 K ambient and initial liquid temperature of 293 K was also tested at a larger initial droplet diameter of 30 µm,

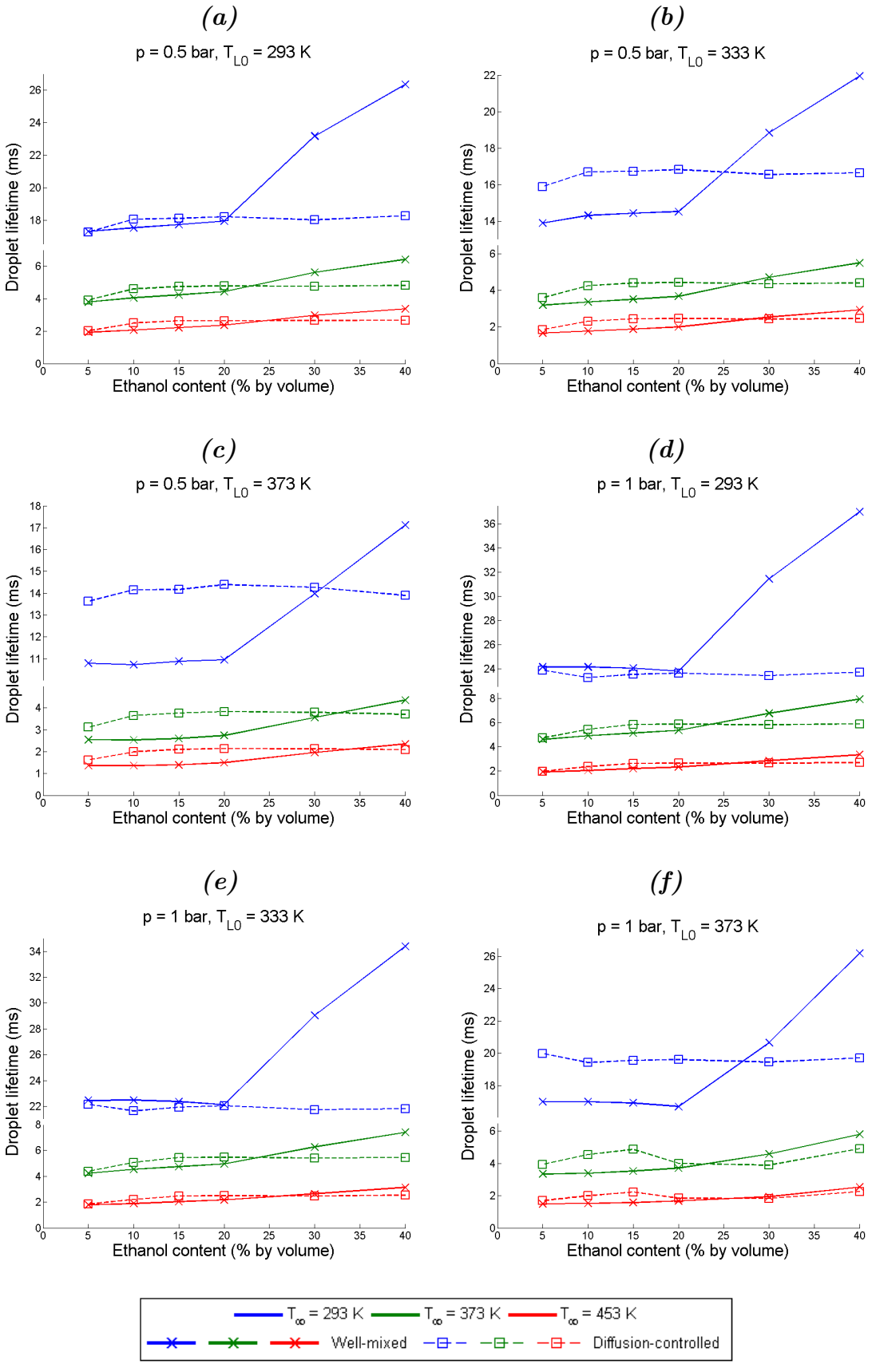


Figure 4.13: Variation of iso-octane/ethanol droplet lifetime with ethanol content for the well-mixed and the diffusion-controlled models, with various initial and ambient conditions. The initial diameter is 15 µm and initial velocity is 80 m/s. Note the axes breaks on the vertical axes

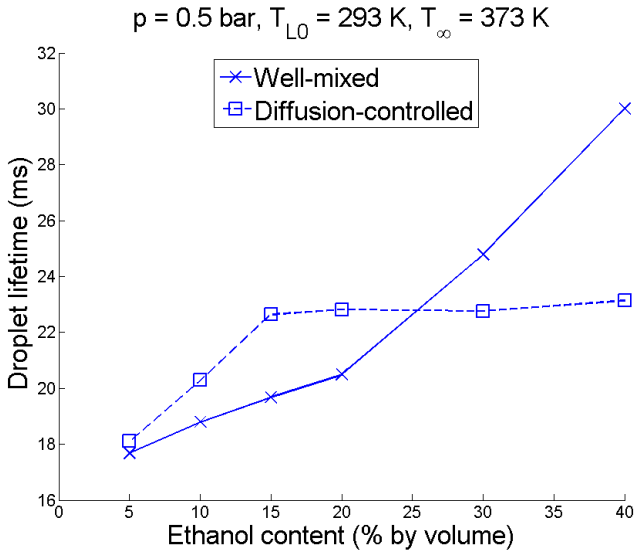


Figure 4.14: Variation of iso-octane/ethanol droplet lifetime with ethanol content for the well-mixed and the diffusion-controlled models, concerning the case with 30 µm initial diameter, ambient pressure of 0.5 bar, ambient temperature of 373 K and initial liquid temperature of 293 K. For comparison with blue line data on Figure 4.13*(c)*

reflecting a largest possible droplet size, possibly formed at the very start or very end of injection. With a larger droplet, there would be a longer droplet lifetime, within which the components could mix during the diffusion-controlled model. There will, of course, be a greater distance between the droplet interior and surface but there will be a relatively thin surface boundary layer, as seen in Figure 4.12. Therefore, some differences in behaviour are expected, which are shown in Figure 4.14.

The E15 droplets simulated at an initial diameter of either 15 µm or 30 µm are predicted to retain ethanol inside the droplet until the end of their lifetime, due to the greatly reduced ethanol diffusivity at these compositions. However, the larger E10 droplet became depleted of ethanol slightly earlier in the droplet lifetime (compared to the total lifetime) than the 15 µm droplet, which resulted in the surface reaching higher temperatures earlier in the droplet lifetime and subsequently a reduced droplet lifetime, such that it was closer to the well-mixed droplet lifetime. Aside from the E10 droplet, there were no significant changes in behaviour between the droplet lifetimes of the well-mixed model compared to the liquid diffusion-controlled model.

4.5.2 Pseudo-binary multi-component liquid diffusion-controlled model

The liquid diffusion-controlled model has been applied to the multi-component model indolene fuel, with varying amounts of ethanol, up to 20% by volume. This uses the pseudo-binary approach discussed in Section 4.5.2 to simplify the number of equations to be solved and eliminate the coupling between the PDEs. Single droplet simulations were run with ambient pressures of 50 kPa and 100 kPa, an initial liquid temperature of 293 K (sub-cooled), and an ambient temperature of 373 K. The droplet temperature was modelled using the heat equation model in both cases, with $N_r = 5$, and the droplet was initially 15 µm in diameter, travelling at 80 m/s. These tests represent cold start conditions under homogeneous operation, with either part throttle or full throttle. The diffusion-controlled model has the effect of the cross-coefficients included, whereby Equation 2.78 is used, instead of simply setting $D_{\mathrm{L}} = D_{\mathrm{L}11}$. The latter approach was employed in the studies in [125]. This has the effect, in general, of increasing the liquid diffusion coefficient for species 1 (here ethanol) as the cross coefficients are typically negative, although not always. Thus, in the results reported here, the ethanol mixing rate is not reduced by as much as was reported in [125], and ethanol does tend to leave the droplet before the end of evaporation, for the compositions investigated. However, the diffusion-controlled model predicts a prolonged ethanol presence at the droplet surface in comparison to the well-mixed model, which affects the evaporation rate and leads to discrepancies between the models.

The droplet lifetimes under these initial conditions are shown in Figure 4.15, for both ambient pressures of 50 kPa and 100 kPa, for both the well-mixed model and the pseudo-binary liquid diffusion-controlled model. The two pressures resulted in different initial droplet volatilities: $B_{Y0} = 4.8$–5.7 at 50 kPa and $B_{Y0} = 1.2$–1.3 at 100 kPa. Both models predict similar droplet lifetimes at low ethanol concentrations, represented by the E5 blend. At higher ethanol concentrations, the composition histories for ethanol surface concentration begin to diverge. This results in a greater surface ethanol concentration, for a longer period of time, which increases the liquid

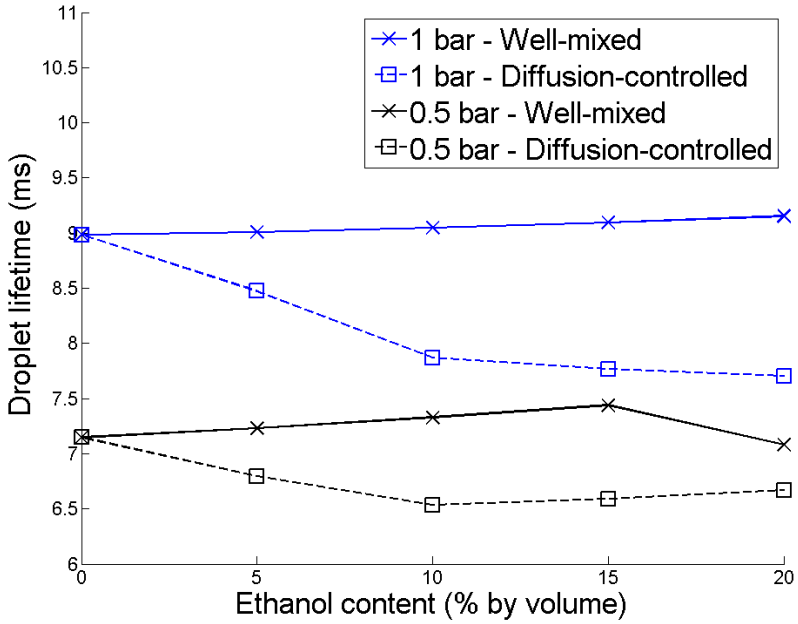


Figure 4.15: Droplet lifetimes predicted by both the well-mixed model and the pseudo-binary liquid diffusion-controlled model. The initial liquid temperature was 293 K, the ambient temperature was 373 K and two pressures were simulated: 0.5 bar and 1 bar. The diffusion-controlled model predicts a shorter lifetime at all ethanol concentrations

volatility and tends to reduce the overall droplet lifetime, although the trends were not so clear with the E20 droplet at 0.5 bar.

To investigate differences between the models further, the droplet surface temperature and droplet surface composition histories for the E20 droplet at 1 bar are presented in Figures 4.16 and 4.17. This case presented the greatest difference in predicted lifetime between the well-mixed and pseudo-binary diffusion-controlled models, which was an over-prediction of almost 19% by the well-mixed model. The droplet surface temperature in the diffusion-controlled case matches that predicted by the well-mixed model at first, before exceeding it around 1 ms into the lifetime. After 3 ms into the lifetime, the diffusion-controlled model predicts a consistently lower surface temperature than the well-mixed model. However, the evaporation rate is faster overall.

Using the surface composition history in Figure 4.17, the surface temperature history can be explained. Initially, ethanol is not the most volatile component and the components n-butane and iso-pentane evaporate preferentially. Under the

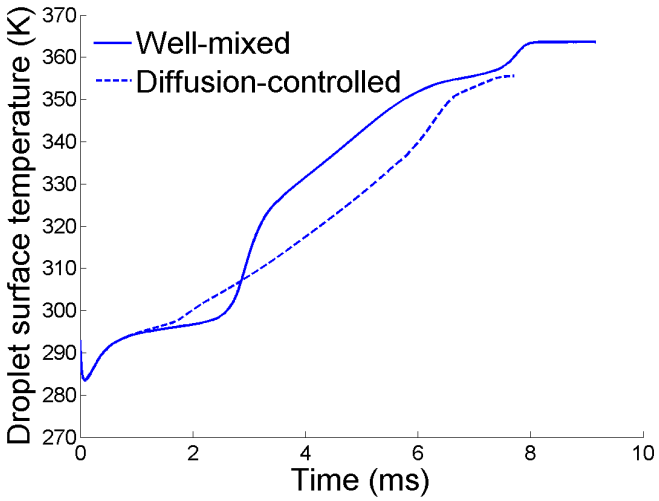


Figure 4.16: Droplet surface temperatures predicted by both the well-mixed model and the pseudo-binary liquid diffusion-controlled model, corresponding to the E20 model indolene fuel, at 1 bar, as shown in Figure 4.15

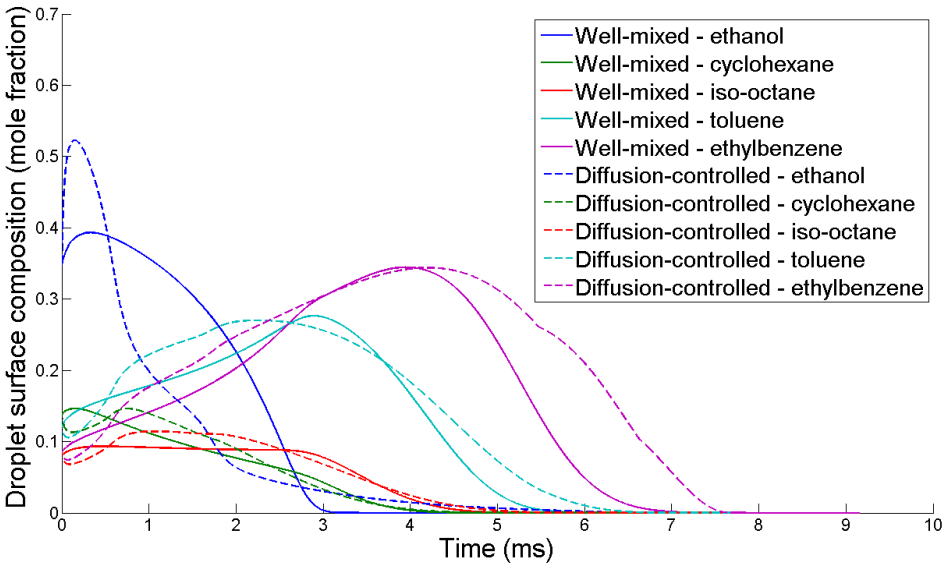


Figure 4.17: Droplet surface composition in terms of mole fraction, for selected components, predicted by both the well-mixed model and the pseudo-binary liquid diffusion-controlled model, corresponding to the E20 model indolene fuel, at 1 bar, as shown in Figure 4.15

well-mixed assumption, ethanol is able to leave the surface towards the interior, in order to accommodate the flux of these lighter components from the interior into the vapour phase. However, under the diffusion-controlled model, the finite mixing rate of ethanol means that this happens more slowly and ethanol accumulates at the surface. Soon after this, ethanol becomes one of the most volatile components (with highest instantaneous value of ε_i), owing both to the loss of some of the more volatile n-butane and iso-pentane and the higher ethanol concentration at the surface. The ethanol surface concentration begins to reduce quickly and the slow mixing means it cannot be easily replenished from the interior. Therefore, the ethanol depletes from the surface. During this time, the interior composition will have barely changed, as shown in Figure 4.18. In this figure, local ethanol mass fraction is presented at eight equally spaced locations for the liquid diffusion-controlled model, corresponding to grid points number 1, 8, 15, 22, 29, 36, 43 and 50, where 1 is the centre and 50 is the surface. The well-mixed ethanol mass fraction is also shown. Therefore, for the remainder of the droplet lifetime (from approximately 3 ms onwards), there remains a small ethanol surface concentration, whilst the ethanol from the interior diffuses towards the surface in order to leave the droplet through evaporation. Due to ethanol's relatively high volatility, high enthalpy of vaporization and the boost to mixture volatility that it causes due to its non-ideal vapour-liquid equilibrium with hydrocarbons, the temperature of the droplet modelled using the diffusion-controlled approach is subsequently lower though the evaporation rate is higher. This compromise, between the effects of higher enthalpy of vaporization and increased volatility, may not always result in faster evaporation but does so at the conditions modelled here.

Figure 4.18 shows that there remains ethanol in the droplet interior until 7 ms into the droplet lifetime for the diffusion-controlled model, whereas in the well-mixed model the ethanol has completely evaporated by 3.5 ms. The internal compositions for the liquid diffusion-controlled model do not exactly match the actual radial positions, due to the use of the effective diffusivity model and presence of the internal vortex. However, they give an indication of the composition within the droplet.

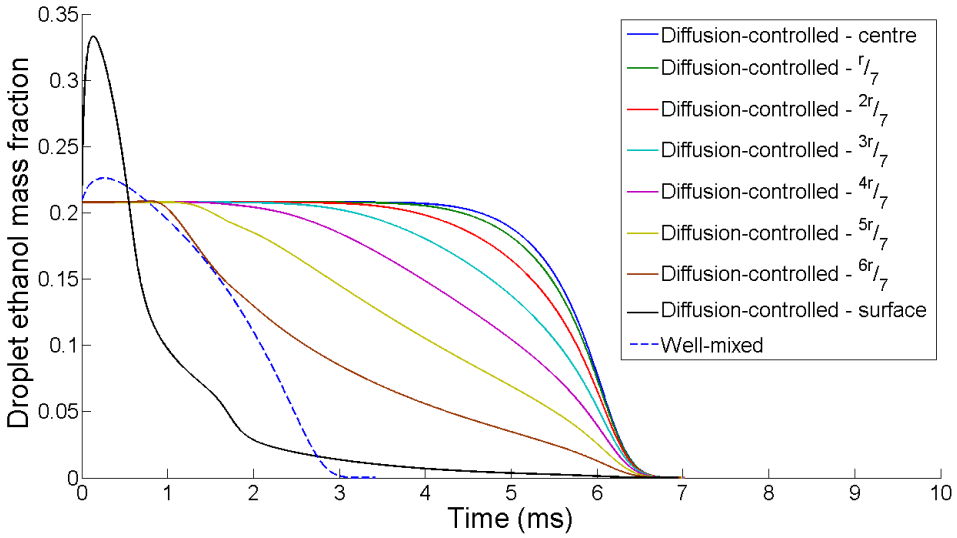


Figure 4.18: Droplet ethanol mass fraction history at various points throughout the droplet, corresponding to the E20 model indolene fuel, at 1 bar, whose diameter history is shown in Figure 4.15. Fractions of 1/7-droplet radius were chosen as these align with the diffusion equation finite difference grid

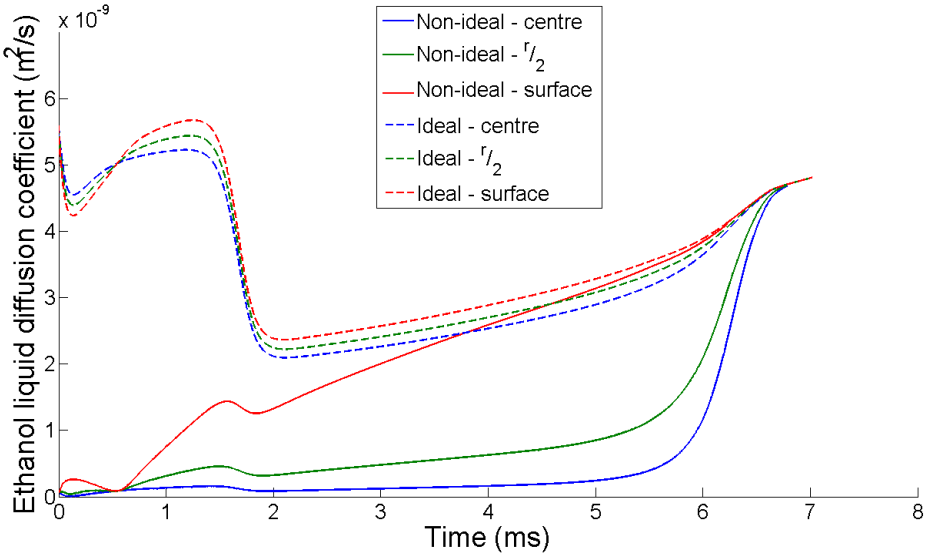


Figure 4.19: Ethanol liquid diffusion coefficient history for the E20 model indolene fuel droplet, at 1 bar, whose diameter history is shown in Figure 4.15. Values at three points throughout the droplet radius are shown, and values both including and ignoring the non-ideal liquid contribution are shown. The reduction and recovery after around 1.5 ms is due to the droplet coming to a rest and the internal vortex stopping, causing the enhancement factor χ_{mass} to drop from 2.72 to 1. At the droplet centre, a minimum of 4.9×10^{-12} m^2/s is reached

The effect of the liquid composition and the non-ideal behaviour on the liquid diffusion coefficient is shown in Figure 4.19. The droplet is in motion until around 1.5–2 ms, meaning that the diffusion coefficient at times earlier than this has been enhanced by the factor $\chi_{\text{mass}} = 2.72$. The liquid diffusion coefficient history has been shown for the droplet surface, the droplet centre and a point midway between these. These coefficients include the contribution from cross-coefficients, as detailed in Equation 2.78. At each time step, the liquid diffusion coefficient that would have resulted from ignoring the diffusion thermodynamic correction factor Γ is also plotted. This is achieved by setting the thermodynamic correction factor matrix equal to the identity matrix in Equation 2.71. In the E20 fuel droplet simulation, at 1 bar, the liquid diffusion coefficients remain positive; however, in some of the multi-component cases investigated this was not the case. The model was able to handle a negative diffusion coefficient for ethanol, which resulted in a greater amount of separation of the ethanol component away from the hydrocarbons, at the surface. However, as ethanol evaporated from the surface later in the droplet lifetime, reducing the overall degree of non-ideal behaviour, the diffusion coefficients returned to values larger than zero.

4.6 Superheated Droplets

To assess how superheated gasoline fuel droplets evaporate and how their temperature evolves, several simulations of superheated, multi-component fuel droplets were carried out. As previously noted, if the cylinder pressure is at 1 bar or below (corresponding to a naturally aspirated or modestly boosted engine, utilizing a homogeneous mode early injection strategy) and the fuel is hot (corresponding to normal engine running), then a typical gasoline fuel will leave the injector superheated, even if it does not undergo a flash boiling atomization process.

Two strategies for dealing with the boiling conditions at the droplet surface were identified in Section 4.6, one of which is taken from Ra and Reitz [87, 88] and another which was developed for this thesis but based on the Ra and Reitz method. Three possible evaporation rates are calculated but used in different

ways by each hypothesis. In the following, the evaporation rate calculated from the fuel species balance (Equation 2.11 or 2.12) is known as $\dot{m}_Y$, the sub-cooled evaporation rate calculated from the energy balance (Equation 2.96 with a calculated value of T_s) is known as $\dot{m}_T$ and the boiling evaporation rate (Equation 2.96 with $T_\mathrm{s} = T_\mathrm{b}$) is known as $\dot{m}_\mathrm{b}$.

In the Ra and Reitz method, $\dot{m}_Y$ is calculated at a slight sub-cooled temperature and, if it exceeds $\dot{m}_\mathrm{b}$, the evaporation rate is set to $\dot{m}_\mathrm{b}$. Otherwise, a sub-cooled approach is used. The droplet surface temperature can be made arbitrarily close to the current boiling temperature, resulting in unrealistically large values of B_Y and $\dot{m}_Y$. Therefore, without a tolerance on the degree of sub-cooling, the droplet will always be predicted as undergoing boiling evaporation, even if the entire droplet has cooled to the boiling temperature, which is non-physical. Various upper thresholds for T_s were tried here, including $T_\mathrm{s} < 0.999T_\mathrm{b}$, $T_\mathrm{s} < 0.99T_\mathrm{b}$, $T_\mathrm{s} < T_\mathrm{b} - 1$ and $\sum p_{\mathrm{vap}i} < 0.99p$.

In the alternative method proposed in Section 4.6, both $\dot{m}_Y$ and $\dot{m}_T$ are calculated at a temperature just below the current boiling temperature, typically 0.1 K below. If $\dot{m}_Y < \dot{m}_T$, then $\dot{m}_\mathrm{b}$ is utilized; otherwise a search is made for a slightly sub-cooled surface temperature, for which it is found that $\dot{m}_Y = \dot{m}_T$. As the sub-cooled temperature used for checking $\dot{m}_Y$ and $\dot{m}_T$ increases towards the current boiling temperature, there will always be a transition to the case where $\dot{m}_Y > \dot{m}_T$, since $\dot{m}_Y$ tends to ∞ at the boiling temperature. This method will force a transition to sub-cooled behaviour if the degree of sub-cooling chosen is inappropriate (*i.e.* too small), rather than force the droplet to remain in the boiling temperature regime as with the Ra and Reitz method. If Equation 2.96 is used, the calculated evaporation rate at boiling temperature and that a very slightly sub-cooled condition (*e.g.* 0.01 K) will be similar, meaning the choice of a very small tolerance will not greatly affect the evaporation rate. Therefore, the new method introduced here is thought to be more robust.

In each case, once T_s is below T_b, the $\dot{m}_Y$ formulation is used in either case, whilst monitoring T_s in case it rises back towards T_b later in the droplet lifetime.

Results for droplet evaporation histories of the nearly ideal mixture of iso-octane and toluene are shown in Figure 4.20. An initial size of 10 µm and an initial velocity of 100 m/s were chosen, with equal parts by mole of each component. Different combinations of initial liquid temperature and ambient temperature were chosen, with initial temperatures of 400 K and 450 K and ambient temperatures of 400 K, 600 K and 900 K. The ambient pressure was 1 bar, giving an initial boiling temperature of 374 K. The heat equation droplet temperature model was used, with $N_r = 10$, and the multi-component mixture was assumed to be well-mixed.

The tolerances of 1 K and of 0.1% absolute temperature failed to allow the droplet to transition to sub-cooled droplet evaporation under the Ra and Reitz assumptions. However, with the 1% tolerance, the droplet temperature results under this assumption were very similar to those under the alternative approach introduced here, after the first few time steps. At the highest temperature condition, there tended to be some oscillation in surface temperature between the current boiling temperature and that predicted by sub-cooled evaporation. It is expected that this could be removed with a change to the temperature tolerance; however, since the new approach is insensitive to the chosen degree of surface sub-cooling, the new approach will be used for the rest of the investigation.

Time-resolved plots of the heat flux, from the droplet interior to the surface, are shown in Figure 4.21 for the iso-octane/toluene droplet simulations. The heat flux from liquid conduction ($-\chi\lambda_{\mathrm{L}}G_{\mathrm{Ls}}$, enhanced by internal mixing due to the presence of the droplet internal vortex), the additional heat flux due to nucleation and flash evaporation ($\alpha_{\mathrm{SH}}\Delta T$) and the sum of these, the total heat flux, are each presented. This shows the relative contribution from each element and shows that the superheated contribution, proposed in [49], is significant early in the droplet lifetime. Ambient temperature has very little effect on the heat flux during the early part of the droplet lifetime.

The superheated model was tested on the multi-component D10 fuel and its oxygenated derivatives. The conditions were the same as for those models presented in Figure 4.3, namely an initial diameter of 15 µm; droplets were modelled as

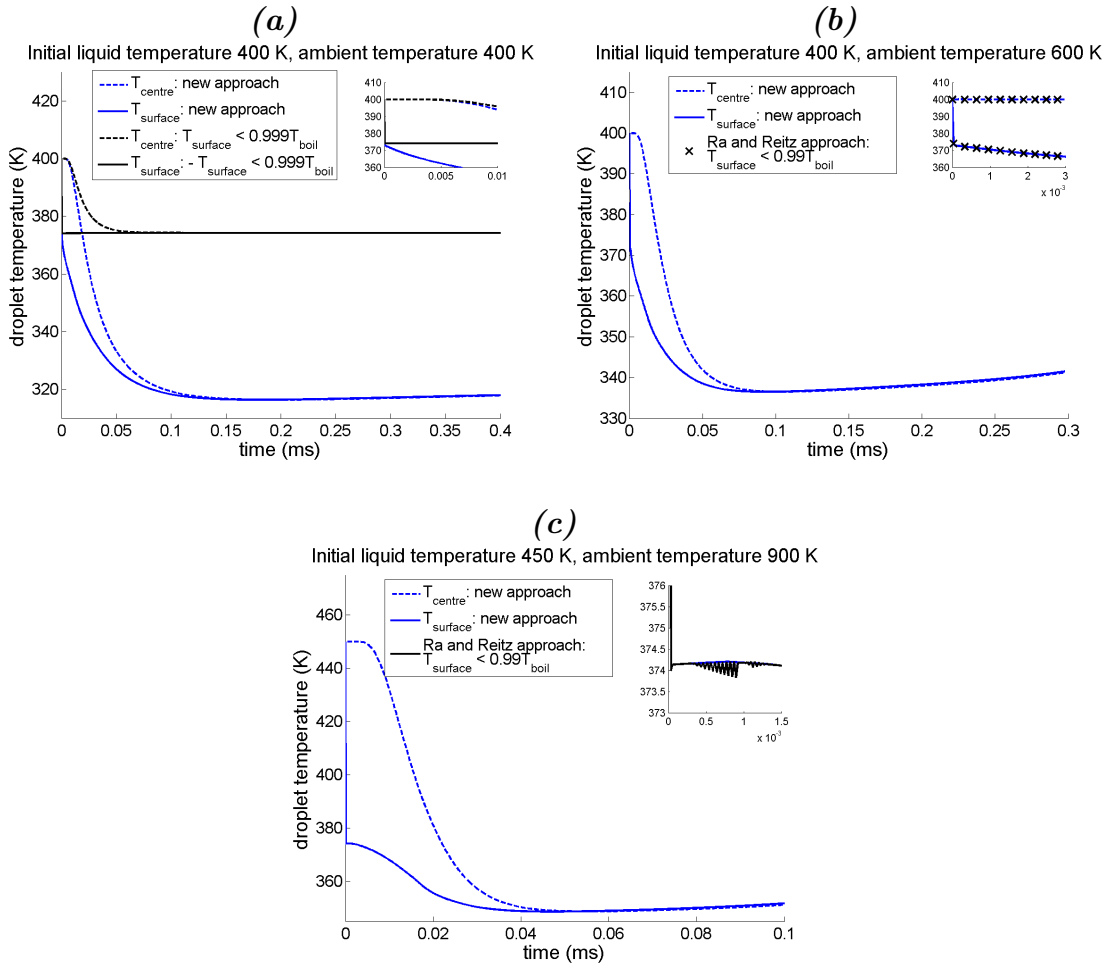


Figure 4.20: Droplet temperature histories for the superheated droplet models at varying superheated conditions, with ambient pressure at 1 bar. Both sets of assumptions have been used. *(a)*: ambient temperature and initial liquid temperature of 400 K. The Ra and Reitz approach with tolerance of $0.99T_{\mathrm{b}}$ was almost indistinguishable from the new approach, whereas erroneous results were returned with the tolerance at $0.999T_{\mathrm{b}}$, *(b)*: ambient temperature of 600 K and initial liquid temperature of 400 K. Both approaches yielded similar temperature histories. *(c)*: ambient temperature of 900 K and initial liquid temperature of 450 K. Both approaches still yielded similar temperature histories but the Ra and Reitz assumptions caused the surface temperature to oscillate early in the droplet lifetime, as seen in the inset

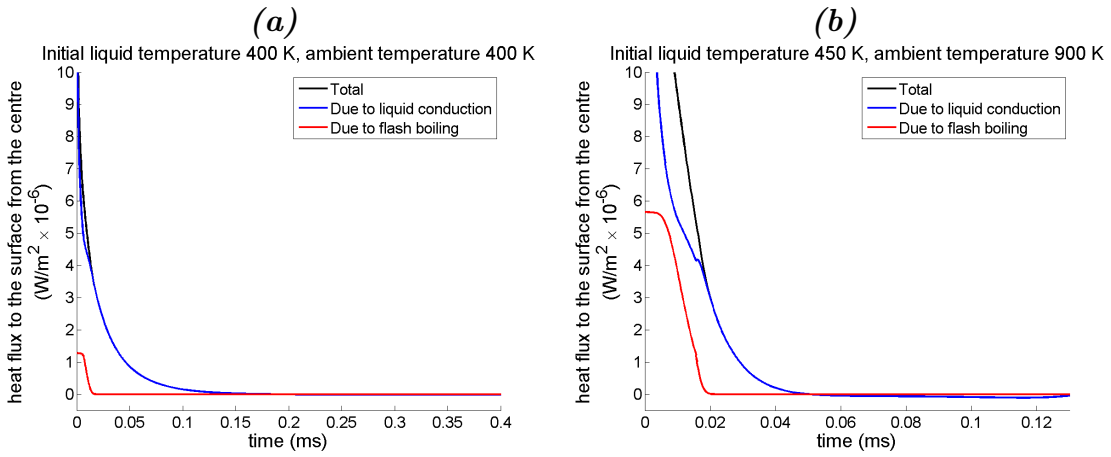


Figure 4.21: Heat flux incident on the droplet, in the positive r-direction (from centre to surface). Initially the values are large and positive since the largest portion of the heat for evaporation comes from the superheated droplet interior. As the interior cools, the heat flux becomes negative, indicating that more heat is incoming from the surroundings to the surface, than from the interior. The superheated contribution to this, postulated to come from flash boiling and vapour nucleation, makes a greater contribution to total heat flux at higher initial liquid temperatures, as in *(b)*

stationary using the heat equation model for droplet temperature calculation, with $N_r = 8$; and ambient conditions of 333 K and 0.5 bar. The initial liquid temperature was then set to 373 K to give a large degree of initial superheat, corresponding to a part load, early injection strategy under hot running conditions. The normalized droplet diameter histories are shown in Figure 4.22. The ordering of shortest droplet lifetimes in this highly superheated case is similar to the sub-cooled case, except M35 is now faster than E50 and M56 is now faster than E85. With the normalized diameter to the power $^3/_2$ plotted against time, there is an initial rapid loss of mass while the droplet is superheated internally, before a roughly linearly decreasing relationship is again obtained, similar to Figure 4.3.

The droplets lose a significant proportion of mass in the first time step, under this type of superheated droplet model. During the first time step, the droplet may become slightly sub-cooled, resulting in the use of Equation 2.11 with a very high value of B_Y and hence evaporation rate. Referring to Section 2.1.4, if it is predicted that the droplet surface will remain at the boiling temperature, then the evaporation rate would be even higher. It is also found that the amount of mass lost, $\dot{m}\Delta t$, in the first time step does not generally decrease as the time step length Δt is reduced: for

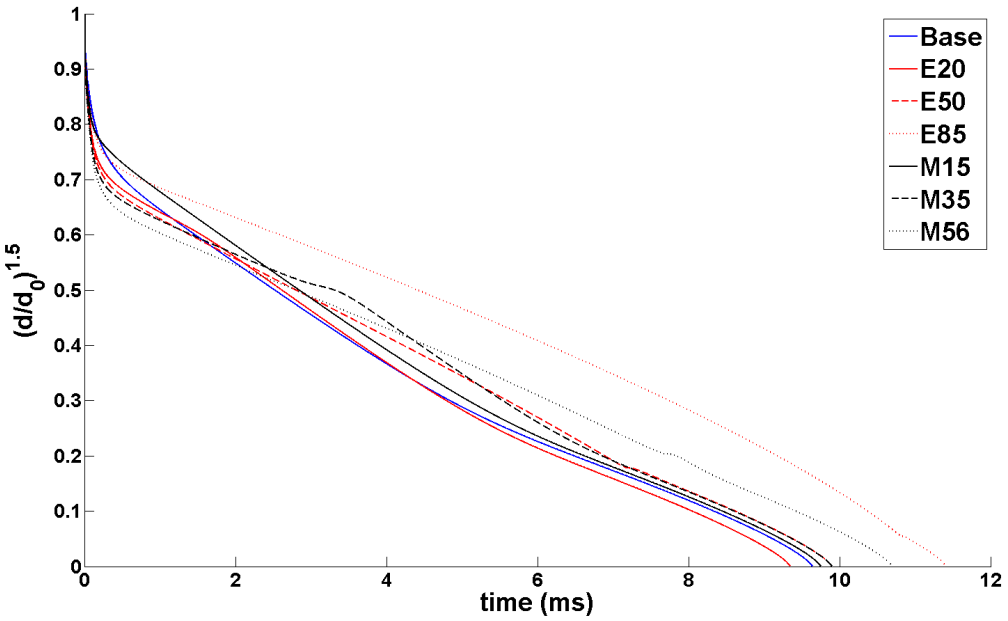


Figure 4.22: Well-mixed model droplet diameter histories for the D10 multi-component blends at 373 K initial liquid temperature, 333 K ambient temperature and 0.5 bar ambient pressure, presented as normalized droplet diameter to the power 3/2

the sub-cooled surface temperature case, a smaller time step means a temperature closer to the boiling temperature and hence a higher evaporation rate; for the boiling surface temperature case, evaporation rate will be higher as previously mentioned. This was also found in the original paper [88]. The droplet mass history for each of the fuels tested, up until 0.2 ms, is shown in Figure 4.23. The time at which the whole droplet ceases to have a liquid temperature above the current boiling temperature is marked with a cross. The initial rapidly lost mass (7%–9% in Figure 4.23) could be thought of as the mass (and associated liquid composition change) that is lost in the flash boiling process. However, it is uncertain whether this process occurs primarily in the nozzle, in the disruption of the atomizing liquid jet, or in the droplets themselves. Therefore, having this flash boiling vaporization occurring at the droplet (and, therefore, subject to artefacts of the droplet evaporation process) is quite arbitrary. In a CFD simulation, this can serve to create the vapour that is observed to appear in flash boiling sprays and transfer it to the Eulerian phase. If a reduction in initial droplet size or release of vapour due to flash boiling is otherwise incorporated in a spray CFD model, then evaporation could be suppressed

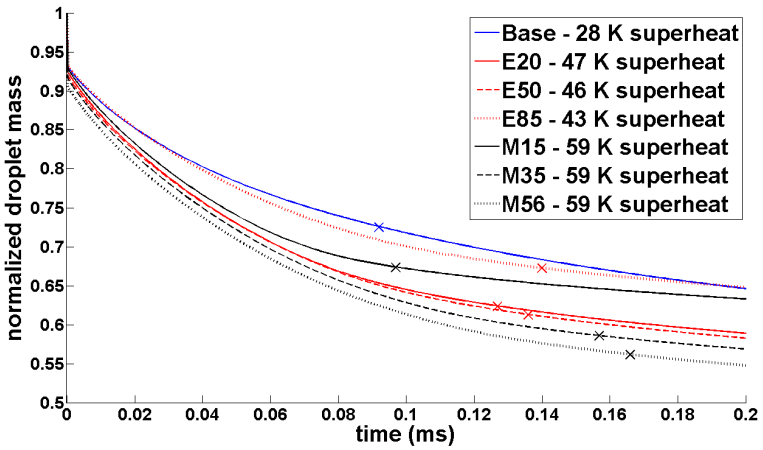


Figure 4.23: Droplet mass history for the early part of the droplet lifetime for the Base D10 fuel blend and its alcohol-containing derivatives. The amount of mass lost in the first time step varies with the fuel blend and depends not just on the degree of superheat but on the initial composition. The '×' signifies the reduction of the droplet centre temperature below the liquid boiling temperature (the removal of all superheat from the droplet)

during the first time step, whilst the droplet temperature model allows the surface temperature to reduce down to the boiling temperature.

Surface temperature histories for the superheated Base, E20 and M15 droplets, as modelled in Figure 4.22, are shown in Figure 4.24. The droplet surface and centre temperatures are shown. The M15 droplet does not as cool as much as the E20 droplet yet its lifetime prediction is still 4% longer than that of the E20 droplet. The lack of a pronounced minimum temperature for the M15 droplet temperature is explained by observing Figure 4.25, which shows the mole fractions for certain species throughout the droplet lifetime. Due to the intense evaporation of light components observed early in the superheated droplet lifetime, the M15 droplet becomes depleted of methanol within 0.2 ms. Ethanol in the E20 droplet persists for longer, as it is a less volatile component. Thus, it is observed that the flash boiling droplet evaporation performance of the M15 fuel is worse than that of the E20 fuel, despite its much greater fuel vapour pressure (see Table 3.3; vapour pressures calculated at 37.8°C). Considering high oxygenate content fuel design in general, these may have a higher than usual vapour pressure or the hydrocarbon part of a gasoline mixture may be altered, to cause the fuel to have a similar

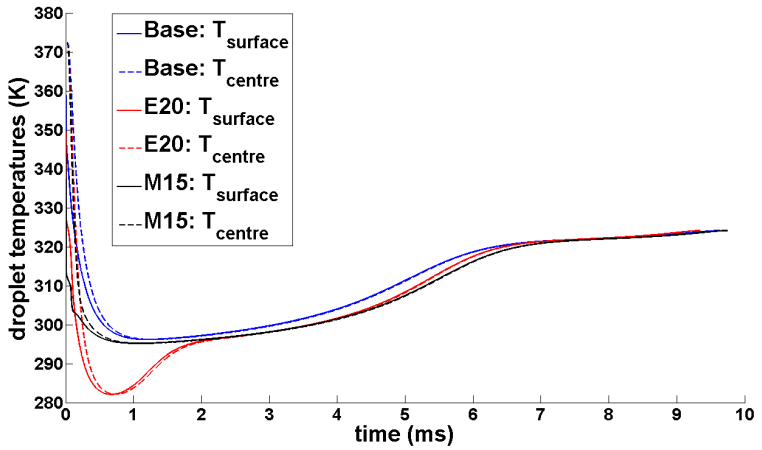


Figure 4.24: Droplet surface temperatures for the Base, E20 and M15 fuel droplets, whose size history is shown in Figure 4.22. Here, the centre temperature is a true centre temperature since the droplet is modelled as stationary

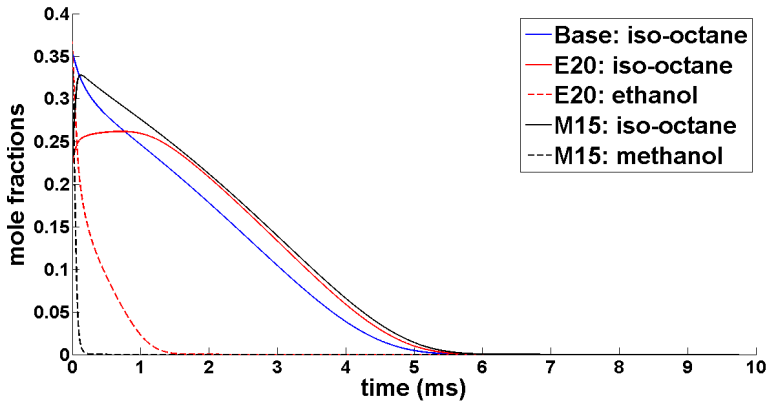


Figure 4.25: Droplet mole fraction histories for the Base, E20 and M15 fuel droplets, showing iso-octane content and alcohol content in the E20 and M15 cases. The E20 droplet and the M15 droplet both have 37.5% initial alcohol content by mole

vapour pressure as that of a fuel with low or zero oxygenate content. In the case of the methanol fuels simulated here, a higher vapour pressure did not result in an improvement in superheated droplet evaporation, in fact the result is the opposite. Since this contradicts the expected trends, assessment of how an oxygenated fuel mixture behaves in a spray condition, including how superheated (flashing) droplets evaporate, must be considered when assessing the engine performance of the fuel.

Considering multi-component fuel droplet evaporation during early injection strategy conditions, the lifetime can be broken into two parts: an initial, possibly superheated, transient cooling phase where a proportion of droplet mass, dependent

on superheat and composition, is evaporated, which can be approximated to take zero time, and a linear decrease in droplet diameter to some power where the remainder of the mass is lost. In Figure 4.3, this initial phase is non-existent due to lack of superheat and rapid transient temperature change (the wet-bulb temperatures at the initial compositions and the ambient conditions were quite close to the initial liquid temperature).

4.7 Summary and Recommendations

The aim of this chapter was to investigate various aspects of multi-component droplet evaporation modelling for GDI sprays and compare and explain discrepancies in droplet lifetime predictions acquired from different modelling approaches. Single droplet simulations were run using initial diameters and velocities based on expected critical droplet sizes and jet velocities from atomization and secondary break-up theory. A range of initial conditions, based on those expected under DISI in-cylinder conditions, were used across the different model runs.

The choice of model fuel used to represent gasoline has been explored, by comparing a two component iso-octane/ethanol mix and a model fuel with seven hydrocarbon species and varying amounts of ethanol and methanol (known as D10). Non-ideal vapour-liquid equilibrium, using either the UNIFAC model or the NRTL model, was utilized throughout. On account of the plateau in evaporation temperature observed due to the non-ideality of the simple binary mixture, the iso-octane/ethanol droplet lifetime varied little for initial ethanol compositions up to 40% by mole (19% by volume); the e40 fuel droplet lifetime was 11% higher than that of the e0 fuel in Figure 4.1*(e)*. This was mirrored in the seven component fuel, where small amounts of ethanol did not greatly affect the droplet lifetime (*e.g.* the 0.8% decrease in Figure 4.3). At higher ethanol concentrations, the droplet lifetime of the binary fuel increases greatly, since the initial composition is now on the ethanol side of the azeotrope. This is seen to a lesser extent in the multi-component D10 fuels, as the oxygenate fuel will always evaporate before the heaviest hydrocarbon species under the well-mixed assumptions, so the surface temperature history is not altered

by as much. Finally, the two different model fuels for gasoline behaved differently when switching between the well-mixed and unmixed (*i.e.* averaged properties) assumptions. The unmixed model, with the D10 fuel and the binary fuel with high concentrations of ethanol, tended to predict a much shorter droplet lifetime, whereas, for the binary fuel with low concentrations of ethanol, the discrepancies in droplet lifetime predictions were similar and condition-dependent.

The droplet heating model has been investigated by contrasting a uniform temperature model, a two-point temperature model and a full heat conduction equation solution. These models were used to evaluate droplet lifetime at a range of conditions, and the predictions were compared. The two-point model (surface and centre) gave predictions within 3.3% of the heat equation model, which was to be expected since the two-point model was derived from the solution of the heat equation. The limit placed on the effective internal thermal boundary layer thickness (Equation 2.36) was derived for one-dimensional heat transfer rather than for a spherically symmetric system, which may be the reason for the slight discrepancy. The predictions from the two-point model are expected, in most cases, to be at least as accurate as the predictions from the heat equation model with a small number of grid points. The uniform temperature model also gave a reasonable approximation of droplet temperature and droplet lifetime, especially at lower liquid and ambient temperature conditions, corresponding to early injection strategies. However, it predicted a lifetime up to 13% longer or shorter than the heat equation model, depending on the conditions. This inaccuracy occurred under conditions where large temperature transients were expected, either increasing or decreasing, during which the uniform temperature model would incorrectly predict the surface temperature, and hence evaporation rate. This observation was quantified using the initial volatility, based on the liquid temperature and ambient conditions through the value of B_Y, whereby particularly large, or small, initial values of B_Y may result in errors in the droplet lifetime predictions from the uniform temperature model.

The droplet internal liquid mixing model was used to assess conditions where the droplet internal composition could be considered well-mixed and conditions

where this assumption led to an error in the droplet lifetime prediction. First, a binary liquid diffusion-controlled model was employed on iso-octane/ethanol mixtures with low amounts of ethanol by volume (0%–40%). Droplet simulations were run across a range of initial and ambient conditions, to represent a large range of GDI spray conditions for an early injection strategy. Under the liquid diffusion-controlled assumption, ethanol remained in the droplet for the whole lifetime for E10 blends and higher. Up to 20% ethanol by volume, the well-mixed model typically under-predicted the droplet lifetime, although at the conditions of slowest evaporation (low temperatures and highest ambient pressure), there was a slight over-prediction. This is due to the higher enthalpy of vaporization of ethanol reducing the surface temperature, which is usually found to be the dominant effect. For the E30 and E40 droplets, the two models rarely agreed. A multi-component indolene fuel, with a full practical range of hydrocarbon volatility and up to 20% ethanol by volume, was also tested, using a pseudo-binary formulation of the multi-component liquid mixing problem for the diffusion-controlled model. With this fuel, the opposite trend was found, in that the well-mixed model over-predicted the droplet lifetime at the two conditions tested. Under the diffusion-controlled assumptions, ethanol remains at the surface for longer; the boosted volatility was the dominant effect of this. Both these ethanol-containing fuels aimed to represent current and near future gasoline blends for the EU and the USA.

Two different approaches for managing droplet superheat have been compared and reconciled. The new model described in Chapter 2 was used to investigate the effect of droplet superheat on the multi-component model Indolene fuel and its oxygenate derivatives. A significant quantity of the droplet's mass and of the most volatile components is typically lost very early in the lifetime (also noted in [87]) before the droplet returns to a sub-cooled state and tends to evaporate subsequently in a normal fashion. Therefore, this model could be used in a spray simulation to model the flash boiling process and rapid loss of volatile components as the liquid phase returns to equilibrium, with possible additional modifications for reduced droplet size or injection of vapour alongside the liquid.

Recommendations will now be made on the most suitable models for use in spray CFD solvers. For complex multi-component fuels such as gasoline it is recommended to use an appropriate multi-component model fuel that matches the real fuel in some way, such as having a similar distillation curve. This is particularly important with non-ideal fuels (*e.g.* ethanol/gasoline blends) since it has been demonstrated that the non-ideal behaviour of a binary fuel with one hydrocarbon component and that of a multi-component fuel with many hydrocarbon components can differ. In order to accurately capture droplet temperature, the use of the two-point model is recommended, since this is always accurate and must be used when the droplet is superheated, which occurs commonly during early injection DISI operation. The uniform temperature model was only accurate at relatively low initial fuel and ambient temperatures. If computational speed is an issue, a lumped (uniform temperature) model may be applied after the initial transient period, which can be determined by a threshold on rate of temperature change. To accurately capture non-ideal multi-component droplet internal compositions, the well-mixed model is good for fuels with low ethanol content and adequate as ethanol content increases. Again, the discrepancies arise in the transient periods, where surface composition is inaccurate. Since the liquid diffusion-controlled model with full diffusion equation solution is too onerous for CFD implementation, a two-point method with an effective internal composition boundary layer, similar to that for the two-point temperature model, could be developed. This would more accurately predict the surface concentration of the components and could have similar computational speed to the existing well-mixed models.

5 Single Hole Spray Simulations

5.1 OpenFOAM Spray Simulation and Sub-Models for GDI Sprays

Spray simulations were undertaken using OpenFOAM, version 2.4. OpenFOAM is an open source CFD code, based on the C++ language, and for which documentation can be found at [126]. OpenFOAM was chosen because of the ease with which additional sub-models may be added to solvers and compared to the existing models employed in the source code.

The aim of this work was not to model any particular spray with great accuracy but to elucidate the differences between various droplet modelling approaches at the whole spray scale, in order to decide appropriate levels of complexity for GDI spray simulations.

Simulation has not been attempted of multi-hole, superheated sprays for the prediction of flash boiling spray behaviour. The single-hole spray simulations are for sub-cooled conditions only. The inclusion of superheated droplet models, of the kind described in this thesis (Sections 2.1.4 and 4.6), will simply increase droplet evaporation rate and create additional vapour near the injector nozzle. Therefore, using these models alone it is difficult to predict well either the observed widening of the individual plumes or the observed interaction of plumes in a multi-hole injector, which lead to spray collapse [127]. Developing a model that does predict these phenomena well may require modelling of the internal nozzle behaviour, *e.g.* as performed by Negro *et al.* [55], and improved resolution of the interaction of the droplets with the gas phase flow [127]. This was outside of the scope of the current work.

The specific solver utilized from the OpenFOAM library is *sprayFoam*, which combines a solver for the gas phase with a parcel tracking solver. The parcels contain a large number of simulated droplets, with identical state (size, temperature, velocity, *etc.*), which are tracked using LPT (see Section 2.2). The gas phase is modelled in a transient, compressible fashion, with turbulence modelling if desired. The solver uses the OpenFOAM PIMPLE algorithm, which stands for merged PISO-SIMPLE. The PISO and SIMPLE algorithms [128, 129] are two methods for calculating pressure and velocity in a flow field [102], which are selected as appropriate by the PIMPLE algorithm.

A case was set up in OpenFOAM to model a single hole injection of fuel into a quiescent volume of air. This was to be representative of a GDI spray, albeit with only one spray plume for simplicity. The initial temperatures, pressures and injection parameters were set to appropriate values for a GDI spray. The case was developed from a tutorial case within OpenFOAM, known as *aachenBomb*, which was designed to simulate diesel spray injection and combustion in a high pressure and high temperature environment. The tutorial is described and discussed in [130], which explains many of the parameters that are required to be set in *sprayFoam*, and the process of running the case. The original simulation used a Reynolds-Averaged (RANS) approach, using a k–ε turbulence model with the standard coefficients, which was also adopted here.

Initial modifications, required to create a case applicable to GDI sprays, are now outlined, with reference to a typical OpenFOAM case structure for a spray simulation, shown in Figure 5.1. The initial conditions are set in the directory *0*, which represents the time when the simulation starts. The initial gas pressure was set to a uniform value of 1.013 bar in the file *0/p* and the initial temperature was set to a uniform value of 310 K in the file *0/T*.

Chemistry and combustion were turned off, since the spray to be simulated was non-combusting. To achieve this, the keyword `chemistry` was set to `off` in *constant/chemistryProperties* and, in *constant/combustionProperties*, `combustionModel`

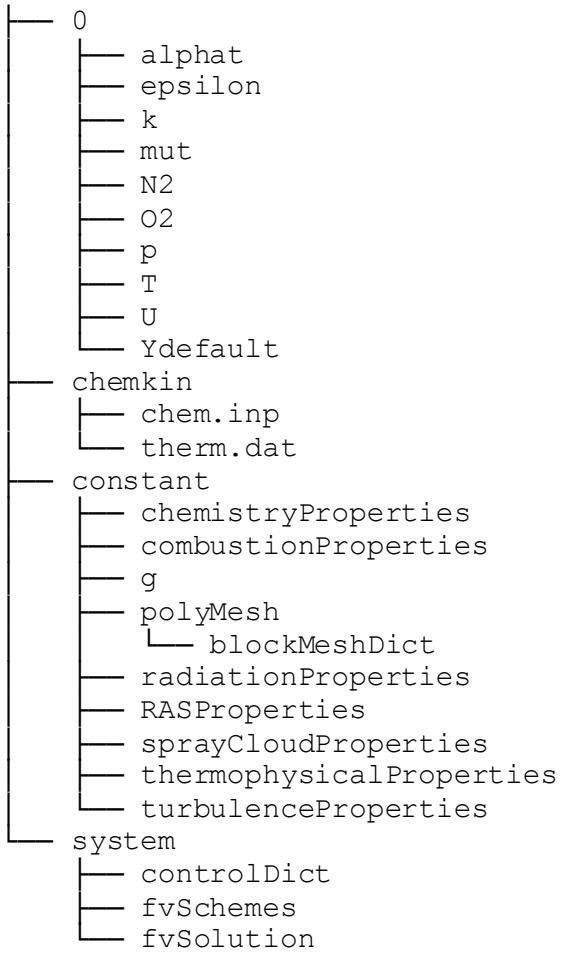


Figure 5.1: A typical file and directory structure in an OpenFOAM *sprayFoam* case. The file *0/Ydefault* sets boundary and initial conditions for the gas phase mass fractions of all the species other than N_2 and O_2, *i.e.* any fuel vapour species

was set to `noCombustion<psiThermoCombustion>`, `active` was set to `no`, and an empty set of parameters was included, named `noCombustionCoeffs`.

The template case uses chemical reaction mechanisms that were provided by the CHEMKIN program [131]. Since no reactions were to be modelled, the simplest approach was to leave the existing input information relevant to combustion modelling in place, and add data for the fuels used into the files relevant for combustion. For iso-octane, `IC8H18` was used, which represents the chemical species 2,2,4–trimethylpentane).

In the file *chemkin/chem.inp*, `IC8H18` was added under the `SPECIE` header. The reaction details under the `REACTION` header can remain the same and, if so, the original fuel inherited from the tutorial case (which was n-heptane, known as `C7H16`) should be left in the `SPECIE` list. Data for the fuel species' heat capacities must be loaded into the file *chemkin/therm.dat*, once again leaving the `C7H16` data in place. The formatting and spacings between data columns in this file are important for the Chemkin reader, so the data was copied directly from the file *OpenFOAM-2.3.x/etc/thermoData/therm.dat*, where *OpenFOAM-2.3.x* is the OpenFOAM source code directory. The `IC8H18` liquid species was added in the file *constant/thermophysicalProperties* under the `liquids` header (retaining `C7H16`) and, in the file *constant/sprayCloudProperties*, `IC8H18` replaced `C7H16` under the headers `liquidEvaporationBoilCoeffs` and `singlePhaseMixtureCoeffs`.

Most of the spray parameters are set in the file *constant/sprayCloudProperties*, including the initial liquid temperature. Under the header `subModels`, in the `injectionModels` section, `flowType` was changed to `pressureDrivenVelocity`, which enables a link between the injection pressure (`Pinj`, which was set at 150 bar) and the initial parcel velocity via the equation

$$U_0 = \sqrt{2(p_{\text{inj}} - p_{\text{amb}})/\rho_{\text{L}}}, \tag{5.1}$$

where the velocity coefficient has been set to unity.

The `outerDiameter` was set to 200 µm, which set the size of the injector nozzle hole at the outlet (not including any pre-hole or stepped hole geometry (see Section 1.3.1)). The injection `type` was left as `coneNozzleInjection`, with `innerDiameter` set to `0`, `innerTheta` set to `0` and `outerTheta` to `10`, which results in a solid cone spray with half-angle of 10° (corresponding to calculations from spray image post-processing). The injection duration, injector position and injector direction are also set here. The tutorial case sets `flowRateProfile` to `table`, in order to give a time-varying injector discharge rate during the injection, by providing a table of volume flow rate (cm^3/s) against time. The existing flow rate table describes a profile consisting of a rapid initial ramp to maximum flow

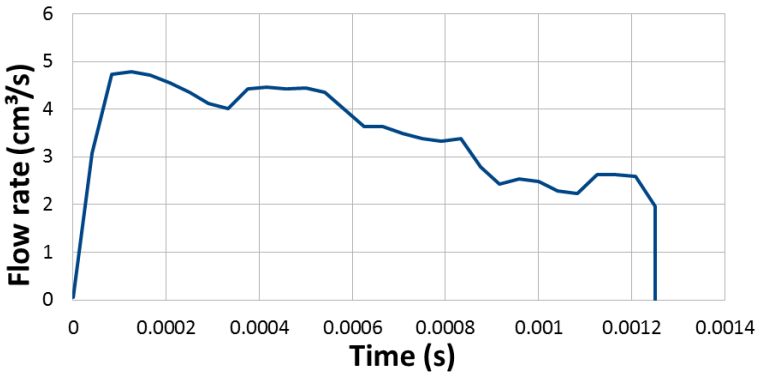


Figure 5.2: Injector flow rate profile initially used for *sprayFoam* spray simulations. Based on existing profile given in *aachenBomb* tutorial and giving correct average flow rate, according to experimental data [123]. The general form of the injection profile is similar to those used in other modelling studies, *e.g.* [40]

rate within 80 µs, before a gradual decline throughout the injection duration. A scaled version of this was employed, which gave the total fuel mass delivered as 3 mg, and is shown in Figure 5.2.

The initial droplet size distribution is set under `sizeDistribution` in *constant/sprayCloudProperties*. The Rosin-Rammler distribution [36] that was used in the tutorial case was retained, with altered constants. The Rosin-Rammler distribution is specified in terms of the volume fraction of droplets V_{RR} that is contained in all droplets below a diameter d, and is given by

$$V_{\mathrm{RR}} = 1 - \exp\left(-\left(\frac{d}{d_{\mathrm{RR}}}\right)^{n}\right). \tag{5.2}$$

The characteristic diameter d_{RR} was set to 14 µm and the exponent n was set to 3 (known as `d` and `n` in the code, respectively). According to Table 3.3 in [36], this results in a Sauter Mean Diameter (SMD) of around 10.3 µm for this distribution, which was deemed appropriate following the discussion in Section 4.1. The upper limit for the size distribution, `maxValue`, was set to 30 µm. No primary atomization model was included, meaning the spray droplets were introduced directly into the computational domain at the injector position, with the assigned size distribution. This reduced the complexity of the simulation and allowed for a closer focus on the evaporation processes.

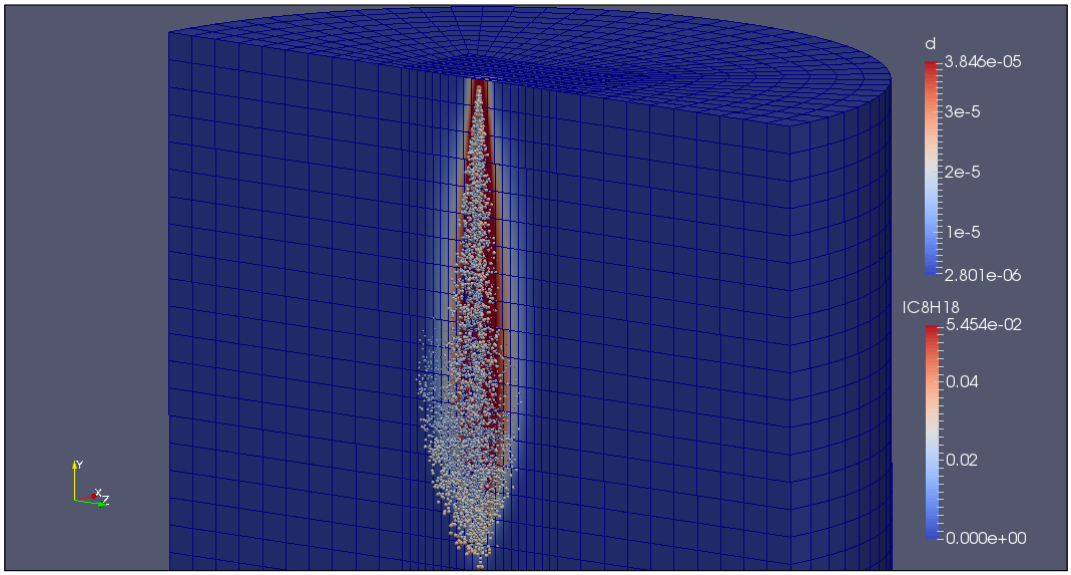


Figure 5.3: A slice view through the original cylinder mesh, showing the mesh on the surface. The Lagrangian parcels are shown, with size and colour scaled by droplet diameter. The surface of the cylinder (diameter 89 mm) shows the iso-octane mass fraction in the gas phase. The instance shown is 300 µs ASOI

Initially, the simulated spray was injected into a mesh representing a cylinder of height 150 mm and diameter 89 mm, along the cylinder axis, to correspond with the spray chamber dimensions (Chapter 3). This arrangement is shown in Figure 5.3. To reduce the computational time, the mesh was later reduced to a wedge shape (a sector prism) with an included angle of 30°, which is shown in Figure 5.4. Cyclic boundary conditions were imposed on the wedge faces. All of the results presented are from the wedge-shaped domain. Direct comparison between results from the two meshes was good, which gave confidence in the application of the wedge-shaped mesh. In the utilization of the wedge-shaped mesh, some spray parcels will be initiated outside of the wedge volume, since the parcels are introduced from a circular disc, of diameter given by `outerDiameter`, centred on the top vertex of the wedge, as shown by the origin in Figure 5.4. However, parcels that appear outside the domain are removed by *sprayFoam* immediately.

Shown in Table 5.1 are the gas phase fields to be solved by the *sprayFoam* solver, complete with their initial and boundary conditions. Since this simulation was intended to model a spray entering a quiescent chamber, the initial value of turbulent kinetic energy k should in theory be zero; however, a non-zero value for

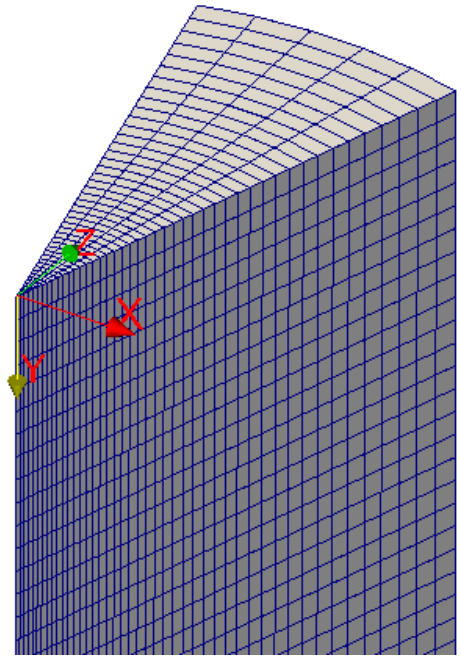


Figure 5.4: Wireframe representation of the 30° wedge-shaped mesh used for rapid spray simulations. The mesh shown here is graded with a factor of five in the radial direction to give a smaller cell size near the spray axis. The spray is injected at the origin, in the positive Y-direction

k was required to start the simulation. The initial condition for ε was adjusted accordingly, using the injector nozzle diameter as the turbulent length scale.

A droplet collision model was used, although the option inherited from the *aachenBomb* simulation has this turned off. Droplet collision allows coalescence, which in reality acts against the droplet size-reducing phenomena of droplet evaporation and droplet secondary break-up. The built-in options for this were the `ORourke` option (based on the work of O'Rourke [132]) and the `trajectory` option (based on the work of Nordin [133]). Both models compare pairs of Lagrangian spray parcels within a computational cell and allow them to collide if their size and velocity meet certain criteria. The Nordin model introduces additional criteria requiring that the parcels also be travelling on, or close to, intersecting trajectories, and that they cross paths at the same time or very close to the same time. The Nordin model was shown to remove the grid dependency of the O'Rourke model

Table 5.1: Gas phase (Eulerian phase) fields and their typical initial and boundary conditions for the modified GDI spray case

Field name	Description	Initial value	Boundary conditions
`alphat`	Turbulent thermal diffusivity(1)	0	Built-in wall function
`epsilon`	Turbulent dissipation rate	500 m^2/s^3(2)	Built-in wall function
`k`	Turbulent kinetic energy	1 m^2/s^2	Built-in wall function
`mut`	Turbulent dynamic viscosity(3)	0	Built-in wall function
`N2`	Nitrogen mass fraction	0.766	Zero gradient (solid wall)
`O2`	Oxygen mass fraction	0.234	Zero gradient (solid wall)
`p`	Pressure	101300 Pa	Zero gradient (solid wall)
`T`	Temperature	310 K	Zero gradient (adiabatic wall)
`U`	Velocity (3-D vector)	0	Zero (no slip and solid wall)
`Ydefault`	Gas species mass fraction (if unspecified)	0	Zero gradient (solid wall)

(1) Actually a 'dynamic' thermal diffusivity with units $[ML^{-1}T^{-1}]$, calculated by dividing turbulent dynamic viscosity by the turbulent Prandtl number (which here equals 1)
(2) Corresponding to length scale of 200 µm
(3) Calculated explicitly from the k–ε model

in [133] and therefore was used here, despite requiring a greater computational time. The two additional constants required by the `trajectory` model are `cSpace` and `cTime`; `cSpace` controls how relaxed is the requirement for intersecting trajectories and `cTime` controls how relaxed is the requirement for the parcels to reach the intersection point at the same time. Typically, the model assigns many droplets to each parcel, modelled to exist at the same point, but in reality they will be distributed over some finite volume in space. Therefore, some degree of relaxation

was thought sensible to allow a realistic degree of droplet collision, and so `cSpace` was set to unity but `cTime` was set to 0.1.

Initially, the default droplet temperature model in OpenFOAM was used, which solves Equation 2.26 with an implicit solution. Nusselt and Sherwood numbers are calculated using the Ranz-Marshall formulae (Equation 2.15), without correction for blowing (see Section 2.1.1). Most physical properties are evaluated in OpenFOAM using a different method from those adopted in Tables 2.1 and 2.2; in particular, the liquid heat capacity estimate was notably different for iso-octane by around 50%. Therefore, to calculate enthalpy of vaporization, the built-in enthalpy of vaporization function was selected within the evaporation model settings (in *constant/sprayCloudProperties*), rather than using the difference between the vapour and liquid enthalpies, so as to avoid errors associated with the iso-octane liquid heat capacity. This was acheived by setting the `enthalpyTransfer` option to `latentHeat`.

Individual Spalding mass transfer numbers, diffusion coefficients and Sherwood numbers were utilized to calculate the evaporation rate of each species, leading to a similar approach to Equation 2.45. In addition, there were two further discrepancies between the methods employed by OpenFOAM and those introduced in Chapter 2; the OpenFOAM methods have been retained for the simulations performed for this chapter. For Reynolds number calculations, OpenFOAM has utilized the density of the air/fuel reference mixture, rather than that of the ambient air, which can have a significant effect on the Reynolds number value. In OpenFOAM, the enthalpy difference between surface vapour and cell vapour ($h_\infty - h_\mathrm{s}$) has been utilized for the calculation of heat transfer and droplet temperature change, whereas, in Equation 2.4, the appropriate expression was shown to be $c_{p\mathrm{F}}(T_\infty - T_\mathrm{s})$, due to the use of reference properties for the vapour and gas phase.

The models that were implemented in OpenFOAM were created under a new Lagrangian library and solver, which used the existing OpenFOAM source code as a template. The process for creating these was developed from the process in [134].

5.2 Multi-Component Evaporation Model and Non-Ideal Fuel Behaviour

Binary multi-component droplet evaporation models that use both ideal and non-ideal representations of the liquid behaviour, as well as both the well-mixed and the unmixed (*i.e.* averaged properties) internal mixing models, were employed in OpenFOAM, as user-defined sub-models. These were implemented through the `phaseChangeModel` sub-model, which calculates the droplet evaporation rate and the internal composition evolution. An existing model called `liquidEvaporationBoil` was used, which utilized a well-mixed, ideal vapour-liquid equilibrium approach and directly references Zuo *et al.* [135]. This served as the template for the other three models: well-mixed and non-ideal; unmixed and ideal; and unmixed and non-ideal. The non-ideal formulation was implemented using the NRTL vapour-liquid equilibrium model, using the model constants for the iso-octane/ethanol mixture. Unmixed models were explored as a very simple multi-component fuel model with constant, averaged properties. Furthermore, from the results for the liquid diffusion-controlled approach in Section 4.5.1, it was expected that some non-ideal binary liquid mixtures may be more accurately described by a constant composition model, due to the slow rate of change of internal composition.

5.2.1 Sensitivity studies

A sweep of key computational parameters was performed, namely the mesh size and the level of parcel discretization (given as number of parcels per second that *sprayFoam* should inject), using the case of a 15% ethanol by volume spray. The initial conditions were a gas pressure of 1 atm, a gas temperature of 310 K and a liquid temperature of 320 K. The injection duration was 1.25 ms. The wedge-shaped mesh was used, with the well-mixed, non-ideal multi-component model for droplet evaporation. The liquid penetration history, mean spray diameter history and spray mass history were compared for a range of values. OpenFOAM, by default, calculates the liquid penetration using the 95% liquid mass threshold, which was adopted for this comparison.

The mesh sizes in the axial and radial direction of the domain were varied to examine the effect of the cell size on liquid penetration, liquid evaporation rate and droplet size. The minimum dimension used in the axial direction was 0.125 mm and the minimum dimension used in the radial direction was 0.0833 mm. Further mesh refinement was not attempted, to avoid any violation of the assumption that the Lagrangian phase remains dispersed. This can affect solution accuracy and stability. For example, it must be ensured that the total volume occupied by the droplets belonging to each parcel within a computational cell does not exceed the cell volume (or even the close packed sphere volume for this region), as noted by Dukowicz [101]. In addition, further inaccuracies will be introduced as the cell size approaches the size of the individual droplets, even if the liquid volume fraction is well-controlled. It is usually assumed that the gas phase properties are uniform or smoothly varying across the cell. In reality, the heat and mass transfer boundary layers and local flow disturbances around the droplets will disrupt this assumption. Sirignano noted that this would cause errors in the computed cell gas field values, as well as in the droplet evaporation rate and energy and momentum exchange, which utilize the cell gas field values [75].

For the radial direction, a sensitivity sweep was performed with the axial mesh size set to 1 mm. Two variants of mesh creation were used for the radial direction. Both a fixed size mesh and a linear graded mesh with a size factor of five were investigated. The graded mesh allowed a much finer mesh within the spray and coarser mesh near the chamber walls, where the flow velocity and velocity gradient would be much smaller and no spray parcels would reach, yet required similar or reduced computational time. For this mesh, the nominal radial mesh size was that at the halfway point of the wedge, between the axis and the chamber edge. With a grading factor of five, the mesh size on the spray axis was one-third of this and the mesh size at the chamber edge was five-thirds of this. The mesh size (both graded and fixed) varied from 1.5 mm to 0.25 mm. Simulations were performed both at cold conditions, with atmospheric pressure, and at hot gas conditions, with 6 bar pressure. For the cold simulations (representing early injection), the fixed size

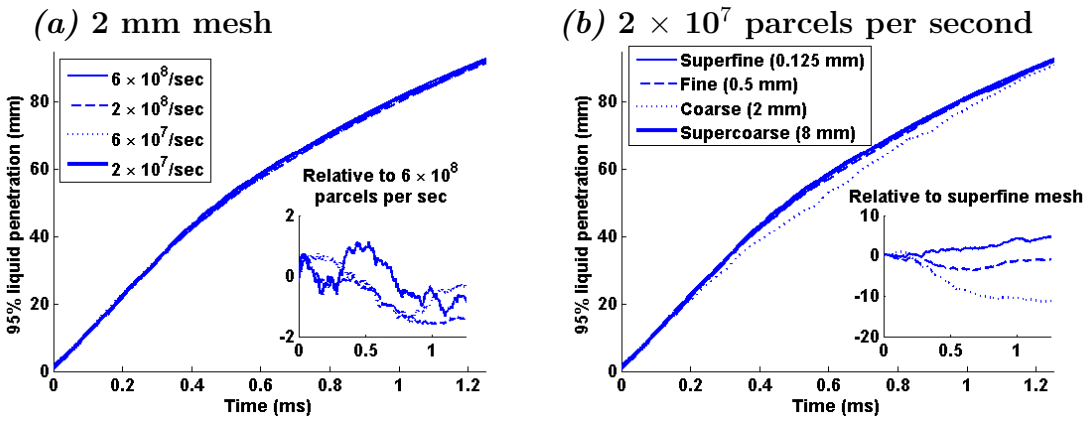


Figure 5.5: Liquid penetration of the 95% liquid mass threshold for various axial mesh sizes and choices of number of parcels per second. The inset plot shows the penetration difference (mm) between the finest mesh and parcel discretization, and the other results. The liquid penetration was least sensitive to the parcel discretization, with a penetration range between the chosen parcel discretizations of 1.3 mm (1.4%) at EOI (1.25 ms) and no clear trends or convergence as the number of parcels was increased. As the mesh was refined in the axial direction, the penetration first decreased before increasing again such that the very coarse mesh resulted in similar penetration lengths to the finer meshes. The largest penetration was predicted from the finest mesh

meshes of 0.5 mm and 0.25 mm, and the graded meshes of 1 mm down to 0.25 mm, each predicted a liquid penetration at EOI within 1% of each other, and a spray-wide SMD at EOI within 0.1 µm. For the hot simulations (representing late injection), there was a greater variation within the finest meshes, with the fixed 0.5 mm mesh resulting in a 5% penetration difference at EOI compared with the finest meshes.

The mesh size was altered in the axial direction, from a minimum of 0.125 mm to a maximum of 8 mm, with the radial mesh size fixed to a nominal 1 mm and a linear grading factor of five. The axial mesh size was constant throughout the computational domain. The number of parcels per second varied from 6×10^6 to 6×10^8.

Figure 5.5 shows the simulated liquid penetrations for the axial mesh and parcel discretization sensitivity studies. The total fuel masses, fuel liquid masses and fuel vapour masses are shown in Figure 5.6. The time variation of overall spray SMD and mean diameter is shown in Figure 5.7.

There was suitable agreement between the two finest meshes used and the two highest levels of parcel discretization to allow confidence in the use of either scheme.

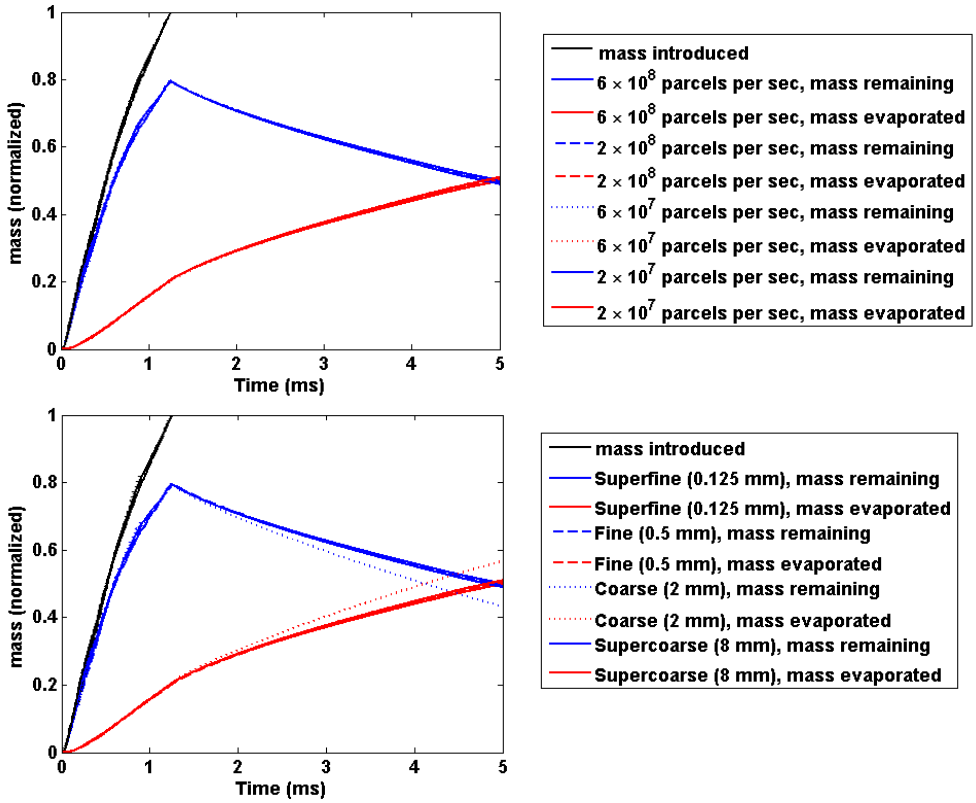


Figure 5.6: Shown are the injected mass (*black*), the mass remaining as liquid (*blue*) and the mass that has become fuel vapour (*red*), each normalized by the total fuel mass. The same ranges of axial mesh size and parcel discretization were used as in Figure 5.5. There was a slight variation in the injected mass with mesh size, attributed to how parcels are tracked between time steps as they are first added to the domain. Discrepancies in evaporated mass as the mesh refinement was varied were most apparent at the simulation end (5 ms), where the 2 mm mesh was greatly different from the other meshes. There was a 1.0% discrepancy in total fuel vapour mass at 5 ms between the results achieved with the two finest mesh sizes (0.125 mm and 0.5 mm). There was also a 1.0% discrepancy in total fuel vapour mass at 5 ms between the results achieved with the two finest parcel discretizations (6×10^8/sec and 2×10^8/sec)

Hence, the use of 2×10^8 parcels per second was adopted, with an axial mesh dimension of 0.5 mm and a graded radial mesh of nominal dimension of 0.5 mm.

5.2.2 CFD results

An investigation was carried out on the effect of the multi-component droplet evaporation model choice on the overall spray behaviour. The wedge-shaped mesh in Figure 5.4 was used throughout, after good comparisons were achieved between results from this mesh and from the larger cylinder. Non-ideal iso-octane/ethanol fuel mixtures were used to highlight differences between the models.

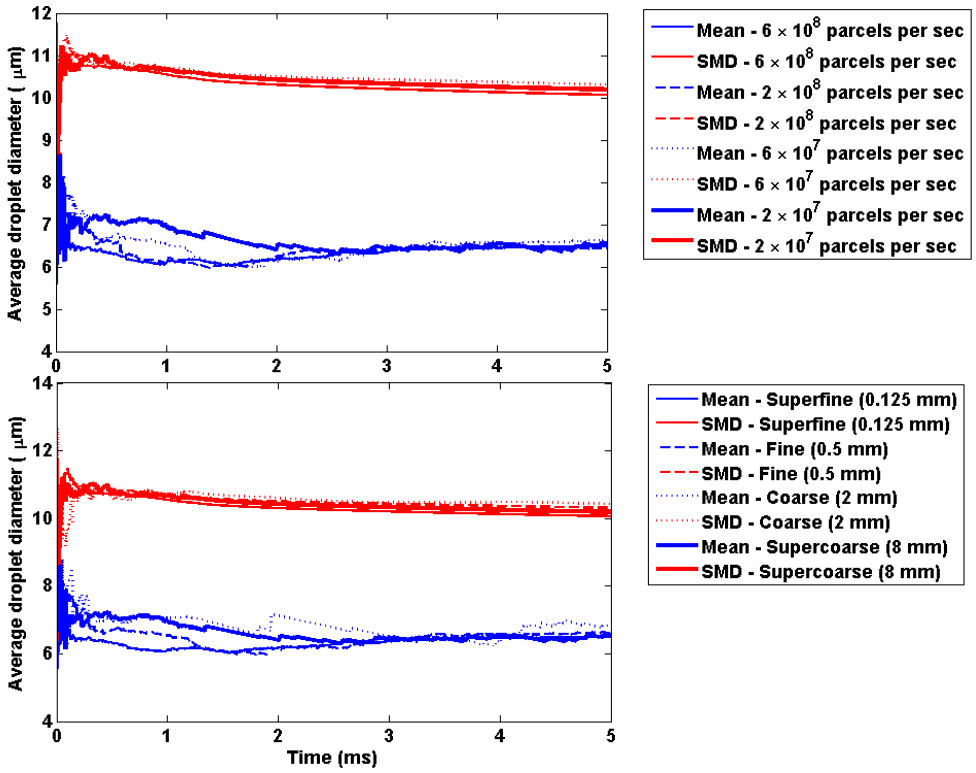


Figure 5.7: Mean diameters for the entire spray were created at each simulation time step by binning the droplets in all the instantaneously present parcels. The mean diameters across the spray show a smoother development over time as the number of parcels is increased or the axial mesh made finer. During each simulation, the SMD across the spray was relatively close to the prescribed value of 10.3 μm; however, the mean value fluctuated as the mesh or number of parcels was changed. Droplet sizes initially increase during the early stages of injection, as collision (and coalescence) and secondary break-up become balanced. After EOI, there is a gradual decrease in the droplet SMD but the mean diameter stops reducing after 3 ms for most of the runs, as evaporation is quite slow at these conditions

E50 Fuels

Initially, a simple equal parts mixture was chosen, with 50% ethanol by mass, which is 53.3% ethanol by volume and 28.7% ethanol by mole. The conditions investigated were a pressure of 1 atm, an initial gas temperature of 310 K and an initial fuel temperature of 320 K. The effects of varying the droplet evaporation model (in terms of ideal or non-ideal vapour-liquid equilibrium, and in terms of well-mixed or unmixed evaporation) are summarized in Figures 5.8, 5.9 and 5.10, which show spray mass histories, spray penetration and droplet size histories respectively.

The E50 blend (50% ethanol by mass) simulated here will tend to deplete of

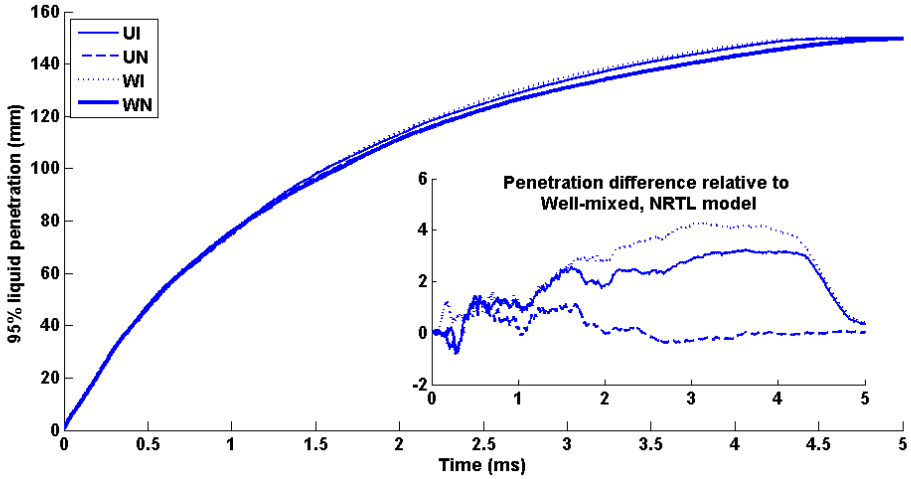


Figure 5.8: The 95% liquid penetration for the 50% ethanol by mass in iso-octane spray, with predictions from four evaporation models: UI - unmixed, ideal; UN - unmixed, NRTL; WI - well-mixed, ideal; and WN - well-mixed, NRTL. The WN model predicts a lower penetration rate. The inset plot shows the penetration difference, in mm, between the well-mixed, NRTL model and the other three models

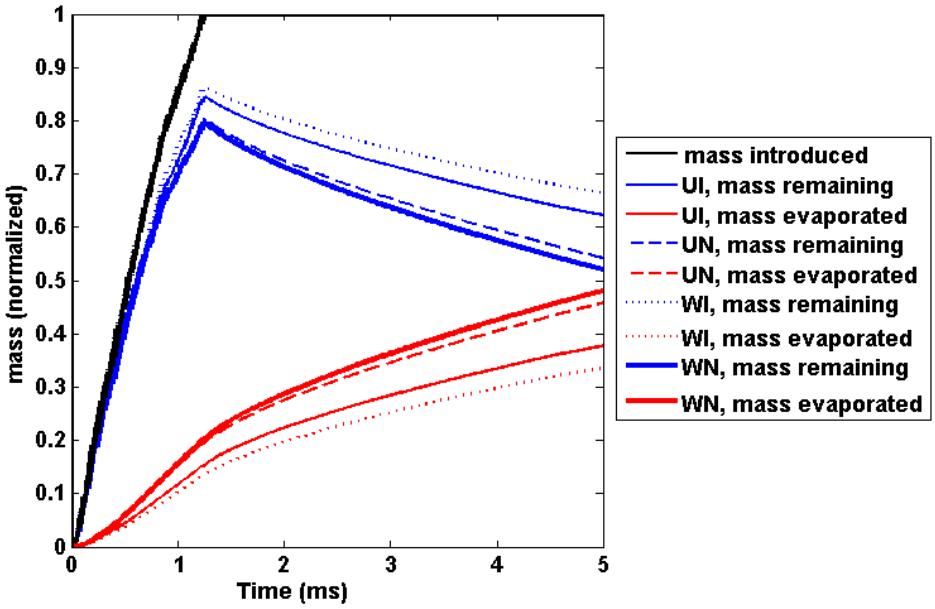


Figure 5.9: Comparison plot showing the total fuel mass introduced, the fuel mass remaining as liquid, and that which has become fuel vapour, for the four evaporation models, for the 50% ethanol by mass in iso-octane spray. The non-ideal models have caused a greater amount of fuel vaporization, in both the well-mixed and unmixed cases, due to the boost to vapour pressure caused by the non-ideality. The well-mixed model provided an increased evaporation rate under non-ideal conditions but a reduced evaporation rate under ideal conditions. This is attributable to the compromise between the increased vapour pressure, due to the continued presence of ethanol in the droplets, and the increased latent heat and subsequent reduced droplet temperature

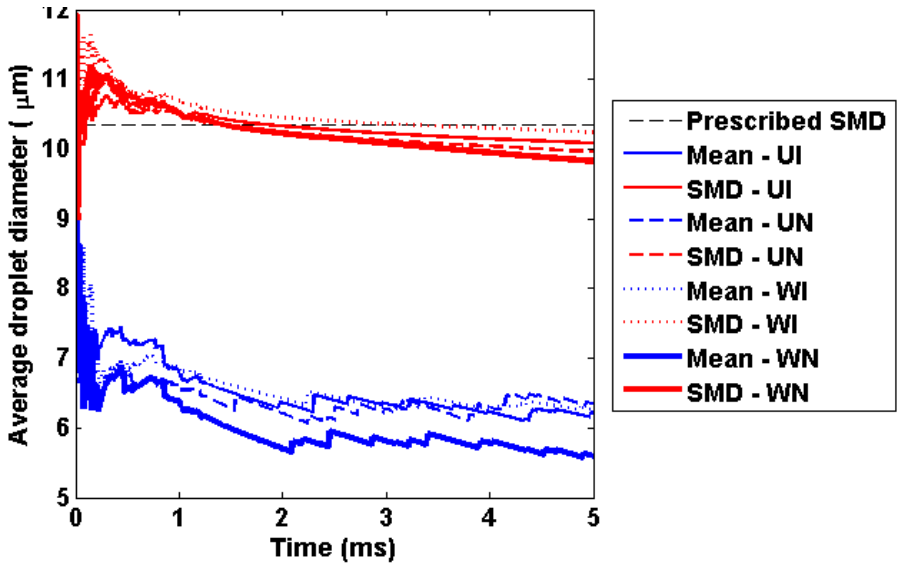


Figure 5.10: The history plots for mean diameter and SMD across the entire spray for the 50% ethanol by mass in iso-octane spray, for the various evaporation models. The size ordering of the SMD after EOI reflects the evaporated mass trends in Figure 5.9, in that models predicting a greater amount of vapour also predicted a smaller average droplet. There are jumps in the mean diameter results, which reflect the sudden changes to the droplet population caused by the secondary break-up and droplet coalescence sub-models. Up to half of the fuel mass is vaporized in 5 ms but the spray SMD has reduced by only around 10% in this period

iso-octane first, under the well-mixed assumption. This was confirmed in the spray simulations, as the droplet ethanol mass fraction tended to unity, although no parcel which remained at the end of the 5 ms simulation reached a pure ethanol composition. Some of the larger droplets were still close to equal parts mass at the end of the simulation, possibly due to their large size and slow overall evaporation rate.

From investigations of ethanol and iso-octane mixtures with single droplet simulations, presented in Section 4.3.1, the effect of the non-ideal behaviour is to increase the mixture volatility and to tend to increase evaporation rate. This is mirrored in the mass evaporated curves in Figure 5.9, where, in both unmixed and well-mixed cases, adding the non-ideal behaviour increased the evaporation rate. The subsequent evaporation rate of a pure ethanol droplet is expected to be slower than intermediate mixtures of iso-octane and ethanol. In the spray simulation, it was observed that the well-mixed, non-ideal model was in fact the fastest evaporating case. This appears to disagree with the single droplet findings

(see in particular the e75 fuel results in Figure 4.1*(f)*, where the unmixed model predicts a much shorter droplet lifetime). However, as noted previously, most of the droplets under the well-mixed assumption did not reach the pure ethanol state within the observed time frame, so many of the droplets in the spray would still experience a boosted volatility, due to the continued presence of a non-ideal mixture in the droplet, and a reduced enthalpy of vaporization. If the spray was observed for longer, it may be expected that the unmixed models would overtake the well-mixed models, in terms of evaporated mass.

With the non-ideal behaviour turned off, the unmixed droplet composition model within the spray simulation does predict a larger evaporation rate than the well-mixed droplet composition model. This is as expected, as the initial droplet mixture will be more volatile than the mixtures found later in the simulation (tending towards pure iso-octane) and there will be a roughly linear reduction in vapour pressure with the ideal behaviour as the more volatile component, ethanol, evaporates. The latent heat of the liquid will tend to reduce as the ethanol evaporates but it appears that this effect is not dominant.

E15 Fuels

Two conditions were selected for simulating fuel sprays of an E15 mixture (15% ethanol by volume, in iso-octane). The case conditions are summarized in Table 5.2. The late injection case corresponds to 'Spray G' of the Engine Combustion Network (ECN) [136]. 'Spray G' is a model gasoline spray condition that allows for collaborative study of SGDI sprays under stratified operating conditions. This standard experiment uses pure iso-octane in its definition.

The results from the early injection strategy case (see Table 5.2) are now presented and discussed. Four models were compared, which were given the following acronyms: UI - unmixed, ideal; UN - unmixed, NRTL; WI - well-mixed, ideal; and WN - well-mixed, NRTL. The spray liquid penetration is shown in Figure 5.11; the evolution of total liquid and vapour mass is shown in Figure 5.12 and the evolution of the spray mean diameters (accounting for every droplet in the spray)

Table 5.2: Initial conditions for the E15 fuel spray cases

Case name	Early injection	Late injection
Gas pressure	1.013 bar	6 bar
Gas initial temperature	310 K	573 K
Fuel initial temperature	320 K	363 K
Other parameters	Injection into air (oxygen/nitrogen mix), at 150 bar injection pressure, with 200 µm hole diameter and 3 mg of fuel injected	The initial gas composition was a mixture of nitrogen, carbon dioxide and water vapour, using the compositions from [136], to give the required initial gas density of 3.5 kg/m^3 at exactly 6 bar. The measured ECN Spray G injector flow rate profile was used. The injection pressure was 200 bar, the hole diameter was 175 µm and the injected mass was 1.25 mg (10 mg from the specification, shared between 8 holes)

is shown in Figure 5.13. A similar set of simulations was run at a reduced pressure of 0.5 bar (with the other conditions the same as in Table 5.2), to simulate a part load condition. The trends and findings from these were very similar to the 1 atm simulation and are not presented here.

Figures 5.11 to 5.13 demonstrate that the trends in the simulated fuel spray evaporation rate, as varying with chosen evaporation model, were similar to those expected from simple single droplet simulations. Here there was a closer agreement to the single droplet expectations than was apparent for the 50% ethanol by mass fuel mixture. Again, inclusion of the non-ideal vapour-liquid equilibrium increased the evaporation rate for both well-mixed and unmixed cases, which resulted in a reduced spray SMD and reduced spray penetration. The unmixed model caused a faster overall spray evaporation rate than the well-mixed model, for both the ideal

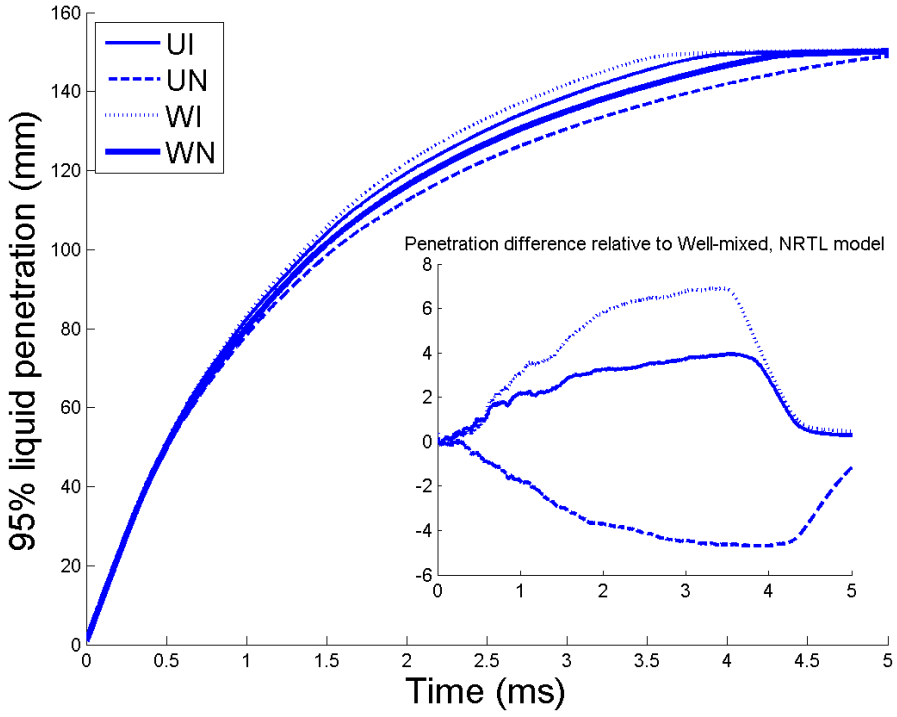


Figure 5.11: The 95% liquid penetration for the E15 spray at 1 atm pressure, with predictions from the four evaporation models. The ideal models predict the largest penetration rates. The inset plot shows the penetration difference, in mm, between the well-mixed, NRTL model and the other three models

and the non-ideal fuel model. The corresponding single droplet simulations at this set of conditions predicted the opposite trend. There will be a compromise in the effect that continued ethanol presence in the droplet has on evaporation rate, due to the additional volatility but increased enthalpy of vaporization. However, the outcome of these competing effects is sensitive to the temperature and pressure, as shown by the single droplet simulation results shown in Figure 4.1.

The local trends in droplet size for the early injection spray simulation, seen in Figure 5.14, compared well with those seen averaged across the whole spray (Figure 5.11) and with those expected from the single droplet simulation. It is clear that the cases with larger droplets throughout the spray correspond to a greater axial penetration, as expected. The droplet sizes towards the spray tip first reduce (as the smaller, older droplets in the recirculation zones start to be included in the SMD calculation), before becoming largest right at the spray tip. Interestingly, the cases which exhibited the largest droplets nearer the nozzle (*e.g.*

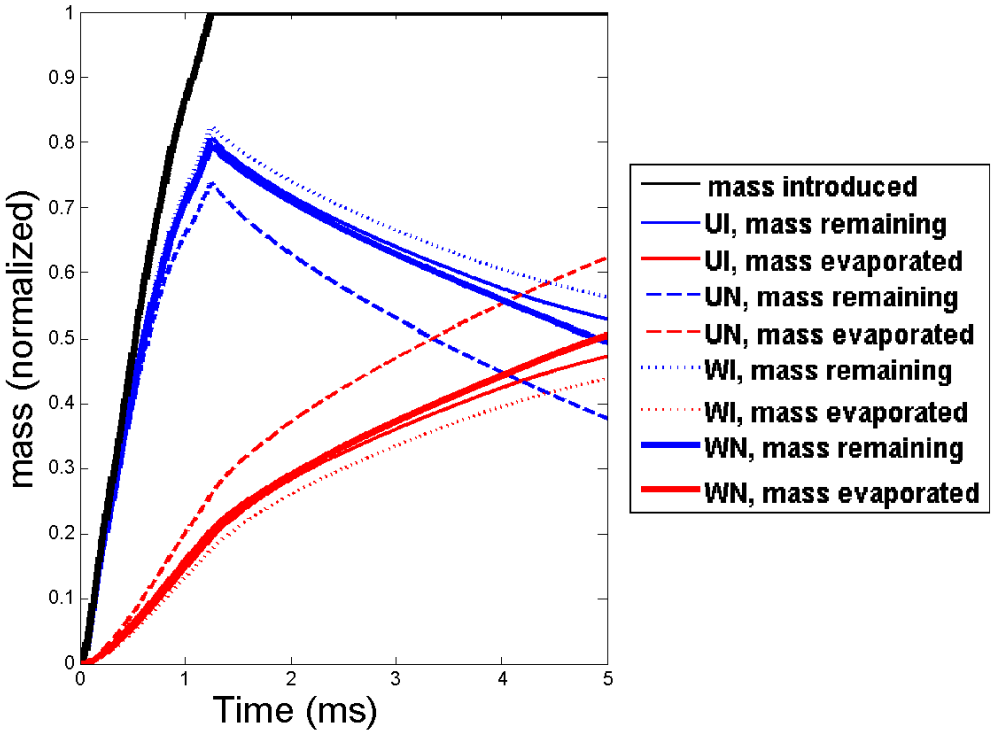


Figure 5.12: Comparison plot showing the total mass introduced, the mass remaining as liquid, and that which has become vapour, for the four evaporation models, for the E15 spray at 1 bar pressure. The trend of models giving larger evaporated mass corresponds well to the models giving the shorter liquid penetration in Figure 5.11

the well-mixed ideal model) resulted in the smallest droplets at the spray tip. The final bin contains only droplets travelling with the main jet, which have not been recirculated. These are exposed to the greatest aerodynamic forces, because they are not shielded by any other droplets ahead of them. It could be that droplets that are initially larger inside the spray jet (due to the choice of evaporation model) show an increased tendency to undergo secondary break-up at the spray tip, resulting in a smaller SMD. This break-up would most likely affect the largest droplets, which are disproportionately represented by the SMD calculation.

The results from the elevated temperature and pressure case, representing a late injection strategy for stratified combustion as specified by the 'Spray G' condition, are presented in Figures 5.15 to 5.17.

The non-ideal models ultimately show the smallest droplet sizes, reflecting the expectation that the non-ideal model would result in a faster evaporation

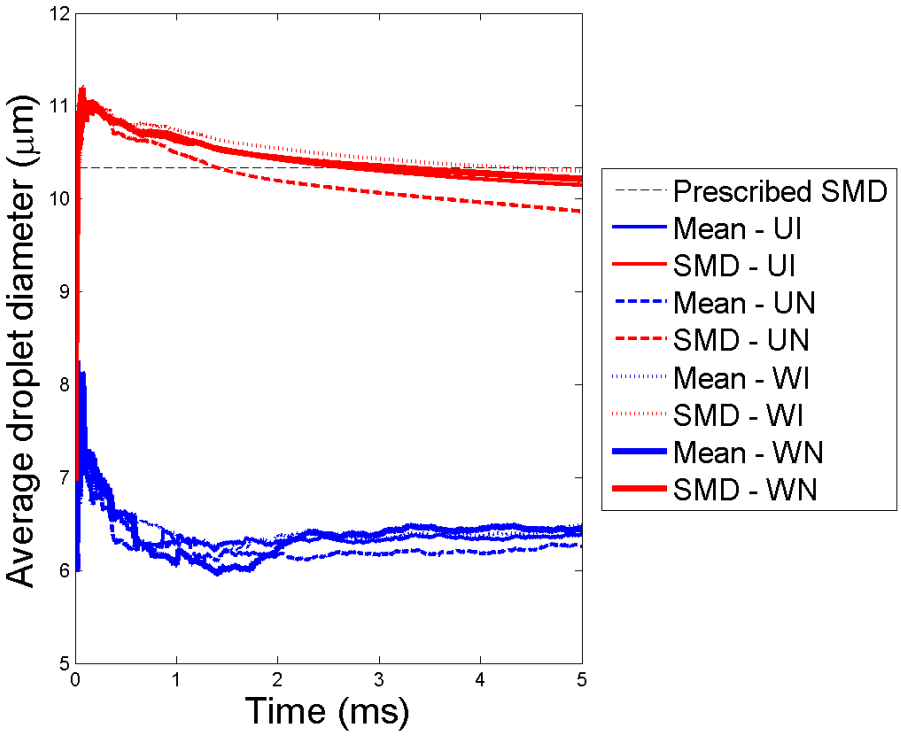


Figure 5.13: The history plots for mean diameter and SMD across the entire spray for the E15 spray at 1 bar pressure, for the various evaporation models. The size ordering of the SMD after EOI reflects the evaporated mass trends in Figure 5.12 though the mean diameter trend is less clear

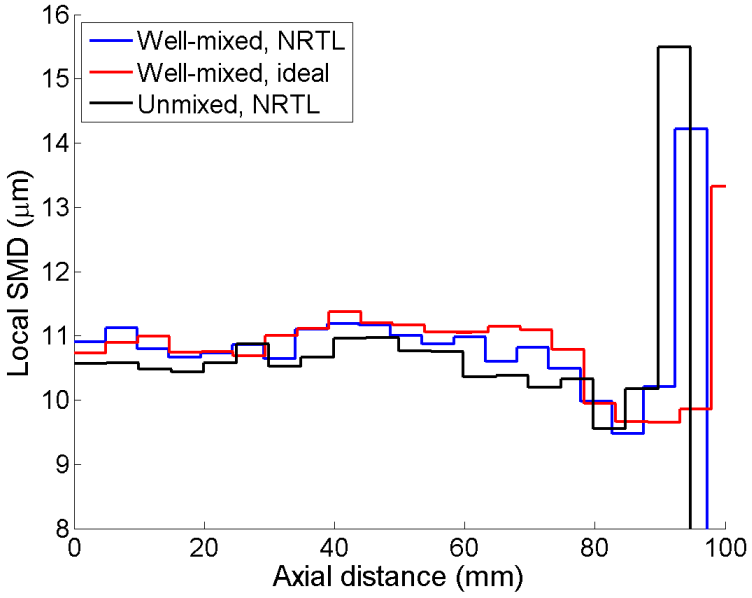


Figure 5.14: Plot of local SMD as a function of axial distance frpm the nozzle, for three of the multi-component droplet model cases, at EOI (1.25 ms). For each case, all of the spray droplets from each run have been binned in 20 bins, based on their axial position

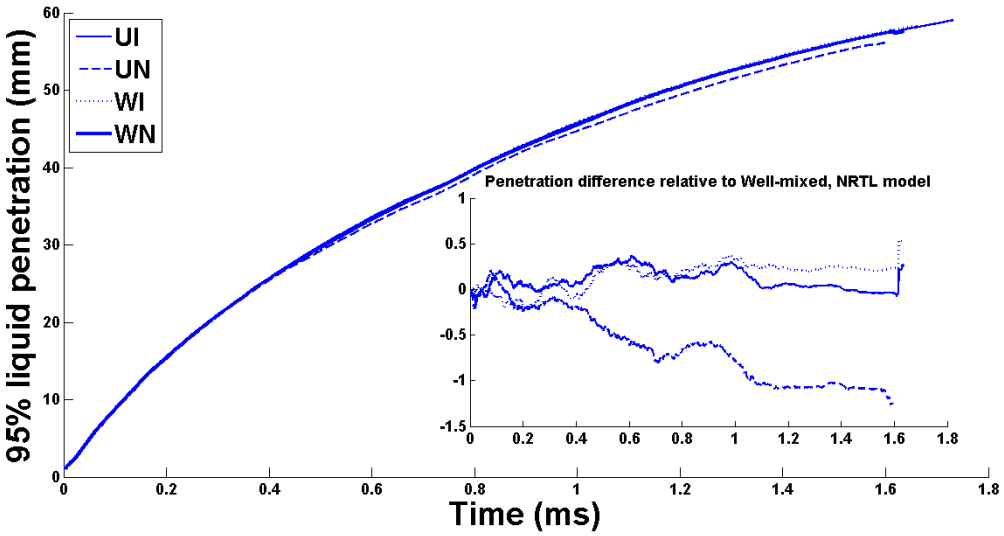


Figure 5.15: The 95% liquid penetration for the E15 spray at the 'Spray G' conditions, with predictions from the four evaporation models. The ideal models predict a slightly faster penetration rate, as for the colder simulations in Figure 5.11. The inset plot shows the penetration difference, in mm, between the well-mixed, NRTL model and the other three models

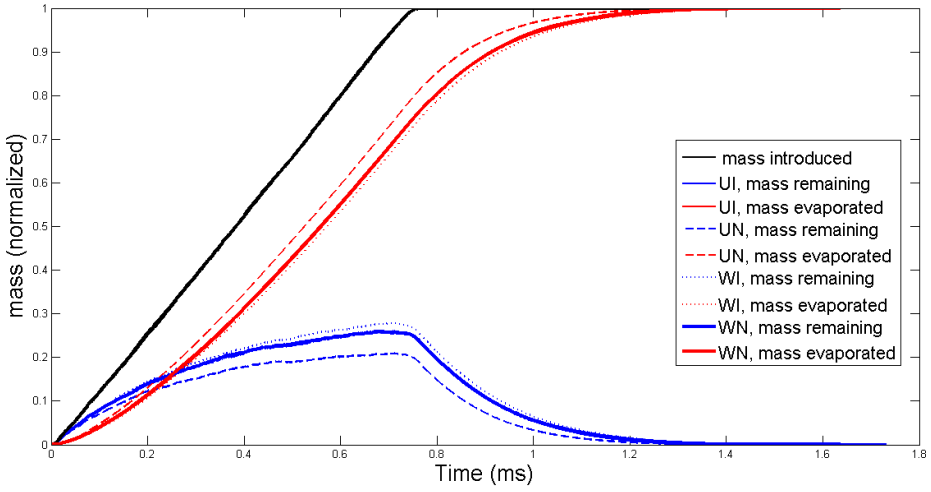


Figure 5.16: Comparison plot showing the total mass introduced, the mass remaining as liquid, and that which has become vapour, for the four evaporation models, for the E15 spray at the 'Spray G' conditions. The non-ideal models predict the greater spray evaporation rate, which corresponds well to the shorter liquid penetration in Figure 5.15

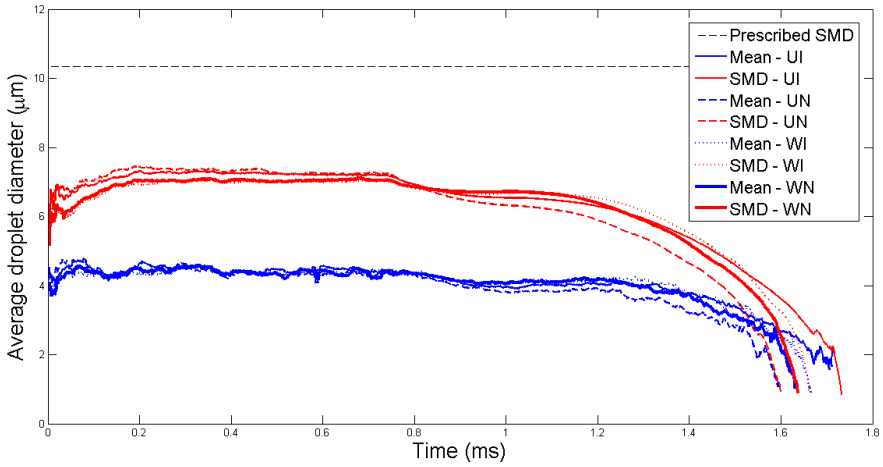


Figure 5.17: Average droplet diameters calculated for the four evaporation models, for the E15 spray at the 'Spray G' conditions

rate. Initially, however, the unmixed, non-ideal model showed the largest SMD. The well-mixed, non-ideal model also predicted a shorter overall lifetime than the unmixed, non-ideal model, which means that the retention of ethanol in the droplet in the unmixed case would slow down droplet evaporation at these higher pressure and temperature conditions, due to the higher enthalpy of vaporization of the liquid. The non-ideal model is assumed to give a more accurate representation of the fuel properties. The much greater gas phase cooling experienced by the higher gas pressure and temperature case (the 'Spray G' condition) will overcome the additional vapour pressure that the fuel mixture gains as a result of ethanol content. Overall, however, at the 'Spray G' conditions, the influence of the choice of evaporation model is reduced compared to the low temperature and pressure case, which is more relevant to homogeneous GDI operation or room temperature rig studies.

The unmixed, ideal model was slowest to vaporize all of the fuel but this was mainly due to a significant reduction in evaporation rate after EOI. The fuel penetration estimates broadly agreed with the average droplet diameter histories.

Multi-component fuel stratification

There was only minimal evidence of species stratification in the gas phase for the sprays simulated. For the unmixed models, the gas phase distribution of ethanol and iso-octane vapour were near identical in shape, due to the composition model.

For the well-mixed cases, there was a greater spatial variation between the two species at lower temperature and pressure conditions (possibly due to greater liquid penetration on account of the lower gas density), with relatively more ethanol nearer to the nozzle than near the spray tip. The iso-octane was more evenly distributed with respect to distance from the nozzle. This is due to the preferential evaporation of ethanol earlier in the lifetime of the droplets.

5.3 Droplet Temperature Models

In OpenFOAM, the two-point temperature model presented in Equations 2.37 and 2.39 was implemented in order to investigate the effects of the non-uniform droplet temperature distribution on the whole spray, in comparison with the default uniform droplet temperature model. This model has been implemented previously in the KIVA-3V CFD code with additional modelling criteria that are not considered here [87, 88].

The implementation of the temperature model was achieved by creating new versions of the codes `thermoParcel` and `reactingParcel`. The code `thermoParcel` deals with the heat transfer and droplet temperature evolution, while the code `reactingParcel` deals with the droplet composition and evaporation rate. Both codes needed to be modified, since a new surface temperature variable was created, required to calculate quantities such as fuel vapour pressure and the vapour phase reference temperature for fuel vapour properties. The calculation for the interior temperature was changed slightly from that used for the uniform temperature (as per Equation 2.37) but was still updated implicitly. The surface temperature was updated implicitly, as for the MATLAB simulations, using an iterative procedure, during which the evaporation rate is calculated at the current surface temperature estimate. The code was changed to ensure that mass was only removed from the parcel once a converged value of surface temperature was attained. The number of iterations was limited to ensure that a lack of convergence of the surface temperature would not prevent the simulation from proceeding. Parcels for which the calculated surface temperature did not converge at a particular time step were recorded, in

Table 5.3: Initial conditions for the cases run for comparison of the lumped and two-zone droplet temperature models. The estimated single droplet lifetime discrepancies are included, defined as $(t_{\text{life, two-point}} - t_{\text{life, lumped}})/t_{\text{life, two-point}}$

Case name	Gas pressure	Gas initial temperature	Fuel initial temperature	Ethanol content (% by volume)	Single droplet lifetime discrepancy
Room temperature rig	1 bar	293 K	293 K	5	-3.3
Early injection (cold fuel)	1 bar	453 K	293 K	5	6.3
Late injection (cold fuel)	6 bar	573 K	293 K	5	13.2
Late injection (hot fuel)	6 bar	453 K	393 K	20	-13.1

order to decide afterwards whether the residual achieved was, in fact, acceptable. The average surface temperature during the time step ($(T_s^{k+1} + T_s^k)/2$) was used to evaluate enthalpy source terms, as for the default lumped model. Here, T_s^k is the old surface temperature and T_s^{k+1} is the new surface temperature.

Four cases were identified that might be better modelled using a surface temperature model rather than a lumped (uniform) temperature model, for the binary mixture of iso-octane and ethanol. These were selected from the well-mixed simulations in Table 4.1, as conditions under which the uniform temperature droplet model predicted a large difference in lifetime compared with the heat equation droplet model. Due to the similarities found between the solutions of the heat equation model and those of the two-point temperature model, it was assumed that these cases could also effect a significant difference between the temperature models now implemented in OpenFOAM. The ethanol contents listed in Table 4.1 were utilized. The cases are summarized in Table 5.3. Simulations were run for 5 ms with all other parameters the same as described for the early injection strategy case in Section 5.2.2, if not specified here.

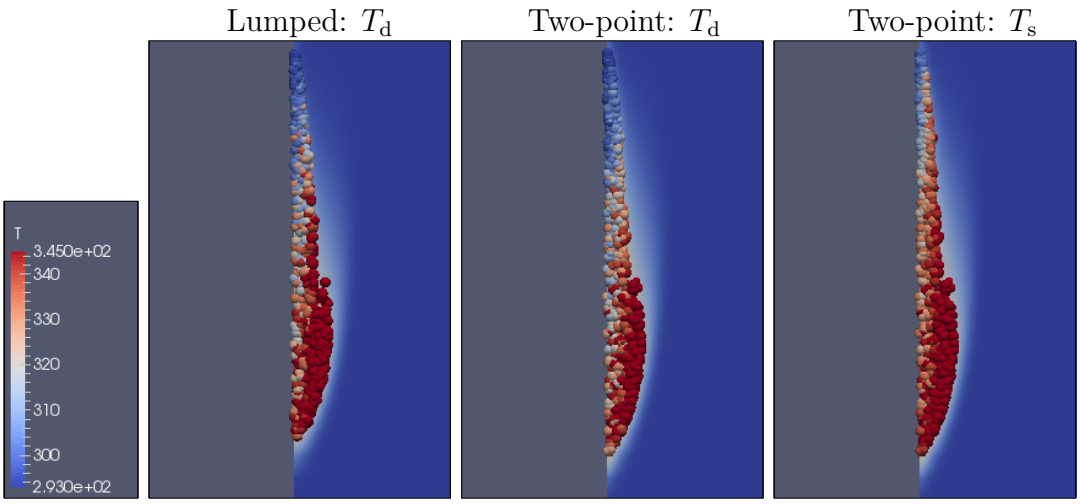


Figure 5.18: Spray parcels coloured by droplet temperature, for the case with gas pressure 6 bar, initial liquid temperature 293 K and initial gas temperature 573 K. In this case, the parcels will heat up towards around 380 K. The instant shown is 0.2 ms ASOI. The two-point temperature model shows a greater proportion of parcels with droplet surface temperature T_s above 345 K (an arbitrary threshold for illustration), whereas the interior temperature T_d is larger for more parcels in the lumped temperature model. This reflects the nature of the models, where the uniform temperature approximation will give a temperature that is somewhere between the actual interior temperature and actual surface temperature

The effects of the droplet temperature model can be seen in Figure 5.18, which shows the distribution of the different droplet temperature variables for the two models, using the case with late injection and cold fuel as an example.

The differences between the uniform temperature (lumped) model and the two-point temperature model are not as significant as those observed between the models examined in Section 5.2.2. Simulations of the cases identified in Table 5.3 were performed initially with a coupled solution and with the droplet break-up and droplet collision models turned on, as described in Section 5.1. In a coupled solution, the Lagrangian source terms are included in the solution of the gas phase equations, meaning that the gas phase temperature, composition and velocity are altered by the presence of the evaporating droplets.

The mean droplet diameter histories for each of the cases are presented in Figures 5.19 and 5.23. It was expected that simulations that resulted in an overall smaller droplet diameter average throughout the simulation would also lead to a reduced liquid penetration and would be accompanied by a faster spray evaporation

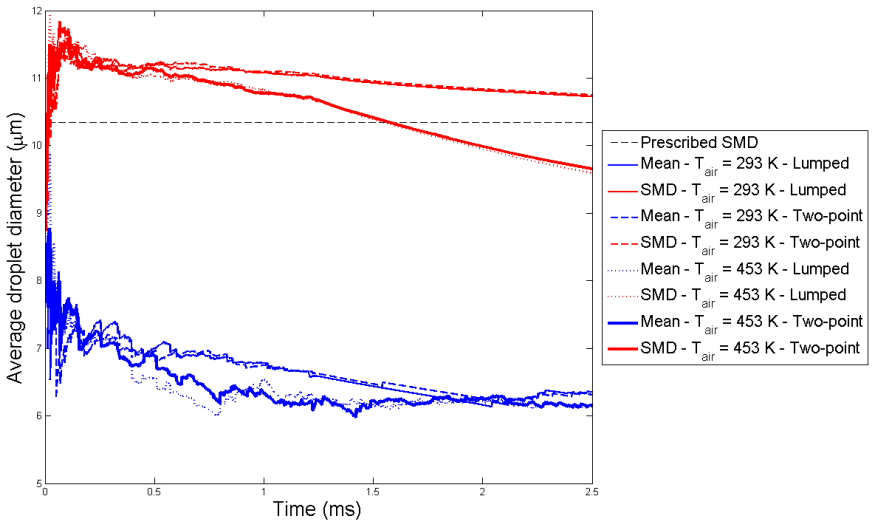


Figure 5.19: The history plots for spray mean diameter and SMD for temperature model comparison simulations, showing the two cases at 1 bar from Table 5.3. The modelling of gas phase coupling, droplet break-up and droplet collision was turned on

rate, as found with the results in Section 5.2.2. However, these trends were not shown as clearly with the droplet temperature model comparison simulations, and further investigation was deemed necessary.

The case with both initial gas and initial fuel temperature set to 293 K behaved in a similar fashion to the corresponding single droplet simulation, when gas phase coupling, droplet break-up and droplet collision were all included. It was expected that the droplets would begin to cool once they were deposited into the gas phase, and that the two-point droplet temperature model would allow the droplet surface to cool more rapidly, as discussed in Section 4.4. Thus, the two-point model would predict, on a droplet level, a slower evaporation rate. This is reflected in Figures 5.19 to 5.21, where this model shows a larger mean spray droplet diameter and spray SMD and a slower rate of vapour creation. Additionally, this caused an increased spray penetration, as to be expected from a spray consisting of droplets of a larger average size. In the early injection stages, up to 0.2 ms ASOI, the lumped model actually predicts the larger average droplet size, although the vapour mass is always larger with this model. This reflects the presence of other modelled spray processes which compete with the droplet temperature model to control the evolution of

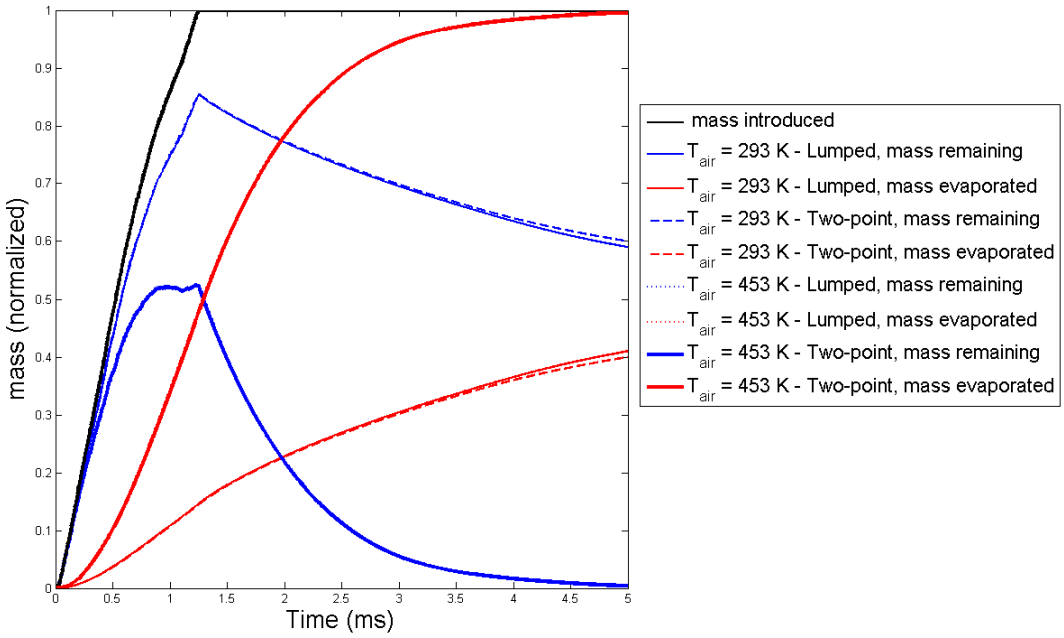


Figure 5.20: The history plots showing the total mass introduced, the mass remaining as liquid, and that which has become vapour for the two cases at 1 bar from Table 5.3. The modelling of gas phase coupling, droplet break-up and droplet collision was turned on

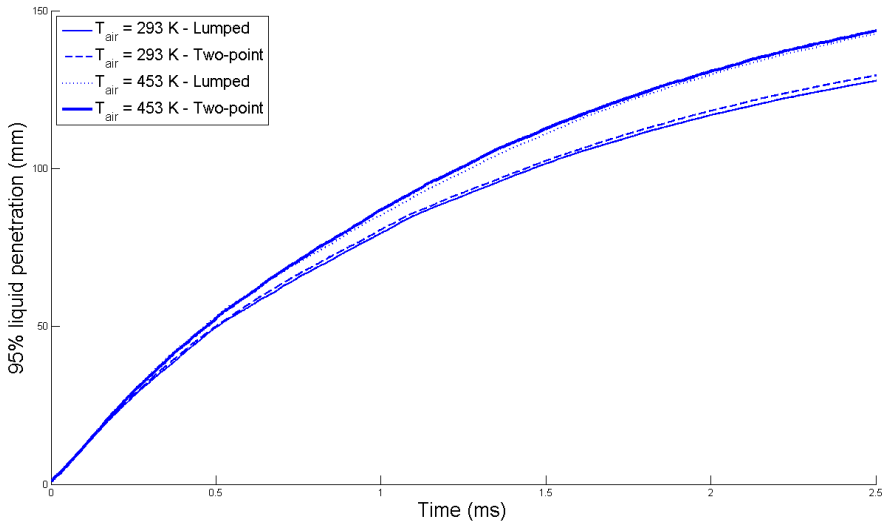


Figure 5.21: The spray penetration of the two cases at 1 bar from Table 5.3, using the 95% liquid mass threshold. The modelling of gas phase coupling, droplet break-up and droplet collision was turned on

droplet size. The actual quantitative difference in vaporization rate is low with this case, although there is a liquid penetration difference of around 1.5%.

With the lumped droplet temperature model, the maximum gas phase cooling at EOI was 15.4 K, and 15.3 K for the two-point model. The gas temperatures along the spray axis in the spray near-nozzle region were typically cooler for the two-point model at EOI and were cooler throughout the spray at earlier times. This seems to agree with the expectation that the choice of temperature model would not affect the amount of steady state cooling, but that the parcels created by the two-point model, with a colder surface temperature, would lead to a quicker removal of heat from the gas phase, due to the higher temperature difference between gas and droplet surface.

For the case shown in Figures 5.19 to 5.21, where the initial gas temperature was hotter at 453 K, it was expected that the two-point model would allow the droplets to heat up more quickly. This in turn would cause the droplets to evaporate more quickly. The droplet size predictions seen early in the spray (0–0.4 ms) follow this expected trend; however, after 0.4 ms, the lumped model simulation shows the smaller average droplet sizes of the two models. This is reflected in the slightly reduced liquid penetration observed in the lumped model case. The overall fuel vaporization rates achieved from the two models are very similar. The amount of fuel vaporized is slightly greater with the two-point model, perhaps due to the initial period where the spray results seem to follow the trend expected from the single droplet results.

The maximum gas phase cooling was much greater at the hotter initial gas temperature of 453 K: around 150 K at EOI. However, there was again very little difference in this steady state cooling between the two droplet temperature models. Along the spray axis, there was no consistent difference between the two models in terms of gas phase temperature. Due to the large overall degree of cooling, the droplets in the whole spray simulation do not undergo such a large transient temperature change as in the single droplet case (where the ambient temperature is fixed). For this case there is a 30 K droplet temperature change in the single droplet simulation and approximately a 15 K change in the CFD simulation.

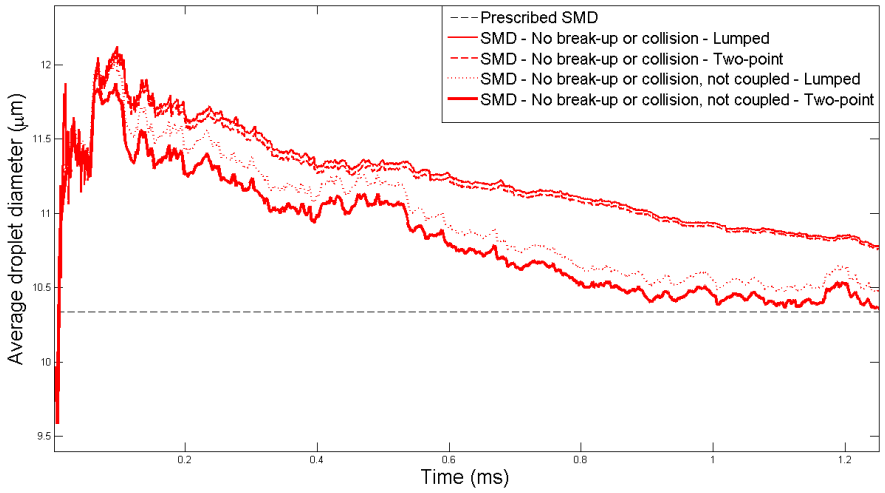


Figure 5.22: Spray SMD histories, across the entire spray, for the 1 bar spray with initial fuel temperature of 293 K and initial gas temperature of 453 K, for both the lumped and two-point temperature models. Two additional cases are shown here as indicated in the legend: one where all droplet collisions and droplet break-up are inhibited and one where additionally the coupling between the gas phase and the liquid phase is inhibited. The period shown is the entire injection duration

One of the cases was re-run with two further model configurations, testing both the uniform temperature model and the two-point model, to investigate the perceived lack of effect of the droplet temperature model. The case with an initial gas pressure of 1 bar and an initial gas temperature of 453 K was re-run firstly with models for droplet collisions (and hence the possibility of coalescence) and droplet break-up turned off; and secondly with the coupling between the Lagrangian and Eulerian phases turned off as well. In the latter case, this would cause the gas temperature to remain approximately constant, with the only changes in gas temperature arising from variations in local pressure and velocity.

Whilst the actual evaporation rate prediction and penetration prediction are heavily dependent on how and whether parcel collisions, secondary break-up and gas phase coupling are modelled, this approach was used to assess the impact of the two-point droplet temperature model in isolation. Without collisions and droplet break-up, the two-point droplet temperature model shows a consistently lower spray SMD throughout injection, which matches with a reduced penetration and faster rate of vaporization. In addition, when gas phase coupling is turned off, the gas

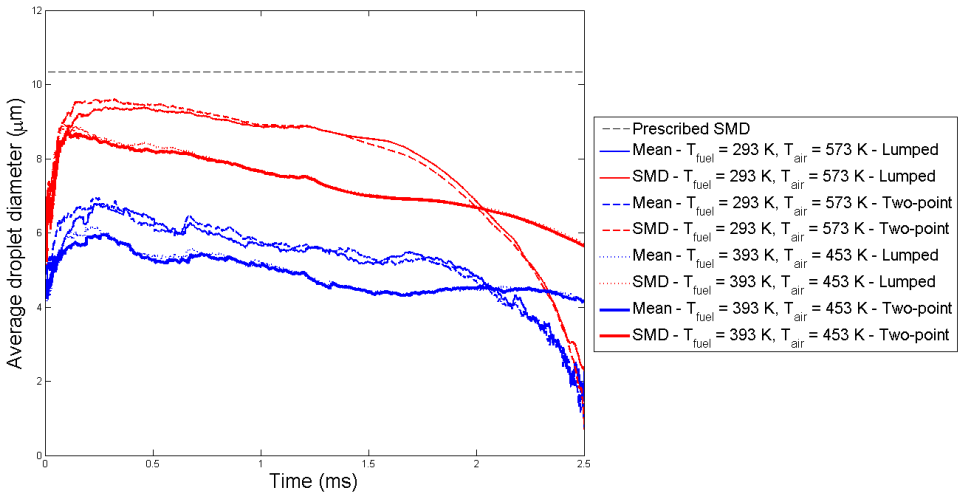


Figure 5.23: The history plots for spray mean diameter and SMD for temperature model comparison simulations, showing the two cases at 6 bar from Table 5.3. The modelling of gas phase coupling, droplet break-up and droplet collision was turned on

phase remains at roughly 453 K throughout, and the gap in spray SMD between the two modelling approaches increased. Thus, it can be concluded that, for these relatively low temperature and pressure cases (corresponding to homogeneous DISI operation), the effects of non-uniform droplet temperature distribution are masked by evaporative cooling of the gas phase and by other phenomena that contribute to the size change of the spray droplets, at the spray scale.

The results from the cases that were run at a gas pressure of 6 bar are shown in Figures 5.23 to 5.25. For the case where the initial liquid temperature was 293 K and the initial gas temperature was 573 K, it was expected from the single droplet modelling that the two-point temperature model would predict a faster droplet surface heat up, leading to a faster evaporation rate. Conversely, in the other case tested, with a high initial liquid temperature of 393 K and lower ambient temperature of 453 K, the droplets will first cool once injected, and the two-point temperature model is expected to predict a faster droplet surface temperature reduction and, hence, evaporation rate in this transient period.

In both cases, the evaporated mass followed the expected trends described, as seen in Figure 5.24, showing a slightly larger discrepancy between the two droplet temperature modelling approaches than was seen in the comparison for the cases at

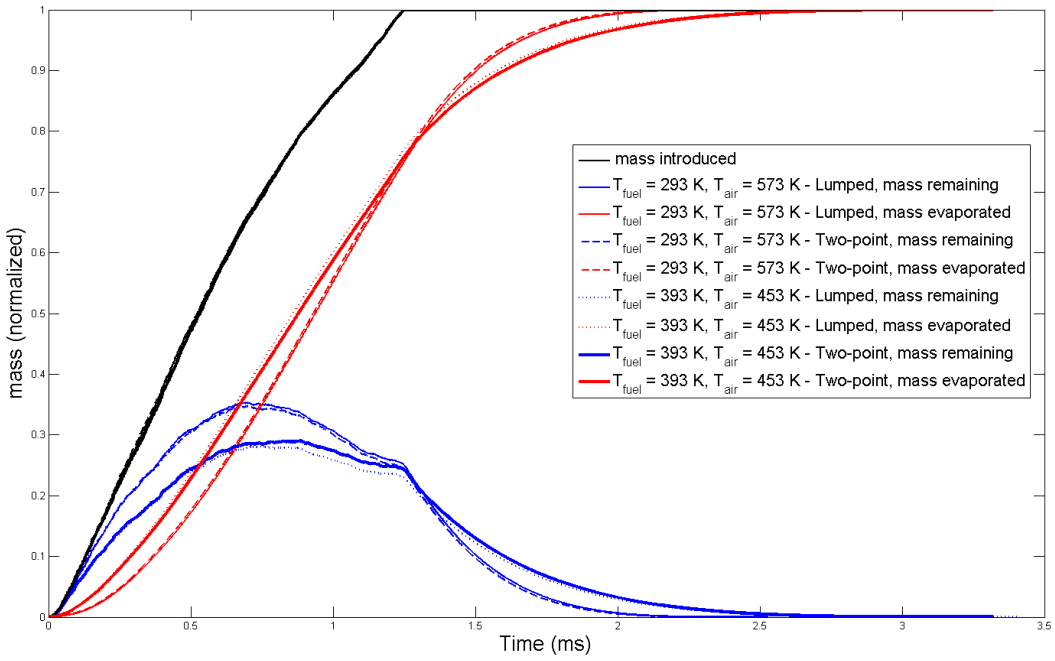


Figure 5.24: The history plots showing the total mass introduced, the mass remaining as liquid, and that which has become vapour for the two cases at 6 bar from Table 5.3. The modelling of gas phase coupling, droplet break-up and droplet collision was turned on

1 bar. There was a 1.5% discrepancy in evaporated mass, as a proportion of total injected mass, for the 393 K initial liquid temperature case at EOI.

However, the average droplet sizes for these cases did not always reflect these trends, with the the 393 K initial liquid temperature case consistently showing a larger mean diameter and SMD for the uniform temperature model, despite this model also showing the faster evaporation rate. This is again ascribed to the other phenomena that were modelled, *i.e.* the droplet collisions and break-up. The spray penetration rates in Figure 5.25 follow the observed average droplet size trends as expected.

Once again, for both of the cases run at 6 bar gas pressure (late injection), the maximum observed gas phase cooling was similar for both the lumped droplet temperature model and the two-point droplet temeprature model; within 2 K for each. For the cold fuel case, the gas temperatures along the spray axis were typically around 5–10 K higher for the two-point droplet temperature model, reflecting the higher droplet surface temperature. For the hot fuel injection case,

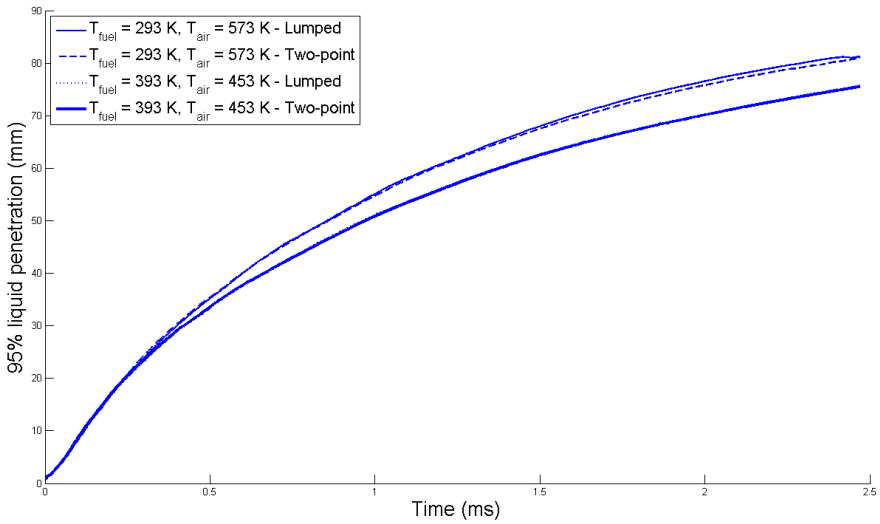


Figure 5.25: The spray penetration of the two cases at 6 bar from Table 5.3, using the 95% liquid mass threshold. The modelling of gas phase coupling, droplet break-up and droplet collision was turned on

this model predicted around a 5 K lower gas temperature along the spray axis, again reflecting the droplet surface temperatures. In both cases, any discrepancies in gas temperature between the two droplet temperature models reduced towards EOI and towards the spray tip.

Average droplet surface temperatures are shown in Figure 5.26 for the late injection, hot fuel case. As predicted and borne out by the fuel mass history, the two-point droplet temperature predicts a more rapid reduction in droplet surface temperature than the uniform temperature model. This discrepancy in average droplet surface temperature soon reduces to within 1 K by an axial penetration of around 15 mm, which is consistent with the observation, for single droplets, namely that the droplet temperature model is most relevant during the transient temperature phase. Similar behaviour was observed for the other cases that were tested.

5.4 Summary

This chapter has presented the development of models for droplet evaporation processes in the context of a Lagrangian Particle Tracking spray CFD solver. Simulations of a simple single hole gasoline spray, at realistic DISI engine and

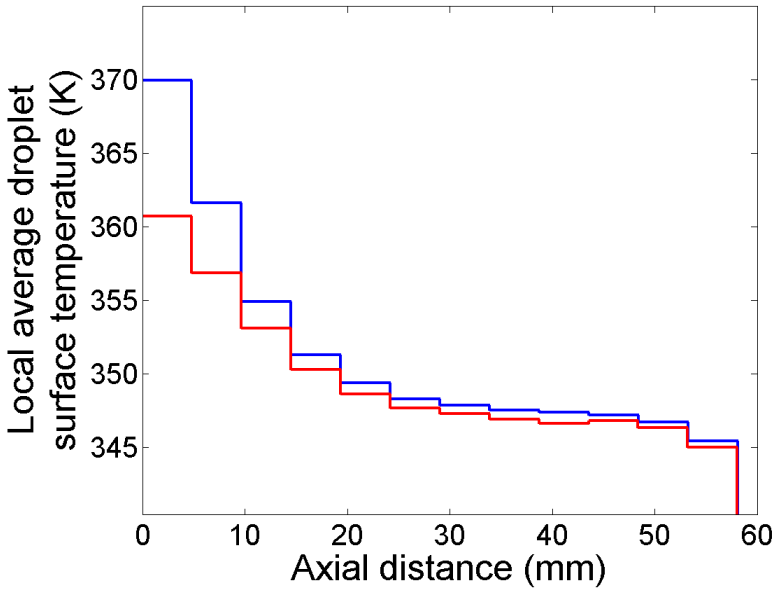


Figure 5.26: Plot of local average droplet surface temperature as a function of axial distance, for the case with 6 bar initial gas pressure, 453 K initial gas temperature and 393 K initial fuel temperature, for both droplet temperature models, at EOI. For each model, all of the spray droplets from each case run have been binned in 20 bins based on their axial position to calculate a mean value

spray conditions, were performed using the OpenFOAM solver *sprayFoam*, with user-defined sub-models. The aim was to incorporate models introduced and investigated in Chapters 2 and 4 into a real spray simulation. This would allow the study of these models and their effect on spray evaporation, combined with other physical effects such as gas phase cooling (or heating), droplet collision and secondary break-up that occur concurrently. Specifically, non-ideal multi-component models and non-uniform droplet temperature models were introduced, and their effects on spray penetration, vaporization rate and droplet size were examined in comparison to the simpler, existing models.

It was found that inclusion of the non-ideal behaviour of the simplest, binary multi-component mixture of iso-octane and ethanol made a significant difference to the overall spray evaporation rate, spray liquid penetration and the SMD across the entire spray, at both low temperature and low pressure rig conditions, and at higher temperature and pressure engine conditions. Since it is known that the real liquids exhibit this non-ideal behaviour, it was deemed necessary to

include this in simulations of non-ideal mixtures, *e.g.* gasoline mixtures containing ethanol or methanol. The differences between well-mixed and unmixed liquid component models were also explored, as these are the limits to the behaviour of multi-component evaporating mixtures. The unmixed model is typically only appropriate at conditions where the evaporation rate is very fast, which may be achievable with very late injection in a DISI engine (in the compression stroke). However, due to the low mixing ability of the non-ideal mixtures, as explored in Section 4.5, this may be an appropriate model for some non-ideal fuel evaporation at lower ambient temperatures. There was some variation in the results for liquid penetration, evaporation rate and droplet size between the well-mixed and unmixed non-ideal simulations, particularly for the E15 fuel at the low temperature and atmospheric pressure condition. Therefore, it is important to understand whether the actual state of the in-droplet composition distribution (and particularly the surface composition) is suitably approximated by the well-mixed model, perhaps through the use of detailed single droplet calculations at the condition of interest, as was investigated in Chapter 4. The variations in evaporation rate caused by the inclusion of non-ideal vapour-liquid equilibrium, or between the well-mixed and unmixed models for droplet composition, were accompanied by expected variations in predicted spray penetration and droplet size. Specifically, the predicted variation of spray results across the four evaporation models were: for the E50 fuel at 1 bar gas pressure, liquid penetration within 4%, evaporated mass within 29%, SMD within 4%; for the E15 fuel at 1 bar gas pressure, liquid penetration within 7%, evaporated mass within 24%, SMD within 4%; for the E15 fuel at 6 bar gas pressure and 573 K gas temperature, liquid penetration within 1%, evaporated mass within 9%, SMD within 11%. These quantities are referred to the well-mixed, non-ideal model and reflect the maximum difference encountered during the 5 ms simulation.

A two-point droplet temperature model was implemented, which tracked the surface temperature as well as the droplet interior temperature, allowing the spray droplets to have a non-uniform temperature distribution. This was compared to the lumped (uniform temperature) model that is ordinarily used. The discrepancies

expected from the single droplet cases were not always clearly apparent, particularly at the low temperature cases relevant to an DISI engine early injection strategy, and, at some conditions, the opposite trend was shown. This was identified as a consequence of the reduced transient temperature change that the droplets undergo when there is also a change in the gas phase temperature and also a consequence of the simultaneous presence of droplet collision and break-up phenomena. Therefore, it is concluded that it is not particularly important to model the non-uniformity of temperature within the spray droplets, for the spray applications studied here. For comparison to single droplet experiments, it is still considered important to include non-uniform droplet temperature models in order to accurately model the evaporation process.

6 Spray Chamber Images and Analysis

The object of capturing fuel spray images in the spray chamber was to gather data on fuel spray structure, penetration and evaporation rate, for different fuels and under various conditions of interest. This would inform predictions of the practical spray behaviour in an engine. In addition, overall trends could be compared to those predicted from the single droplet simulations, to see how applicable such a simple model of a 'fuel spray' could be for predicting trends in in-cylinder fuel evaporation. Since the pressure is fixed to be atmospheric, different fuel injection modes (*i.e.* sub-cooled or superheated) were obtained by heating the fuel or changing its volatility.

In particular, a range of model gasoline blends containing 15% methanol by volume (M15 fuels) was tested. Experiments involving these fuels, as stated in Section 3.4, have resulted in unexpected and conflicting reports of spray performance and subsequent particulate matter measurements. These fuels were also tested in the optical engine.

6.1 Backlit Images

A typical raw, backlit spray image is shown in Figure 6.1. The fuel is sub-cooled, giving a spray structure with distinct, non-interacting spray plumes. This is the nominal injector orientation. The injector is oriented so that the three plumes furthest from the camera are obscured by those closest to the camera. Due to the discrete nature of the light source, the light background is not uniform in intensity. This necessitates a background subtraction, which will eliminate this

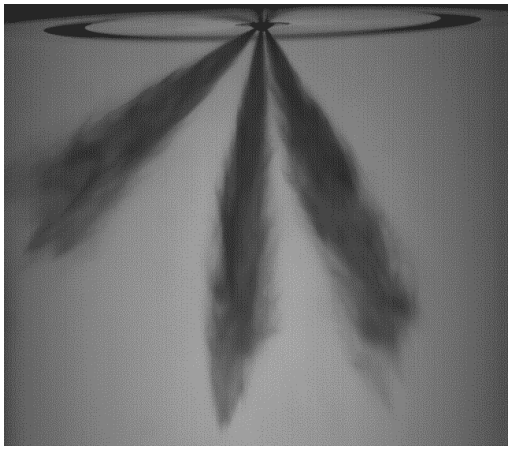


Figure 6.1: A fuel spray using trimethylbenzene as the fuel, with the air and fuel at room temperature. The exposure duration was 10 µs, which was longer than that used during subsequent experiments, due to the use of a lower LED power. The lens used had a 50 mm focal length and $f/1.2$ aperture size. The injector power lead is facing towards the camera and all subsequent injector positions are measured relative to this one

visually. However, it must be remembered that the contrast and amount of detail will be lower at the sides of the image, even after background subtraction, due to the darker background pixel values there.

Backlit images were captured of two fuels: pure iso-octane and the M15 Fuel A. The M15 fuels are fully described in Table 3.5 and Figure 3.16. The injector block was heated to a range of temperatures to give different fuel temperatures, which in turn would lead to different spray structures. In particular, once the fuel temperature exceeded its boiling point (the spray was injected into atmospheric pressure conditions), rapid changes in fuel structure were expected, as explained in Chapter 1 and as found in the literature [44]. There was a 30 minute dwell time between the injector block PRT reaching the desired temperature and the spray event, during which the measured temperature was held within 1–2 K of the set point by the heater controller described in Chapter 3. Ten injections were made at each temperature. For these batches of injections (sets of ten), it was verified that there was no systematic variation in calculated spray angle, spray evaporation rate, or spray penetration throughout the batch. This indicates that the sprayed fuel temperature was consistent. The second event from each set is shown for both fuels and a range of temperatures in Figures 6.2 and 6.3. The injector position for

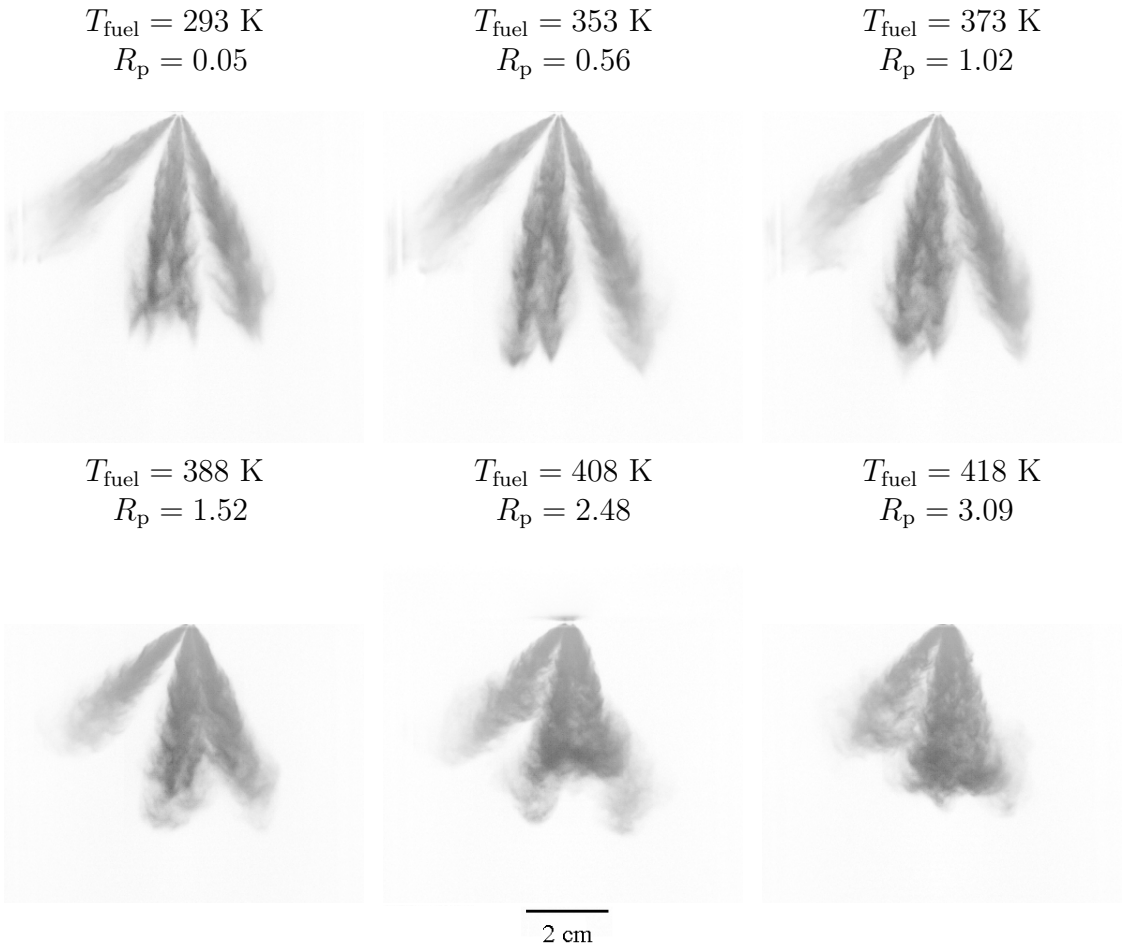


Figure 6.2: Spray images of iso-octane taken across the full range of fuel temperatures possible for this spray chamber. Each image was taken 1.11 ms ASOI using a shutter duration of 1.98 µs. The raw image was inverted before an inverted background image was subtracted. Above each image is shown the measured injector block temperature and the fuel saturation pressure ratio, as calculated in Equation 6.1

these images was slightly rotated from that in Figure 6.1. Each image is labelled with its associated fuel saturation pressure ratio, which is defined as the calculated saturation pressure at the fuel temperature divided by the pressure into which the fuel is injected. Using Equation 2.48, this may be written as

$$R_{\text{p}} = \frac{\sum_i \gamma_i(T_{\text{fuel}})\widetilde{X}_i p_{\text{vap}\,i}(T_{\text{fuel}})}{p_{\text{amb}}}. \tag{6.1}$$

This definition is the reciprocal of that used in [43, 44]. The ambient pressure in the spray chamber was assumed to be 1.0 bar and the fuel temperature was assumed to be equal to the injector block temperature measurement.

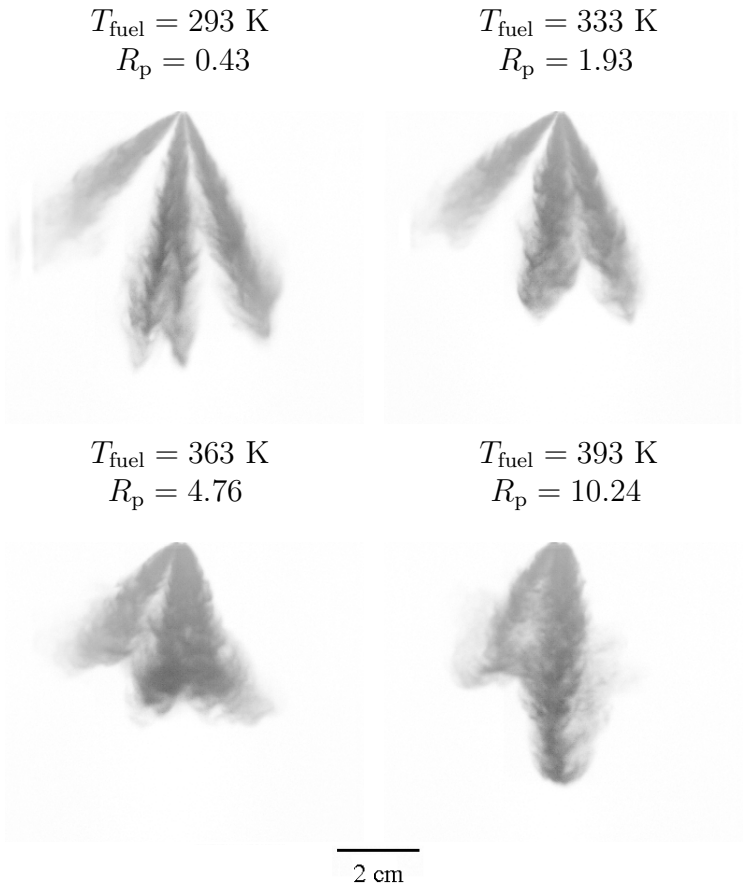


Figure 6.3: Spray images of Fuel A taken at four fuel temperatures. Each image was taken 1.11 ms ASOI using a shutter duration of 1.98 µs. The raw image was inverted before an inverted background image was subtracted. Above each image is shown the measured injector block temperature and the calculated saturation pressure ratio. As the temperature is increased, the central and right hand plume pairs are drawn together during injection, as typified by the loss of clear air between these plumes and movement and bending of the central plumes (2 and 5) towards the right, for $R_{\text{p}} = 1.93$

The fuel saturation pressure ratio R_{p} will describe whether a fuel is superheated and to what degree. When $R_{\text{p}} < 1$, the fuel is sub-cooled with respect to the atmosphere into which it is injected. In the sub-cooled regime, the exact value of R_{p} is expected to have little effect on the spray structure and a multi-hole spray is expected to retain a distinct plume structure. For higher values of R_{p} the fuel will be hotter, so there will be a faster evaporation rate.

If $R_{\text{p}} > 1$, then the fuel is said to be superheated and flash boiling occurs. At values slightly above 1, the spray structure is not expected to change greatly from sub-cooled as there will be only a small driving force for fuel boiling and a very

short time in which to achieve significant nucleation and growth of the vapour phase. However, as R_p is further increased there will be a greater degree of flash boiling, and individual plumes are expected to be drawn inwards, or collapse, as discussed in Section 1.3.1. It was found in [43, 44] that there was a threshold of the value of R_p beyond which the behaviour would alter again. This threshold corresponds to a value of $R_p = 3.3$. At values higher than this, the spray is expected to completely collapse, with no distinct plumes remaining, although the threshold value should depend on the injector design.

The most commonly used gasoline surrogate fuel, iso-octane, does not capture all of the flash boiling behaviour trends as, unlike gasoline, it has no light components. A similar result was found by [41]. Fuel A shows a wider range of behaviour as temperature is increased due to the inclusion of realistic lighter components.

With the sub-cooled sprays and superheated spray with R_p below 2, the spray retained its nominal structure and there was still significant liner impingement by plumes 1 and 6, which has implications for fuel film generation.

As superheat is increased, individual plumes can be seen to increase their plume angle, leading to intermingling of plumes close to the nozzle. This causes the opposite effect in the overall spray cone, *i.e.* a reducing (collapsing) spray angle. There is also evidence of larger spray tip vortex structures as superheat increases, which act to push droplets towards the spray centre. For Fuel A, penetration decreases past the $R_p = 3.3$ threshold suggested by Zeng *et al.* [43] but does increase again at $R_p = 10.24$. Even at this high temperature, the most laterally targeted plumes (plumes 1 and 6, with reference to Figure 3.1) have not fully joined the collapsed structure. The overall nominal spray angle at this temperature is very similar to that used in [43], but the plumes are fewer and irregularly spaced for this injector. Therefore, it would be expected that a greater degree of superheat would be required to draw together all of the plumes of this injector into a single jet. An image sequence for a superheated spray with $R_p = 2.48$ has been presented in Figure 6.4, which shows the beginning of the process of collapse of the left hand plumes (1 and 6) and their change in direction towards the spray centre.

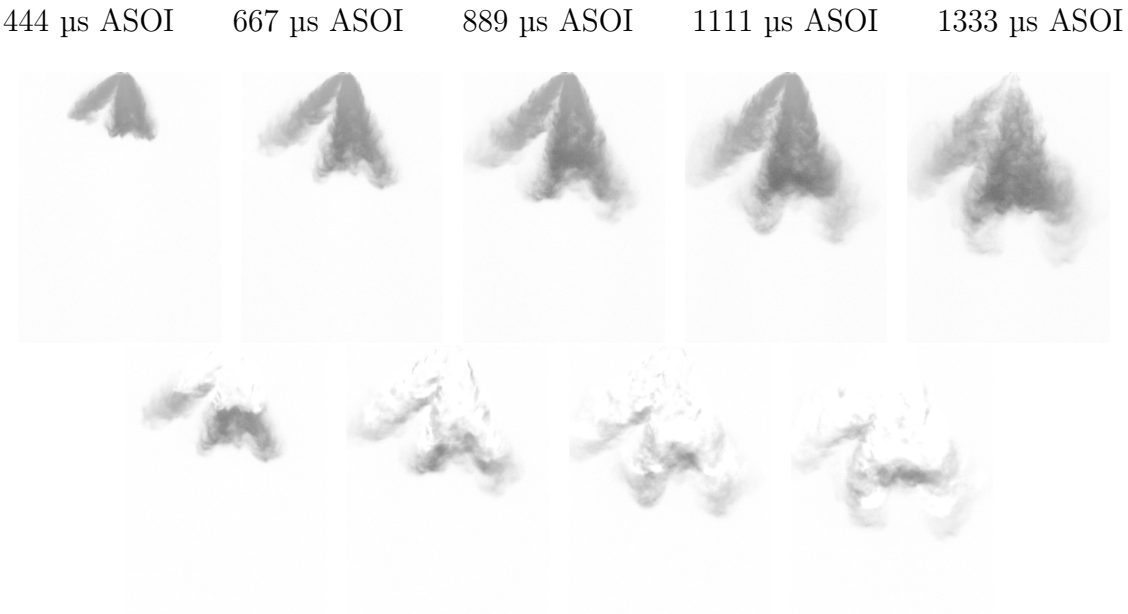


Figure 6.4: Evolution of a spray event, for pure iso-octane with fuel temperature 408 K and $R_p = 2.48$: the first row shows the background subtracted images and the second row shows the change between frames. The injection duration was 1.25 ms. The plumes on the right hand side have formed a continuous cone, due to early plume interaction. Some of the fuel from these plumes can be seen continuing in the original direction at 1111 µs ASOI and 1333 µs ASOI (possibly the fuel injected shortly after SOI), whereas some has been drawn into the centre (possibly later injected fuel). Between 889 µs ASOI and 1111 µs ASOI, there is a change in direction of the left hand plumes. It is expected that as superheat is increased, this action will occur earlier and to a greater degree, causing a complete collapse into a single jet

The images acquired of Fuel A sprays were averaged for each fuel temperature and subjected to a relevance index analysis. This follows the work of [137] in order to give a quantitative description of the similarity of two images. To compare two arrays, I_1 and I_2, of the same dimensions, representing two spray images, they are initially converted to column vectors V_1 and V_2. Then, the relevance index is calculated as

$$RI = \frac{V_1^{\mathrm{T}} V_2}{||V_1||\ ||V_2||}, \tag{6.2}$$

where $||\cdot||$ represents the 2-norm (the square root of the sum of the squares of the elements). This was used to compare individual images to the mean image at that time step. This gives a number between 0 and 1, where 1 will be achieved if both I_1 and I_2 are pixel-wise identical or scaled versions of each other. Typically, values greater than 0.9 are achieved if the sprays are similar. Since the images have

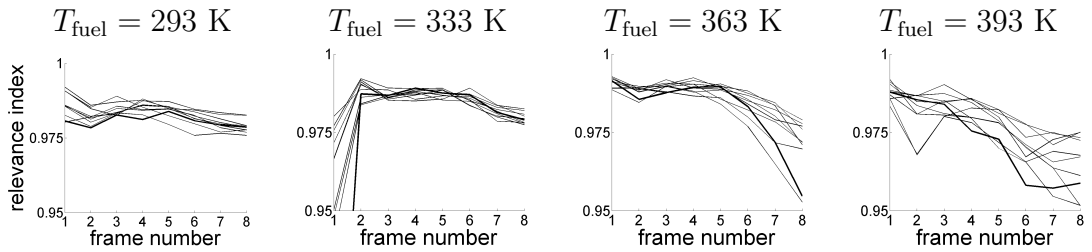


Figure 6.5: Relevance index variation for the backlit Fuel A images, at the four temperatures tested. The lines represent the relevance index values acquired by comparing the individual images with the mean image for that frame. The thicker line represents the first image acquired in the set. This first spray event does not show a consistently lower or higher relevance index value or visible variation across the investigated temperatures. This allows greater confidence in the experimental technique

been background subtracted, there are large areas of the two compared images that will be identical, *i.e.* with a pixel value of zero. However, this will not skew the relevance index towards a higher value, since the zero values will not contribute to the scalar products on the numerator or denominator of Equation 6.2.

In Figure 6.5, the relevance index value for individual images, compared to the mean image for each frame, is plotted for the first eight frames after the first visible fuel, for the four temperatures at which Fuel A was tested. There were ten images taken at each temperature.

At 333 K, the amount of fuel visible at the first frame was much smaller than at the other temperatures, hence there was much greater initial variation. As the degree of superheat is increased, the relevance index drops, particularly later in the spray lifetime, which reveals a greater variability in the flash boiling sprays observed here. In general, the spray results are consistent, with low variability around the mean image.

6.2 Mie Scattering Images

Fuel spray images were captured using the Mie scattering technique. This involved directing light from the LED array onto the spray at an angle of 90° to the imaging position. In comparison to the backlit images, a longer exposure time was necessary as the technique was reliant on the light reflected off the spray liquid and not just the obscuration of light by the spray. However, the images may contain more



Figure 6.6: A backlit image of a sub-cooled spray, with the fuel injector in the position that was then utilized for the Mie scattering images in this thesis. The image has undergone background subtraction. With reference to Figure 3.1, the plumes as visible in this image are numbered 6, 1, 5, 4, 2, 3 from left to right. With reference to Figure 6.1, the injector has been rotated 45° anti-clockwise, as viewed from above

quantitative information regarding the spray droplets, since the local light signal will be proportional to the total surface area of the spray droplets that are illuminated. There will be obscuration and multiple scattering events, which will affect the accuracy of the quantitative measurement.

The Mie scattering images were all captured with the injector in a rotated position, shown in Figure 6.6, in order to observe more of the spray plumes. This position was also a good compromise in terms of allowing as many of the spray plumes as possible to be illuminated fully from the side, to get an even illumination of the spray.

In this work, each spray was imaged for 50 frames at 4500 frames per second, which means that the final image is at 10.9 ms ASOI. At each temperature, 50 injections were performed to acquire a large enough sample of spray images. The injection duration was set to 2 ms on the LabVIEW interface and the injection pressure was 150 bar.

The methanol/gasoline blends Fuel A and Fuel B (see Table 3.5) were used to capture spray images using Mie scattering, using the injector position in Figure 6.6. Tests were performed at the fuel temperatures of 20°C, 60°C, 90°C, 105°C, 120°C and 135°C, giving the fuel saturation pressure ratios shown in Table 6.1. The

Table 6.1: Fuel saturation pressure ratios (p_{vap}/p_{amb}) for Fuel A and Fuel B for the spray chamber experiments, assuming an ambient pressure of 1.013 bar

Fuel temperature	Fuel A	Fuel B
20°C	0.43	0.44
60°C	1.93	1.94
90°C	4.76	4.73
105°C	7.09	7.02
120°C	10.24	10.12
135°C	14.40	14.20

two fuels have very similar volatilities (as represented by the saturation pressure ratio) throughout the range of fuel temperatures that are of interest to DISI engine operation.

The set of 50 spray images for each fuel, at each temperature, was subject to background subtraction and thresholding, to identify the spray plumes. By visual inspection, a 7% threshold gave a good qualitative representation of the early spray but missed much of the spray towards the end of the image set, which was instead captured best with a 2% threshold. However, with a 2% threshold, spurious light is captured earlier on, distorting the quantitative information from the image. Two thresholding strategies were tested: a flat threshold of 7% and a varying threshold that started at 7% for the first 1.33 ms, reduced linearly to 5% by 2 ms, then to 3% at 4.22 ms and to 2% by 5.33 ms, where it remained. The varying threshold was created by manual inspection of the quality of thresholded images during injection, at 2 ms and 4 ms ASOI, and at the final few frames out of the batch of 50.

After thresholding, the axial penetration was calculated and spray pixel values were summed to give a spray integral indicative of the amount of spray present, for each frame. In Figure 6.7, the mean spray axial penetration for Fuel B is presented, for both thresholding methods. The error bars show one standard deviation above and below the mean, calculated from the 50 images, for the varying threshold calculation. There is a good comparison in spray penetration between the two

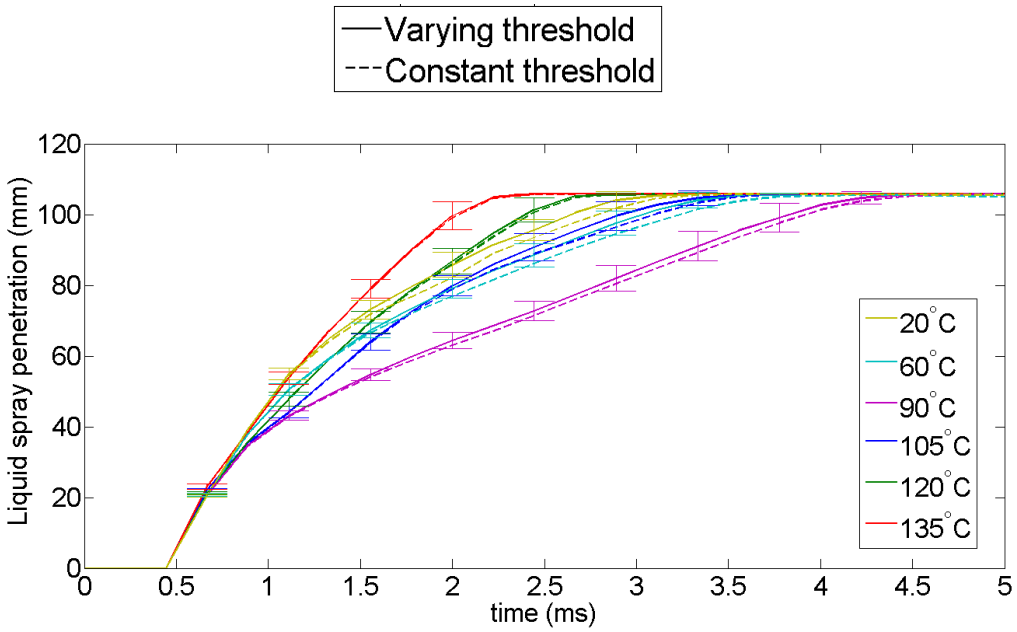


Figure 6.7: Spray axial penetration for Fuel B experiments at the full range of fuel temperatures, comparing the constant threshold of 7% (dotted lines) and the varying threshold, 7% down to 2% (solid lines). Each spray penetration reaches a steady value once it leaves the field of view

methods. The varying threshold technique was therefore utilized, as it enabled a more detailed investigation about the later part of the spray, after EOI.

The spray pixel integrals for Fuel A and Fuel B are shown in Figure 6.8, for the full range of fuel temperatures, using the varying threshold. The data in these figures have been created by summing all the pixel values at each frame, averaging across the 50 spray images and plotting against time. At each frame an estimate of the incoming light levels, as indicated by the light incident on the barrel, away from the spray (see Figure 3.18) is also recorded. The pixel integrals have been weighted by this incident light level at every frame before averaging. The incident light level was observed to reduce as the injection proceeded, which was concomitant with the measured reduction of current through the LED array after initial energizing. Vertical dotted lines of the appropriate colour indicate the mean time when the spray begins to leave the field of view. The height of the optically accessible region of the spray chamber was designed to correspond to the axial distance between the injector and the piston crown, at BDC, for the optical engine used in this thesis,

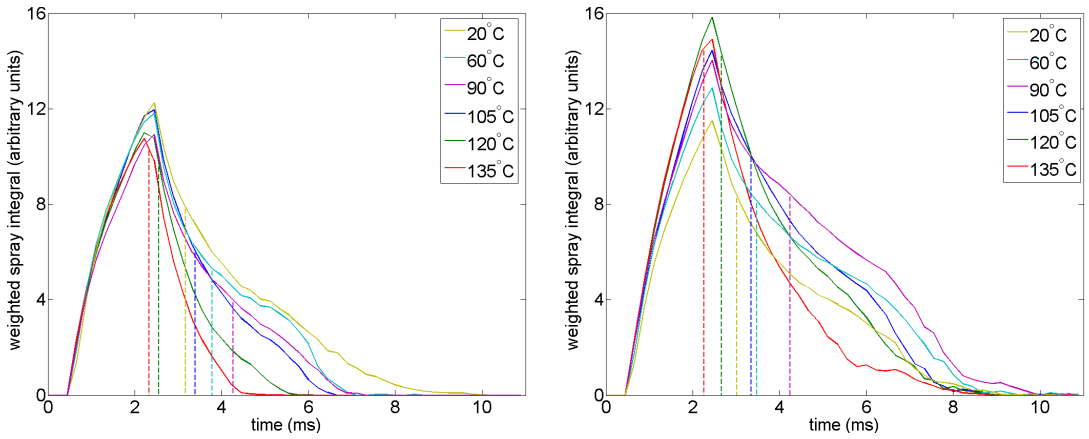


Figure 6.8: Weighted spray pixel integrals against time after SOI, averaged across 50 sprays. *Left*: Fuel A, *Right*: Fuel B. The broken line indicates when the tip of the fuel spray leaves the field of view

representing a maximum possible spray penetration in the engine. Therefore, after the vertical dotted line, fuel will certainly have impinged on the piston.

The heavier Fuel B shows a larger absolute value of peak spray integral, across all temperatures apart from the cold room temperature condition. This trend is also seen in the unweighted spray integral results, which are not presented here. Both fuels have similar initial boiling points and vapour pressures within the observed temperature range (see Table 6.1) but Fuel B has a much higher T90 and final boiling point (see Figure 3.16), meaning that droplet lifetimes would be expected to be longer. This difference in expected lifetimes is manifest in the observed amount of liquid present (in terms of both number and size of droplets) even before EOI, for the sprays at 60°C and above, shown in Figure 6.8. When the sprays collapse to a greater extent, due to a higher degree of superheat, more liquid fuel will be obscured behind the visible part of the spray, which could affect the trends seen here. Differences may exist in the flash boiling atomization, due to variations in fuel properties, such as enthalpy of vaporization and fuel viscosity, which could also contribute to differences in light levels.

At the 20°C condition, Fuel A showed, on average, a slightly higher peak spray integral than Fuel B. Since the vaporization will be very slow at this fuel temperature (the air temperature during the 20°C fuel temperature experiments was less than 20°C), the spray droplets are expected to be in the early stage of evaporation,

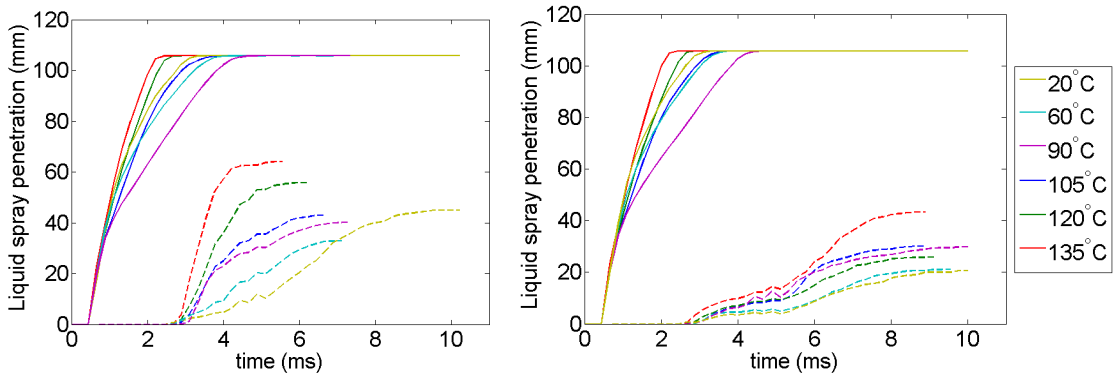


Figure 6.9: Spray axial penetration against time after SOI, averaged across 50 sprays. *Left*: Fuel A, *Right*: Fuel B. The solid line represents the maximum penetration (spray tip) and the broken line represents the minimum penetration (trailing edge). Each curve ends at the time when the mean spray integral for that temperature became zero, *i.e.* when all the droplets have evaporated or have moved out of view

undergoing vaporization of only the most volatile components within the first 10 ms of evaporation. This means that the difference in the heavy end composition of the fuels will not have come into effect. Therefore, this discrepancy could be due to experimental variation, or due to the slightly larger n-pentane content in Fuel B causing a slightly faster initial vaporization. As the temperature was increased, the Fuel A peak spray integral tended to decrease a little but with no real trend. However, for Fuel B, the peak spray integral tended to increase up to 120°C, before reducing slightly at 135°C. The increase in the degree of flash boiling tended to cause a higher light level near to the nozzle for both fuels, due to a greater density of droplets in this region. It is thought that this higher density has the greatest impact on the overall spray integral value for Fuel B as the evaporation rate is slow, whereas the faster evaporation rate for Fuel A counteracts the increase in density.

The degree to which the spray droplets become axially dispersed within the cylinder can be examined by looking at the axial penetration of both the spray tip and the trailing edge of the spray as it leaves the injector. Both of these penetrations are plotted in Figure 6.9, for each fuel investigated.

In Figure 6.9, the spray tip axial penetration rate decreases as the fuel temperature is increased, before beginning to increase again, after a minimum at 90°C, for both fuels. The penetration has been plotted in Figure 6.10 as a function of fuel saturation

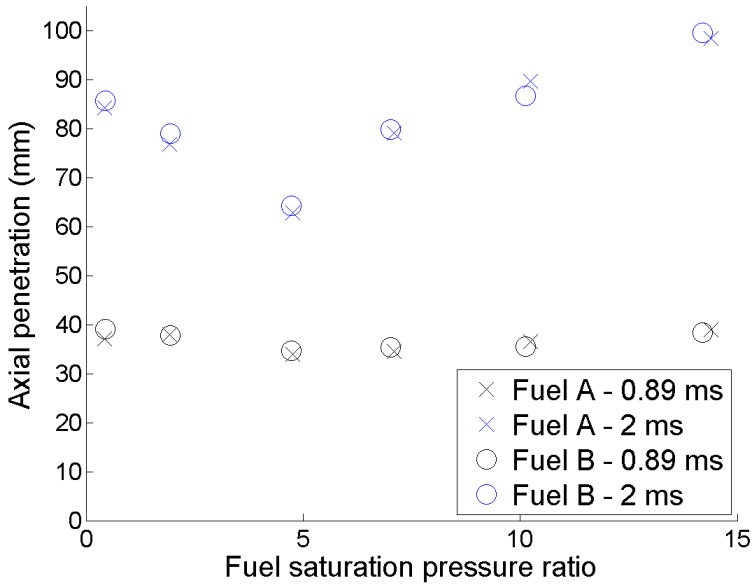


Figure 6.10: The average measured spray axial penetration from 50 spray images as a function of the fuel saturation pressure ratio, for both Fuel A and B, for both 0.89 ms ASOI and 2 ms ASOI. The axial penetration measured at 2 ms is a strong function of the fuel saturation pressure ratio, despite Fuel A and B having very different heavy component compositions

pressure ratio. This behaviour is similar to that predicted by previous studies [43, 44], where sprays that had become fully collapsed, and for which penetration had begun to increase with further superheat, were classified as flare flashing sprays. It was found in [43] that the minimum penetration was at a fuel saturation pressure ratio of 3.33. For the fuels tested here, this would require a fuel temperature between 60°C and 90°C, in which interval there may be a minimum in axial penetration. The alteration in behaviour upon further increase in fuel superheat is hypothesized to begin when the multi-hole plumes begin to coalesce into one axial jet [9, 41], with the momentum of each plume concentrated in a common direction and a greater level of air entrainment into the spray, counteracting the effects of the reduction in droplet size due to flash boiling atomization. It was also found by Xu *et al.* [44] that sprays with levels of superheat above the transition into the flare flashing regime exhibited no further reduction in spray SMD.

However, it must be noted that the air into which the fuel was injected was heated indirectly by contact with the heated injector block; the air temperature

increased from 20°C or less when the fuel was at 20°C, to 40°C at the highest fuel temperature. This produces two additional competing effects: reduced chamber air density, causing reduced droplet drag; and increased droplet evaporation rate, causing reduced droplet size and higher droplet drag.

There was a general trend that an increase in the fuel temperature (and hence also in the air temperature) increased the penetration rate of the spray trailing edge. As all of the spray plumes begin to be turned towards the axial direction during spray collapse, this is to be expected. This phenomenon may influence the amount of liquid that is deposited onto the piston crown versus the cylinder liner, or how vapour is initially distributed in different parts of the combustion chamber. These trailing edge spray droplets moved more slowly in the Fuel B experiments, due to the slower vaporization rate, which caused droplets in this less dense region of spray to persist longer before completely vaporizing.

Figure 6.11 is a selection of individual images from the experiments with Fuels A and B, with false colouring of the identified spray region, after background subtraction and thresholding. These images show the distribution of the spray around the cylinder for both fuels across the range of temperatures.

The spray images taken at 20°C are very similar for both fuels, in terms of penetration and overall spray angle (as seen from this viewing angle). Plume 2 is seen to impinge on the liner at the same location and time in both cases, in the bottom right of the image. For most injection timings, it is expected that this plume, and some of the others, would impact with the piston first, before it could reach the liner. When the fuel temperature is increased to 60°C, both fuels become superheated, with a fuel saturation pressure ratio of 1.9. The spray angle and axial penetration are slightly reduced but the spray does not visibly collapse to any degree. The plumes do, however, appear to have drawn together slightly at 60°C as there is less clear space between the left hand plumes (6, 1 and 5) and the right hand plumes (4, 2 and 3).

The fuel temperature was further increased to 90°C, which caused the fuel saturation pressure ratio to increase to around 4.75 for both fuels, accompanied

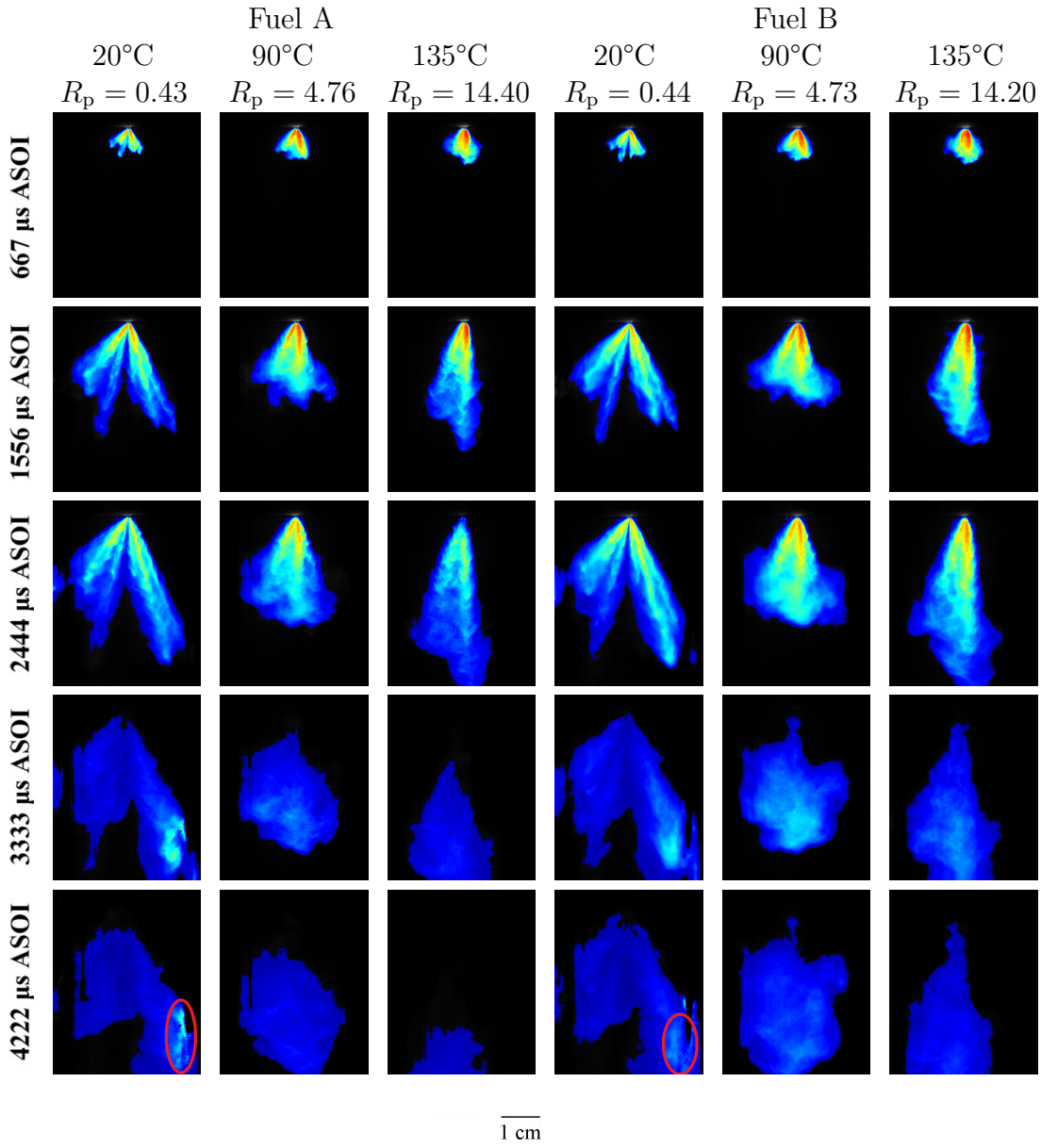


Figure 6.11: Sample individual spray images for three temperatures and for Fuels A and B, showing the variations in how each fuel and fuel temperature combination fills the cylinder with spray (each row displays time ASOI in µs). The demanded injection duration was 2 ms; however, the visible EOI occurred later than this for all fuels and at all temperatures. Liner impingement is highlighted in red. The reflection from the illuminated spray onto the underside of the injector block is seen above the spray but is not false coloured or included in spray integral calculations. The plume pattern is as given in Figure 6.6

by a significant change in fuel spray structure: a reduction in both the fuel pene tration and overall spray angle. This was despite a modest 30 K change in fuel temperature. A similar increase in fuel saturation pressure ratio (from 1.9 to 4.75) could also be effected by reducing the ambient pressure from 1.0 bar to 0.41 bar, at a fuel temperature of 60°C.

As seen in Figure 6.9, the penetration at 90°C fuel temperature is always the smallest, by a significant margin. Plumes 2, 3, 4 and 5 have merged early in the spray lifetime, by the time of the first row of images in Figure 6.11, and have embarked on a trajectory closer to the axial direction. By EOI, the tip of these merged plumes has been drawn further inwards and travels more closely to the axial direction. The spray is still quite wide; on the left hand side, plumes 1 and 6 initially travel in a direction close to the nominal, before being drawn inwards later in the spray lifetime (see Figure 6.4). Both sides of the spray exhibit a vortex motion of droplets at the tip, from around 1.5 ms ASOI, which spreads droplets towards the chamber walls and back towards the injector block. This achieves a good distribution of spray droplets around the cylinder at the point of EOI.

In Figure 6.12, spray images from the 90°C and 105°C tests for Fuel B are shown, which compare the fuel droplet motion for both temperatures near the collapsed spray tip. At the hotter temperature, where the fuel saturation pressure ratio was 7.02, the phenomenon of recirculation of droplets is also observed but is seen at a larger axial distance from the injector for the merged plumes 2, 3, 4 and 5. By this time the fuel spray would likely have impinged onto the piston crown. At further increased temperature, the recirculation and broadening of the collapsed spray tip occurs at greater axial penetrations, leading to a more jet-like structure in the visible region imaged, as shown by the sprays at 135°C in Figure 6.11.

The hottest sprays (135°C with a fuel saturation pressure ratio of 14.20/14.40) show the highest pixel intensity values of any image, in the region nearest the injector tip. This is thought to be due to the merging of the plumes, which creates a dense region of droplets which has a greater impact on observed light scatter than any reduction in droplet size from improved atomization. In addition, the

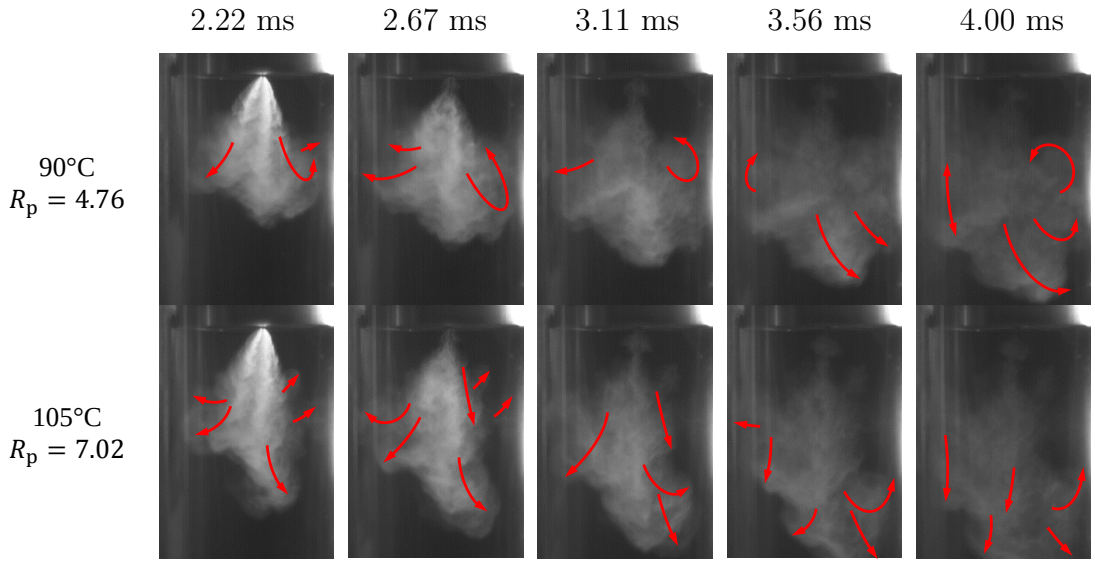


Figure 6.12: Spray images (without background subtraction) around the time of EOI, for *top*: Fuel B at 90°C and *bottom*: Fuel B at 105°C. Arrows have been placed to show the visually identified trends in the motion of the unevaporated spray droplets at the spray periphery

structure of the spray at this temperature is most jet-like with a narrower overall spray angle. The first evidence of recirculation, as identified in Figure 6.12, occurs at 2.89 ms ASOI, very close to the bottom of the image. This allows the avoidance of all liner impingement but leaves the area near the top of the cylinder and near to the liner without droplets, as seen in previous work for sprays at the highest superheat levels [43, 44]. At this fuel saturation pressure ratio, the spray has not yet collapsed into a single jet, due in part to the distance between plumes 1 and 6, and the other plumes. Between Fuels A and B, there is little difference between the spray images for any given fuel temperature until after EOI, suggesting that it is the early phase of the fuel distillation curve (low temperature or light end) that has the most impact on the flash boiling spray structure during injection, even at high levels of superheat. As seen in Figure 3.16, the distillation temperatures (and hence the fuel vapour pressure) of Fuels A and B diverge at around 320 K, and at 135°C Fuel A is completely evaporated under distillation conditions; yet these differences do not affect the early spray structure.

The spray angles observed for Fuel A and Fuel B, at each different fuel temperature, were also very similar. Spray angle has been measured in accordance

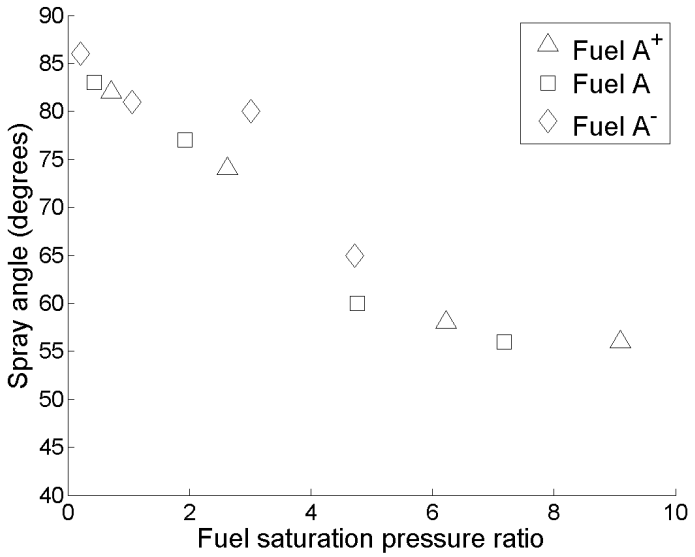


Figure 6.13: Variation of M15 fuel spray angle, taken from spray images found in [46], and measured in accordance with SAE J2715 [104]. The injector was oriented as depicted in Figure 6.1. The fuel temperature was varied from room temperature (∼293 K) up to 378 K

with SAE J2715 [104], whereby the angle is measured at 1.5 ms ASOI, using straight lines between an axial distance of 5 mm and 15 mm to define the left hand and right hand edges of the overall spray. The spray angle variation with fuel saturation pressure ratio for Fuels A, A^+ and A^- that was observed with this fuel injector is shown in Figure 6.13, using data from [46]. There is a trend of decreasing overall spray angle with increasing fuel saturation pressure for these fuels, even during the range of sub-cooled conditions ($R_p < 1$).

6.2.1 Comparison to single droplet simulations

Single droplet simulations were run to complement the findings from the spray chamber experiments. Fuels A and B were used and a representative initial droplet diameter of 10 µm was chosen for the simulations. The models used were: the well-mixed model for droplet composition; the droplet heat equation model for droplet temperature and, in the case of the superheated droplets, the model introduced in Section 2.1.4. The more complex liquid diffusion-controlled model for liquid composition was not necessary, as the quantity of methanol was

not varied. Methanol is the component responsible for the non-ideal behaviour. The air temperature chosen for these simulations was the measured air temperature from the spray chamber tests. As the fuel temperature was increased, the air was also heated by its contact with the heated injector block, which would affect the droplet lifetime in the spray.

Results in Figure 6.14 show the droplet size histories for the Fuels A^+, A and A^- in terms of normalized droplet diameter squared, for both a sub-cooled and a superheated condition. The fuel compositions are given in Table 3.5. For Fuel A+, the hydrocarbon components leave the droplet first (since these consist mostly of the highly volatile n-pentane) before slower evaporation of the remaining methanol occurs. The 5% iso-octane by volume evaporates with the n-pentane, despite being less volatile than methanol, due to its low concentration and the non-ideal vapour-liquid equilibrium. The pure alcohol fuel on its own does not evaporate as fast as might be expected, as there is a much increased enthalpy of vaporization and no boost to vapour pressure from non-ideal vapour-liquid equilibrium. For Fuels A and A-, the methanol evaporates first (alongside the n-pentane in the case of Fuel A). Both fuels contain 3% iso-butanol by volume to act as a co-solvent between the alcohol and hydrocarbon species. For Fuel A, iso-butanol was observed the last species to evaporate, as iso-octane would deplete first. Once this occurred, the vapour pressure would drop and enthalpy of vaporization would rise, as for the pure methanol evaporation at the end of the droplet lifetime for Fuel A^+. This results in a much longer lifetime for Fuel A than expected, which in fact exceeds that of the less volatile Fuel A^- at 20°C. In all the studied cases of droplets of Fuel A^-, the iso-octane and iso-butanol co-evaporated until all liquid had vaporized, which meant that there was no elongation to the droplet lifetime.

For Fuel B, a much longer droplet evaporation time was predicted, which was expected due to the presence of much heavier components in the mixture, included to create a more representative model fuel for gasoline. The droplet size histories for various fuel temperatures are shown in Figure 6.15. The sharp change in gradient at approximately $d^2(t) = 0.2d_0^2$ corresponds to the evaporation

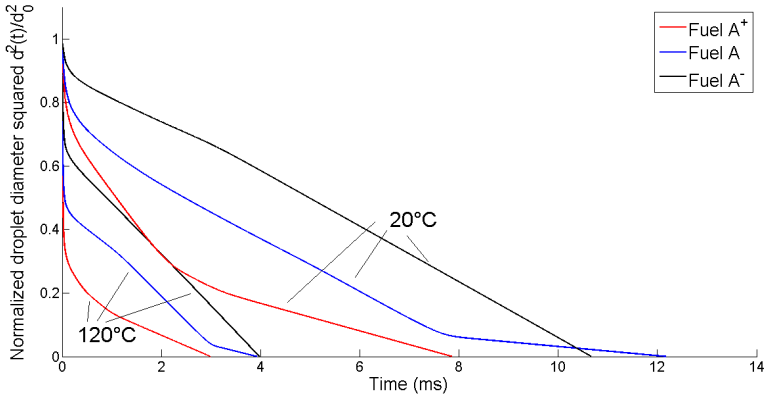


Figure 6.14: Droplet size histories for the 'A' fuels, which contain no aromatic or heavy components (n-decane, n-undecane). Two temperatures are shown (20°C and 120°C). For Fuel A$^-$ at 120°C, 75% of the droplet mass is lost in the initial superheated phase. At each of the other initial fuel temperatures tested, the shape of the curve was similar

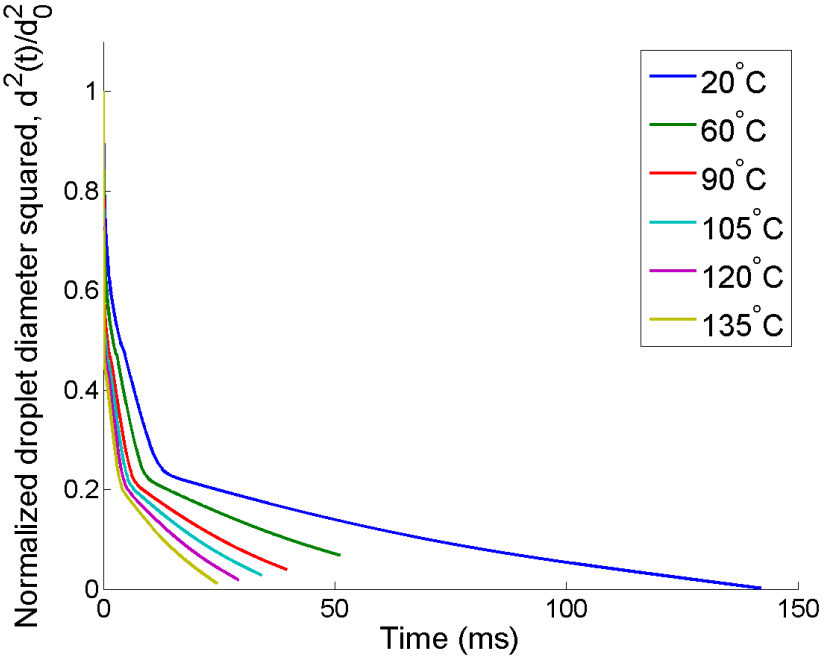


Figure 6.15: Droplet size histories for Fuel B at the range of fuel temperatures corresponding to those tested in the spray chamber

of the final toluene fuel from the droplet, such that the liquid becomes solely a mixture of n-decane and n-undecane.

The single droplet simulations for Fuel A predict that, at all temperatures other than 20°C, the 10 µm droplet will fully evaporate before the 11 ms imaging window of the spray chamber experiments. Observation of the real fuel sprays, showed that

this was not the case. This may be attributed to local gas cooling that reduces the real evaporation rate. This phenomenon was observed in Chapter 5, where the local value of gas temperature that each modelled droplet experienced could be much lower than the ambient gas temperature. A similar effect could be expected for the Fuel B sprays, which would mean that for all of the fuel temperatures tested there could be droplets which were composed mainly of the heavy n-decane and n-undecane components by the end of the 11 ms imaging window. Thus, the observed difference in evaporation rate between Fuels A and B after EOI, and of the spray trailing edge, can be largely attributed to the presence of these heavy components.

Another method to simulate the flash evaporation of the M15 fuels was utilized. An adiabatic flash calculation was performed for the superheated liquid mixture, based on the solution of the Rachford-Rice equation (*e.g.* Perry's Chemical Engineers' Handbook [138]) and the conservation of energy and conservation of the injected species. These equations were solved via a MATLAB optimization, using the built-in function *lsqnonlin*, which searches for minima in a given multi-variable function set (here the Rachford-Rice equation and conservation of each species), subject to constraints on the variables, *e.g.* that temperature is positive and that mole fraction is between zero and one. This calculation outputs the multi-component mixture of liquid and vapour at the decreased temperature that would result if a liquid mixture was injected into an atmosphere with respect to which it was superheated, and was allowed time to come to equilibrium (*i.e.* the total liquid vapour pressure was equal to the ambient pressure). This process is depicted in Figure 1.5 for a single component fuel. This method utilized the vapour-liquid approach outline in Section 2.1.3, with the UNIFAC method adopted for the M15 mixtures. The adiabatic flash calculation explicitly accounts for the difference in enthalpy of the liquid and vapour phase, *i.e.* the enthalpy of vaporization, and hence the potential gas phase cooling. The evaporative cooling of the gas into which the fuel is injected will be similar for each of the M15 fuel blends, as shown in Table 6.2, but is expected to be higher than a typical ULG fuel.

Table 6.2: Enthalpies of vaporization for the M15 fuel blends used in this thesis. The values are considerably higher than the typical value for ULG given in Table 1.2, due to the methanol content

	Fuel A^-	Fuel A	Fuel A^+	Fuel B
Vaporization enthalpy (kJ/kg)	704	684	663	677

As the degree of superheat was increased by increasing the fuel temperature, it was found that the adiabatic flash calculation resulted in a greater proportion of the initial liquid tending to vapour, and a greater proportion of more volatile components becoming vapour. This resulted in a reduced volatility of the remaining liquid, which was compensated for by an increase in the temperature of the equilibrium mixture of remaining liquid and flash evaporated vapour. However, the degree of liquid phase cooling increased as the superheat level increased, which suggests a potential offset in the evaporation rate of the remaining liquid after a flash boiling injection. This is mirrored by the gradients in the droplet diameter squared curves in Figures 6.14 and 6.15. In these plots, the more volatile fuels (with the larger fuel saturation pressure ratio) exhibited a slower evaporation rate, after the initial phase of rapid evaporation whilst the liquid surface remained at the liquid boiling temperature.

At no simulated condition did all of the methanol fraction deplete, for either the adiabatic flash calculation or during the rapid initial boiling phase of evaporation in the single droplet calculations. The loss of mass predicted by the adiabatic flash calculation (upon reaching phase equilibrium) was actually less than that predicted during the single droplet calculation boiling phase. This is presumably due to the internal droplet temperature gradients that exist in the single droplet model, which act to supply additional energy for evaporation at the droplet surface. As it is expected that the single droplet calculations may have overestimated evaporation rate (since the phenomenon of gas phase cooling is not included) the adiabatic flash calculations may give a more accurate description of the conditions within the flashing sprays.

Therefore, the single droplet lifetime results with constant ambient conditions may be seen as an estimate for droplet lifetime under homogeneous DISI conditions. With the correct selection of droplet temperature and composition routines, as identified in Chapter 4, this model could be of use both in analysing expected trends as conditions or fuel composition is varied, or in ascertaining the extent to which droplets will survive until spray impingement, or, by utilizing time-varying boundary conditions, to assess whether droplets will survive during the compression stroke, until spark ignition occurs.

6.3 Comparison With Engine Particulate Emissions

6.3.1 Experiments performed

In-cylinder fuel spray imaging and exhaust particulate matter emission measurements were performed on the single cylinder optical DISI engine described in Section 3.3. These results are fully presented and analysed in [46], with selected data discussed here. The experiments aimed to evaluate the effects of the spray regime on the subsequent GDI engine combustion and PM emission levels, during homogeneous operation, as characterized by fuel saturation pressure ratio. These experiments were performed with the set of methanol/gasoline blend fuels (M15) described in Section 3.4. This type of fuel has a high volatility, which allows a wide range of fuel spray behaviour, from sub-cooled to highly superheated, under normal GDI engine operating conditions. This may lead to undesirable fuel spray structures and piston impingement, as discussed earlier in this chapter. However, the high oxygen content in the fuel has been reported to aid a decrease in the overall particulate matter emissions released over a drive cycle or at a fixed test point.

All of the engine tests were conducted at 1000 rpm and a manifold absolute pressure of 0.5 bar, which corresponds to a throttle setting of 14% open and an air induction rate of about 2 L/s. This represents a common low speed, part load engine condition, corresponding to a brake mean effective pressure of about 2 bar.

Table 6.3: Fuel saturation pressure ratios ($p_{\mathrm{vap}}/p_{\mathrm{amb}}$) for Fuel A and Fuel B for the optical engine experiments. All of the sprays were superheated to some degree, but at 23°C the spray structure was very similar to that of a sub-cooled spray

Fuel (cylinder head) temperature	Fuel A	Fuel B
23°C	1.00	1.02
60°C	3.90	3.92
90°C	9.64	9.59
105°C	14.40	14.20

The intake air was heated to 40°C for each test. The spark timing was fixed at 35°CA BTDC. The injection timings examined were 250, 280 and 310°CA BTDC.

A range of fuel temperatures were utilized, which were achieved by varying the temperature of the engine cylinder head coolant. The cylinder head temperature was varied between 23°C and 105°C, which allowed the study of a range of fuel saturation pressure ratios. These fuel saturation pressure ratios are shown in Table 6.3, using the manifold pressure of 0.5 bar as the ambient pressure p_{amb} for the calculation of R_{p}. By comparison with the fuel saturation pressure ratios in Table 6.1, the optical engine fuel sprays at 60°C will have a similar structure to the spray chamber sprays at 90°C and the optical engine fuel sprays at 105°C will have a similar structure to the spray chamber sprays at 135°C. The fuel spray images taken in the spray chamber at these temperatures are shown in Figure 6.11.

Each fuel was first utilized under motoring conditions, with a full optical cylinder liner installed. This allowed almost complete optical access to the fuel spray and allowed comparison with images taken in the spray chamber. The fuel sprays imaged inside the engine will differ from those injected into the spray chamber due to the air motion during the induction stroke. The spray was illuminated from below, which provided high quality Mie scattering images with few unwanted light reflections. Then, firing engine experiments were performed with fuel sprays imaged through an optical annulus (height 30 mm). These fuel spray images were used to confirm that the spray behaved similarly under the hotter conditions of the firing engine, as to under the colder conditions of the motoring experiments.

Finally, firing experiments were performed using a full metal cylinder liner and full metal piston, during which exhaust particulate matter emissions levels were measured using the DMS500 fast particulate spectrum analyser. Particulates were recorded over a period of 90 sec, during which the engine condition was maintained. Measurements were taken at both $\lambda = 1.01$ and $\lambda = 0.9$. A set point of $\lambda = 1.01$ was used to represent stoichiometric combustion, which eliminated any slightly rich combustion arising from cycle-to-cycle variations. The set point of $\lambda = 0.9$ represents a rich mixture transient event (albeit here simulated with a fixed engine speed); these events can have a significant impact on the total PM emissions measured across a drive cycle [139].

6.3.2 Particulate matter measurement results

The engine-out particulate matter results were measured for each M15 fuel. For Fuels A^-, A and A^+, injected with an SOI of 280°CA BTDC, the general level of exhaust particulate matter was low after the Wiebe filter was applied (see Equation 3.2), for most investigated fuel injector temperatures. This was anticipated, due to the lack of aromatic components and heavy gasoline component species in these fuels. A higher particulate number count was observed for Fuel A in the range of particulates up to 100 nm in size, at the fuel temperatures of 90°C and 105°C only. Fuel A was expected to be more volatile than Fuel A^-, yet some of the calculated droplet lifetimes were in fact longer, due to the presence of 3% iso-butanol by volume. This could be one explanation for these unexpected results. An alternative explanation is that there is a strong compromise between beneficial enhanced fuel evaporation rate and potentially undesirable fuel impingement, leading to certain combinations of temperature and fuel saturation pressure ratio that create persisting fuel films and unfavourable rich mixture combustion events.

The remainder of this section will focus on the experimental results from the Fuel B tests. The measured particulate size spectra for these are presented in Figure 6.16, for a selection of fuel temperatures and injection timings.

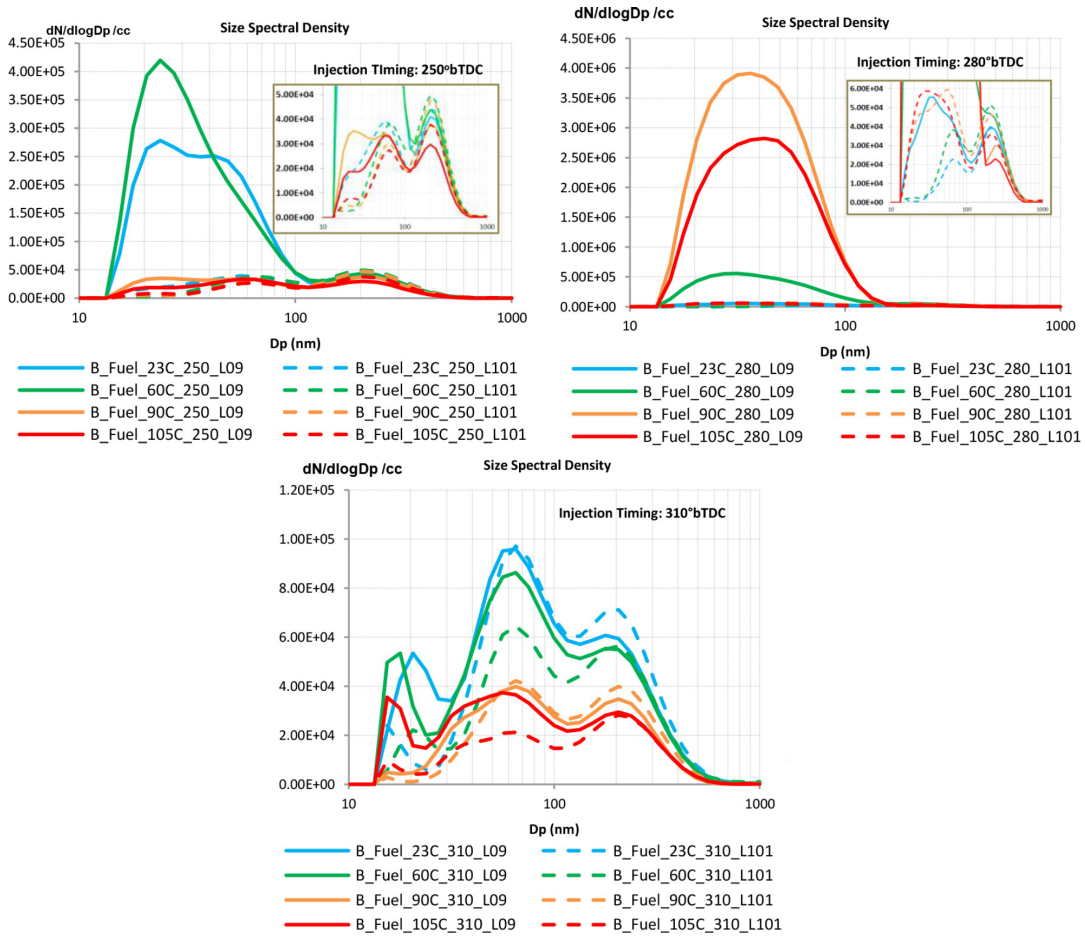


Figure 6.16: Particulate matter emissions size spectra measured by the DMS500 during the Fuel B combustion tests. The engine was at 1000 rpm, 0.5 bar manifold absolute pressure and was fitted with a full metal cylinder liner and full metal piston. Three injection timings are shown, showing the range of results achieved with both $\lambda = 1.01$ and $\lambda = 0.9$, for a range of engine cylinder head temperatures. Data gathered, analysed and presented by Safwan Bin Mohd Murad

The earliest injection timing of 310°CA BTDC resulted in a consistently low level of particulate matter at all of the cylinder head temperatures that were investigated. The rich combustion tests produced a greater number of particulates at most, but not all, sizes for all temperatures investigated with this injection timing. Additionally, increasing the temperature of the injected fuel (resulting in a move from sub-cooled to superheated fuel spray) consistently lowered the number of particulates that were measured, across the spectrum. The size distribution is trimodal, instead of the ordinary bimodal distribution - nucleation and accumulation - expected with GDI engine emissions. The Wiebe function (see Equation 3.2) aims

to remove the volatile nucleation mode, which suggests that the peak at sizes around 20 nm may be the remnants of this mode. There appear to be two groups of accumulation mode particulates, one centred on 60 nm and one centred on 200 nm; potentially these have been formed by different rich combustion events, or at different locations in the combustion chamber.

As the injection is retarded to 280°CA BTDC, the stoichiometric results stay broadly at the same particulate count levels across the spectrum. However, during the rich experiments, at 60°C, 90°C and 105°C, there was a great increase in the number of particulates below 100 nm. Additionally, the effect of temperature was seen to reverse, with increased fuel temperature causing higher peak values in the spectrum, up to 90°C before a slight decrease at 105°C. This is thought to result from the difference in levels of piston impingement, due to the increased injector to piston distance and the different spray patterns that result as fuel superheat is increased. At all temperatures, the spray will still hit the piston crown. Some of the particulate matter in the sub-100 nm region will be in the nucleation mode (at around 30 nm) but there are also a considerable number of particulates of size 60 nm or more, which are expected to be in the solid accumulation mode.

At the latest injection timing, 250°CA BTDC, a relatively low particulate count was once again found across the spectrum for most tests. The exception was for the colder fuel tests (23°C and 60°C) under rich conditions. With the piston further away from the injector during injection, the influence of piston impingement is thought to be reduced. The lower piston position also caused the sprays at 23°C and 60°C to impinge onto the liner, which may influence the particulate matter levels. The delay in injection from 280 to 250°CA BTDC corresponds to a time delay of 5 ms. This may have also affected the chances of full fuel vaporization before the spark timing, particularly affecting the colder fuel sprays.

The particulate mode centred around 200 nm was similarly behaved at the operating points investigated, with the peak value reducing as fuel temperature was increased and little variation in count value as λ was varied. This suggests the

mechanism for the creation of these particulates was very similar in each test and was not a result of variations in the fuel vaporization rate or the fuel spray structure.

It is known that the air density (and the liquid density) is of particular importance in determining the progress and behaviour of individual spray plumes (*e.g.* the work by Naber and Siebers [38]). The liquid density is determined purely by the fuel pressure and temperature, which allows direct comparison between engine and spray chamber experiments. The air density into which the spray is injected will vary with gas pressure (p) and gas temperature (T) and, assuming an ideal gas, will scale with p/T. The cylinder pressure in the engine was kept to a nominal 0.5 bar by necessity, to restrict load on the optical engine, and the air temperature for the motoring experiments will be close to the induction temperature of 40°C as injection is during the induction stroke. The air temperature during the firing experiments, during which the emissions measurements were taken, will be higher but no direct measurement or estimation of this has been made. For the spray chamber experiments, the air pressure was 1.0 bar (atmospheric) and the air temperature was between 20°C and 40°C. Therefore, the main parameter varied between the two experiments that will have affected the spray development is the air pressure, and there will be a factor of approximately two difference between the air density in the engine and the spray chamber (due to the factor of two difference in the pressures). In the work of Aleiferis and van Romunde [41], the variation of chamber density at constant fuel vapour pressure (R_p) had little effect on axial spray penetration in the sub-cooled regime. For n-pentane experiments, there was a reduction in measured penetration from approximately 46 mm to 42 mm (9%), when the chamber density was increased by a factor of two at roughly constant fuel superheat (R_p was calculated from their data as 9.4 at a 0.5 bar test, and 9.0 at a 1.0 bar test). This study [41] used the same injector type as in this thesis, with 150 bar fuel pressure, and measurements were taken 1.2 ms ASOI. Alefeiris and van Romunde also performed near-nozzle high-speed backlit imaging of the early spray development and steady state spray development for n-pentane, iso-octane and a commercial gasoline mixture. The images at two conditions (again with similar R_p

but a factor of two difference in the chamber density) showed very similar spray structures for each fuel, in terms of plume interaction and individual plume shape and angle. For n-pentane only, with $R_p \sim 9$, there was a small decrease in penetration and a small increase in overall spray angle when the density was reduced. Thus it is expected that the air density (and hence air pressure and temperature combination) will have a small impact on the fuel spray development, which will be more apparent at higher amounts of fuel superheat. Therefore, there can be a suitable comparison of spray penetration and structure between the conditions imaged in the spray chamber and those expected in the optical engine. However, the air density and specific ambient pressures and temperatures experienced by the spray will have an absolute effect on droplet evaporation rate and hence the long term development of the spray (*e.g.* in terms of spray impingement), as discussed in Chapter 1.

6.3.3 Motoring fuel spray images

Mie scattering images are now presented of the fuel sprays for Fuel B, under motored conditions, for the test conditions of interest. These are taken from the study conducted in [46], and were gathered using the full optical liner and the optical piston window, which are both manufactured from fused quartz. The structure and evaporative behaviour of these sprays allow insight into some of the trends seen in particulate matter emissions measurements.

In Figure 6.17, a series of motoring spray images for Fuel B is shown for each of the injection timings that were investigated. At 310°CA BTDC and 280°CA BTDC, the cylinder head temperature selected for presentation was 105°C, and at 250°CA BTDC it was 60°C. The orientation of the camera provides a view of the spray that is similar to that used to capture the Mie scattering images in the spray chamber in Section 6.2, so as to allow good comparison to those images. At the nominal in-cylinder pressure of 0.5 bar, the 105°C temperature sprays have a fuel saturation pressure ratio of 14.2, which closely compares to the spray chamber tests conducted at 135°C, where $R_p = 14.4$. At the 60°C condition,

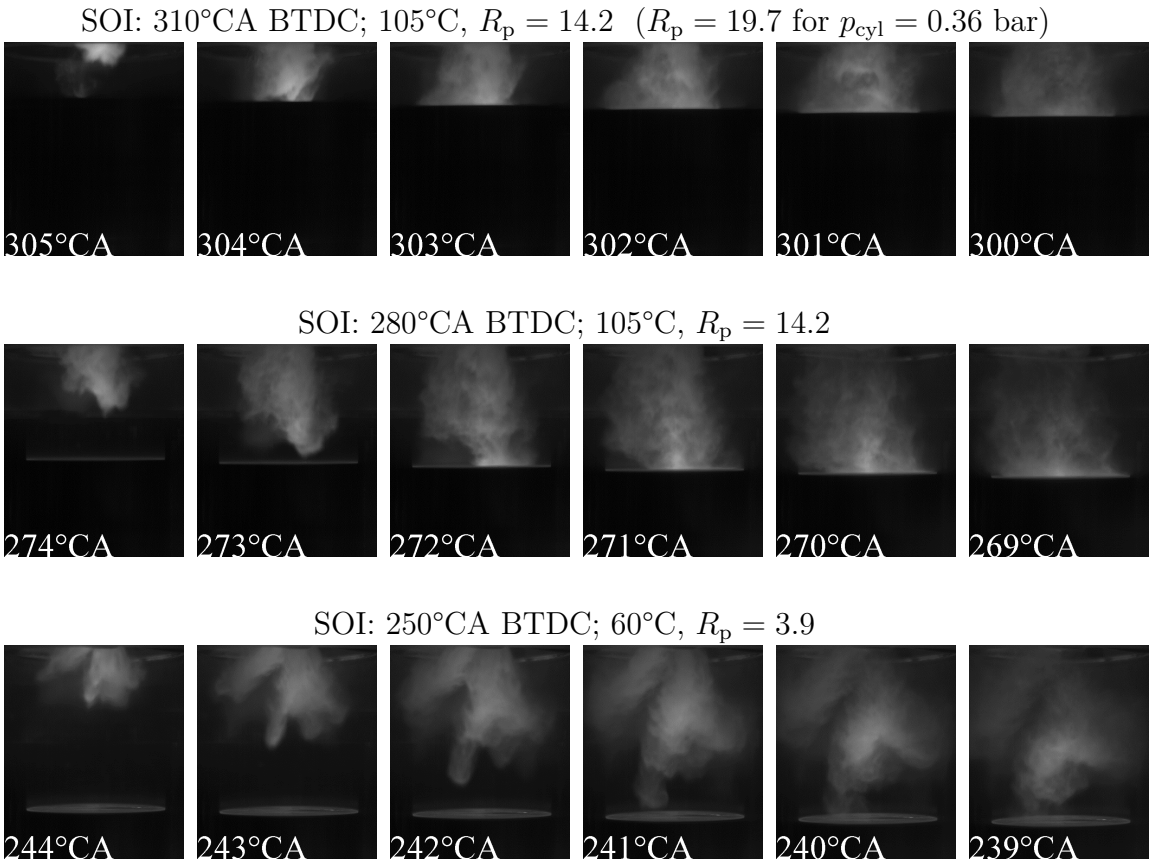


Figure 6.17: Raw spray images captured from the motored single cylinder. Illumination is from below, off the 45° Bowditch mirror and through the fused quartz piston window. Crank angle timings are shown for each image, as well as the cylinder head temperature and corresponding value of R_p

$R_p = 3.9$, which is close to the spray chamber tests at 90°C, where $R_p = 4.7$, which corresponded to minimum axial penetration.

There is a high level of piston impingement in the case of the 310°CA BTDC fuel sprays. This occurs at all fuel temperatures. At the highest fuel temperature of 105°C, the fuel spray has formed the expected narrow jet, with most of the fuel impacting at the same time: plumes 1 and 6 (the leftmost plumes) do not appear to be distinct from this viewing angle.

The actual pressure in the engine cylinder during fuel injection was measured during the combustion tests corresponding to this injection timing. The IVO timing for this engine was 327°CA BTDC, with the maximum opening point for the inlet valve occurring at 222°CA BTDC. Therefore, the 310°CA BTDC injection occurred very early during the engine intake, with very low valve lift and a cylinder

pressure during injection of between 0.36 bar and 0.39 bar, compared to the nominal manifold pressure of 0.5 bar. This increases the fuel saturation pressure ratio from the nominal 14.2 to the range 18.2–19.7. This may cause an even greater degree of flash boiling collapse than that observed in Figure 6.11 and altered atomization behaviour. At the later injection timings, there was sufficient valve lift for the in-cylinder pressure to closely match the manifold pressure.

In addition, the low valve lift will cause the curtain flow of air into the cylinder to have a higher velocity. This may disrupt the spray and subsequently formed fuel films to a greater extent than for the later injection timings.

The rate of evaporation, based on the attenuation of the Mie scattering spray integral, is higher during the sprays injected at 310°CA BTDC than during those injected at 280°CA BTDC. Furthermore, at this injection timing, fuel impinged onto the piston at all fuel temperatures. This suggests that improvements to evaporation rate and flash boiling atomization, due to the lowered cylinder pressure, dominate any reduction in vaporization rate to the closer confinement of the spray or heavy impingement.

This analysis of the spray behaviour during and after injection may help to explain why, at the 310°CA BTDC injection timing, no fuel temperature resulted in an unexpectedly high particulate number count.

At the injection timing of 280°CA BTDC, there is still impingement onto the piston crown for all cylinder head temperatures. The shape and intensity of the impinging spray at 265°CA BTDC (*i.e.* 15°CA ASOI) is quantitatively similar for the coolant temperatures of 60°C and higher (not shown here). The spray plumes 2, 3, 4 and 5 impinge near to the centre of the piston due to spray collapse, before rebounding and forming a layer of droplets that covers the width of the cylinder bore. This spreading of fuel was also found for injections at 310°CA BTDC, however the local reflected light intensity at the piston surface was higher with the 280°CA BTDC timing. The spray structure in Figure 6.17 (at $R_\mathrm{p} = 14.2$) is similar to that captured in the spray chamber with $R_\mathrm{p} = 14.4$, possibly with a slightly broader downwards jet. Direct liner impingement is avoided, but the combination

of slower evaporation rate and heavy piston impingement is expected to be the cause of the large rise in the number of sub-100 nm particulates that were measured at the hottest fuel temperatures, for this injection timing.

There was a small amount of both piston and liner impingement for cylinder head temperatures of 23°C and 60°C, for the sprays imaged at an injection timing of 250°CA BTDC. Coupled with the shorter available time for fuel film and droplet evaporation, and lower fuel temperatures, this may offer an explanation for the greater particulate number count at these two conditions, for the rich combustion at $\lambda = 0.9$.

For the 250°CA BTDC images in Figure 6.17, in the region of plumes 2, 3, 4 and 5, there are more than four identifiable plume structures, suggesting a change in plume behaviour during injection. Plumes have possibly initially proceeded in their nominal directions before collapsing towards the cylinder axis. This was also seen in Figure 6.4, at $R_{\mathrm{p}} = 2.48$. This explains why some fuel does go on to hit the piston.

In general, it was observed that the intake air motion has not greatly disrupted the overall structure of the sprays from that which was expected from the spray chamber experiments. This is difficult to ascertain for the 310°CA BTDC tests, as most of the spray is obstructed by the cylinder head.

6.4 Summary

Iso-octane and a range of M15 methanol/gasoline blends have been investigated using an atmospheric pressure spray chamber with continuous purging. Both diffuse backlit and Mie scattering images were acquired using a high speed camera and post-processed, using the hardware and image analysis described in Chapter 3. The M15 fuels were designed to independently vary the fuel volatility and the heavy component and aromatic content in order to understand the effect of the fuel composition on GDI fuel spray formation and inform the analysis of subsequent particulate number emissions. Each fuel was imaged at a range of fuel temperatures in the spray chamber, from non-flashing sprays through transition to flare flashing sprays, as characterized by the fuel saturation pressure ratio. The

spray axial penetration and spray evaporation rate was extracted from the images. Individual images were contrasted with mean images from batches taken at each fuel temperature, using a relevance index calculation. This indicated that the spray images were consistent within each batch. Furthermore, there was no systematic drift in penetration or spray evaporation results extracted from the spray images.

The data from the Mie scattering images was used to characterize the change in axial spray penetration with fuel saturation pressure ratio. As previously noted in the literature (for an eight-hole GDI injector) [44], the axial penetration first decreased as the degree of superheat was increased before increasing as the degree of superheat was further increased. There was a clear transition into a jet-like structure, where most of the plumes interacted very soon after exiting the nozzle. The creation of jet or plume tip vortex structures was delayed to a larger axial distance, resulting in an initially narrower spray. The critical fuel saturation pressure ratio, when axial penetration would start to increase with additional superheat, was found to be in the region of 2–5. The early structure of the spray changed very little with the addition of heavier components to the fuel, when comparing Fuel A and Fuel B. Thus, the fuel most closely representing a realistic gasoline, Fuel B, showed complete spray collapse at very high degrees of fuel superheat. This would likely cause piston impingement, for a homogeneous operation injection strategy, regardless of injection timing. Similarly, for this injector design, each sub-cooled spray test, and some of the slightly superheated tests, resulted in liner impingement by plumes 1 and 6.

Findings from the spray chamber experiments, for the various fuels and injection conditions, were compared with single droplet studies, using the models analysed in Chapter 4 and using adiabatic flash calculations for the flash boiling spray conditions. It was found that the single droplet lifetimes were longer than those that could be expected from the spray experiment observations, possibly due to local gas phase cooling, which was not taken into account in the single droplet simulations. The adiabatic flash calculations predicted similar trends in the quantity of flashed liquid as the single droplet calculations but with a smaller amount of liquid vaporization predicted. Based on the observations, the adiabatic flash calculation may provide

useful data on the conditions within a flashing fuel spray. Both calculations predict that, as the degree of superheat is increased, a larger amount of liquid is lost initially to vapour, tending towards an overall faster spray evaporation rate, but causing a reduction in volatility of the remaining liquid, which tends towards a reduction in the evaporation rate of the overall liquid. The adiabatic flash calculation also accounts for the reduction in equilibrium liquid and vapour temperature, which alters evaporation rate. Neither method explicitly allows quantification of any additional mechanical break-up provided by the flash boiling process.

Both the spray chamber images and the motored spray images taken in the corresponding optical engine have been used to understand particulate matter emissions results obtained from the combustion of the M15 fuels (Fuels A^+, A, A^- and Fuel B) using a DMS500. The experiment was performed at a part load condition at 1000 rpm. The results from the Fuel A family show that the particulate number counts were consistently low as the fuel composition and fuel temperature were varied, using an injection timing of 280°CA BTDC, with the exception of Fuel A at 90°C and 105°C and $\lambda = 0.9$. The Fuel B particulate matter measurements produced more varied results as injection timing and cylinder head temperature were changed. At some conditions, the particulate matter emissions from the combustion of Fuel B were at a similar level to those from Fuel A, despite the addition of aromatic and heavy components to Fuel B. At a very early injection timing (310°CA BTDC), the level of piston impingement was high. However, it is thought that the low valve lift at this timing allowed a combination of lowered cylinder pressure and closer interaction with a faster intake air flow to actually improve mixture preparation and prevent the formation of potential rich combustion sites. The particulate matter results for this injection timing were consistently low, even for rich mixtures.

For the later injection timings investigated, the cylinder pressure was higher due to the increased valve lift. At 280°CA BTDC, a large number of particulates were measured during the rich combustion studies at cylinder head temperatures of 90°C and 105°C. This increase was for the smaller sizes of particulate matter, with significant increases in count up to 100 nm and a peak at around 40 nm with an

increase in count value of two orders of magnitude. It is thought that, in this case, the highly collapsed spray with heavy piston impingement does create conditions favourable for particulate matter formation (persistent fuel films), due to the lack of favourable low valve lift effects that would be present at the earlier injection timing.

At an injection timing of 250°CA BTDC, the flash boiling sprays no longer produced large levels of piston impingement. However, increased particulate number counts were observed (again at sizes below 100 nm), at the colder fuel temperatures, which are attributed to liner impingement and a reduction in the time available for fuel film evaporation and mixture preparation.

7 Original Work, Conclusions and Future Work

7.1 Originalities

Specific originalities and novel aspects to the research work presented in this thesis include:

- An atmospheric pressure continually-purging spray chamber that was designed, built and operated, complete with a novel fuel delivery and pressurization system, operable to 400 bar. This allows convenient testing of gasoline injectors under a range of early injection strategy operating conditions, for future spray research.

- Multi-component droplet evaporation models were created that accounted for non-ideal fluid diffusion within the droplets, for alcohol-containing model gasoline fuels. The incorporation of these models was deemed important due to the highly non-ideal nature of these fuel mixtures. This was simplified to a pseudo-binary liquid diffusion-controlled approach for practical application to droplet evaporation calculations.

- A method to combine the droplet heat equation (for droplet temperature calculation) with superheated boundary conditions (for flash boiling sprays) was introduced. A simplified decision process was created to track whether the droplet surface temperature remains at the boiling temperature, with no dependence on a choice of temperature threshold.

- A comparison of modelling approaches for droplet heating and non-ideal multi-component droplet evaporation was performed, in order to select the most appropriate techniques under different operating conditions, both for single droplet modelling and within a LPT, RANS CFD simulation.

- M15 methanol/gasoline blend fuels were designed to assess independently the effects of spray behaviour and of fuel composition on subsequent particulate matter emissions. As the degree of fuel superheat was increased, the M15 sprays produced a range of behaviour similar to previous studies of superheated gasoline sprays (*e.g.* [44]), including a very high axial penetration at the highest degree of superheat. Increased axial penetration, due to the very high vapour pressure of the M15 blends, is expected during engine operation. This may help to explain why, at some conditions, there have been reports of unexpectedly high measured PM emissions from GDI engines fuelled with similar blends.

7.2 Conclusions

The air/fuel mixture preparation in a DISI engine can have a strong influence on the subsequent combustion and particulate emissions. Due to the increased uptake of this type of engine for passenger vehicles in many markets, and the increasingly tight emissions standard that all vehicles must meet, improvements in our understanding of mixture preparation will allow progress to be made on the reduction of tailpipe particulate emissions and better air quality. In this thesis GDI fuel sprays and fuel vaporization have been studied, along with the particulate matter emitted from GDI combustion, to help in this process. The main findings from the research are summarized in the following sections.

7.2.1 Non-ideal multi-component fuel models

Many fuels in current use for gasoline engines contain oxygenated components, such as ethanol and methanol, with the overall proportion of these components expected to rise. As the basic gasoline in markets such as the EU and the USA shifts from E5 towards E15 or E20, the need to incorporate the modelling of the

non-ideal interactions between ethanol and hydrocarbons will increase. This was achieved in this work using a non-ideal vapour-liquid equilibrium model with activity coefficients calculated from the UNIFAC model for multi-component mixtures and the NRTL model for mixtures of iso-octane and ethanol. The effect of this was demonstrated in the marked increase in vapour pressure for binary fuel blends and the multi-component model gasoline blends studied in this thesis. This in turn affects the evaporation rate of droplets. The non-ideality exhibited above around 10% ethanol content by volume was also shown to affect the ability of hydrocarbon species and ethanol to mix inside the droplets within the short timescales available during droplet evaporation, from the results of a detailed single droplet simulation.

Both binary model fuels and multi-component model fuels were investigated in this thesis to represent gasoline. Whilst the iso-octane/ethanol model fuel ably captures the non-ideal behaviour of a gasoline/ethanol mix, it was found that, as the amount of ethanol, or the internal mixing model, was varied, the trends seen from the seven component model fuels with ethanol were different to those observed with the iso-octane/ethanol model fuel.

The non-ideal fuel formulations were then included in a spray CFD solver (in OpenFOAM), that employed Lagrangian Particle Tracking to model the droplets and a RANS approach for gas phase turbulence. When the non-ideal behaviour is ignored in a spray CFD simulation, the expected errors in spray evaporation rate are found to be largest for cases that represent an early injection strategy. At these conditions, with a E15 ethanol/iso-octane blend, there was up to a 7% difference in predicted liquid penetration and up to a 24% difference in vapour mass produced, when the non-ideal fuel model was included. In the late injection cases that were studied, as the liquid volatility increased (by inclusion of non-ideal vapour-liquid equilibrium), a greater degree of spray cooling occurred, which negated much of the effect of the change in intrinsic evaporation rate. Therefore, the differences observed between the ideal and non-ideal fuel models were much smaller: up to a 1% difference in predicted liquid penetration and up to a 9% difference in vapour mass produced.

7.2.2 Spray droplet temperature and superheat models

The droplet surface temperature of an evaporating droplet will determine how fast liquid evaporates from the surface. Therefore, models that calculate the non-uniform temperature distribution within a droplet, in order to calculate the surface temperature more accurately, are thought to lead to a more accurate solution for droplet and spray evaporation. Models for transient droplet temperature change were implemented for single droplets and as a sub-model in a spray CFD solver. The default uniform temperature (lumped) model was compared with techniques that calculated the temperature distribution within the droplet. In the single droplet cases, it was found that, across a range of temperature and pressure conditions appropriate for GDI fuel sprays (both early and late injection), the lumped model droplet lifetime could be in error by up to 13%. The worst cases corresponded strongly with conditions where the droplet would undergo a large transient temperature change, either cooling or heating. All models predicted the same steady state temperature, under steady conditions, and therefore the same steady evaporation rate.

In the spray simulations, it was found that the evaporation rate errors between the lumped model and the non-uniform temperature models were much smaller than those found in the single droplet cases. This is partly due to the convergence of the gas phase temperature towards the spray liquid temperature (either heating or cooling), which leads to the droplets undergoing a smaller transient temperature change. Thus, the accumulated error from the lumped model over the transient phase was smaller. In addition, during a spray simulation, phenomena such as secondary break-up and droplet coalescence are modelled. This will reset the temperature distribution of the modelled spray droplets and otherwise obscure the effects of a small change to evaporation rate. Therefore, unless there is a more detailed, validated model of how droplet temperature distribution is conserved during collision, it is expected to be of little benefit to include non-uniform droplet temperature models in spray simulations at conditions relevant to GDI engines.

Droplet superheat models were explored for the single droplet simulations, since most conditions of relevance to GDI early injection strategy will cause fuel to be injected with some degree of superheat. A new model was put forward to decide whether the droplet surface remained at its boiling temperature. This model considered the energy balance between the droplet and its surroundings to decide if more or less heat should pass from the droplet to the surroundings (or *vice versa*) depending on the fuel species mass balance. This method was found to be more robust and was insensitive to the chosen threshold of sub-cooled surface temperature. This model was then applied in conjunction with the non-uniform droplet temperature model solution.

However, full modelling of a superheated fuel spray from a multi-hole GDI injector, in order to predict the change in structure associated with increasing degrees of flash boiling behaviour, was not carried out. This will require additional modelling effort in terms of understanding the growth of the vapour phase inside the injector nozzle, and the interaction between droplet plumes and the induced air motion created under flash boiling conditions.

7.2.3 Spray droplet internal composition models

A multi-component fuel droplet in a GDI engine will vaporize in a short space of time, and many components with a large range of volatility must evaporate. Different models for this process have been explored, including the well-mixed model, where fuel species leave the droplet in a distillation-like fashion; the unmixed model, where the liquid composition does not change; and the liquid diffusion-controlled model with internal vortex enhancement, where the finite diffusion time of species through the droplet to the surface is explicitly modelled.

For the binary fuel mixture iso-octane/ethanol, the liquid diffusion-controlled model predicted a very slow mixing of the two fuel species, due to their highly non-ideal interaction. This meant that ethanol was expected to remain in the droplet throughout the droplet lifetime, unless another mechanism exists that tends to distribute the fuel species throughout the droplet. This led to the use of the unmixed

model in the CFD spray simulations, for comparison with the well-mixed model, since the full diffusion-controlled model would require an impractical computational effort. In single droplet liquid diffusion-controlled simulations, the lifetime was predicted to be extended in most cases; whereas, in the equivalent unmixed spray CFD simulations, the spray evaporation rate was predicted to increase, particularly at early injection conditions. This emphasises the requirement to investigate the effects of detailed droplet models at a whole spray level, due to the interplay of droplet evaporation, gas phase cooling and other spray phenomena.

With the multi-component fuels, single droplet simulations predicted an improved mixing rate of the ethanol through the hydrocarbon species, due in part to the cross-diffusion terms in the multi-component case. Therefore, in the simulations performed here, ethanol always left the droplet before the droplet had fully evaporated, although more slowly than during the well-mixed case. This boosted the volatility of the remaining liquid, and tended to decrease droplet lifetime in comparison to the well-mixed assumption. This is in contrast to many of the findings from the single droplet binary fuel simulations.

7.2.4 Suitable model fuels for spray droplet evaporation

To capture enough of the real behaviour of a multi-component gasoline spray and droplet evaporation process, a realistic multi-component model fuel should be used. This should match the volatility trends of the real fuel throughout the distillation curve. It has been shown throughout this thesis that the binary non-ideal mixtures and multi-component non-ideal fuels tended to behave differently to each other and to ideal mixtures, with respect to modelling assumptions. So to move to a more detailed model for a spray simulation, without also using an appropriate fuel model, could lead to erroneous results.

7.2.5 Effect of fuel saturation pressure on spray structure

High speed fuel spray images, with a short shutter duration, were captured using an atmospheric pressure, continually-purging chamber, using both backlit shadowgraphy and Mie scattering techniques. The injector block temperature was

controlled in order to vary the fuel temperature as it emerged into the chamber. In this way, flash boiling fuel sprays could be created with varying degrees of superheat. Fuel spray superheat was characterized by the fuel saturation pressure ratio R_{p}, defined as the calculated vapour pressure at the injector temperature divided by the ambient pressure. The injector position and chamber scale matched that of the accompanying optical engine. Poor evaporative performance or surface impingement may lead to the creation of conditions where particulate matter may be formed during combustion.

It was found that spray chamber liner impingement occurred for sub-cooled sprays and for superheated sprays up to $R_{\mathrm{p}} = 2$, which would directly correspond to liner impingement in the optical engine for an early injection strategy.

As the spray became more superheated, individual spray plumes would broaden, leading to plume interaction. This caused a spray collapse phenomenon, which, at low levels of fuel superheat, tended to reduce the overall axial penetration of the spray. This is considered a positive action, as it would reduce the likelihood of piston crown impingement. In addition, plumes are drawn away from the liner, removing the chance of impingement at this location. As superheat was increased further, spray collapse increased further, narrowing the overall spray angle and increasing the axial penetration rate. This would tend to increase the likelihood of piston impingement. The minimum axial penetration rate was found to occur in this work at a fuel saturation pressure ratio of 4.8, and the ranges where different behaviour occurred corresponded well with previous studies.

Two M15 methanol/gasoline blends were studied in the spray chamber, Fuel A and B. These fuels had a very similar distillation curve up until the T50 point, after which they diverged due to the presence of heavy components in Fuel B. However, the spray shape and early structure were very similar to each other. This means only the light end of the fuel dictates the spray flash boiling behaviour for a given injector. The fuel temperature exceeded the T50 value for the fuels yet the spray structure was still very similar. This confirms that flash boiling is a non-equilibrium process, during which there will not be time for the light

components to evaporate from the liquid, in order to achieve the position on the distillation curve corresponding to the initial liquid temperature. For some of the Fuel A experiments, the fuel injection temperature exceeded the final boiling point of Fuel A yet instantaneous, complete evaporation did not occur and there was no significant difference in the spray structure between Fuel A and Fuel B (which had a much higher final boiling point) at these temperatures.

7.2.6 Usage of single droplet models to predict spray trends

The single droplet simulations (performed at conditions equivalent to those examined in the spray chamber experiments) were useful in analysing trends in fuel spray evaporation. The superheated droplet simulations predicted that large amounts of the liquid fuel would vaporize very shortly after injection. However, the amount of liquid fuel observed from Mie scattering experiments just after injection did not greatly decrease as the degree of superheat was increased. Thus, the experiment may be observing smaller droplets, more finely packed, as plumes intermingle near the nozzle. There was a corresponding adiabatic flash calculation, which predicted that a smaller amount of liquid fuel would vaporize upon superheated injection than the superheated single droplet simulations had predicted. No quantitative comparisons of either numerical approach to the experimental data were possible.

7.2.7 Injection timing and spray superheat effects on M15 combustion and particulate emissions

The experience gained from single droplet studies and spray chamber fuel spray images was used to help explain the PM emissions results from the M15 fuels (Fuels A^+, A, A^- and Fuel B) that were obtained using the optical engine and associated equipment (described in Section 3.3). These results are fully presented in [46]. It was found that for the Fuel A family, whose heaviest component was iso-octane, the particulate number counts were consistently low as the fuel composition was changed and as the fuel temperature was varied, with the exception of the medium volatility fuel (Fuel A) at the highest fuel temperatures under rich conditions. This increase occurred solely in particulates of size less than 100 nm.

There was also a mode consisting of a larger size of PM, in the range 100–400 nm, which tended to increase in number slightly as fuel temperature decreased, and was broadly similar in number at both rich and stoichiometric conditions. The discovery that the particulate number counts increased for one mode only indicated that they were likely generated by a particular source of locally rich mixture combustion. This coincides with the increased level of piston impingement expected from the M15 spray images captured in the spray chamber and in motoring engine experiments with a full optical liner (performed in [46]).

The Fuel B that was tested contained aromatic and heavy components, and therefore had a higher final boiling point, but a similar light end to Fuel A. At a very early injection timing (310°CA BTDC), there was a great amount of piston impingement at all fuel temperatures. However, this did not correspond with a great increase in particulate number count. The coldest fuel temperatures investigated at this injection timing resulted in the highest particulate number counts. The total counts across the temperature range were typically slightly higher than those seen at the other injection timings.

As the injection was retarded to 280°CA BTDC, the amount of particulate matter measured when the fuel temperature was high (90°C and 105°C) greatly increased for the rich combustion studies, by two orders of magnitude at the modal particulate size. This corresponded with a highly superheated fuel spray and a collapsed spray structure with increased axial penetration, causing significant piston impingement. Again, this increase was in the range of particulate size up to 100 nm, with the larger particulates mainly unaffected. It is concluded that the improved atomization at the 310°CA BTDC timing (due to reduced in-cylinder pressure, which caused the fuel to experience an even greater degree of superheat), and the improved interaction of the spray with the higher air induction velocity at the low valve lift, prevent the creation of extensive piston crown fuel films, which could persist until the start of combustion. The tests performed at stoichiometric conditions showed a more modest increase in particulate number count in the smaller size range.

Retarding the injection timing further to 250°CA BTDC reduced the level of piston impingement caused by the highly superheated sprays. The particulate number counts returned to a similarly low level to that found at 310°CA BTDC. However, for the 23°C and 60°C fuel sprays, particulate numbers increased in the size range below 100 nm. This was attributed both to the reduced evaporation rate due to the colder fuel temperatures, and a greater degree of liner impingement due to the difference in piston position when injection occurred.

7.3 Possible Extension Work

7.3.1 Droplet simulations

Simplified multi-component liquid diffusion-controlled simulations

To perform simplified liquid diffusion-controlled studies for multi-component mixtures, a similar approach to the two-point temperature model could be explored. This would involve the tracking of both the interior and the surface mass fraction for each species, using an internal mass transfer film thickness of size $\sqrt{\pi \chi D_{\mathrm{L}} t}$. If successful, this would result in a much shorter computational time, which may enable this model to be practically implemented within spray solvers, in a similar way to the two-point temperature model (see Chapter 5).

Low temperature non-equilibrium studies

Some of the droplet simulations performed at relatively low temperatures and pressures (part load, early injection strategy) have resulted in the droplet temperature cooling well below 0°C during the transient phase, due to the requirement for vapour-liquid equilibrium at the droplet surface. This occurs in particular with fuel blends that contain methanol and ethanol, due to their large enthalpy of vaporization and vapour pressure. In order to check the accuracy of these temperature results, a non-equilibrium model could be employed, which would relax the assumption of vapour-liquid equilibrium at the droplet surface and may alter the evaporation rate. This has been performed for droplets in hot environments (see, for example, Miller *et al.* [91]), but not for the relatively cold environments of early DISI injection strategy.

Quantitative comparison to Mie scattering images

In order to more quantitatively compare single droplet results with spray image data, droplets could be simulated with an altered gas phase temperature to mirror more closely the conditions actually experienced by droplets within a spray. This could be calculated by allocating each droplet a sphere of influence and finding the reduction in gas temperature which is due to droplet evaporation. Gas temperatures thus estimated could be validated against experimental data and experience from CFD simulations. This would enable a more accurate fitting of an initial droplet size distribution to spray Mie scattering data, as performed in [140].

7.3.2 CFD simulations

For simplified GDI spray modelling, a bespoke non-reacting solver would be helpful for OpenFOAM, which may find wider use.

Two-point superheated temperature model

To aid in the modelling of flash boiling fuel sprays, the two-point (non-uniform) temperature distribution model introduced in this thesis for OpenFOAM should be formally extended to deal with superheated droplets. There is an existing model for uniform temperature, superheated droplets, which can inform this work. It is here that the two-point models are most likely to have improved accuracy in the simulation, due to the large transient changes that are expected in the droplet temperatures.

Multi-component mixtures

Each of the model variations investigated in this thesis (*i.e.* models for vapour-liquid equilibrium, droplet internal composition and droplet temperature) should be extended to true multi-component mixtures. This would be most efficiently performed as part of the validation of multi-component fuel spray modelling, as compared with data from the spray chamber or another optically accessible experiment.

7.3.3 Experimental work

Chamber air density

In future comparisons of static spray images from the spray chamber, and motored spray images from optical engines, an additional parameter - the liquid/air density ratio - could be included to characterize the sprays. Under different ambient density conditions, the aerodynamic forces on the plumes will change. This will affect not only the spray penetration rate but also the distance from the injector at which neighbouring plumes begin to interact, which in turn will influence the structure of flash boiling sprays.

Alcohol components - effect on spray and combustion

To further investigate the effect of fuel alcohol composition, experiments could be carried out which attempted to isolate and independently vary the fuel oxygen content, the fuel enthalpy of vaporization and the fuel vapour pressure. Some of these will be difficult to match between oxygenated and non-oxygenated fuels, due to the very high enthalpy of vaporization of ethanol and methanol. However, other oxygenated components may be sought. Then, predicted droplet evaporation rate, spray characteristics, and combustion and particulates behaviour could be analysed. This may help in understanding which properties of alcohol species are most significant in determining the behaviour of alcohol/gasoline blended fuels.

M15 fuels - effect on spray and combustion

Regarding the M15 model fuel studies, comparison could be made with M0 fuels that had the same underlying hydrocarbon (gasoline) mixture, and with M15 fuels that had varying hydrocarbon contents and final boiling point. It would also be interesting to vary the aromatic content, as well as the aromatic species used, since toluene is not particularly representative of the aromatic content of gasoline (as it is the simplest species apart from benzene). This would allow a breakdown of contributions to PM emissions, in terms of the contribution from the change in fuel light end volatility (which mainly affects superheated spray structure), the amount and type of aromatic components, and the heavy end of fuel.

A greater range of speed and load conditions could be investigated in spray imaging experiments and particulate measurements. This would map out which engine conditions and injection timings allowed the oxygen content in an M15 fuel to be of benefit in terms of reduced PM emissions, and which conditions would require more careful engine calibration, for markets with methanol-containing fuels.

Better prediction of PM emissions

The PN index of Leach [13] intended to quantify the effects of both the fuel volatility and the fuel composition on the PN measurement from a DISI engine. This might be extended to an operating point-specific metric, to include the effects of the actual fuel saturation pressure ratio experienced by the fuel spray (given the coolant temperature and the cylinder pressure during injection). Additionally, the metric might include the injection timing, as described by some non-dimensionalized injector-to-piston axial distance or injector-to-liner distance at SOI, depending on the orientation and positioning of the GDI injector.

7.4 Publications Relating to this Thesis

Some of the work in this thesis draws on or is related to the work in the following:

- JD Camm, R Stone, MH Davy, and D Richardson, (2014). The Modelling of Single and Multi-Component Droplet Evaporation. THIESEL 2014 Conference on Thermo- and Fluid Dynamic Processes in Direct Injection Engines, Universitat Politècnica de València, València, Spain.

- JD Camm, R Stone, MH Davy, and D Richardson, (2015). The Modelling of Multi-Component Droplet Evaporation, Including Superheated Droplets. Fuel Systems for IC Engines, IMechE, London, UK.

- JD Camm, R Stone, MH Davy, and D Richardson, "The Effect of Non-Ideal Vapour-Liquid Equilibrium and Non-Ideal Liquid Diffusion on Multi-Component Droplet Evaporation for Gasoline Direct Injection Engines," SAE Technical Paper 2015-01-0924, 2015, doi:10.4271/2015-01-0924.

- SH Mohd Murad, JD Camm, MH Davy, R Stone, and D Richardson, "Spray Behaviour and Particulate Matter Emissions with M15 Methanol/Gasoline Blends in a GDI Engine," SAE Technical Paper 2016-01-0991, 2016, doi:10.4271/2016-01-0991.

References

[1] M Sandford, G Page, and P Crawford. The All New AJV8. *SAE Technical Paper 2009-01-1060*, 2009.

[2] Audi. The New Audi V8 TFSI Engine Part 1: Design and Mechanics. *MTZ Worldwide*, 02, 2013.

[3] UK-developed high-tech Ford 1.0-litre EcoBoost engine launched by Mulally. `www.ford.co.uk/FordFleet/NewsAndReviews/FordForBusiness/2012/January/Ecoboost-Engine`, accessed 12$^{\text{th}}$November 2015, January 2012.

[4] Lars Christian, Riis Johansen, Ingemar Denbratt, and Stina Hemdal. Drive cycle particulate and gaseous emissions from a parallel hybrid combustion engine and electric powertrain. *SAE Technical Paper 2015-24-2538*, 2015.

[5] U Spicher and T Heindenreich. *Stratified-charge combustion in direct injection gasoline engines, Ed. H Zhao.* Woodhead Publishing Ltd and CRC Press, 2010.

[6] Longfei Chen, Mike Braisher, Alison Crossley, Richard Stone, and Dave Richardson. The influence of ethanol blends on particulate matter emissions from gasoline direct injection engines. *SAE Technical Paper 2010-01-0793*, 2010.

[7] Richard Stone. *Introduction to Internal Combustion Engines.* Basingstoke: Palgrave Macmillian, 4th edition, 2012.

[8] H Ando. Combustion control technologies for gasoline engines. *Lean Burn Combustion Engines, IMechE*, page S433/001/96, 3–4 December 1996.

[9] A Kufferath, W Wiese, W Samenfink, H Dageförde, T Knorsch, and P Jochmann. Assessment of feasible systems solutions for future particle emission requirements. *Fuel Systems for IC Engines, IMechE*, 10–11 March 2015.

[10] G Hoffmann, B Befrui, A Berndorfer, WF Piock, and DL Varble. Influence of GDi multi-hole fuel system pressure on spray and engine emissions. *Fuel Systems for IC Engines, IMechE*, 10–11 March 2015.

[11] H Shibata, T Kito, S Saitoh, M Walford, I Williams, and H Kaneta. Gasoline direct injection spray improvements for future emission legislation. *Fuel Systems for IC Engines, IMechE*, 10–11 March 2015.

[12] Peter Eastwood. *Particulate Emissions from Vehicles.* Wiley, SAE International, 2008.

[13] Felix Leach. *Particulate Matter Emissions from Gasoline Direct Injection Engines.* DPhil thesis, Department of Engineering Science, University of Oxford, 2014.

[14] A Nemmar, PHM Hoet, B Vanquickenborne, D Dinsdale, M. Thomeer, MF Hoylaerts, H Vanbilloen, L Mortelmans, and B Nemery. Passage of inhaled particles into the blood circulation in humans. *Circulation*, 105(4):411–414, 2002.

[15] Roy Harrison and Jianxin Yin. Characterisation of particulate matter in the United Kingdom: Literature Review. Technical report, University of Birmingham, 2004.

[16] Michael Braisher. *Particulate Matter Emissions Measurements from Engines and Vehicles.* DPhil thesis, Department of Engineering Science, University of Oxford, 2010.

[17] A Seaton, W MacNee, K Donaldson, and D Godden. Particulate air pollution and acute health effects. *Lancet*, 345(8943):176–178, 1995.

[18] J Spengler and R Wilson. *Particles in our air – Concentration and health effects, Eds. J Spengler and R Wilson.* Harvard University Press, 1996.

[19] International Commission on Radiological Protection. Task Force on Lung Dynamics. *Health Physics*, 12:173–207, 1966.

[20] David B Kittelson. Engines and nanoparticles: A review. *Journal of Aerosol Science*, 29(5-6):575–588, 1998.

[21] European Comission. Amendment No 459/2012 as regards emissions from light passenger and commercial vehicles (Euro 6). *Official Journal of the European Union*, 2012(459/2012):16–24, 2012.

[22] Environmental Protection Agency. Control of Air Pollution From New Motor Vehicles: Tier 2 Motor Vehicle Emissions Standards and Gasoline Sulfur Control Requirements. *Federal Register*, 65:6698–6870, 2000.

[23] Environmental Protection Agency. Control of Air Pollution From Motor Vehicles: Tier 3 Motor Vehicle Emission and Fuel Standards. *Federal Register*, 79:23414–23886, 2014.

[24] California Code of Regulations. California 2015 and subsequent model criteria pollutant exhaust emission standards and test procedures and 2017 and subsequent model greenhouse gas exhaust emission standards and test procedures for passenger cars, light-duty trucks, and medium-duty vehicles . Technical report, California Environmental Protection Agency Air Resources Board, 2012.

[25] Japan: Light-duty: Emissions. `transportpolicy.net/index.php?title=Japan:_Light-duty:_Emissions`, accessed 12th November 2015, September 2013.

[26] China: Light-duty: Emissions. `transportpolicy.net/index.php?title=China:_Light-duty:_Emissions`, accessed 12$^{\text{th}}$November 2015, April 2015.

[27] AECC. AECC Newsletter. `http://www.aecc.eu/en/Newsletter/Newsletter.html`, 2014.

[28] CARS 2020 Report. Technical Report October, European Commission, 2014.

[29] International: Light-duty: Wltp. `transportpolicy.net/index.php?title=International:_Light-duty:_WLTP`, accessed 12$^{\text{th}}$November 2015, January 2014.

[30] M Tutuianu et al. Development of a Worldwide harmonized Light duty driving Test Cycle (WLTC). Technical report, United Nations Economic Commission for Europe - UN/ECE/WP.29/GRPE/WLTP-IG, 2013.

[31] European Commission. A Clean Air Programme for Europe. *Communication from the Commission to the European Parliament, the Council, the European Economic and Social Committee and the Committee of the Regions*, COM(2013), 2013.

[32] Fabian Köpple, Dimitri Seboldt, Paul Jochmann, Alexander Hettinger, Andreas Kufferath, and Michael Bargende. Experimental investigation of fuel impingement and spray-cooling on the piston of a GDI engine via instantaneous surface temperature measurements. *SAE Int. J. Engines*, 7:1178–1194, 2014.

[33] Philip Price. *Direct Injection Gasoline Engine Particulate Emissions*. DPhil thesis, Department of Engineering Science, University of Oxford, 2009.

[34] Grant Lumsden, Dave OudeNijeweme, Neil Fraser, and Hugh Blaxill. Development of a turbocharged direct injection downsizing demonstrator engine. *SAE Int. J. Engines*, 2(1):1420–1432, 2009.

[35] MM Elkotb. Fuel atomization for spray modelling. *Progress in Energy and Combustion Science*, 8(1):61–91, 1982.

[36] Arthur H Lefebvre. *Atomization and Sprays*. CRC Press, 1989.

[37] RD Reitz and R Diwakar. Effect of drop breakup on fuel sprays. *SAE Technical Paper 860469*, 1986.

[38] J Naber and D Siebers. Effects of gas density and vaporization on penetration and dispersion of diesel sprays. *SAE Technical Paper 960034*, 1996.

[39] Markus Behringer, Pavlos Aleiferis, Dave OudeNijeweme, and Paul Freeland. Spray formation from spark-eroded and laser-drilled injectors for DISI engines with gasoline and alcohol fuels. *SAE International Journal of Fuels and Lubricants*, 7(3), 2014.

[40] Maryam Moulai, Ronald Grover, Scott Parrish, and David Schmidt. Internal and near-nozzle flow in a multi-hole gasoline injector under flashing and non-flashing conditions. *SAE Technical Paper 2015-01-0944*, 2015.

[41] PG Aleiferis and ZR Van Romunde. An analysis of spray development with iso-octane, n-pentane, gasoline, ethanol and n-butanol from a multi-hole injector under hot fuel conditions. *Fuel*, 105:143–168, 2013.

[42] Joseph Kazour, Bizhan Befrui, Harry Husted, Michael Raney, and Daniel Varble. Innovative sprays and particulate reduction with GDi injectors. *SAE Technical Paper 2014-01-1441*, 2014.

[43] Wei Zeng, Min Xu, Gaoming Zhang, Yuyin Zhang, and David J. Cleary. Atomization and vaporization for flash-boiling multi-hole sprays with alcohol fuels. *Fuel*, 95:287–297, 2012.

[44] Min Xu, Yuyin Zhang, Wei Zeng, Gaoming Zhang, and Ming Zhang. Flash boiling: Easy and better way to generate ideal sprays than the high injection pressure. *SAE International Journal of Fuels and Lubricants*, 6(1):2013–01–1614, 2013.

[45] A Wood, G Wigley, and J Helie. Analysis of multi-hole GDI injectors under flash boiling conditions experimental test-rig, 2013.

[46] Safwan Hanis bin Mohd Murad, Richard Stone, Joseph Camm, Martin Davy, and Dave Richardson. Spray behaviour and particulate matter emissions with M15 methanol/gasoline blends in a GDI engine. *SAE Technical Paper*, 2015-01-0206, 2016.

[47] RD Oza and JF Sinnamon. An experimental and analytical study of flash-boiling fuel injection. *SAE Technical Paper 830590*, 1983.

[48] Jiro Senda, Tamaki Nishikori, Tokihiro Tsukamoto, and Hajime Fujimoto. Atomization of spray under low-pressure field from pintle type gasoline injector. *SAE Technical Paper 920382*, 1992.

[49] Masayuki Adachi, Vincent G McDonnell, Daisuke Tanaka, Jiro Senda, and Hajime Fujimoto. Characterization of fuel vapor concentration inside a flash boiling spray. *SAE Technical Paper 970871*, 1997.

[50] Daisuke Kawano, Yuichi Goto, Matsuo Odaka, and Jiro Senda. Modeling atomization and vaporization processes of flash-boiling spray. *SAE Technical Paper 2004-01-0534*, 2004.

[51] D Kawano. Numerical study on flash-boiling spray of multicomponent fuel. *FISITA World Automotive Congress, Barcelona 2004*, 2004.

[52] K Neroorkar and DP Schmidt. A computational investigation of flash-boiling multi-hole injectors with gasoline-ethanol blends. *SAE Technical Paper 2011-01-0384*, 2011.

[53] Z Bilicki and J Kestin. Physical aspects of the relaxation model in two-phase flow. *Proceedings of the Royal Society A: Mathematical, Physical and Engineering Sciences*, 428(1875):379–397, 1990.

[54] GM Bianchi, C Forte, S Negro, and P Pelloni. A 1d model for the prediction of flash atomization in gdi multi-hole injectors: Preliminary results. *SAE International Journal of Engines 2008-01-2516*, 1(1):1278, 2009.

[55] Sergio Negro, Federico Brusiani, and Gian Marco Bianchi. Superheated sprays of alternative fuels for direct injection engines. *SAE Technical Paper 2012-01-1261*, 2012.

[56] Robert C Reid, John M Prausnitz, and Bruce E Poling. *The Properties of Gases and Liquids*. New York: McGraw-Hill, 4th edition, 1987.

[57] BSI. BS EN 228:2012 - Automotive fuels. Unleaded petrol. Requirements and test methods. Technical report, British Standards Institution, 2012.

[58] Felix Leach, Richard Stone, and Dave Richardson. The influence of fuel properties on particulate number emissions from a direct injection spark ignition engine. *SAE Technical Paper 2013-01-1558*, 2013.

[59] F Leach, R Stone, D Fennell, D Hayden, D Richardson, and N Wicks. Particulate matter emissions from gasoline direct injection spark ignition engines. In *IC Engines*. IMechE, 2013.

[60] K Aikawa and JJ Jetter. Impact of gasoline composition on particulate matter emissions from a direct-injection gasoline engine: Applicability of the particulate matter index. *International Journal of Engine Research*, 15(3):298–306, 2013.

[61] Aron Butler, Rafal Sobotowski, George Hoffmann, and Paul Machiele. Influence of fuel PM index and ethanol content on particulate emissions from light-duty gasoline vehicles. *SAE Technical Paper 2015-01-1072*, 2015.

[62] Rafal A Sobotowski, Aron D Butler, and Zuimdie Guerra. A pilot study of fuel impacts on PM emissions from light-duty gasoline vehicles. *SAE Int. J. Fuels Lubr.*, 8:214–233, 2015.

[63] Carl Vuk and Steven J Vander Griend. Fuel property effects on particulates in spark ignition engines. *SAE Technical Paper 2013-01-1124*, 2013.

[64] European Commission. Comission regulation (EC) No 692/2008 of 18 July 2008. *Official Journal of the European Union*, page 136, 2008.

[65] Tetsuya Aizawa, Nozomi Takahata, Kei Okabe, and Yuta Mizutani. Effect of fuel aromatics on in-flame diesel soot nanostructure via HRTEM. *JSAE Technical Paper 20159155*, 2015.

[66] F Leach, R Stone, M Davy, and D Richardson. Comparing the effect of different oxygenate components on PN emissions from GDI engines. In *IC Engines*. IMechE, 2015.

[67] Hwanam N Kim and Byungchul C Choi. Effect of ethanol-diesel blend fuels on emission and particle size distribution in a common-rail direct injection diesel engine with warm-up catalytic converter. *Renewable Energy*, 33(10):2222–2228, 2008.

[68] T Litzinger, M Stoner, H Hess, and A Boehman. Effects of oxygenated blending compounds on emissions from a turbocharged direct injection diesel engine. *International Journal of Engine Research*, 1(1):57–70, 2000.

[69] J Trost, L Zigan, and A Leipertz. Quantitative vapor temperature imaging in DISI-sprays at elevated pressures and temperatures using two-line excitation laser-induced fluorescence. *Proceedings of the Combustion Institute*, 34(2):3645–3652, 2013.

[70] M Storch, T Knorsch, L Zigan, M Wensing, and S Will. High-speed visualization of ignition processes and sooting combustion at DISI conditions for different ethanol-gasoline fuel blends. In *European Combustion Meeting*, 2013.

[71] PJ Linstrom and WG Mallard, editors. *NIST Chemistry WebBook, NIST Standard Reference Database Number 69*. National Institute of Standards and Technology, Gaithersburg MD, 20899, http://webbook.nist.gov, (retrieved November 11, 2015).

[72] DB Spalding. Combustion of fuel particles. *Fuel*, 30:121, 1951.

[73] GAE Godsave. Studies of the combustion of drops in a fuel spray: The burning of single drops of fuel. In *Fourth Symposium (International) on Combustion, Williams and Wilkins, Baltimore*, 1953.

[74] GM Faeth. Current status of droplet and liquid combustion. *Energy and Combustion Science*, 3(4):149–182, 1977.

[75] William A Sirignano. *Fluid Dynamics and Transport of Droplets and Sprays*. Cambridge: CUP, 2010.

[76] Chung K Law. *Combustion Physics*. Cambridge: CUP, 2006.

[77] Bruce E Poling, John M Prausnitz, and John P O'Connell. *The Properties of Gases and Liquids*. New York: McGraw-Hill, 5th edition, 2001.

[78] RB Bird, WE Stewart, and EN Lightfoot. *Transport Phenomena*. New York: Wiley, 1960.

[79] B Abramzon and WA Sirignano. Droplet vaporization model for spray combustion calculations. *International Journal of Heat and Mass Transfer*, 32(9):1605–1618, 1989.

[80] Zhou Zhifu, Wang Guoxiang, Chen Bin, Guo Liejin, and Wang Yueshe. Evaluation of evaporation models for single moving droplet with a high evaporation rate. *Powder Technology*, 240:95–102, 2013.

[81] R Clift, JR Grace, and ME Weber. *Bubbles, Drops, and Particles*. New York; London: Academic Press, 1978.

[82] RJ Haywood, R Nafziger, and M Renksizbulut. A detailed examination of gas and liquid phase transient processes in convective droplet evaporation. *Journal of Heat Transfer*, 111(2):495, 1989.

[83] CD-adapco. STAR ® Methodology for Internal Combustion Engine Applications. Technical Report VERSION 4.22, 2014.

[84] S Prakash and WA Sirignano. Liquid fuel droplet heating with internal circulation. *International Journal of Heat and Mass Transfer*, 21(7):885–895, 1978.

[85] MJM Hill. On a spherical vortex. *Phil. Trans. Roy. Soc. A*, 185:213–245, 1894.

[86] IE Johns Jr and RB Beckmann. Mechanism of dispersed-phase mass transfer in viscous, single-drop extraction systems. *AIChE Journal*, 12(1):10–16, 1966.

[87] Y Ra and RD Reitz. The application of a multicomponent droplet vaporization model to gasoline direct injection engines. *International Journal of Engine Research*, 4(3):193–218, 2003.

[88] Youngchul Ra and Rolf D Reitz. A model for droplet vaporization for use in gasoline and HCCI engine applications. *Journal of Engineering for Gas Turbines and Power*, 126(2):422, 2004.

[89] A Bader, P Keller, and C Hasse. The influence of non-ideal vapor–liquid equilibrium on the evaporation of ethanol/iso-octane droplets. *International Journal of Heat and Mass Transfer*, 64:547–558, 2013.

[90] Aage Fredenslund, Russell L Jones, and John M Prausnitz. Group-contribution estimation of activity coefficients in nonideal liquid mixtures. *AIChE Journal*, 21(6):1086–1099, 1975.

[91] RS Miller, K Harstad, and J Bellan. Evaluation of equilibrium and non-equilibrium evaporation models for many-droplet gas-liquid flow simulations. *International Journal of Multiphase Flow*, 24(6):1025–1055, 1998.

[92] MA Rahman and MZ Saghir. Thermodiffusion or Soret effect: Historical review. *International Journal of Heat and Mass Transfer*, 73:693–705, 2014.

[93] R Taylor and R Krishna. *Multicomponent Mass Transfer*. New York: Wiley, 1993.

[94] William A Sirignano and Guang Wu. Multicomponent-liquid–fuel vaporization with complex configuration. *International Journal of Heat and Mass Transfer*, 51(19-20):4759–4774, 2008.

[95] William A Sirignano and Randall T Imaoka. Vaporization and combustion in three-dimensional droplet arrays. *Proceedings of the Combustion Institute*, 30(2):1981–1989, 2005.

[96] V Deprédurand, G Castanet, and F Lemoine. Heat and mass transfer in evaporating droplets in interaction: Influence of the fuel. *International Journal of Heat and Mass Transfer*, 53(17-18):3495–3502, 2010.

[97] SS Sazhin, AE Elwardany, PA Krutitskii, V Deprédurand, G Castanet, F Lemoine, EM Sazhina, and MR Heikal. Multi-component droplet heating and evaporation: Numerical simulation versus experimental data. *International Journal of Thermal Sciences*, 50(7):1164–1180, 2011.

[98] A Daïf, M Bouaziz, X Chesneau, and A Ali Chérif. Comparison of multicomponent fuel droplet vaporization experiments in forced convection with the Sirignano model. *Experimental Thermal and Fluid Science*, 18(4):282–290, 1998.

[99] G. Brenn, L. J. Deviprasath, F. Durst, and C. Fink. Evaporation of acoustically levitated multi-component liquid droplets. *International Journal of Heat and Mass Transfer*, 50(25-26):5073–5086, 2007.

[100] John Measures. Final year project report: Experimental investigation into the vaporisation of single component liquid fuel droplets. Technical report, University of Oxford, 2007.

[101] JK Dukowicz. A Particle-Fluid Numerical Model for Liquid Sprays. *Journal of Computational Physics*, 35:229–253, 1980.

[102] HK Versteeg and W Malalasekera. *An Introduction to Computational Fluid Dynamics: The Finite Volume Method*. Harlow: Pearson, 2ndedition, 2007.

[103] J Serras-Pereira, Z Van Romunde, PG Aleiferis, D Richardson, S Wallace, and RF Cracknell. Cavitation, primary break-up and flash boiling of gasoline, iso-octane and n-pentane with a real-size optical direct-injection nozzle. *Fuel*, 89(9):2592–2607, 2010.

[104] SAE International. Gasoline Fuel Injector Spray Measurement and Characterization. Technical report, 2007.

[105] A Sobachkin and G Dumnov. Numerical Basis of CAD-Embedded CFD. In *NAFEMS World Congress 2013*, 2013.

[106] NI USB-621x User Manual, Bus-Powered M Series USB Devices. Technical report, National Instruments, 2009.

[107] Ziegler-Nichols Open-Loop Tuning Rules . `blog.opticontrols.com/archives/477`, accessed 5thJanuary 2016, May 2011.

[108] H Zhao. *Laser Diagnostics and Optical Measurement Techniques in Internal Combustion Engines*. Warrendale: SAE International, 2012.

[109] Xiaowei Wang. *Instantaneous In-cylinder Heat Transfer and Combustion Analysis in Spark Ignition Engines*. DPhil thesis, Department of Engineering Science, University of Oxford, 2008.

[110] Kingsley Reavell, Tim Hands, and Nick Collings. A fast response particulate spectrometer for combustion aerosols. *SAE Technical 2002-01-2714*, 2002.

[111] J Andersson et al. Particle Measurement Programme (PMP) Light-duty Inter-laboratory Correlation Exercise (ILCE-LD) Final Report. Technical report, European Commission Joint Research Centre Institute for Environment and Sustainability, 2007.

[112] Directive 2003/30/EC of the European Parliament and of the Council of 8 May 2003 on the promotion of the use of biofuels or other renewable fuels for transport, OJ L 123, 17.5.2003, p. 42-46.

[113] Environmental Protection Agency. Partial grant and partial denial of clean air act waiver application submitted by growth energy to increase the allowable ethanol content of gasoline to 15 percent; decision of the administrator. *Federal Register*, 75:68093–68150, 2010.

[114] Peng Geng, Hui Zhang, and Shichun Yang. Experimental investigation on the combustion and particulate matter (PM) emissions from a port-fuel injection (PFI) gasoline engine fueled with methanol – ultralow sulfur gasoline blends. *Fuel*, 145:221–227, 2015.

[115] P Trop, B Anicic, and D Goricanec. Production of methanol from a mixture of torrefied biomass and coal. *Energy*, 77:125–132, 2014.

[116] George A Olah, Alain Goeppert, and GK Surya Prakash. Chemical recycling of carbon dioxide to methanol and dimethyl ether: From greenhouse gas to renewable, environmentally carbon neutral fuels and synthetic hydrocarbons. *Journal of Organic Chemistry*, 74(2):487–498, 2009.

[117] Chao-Cheng Wen and Chein-Hsiun Tu. Vapor–liquid equilibria for binary and ternary mixtures of ethanol, 2-butanone, and 2,2,4-trimethylpentane at 101.3kPa. *Fluid Phase Equilibria*, 258(2):131–139, 2007.

[118] James Turner, Richard Pearson, Ralph Purvis, Eelco Dekker, Kenth Johansson, and Kjell ac Bergström. GEM ternary blends : Removing the biomass limit by using iso-stoichiometric mixtures of gasoline , ethanol and methanol. *SAE Technical Paper 2011-24-0113*.

[119] ML Greenfield, GA Lavoie, CS Smith, and EW Curtis. Macroscopic model of the D86 fuel volatility procedure. *SAE Technical Paper 982724*, 1998.

[120] D86-12: Standard test method for distillation of petroleum products at atmospheric pressure.

[121] Private communication with David LS Hung, 2015.

[122] F Zhao, MC Lai, and DL Harrington. Automotive spark-ignited direct-injection gasoline engines. *Progress in Energy and Combustion Science*, 25(5):437–562, 1999.

[123] Zane van Romunde. Combustion concepts for sustainable premium vehicles: Spray imaging. Technical report, University College London, 2005.

[124] Todd D Fansler and Scott E Parrish. Spray measurement technology: a review. *Measurement Science and Technology*, 26(1):012002, 2015.

[125] Joseph Camm, Richard Stone, Martin Davy, and Dave Richardson. The effect of non-ideal vapour-liquid equilibrium and non-ideal liquid diffusion on multi-component droplet evaporation for gasoline direct injection engines. *SAE Technical Paper 2015-01-0924*, 2015.

[126] OpenFOAM C++ documentation. `www.openfoam.org/docs/cpp/`, accessed 9$^{\text{th}}$February 2016, 2015.

[127] Christopher Price, Arash Hamzehloo, Pavlos Aleiferis, and David Richardson. Aspects of numerical modelling of flash-boiling fuel sprays. *SAE Technical Paper 2015-24-2463*, 2015.

[128] R Issa. Solution of the implicitly discretized fluid flow equations by operator-splitting. *Journal of Computational Physics*, 62:40–65, 1985.

[129] SV Patankar and DB Spalding. A calculation procedure for heat, mass and momentum transfer in three-dimensional parabolic flows. *International Journal of Heat and Mass Transfer*, 15:1787–1806, 1972.

[130] Per Carlsson. Tutorial dieselFoam. Technical report, Luleå University of Technology, 2009.

[131] CHEMKIN | Reaction Design. `http://www.reactiondesign.com/products/chemkin/`, accessed 7$^{\text{th}}$April 2016, 2015.

[132] PJ O'Rourke. Collective drop effects on vaporizing liquid sprays. Technical Report LA-9069-T, Los Alamos National Lab., NM (USA), Nov 1981.

[133] PA Niklas Nordin. *Complex Chemistry Modeling of Diesel Spray Combustion*. PhD thesis, Department of Thermo and Fluid Dynamics, Chalmers University of Technology, 2001.

[134] Matteo Nobile. Improvement of Lagrangian approach for multiphase ow. Technical report, Chalmers University of Technology, 2015.

[135] B Zuo, AM Gomes, and CJ Rutland. Modelling superheated fuel sprays and vaporization. *International Journal of Engine Research*, 1(4):321–336, 2000.

[136] Spray G. `http://www.sandia.gov/ecn/G/targetCondition/sprayG.php`, accessed 7$^{\text{th}}$April 2016, December 2014.

[137] H Chen, DL Reuss, DL Hung, and V Sick. A practical guide for using proper orthogonal decomposition in engine research. *International Journal of Engine Research*, 14(4):307–319, 2013.

[138] Robert H Perry and Don Green. *Perry's Chemical Engineers' Handbook*. New York: McGraw-Hill, 50$^{\text{th}}$edition, 1984.

[139] MS Peckham, A Finch, B Campbell, P Price, and MT Davies. Study of particle number emissions from a turbocharged gasoline direct injection (GDI) engine including data from a fast-response particle size spectrometer. *SAE Technical Paper 2011-01-1224*, 2011.

[140] JD Camm, R Stone, MH Davy, and D Richardson. The modelling of single and multi-component droplet evaporation. *THIESEL 2014 Conference on Thermo- and Fluid Dynamic Processes in Direct Injection Engines, Universitat Politècnica de València, València, Spain.*, 2014.